

Molecular insights in aqueous systems: From electrolyte solutions to aqueous nanoscale interfaces

THÈSE N° 7646 (2017)

PRÉSENTÉE LE 27 AVRIL 2017

À LA FACULTÉ DES SCIENCES ET TECHNIQUES DE L'INGÉNIEUR
CHAIRE JULIA JACOBI DE PHOTOMÉDECINE - LABORATOIRE DE BIOPHOTONIQUE FONDAMENTALE
PROGRAMME DOCTORAL EN PHOTONIQUE

ÉCOLE POLYTECHNIQUE FÉDÉRALE DE LAUSANNE

POUR L'OBTENTION DU GRADE DE DOCTEUR ÈS SCIENCES

PAR

Yixing CHEN

acceptée sur proposition du jury:

Prof. M. Chergui, président du jury
Prof. S. Roke, directrice de thèse
Prof. P. B. Petersen, rapporteur
Prof. T. Weidner, rapporteur
Prof. M. Ceriotti, rapporteur



ÉCOLE POLYTECHNIQUE
FÉDÉRALE DE LAUSANNE

Suisse
2017

To my parents

Acknowledgements

First of all, I would like to express my sincere gratitude to my thesis director Prof. Sylvie Roke. During the past five years, she has always been standing by me, guiding me, and motivating me to overcome all the difficulties in my Ph.D. study and research. Without her continuous support, I would not be able to be here writing this thesis. I could not have imagined having a better advisor and mentor for my Ph.D. study.

Besides my thesis director, I also would like to thank the other members of my thesis committee: Prof. Majed Chergui, Prof. Michele Ceriotti, Prof. Poul B. Petersen, and Prof. Tobias Weidner, for their insightful comments on this thesis and for the inspiring discussion we had during and after the defense. As well, I would like to thank Prof. Paul S. Cremer, Prof. Poul B. Petersen, Prof. Michele Ceriotti, and all our collaborators for their valuable contributions to the work in this thesis.

I would like to thank all my colleagues in the LBP group for their valuable advice and help and most importantly for creating a harmonious, positive working atmosphere. Especially, I would like to thank Cornelis Lütgebaucks, Halil I. Okur, Carlos Macias Romero, and Rüediger Scheu, the great office BM4113. We had so much memorable time in this office, good and bad, easy and hard, sunny and cloudy. I enjoy very much and am proud of working with them.

Also, I would like to thank our secretary Rebecca Veselinov for her countless kind help and supports.

My sincere thanks also go to Jianwen Sun, Yankai Shao, Dong Xia, . . . , all my dear friends, for accompanying me, encouraging me, fighting with me . . . I am so lucky to have them in my life.

Last but not least, I would like to thank my parents, my family for their unre-served and unconditional love and support.

Lausanne, 21 March 2017

Yixing Chen

Abstract

The unique structure and dynamics of the water hydrogen (H)-bond network enable a multitude of structures and chemical reactions in both bulk solutions and at interfaces. The underlying molecular interactions between water and dissolved electrolytes, organic molecules, and nanoscale interfaces are difficult to study and hence not fully understood, especially when it involves interactions of length scales larger than one nanometer. In this thesis, we perform second order nonlinear light scattering experiments to investigate extended hydration shells (over one nanometer) and interfacial structures of buried aqueous interfaces that surround nanodroplets.

We investigate the spatial range of ion-water interactions by probing the molecular structure of the water network in dilute electrolyte solutions. We find that electrolytes induce long-range, non-ion-specific orientational order in the H-bond network of water (over distances up to 70 hydration shells or 20 nm). These modifications in the water network start at electrolyte concentrations as low as 10 μM . The amount of induced orientational order and the concentration at which it occurs is different between light and heavy water. We link the observed ion induced changes in the bulk H-bond network of water to ion induced surface tension anomalies that occur in the same concentration range.

We also study the same interactions in solutions with higher electrolyte concentrations focusing on cations. We observe specific ion effects in both the local charge distribution and water ordering in extended hydration shells of ions. Cations with larger charge densities induce larger changes in these two observables that follow a direct Hofmeister trend. The ion-induced structural changes in the water network are strongly correlated with the viscosity B-coefficient and hydration free energy of cations. These correlations facilitate constructing a better molecular model for specific ion effects in aqueous solutions.

Next, we study the nanoscale hydrophobe/water interface and related interactions by probing the molecular structure of the interface formed with amphiphilic alkanols. We find that alkanols form a fluid film at the oil nanodroplet surface. Long chain alkanols show similar molecular structures and number densities at the inter-

face. With increasing alkanol density, interfacial water loses its initial orientational alignment. The structure of interfacial oil molecules is more distorted for shorter alkanols. This interfacial structure differs significantly from those of macroscopic planar alkanol/water and alkanol/air interfaces and charged surfactant/oil/water interface, which can be explained by the balance between dispersive and H-bonding interactions.

Finally, we develop a new membrane model system: 3D-lipid monolayers with tunable molecular structure on oil nanodroplets in water. This in-situ prepared system mimics the structure of lipid droplets in cells. The interfacial structure of lipids can be tuned from a tightly packed monolayer (liquid condensed phase) to a dilute one (liquid condensed/liquid expanded coexistence phase) by varying the lipid/oil/water ratio. The tunability of the chemical structure, the high surface-to-volume ratio, and the small sample volume make this system ideal for studies of molecular interactions of lipids in membranes.

Keywords: water, electrolytes, lipid, nanoscale interfaces, membrane, specific ion effects, hydrophobicity, second harmonic generation, sum frequency generation, nonlinear light scattering.

Zusammenfassung

Die einzigartige Struktur und Dynamik des Wassernetzwerks durch Wasserstoffbrückenbindungen ermöglicht eine Vielzahl von Strukturen und chemischen Reaktionen sowohl in Bulk-Lösungen als auch an Grenzflächen. Die zugrunde liegenden molekularen Wechselwirkungen zwischen Wasser und gelösten Elektrolyten, organischen Molekülen und nanoskaligen Grenzflächen sind sehr komplex und daher noch nicht vollständig verstanden. Dies gilt vor allem für die Wechselwirkungen, welche einen Wirkradius von mehr als einem Nanometer haben. In dieser Arbeit wenden wir nicht-lineare Lichtstreuungsexperimente der zweiten Ordnung an, um die ausgedehnten Hydratationsschalen (länger als ein Nanometer) und die Struktur der Grenzfläche zwischen Nanotröpfchen und wässrigen Lösungen zu studieren.

Wir untersuchen den dreidimensionalen Raum von Wechselwirkungen zwischen Ionen und Wasser, indem wir die molekulare Struktur des Wassernetzes in verdünnten Elektrolytlösungen bestimmen. Wir finden, dass Elektrolyte eine weitreichende, nicht ionenspezifische Orientierungsordnung im H-Bindungsnetzwerk vom Wasser induzieren (über Distanzen, die äquivalent zu maximal 70 Hydratationsschalen bzw. 20 nm sind). Diese Veränderungen im Wassernetz beginnen bei Elektrolytkonzentrationen von nur 10 μM . Der Umfang der induzierten Strukturveränderung sowie die Elektrolytkonzentration, bei der sie auftritt, ist verschieden für leichtes und schweres Wasser. Die beobachteten ioneninduzierten Veränderungen im H-Bindungsnetz des Wassers verknüpfen wir mit Ionen induzierten Oberflächenspannungsanomalien, welche bei gleichen Elektrolytkonzentrationen auftreten.

Nachfolgend untersuchen wir dieselben Wechselwirkungen in höher konzentrierten Lösungen und betrachten dabei schwerpunktmäßig die Kationen. Wir beobachten spezifische Ionenwirkungen sowohl in der lokalen Ladungsverteilung als auch in der Orientierung von Wassermolekülen, welche sich in der erweiterten Hydratationsschale der Ionen befinden. Kationen mit größeren Ladungsdichten induzieren größere Veränderungen in diesen beiden Parametern. Beide Parameter folgen dabei einem direkten Hofmeister-Trend. Die ioneninduzierten Strukturveränderungen im Wassernetzwerk korrelieren stark mit dem Viskositäts-B-Koeffizienten und der

freien Energie, welche die Hydratation der Kationen beschreibt. Diese Korrelationen erleichtern die Konstruktion eines besseren Modells für spezifische Ionenwirkungen in wässrigen Lösungen auf einer molekulare Ebene.

Als nächstes untersuchen wir die nanoskalige Grenzfläche zwischen hydrophoben Molekülen und Wasser und die damit verbundenen Wechselwirkungen. Dazu sondieren wir die molekulare Struktur der durch amphiphile Alkanole modifizierten Oberfläche. Wir zeigen, dass Alkanole einen flüssigen Film an der Ölnanotröpfchenoberfläche bilden. Langkettige Alkanole zeigen vergleichbare Molekülstrukturen und Anzahldichten an diesen Grenzflächen. Mit zunehmender Alkanoldichte verlieren die Wassermoleküle an der Grenzfläche ihre anfängliche Orientierungsausrichtung. Um so kürzer die Alkanketten der Alkanole sind, desto stärker ist die Struktur der Ölmoleküle an der Grenzfläche verzerrt. Die Grenzflächenstruktur an den Öltröpfchen unterscheidet sich deutlich von der Grenzflächenstruktur makroskopisch planarer Alkanol/Wasser-, Alkanol/Luft- und geladenen Tensid/Öl/Wasser-systemen. Dieser Unterschied kann durch das Gleichgewicht zwischen dispersiven Wechselwirkungen und Wasserstoffbrückenbindungwechselwirkungen erklärt werden.

Anschließend entwickeln wir ein neues Membranmodell-System: 3D-Lipid-Monoschichten mit abstimmbarer Molekülstruktur auf Öl-Nanotröpfchen in Wasser. Dieses in situ vorbereitete System imitiert die Struktur von Lipidtröpfchen in Zellen. Die Grenzflächenstruktur der Lipide kann durch Variation des Lipid/Öl/Wasser-Verhältnisses von einer dicht gepackten Monoschicht (flüssig kondensierte Phase) auf eine verdünnte (flüssig kondensierte/flüssig expandierte Koexistenzphase) abgestimmt werden. Die Abstimbarkeit der chemischen Struktur, das hohe Oberflächen-zu-Volumen-Verhältnis und das geringe Probenvolumen machen dieses System ideal für Untersuchungen von Wechselwirkungen zwischen Lipiden in Membranen auf molekularer Ebene.

Stichwörter: Wasser, Elektrolyte, Lipide, nanoskaligen Grenzflächen, Membranen, spezifische Ioneneffekte, Hydrophobizität, Frequenzverdopplung, Summenfrequenzgeneration, nichtlineare Lichtstreuung

Table of Contents

Acknowledgements	i
Abstract (English/Deutsch)	iii
List of figures	xi
List of tables	xiii
1 Introduction	1
1.1 Water	1
1.2 Electrolyte solutions	2
1.3 Aqueous nanoscale interfaces	4
1.3.1 The transition from hydrophobic to hydrophilic bulk material	5
1.3.2 Lipid monolayers	6
1.4 Nonlinear optical methods	7
1.4.1 Second harmonic scattering	8
1.4.2 Vibrational sum frequency scattering	9
1.5 This thesis	10
I Electrolyte Solutions	13
2 Background of Second Harmonic Scattering	15
2.1 Theoretical background	16
2.1.1 Geometry of SHS	16
2.1.2 SHS from aqueous solutions	17
2.1.3 Symmetry properties of $\beta^{(2)}$	20
2.1.4 Calculation of the incoherent SHS intensity	23
2.1.5 Coherent SHS	28
2.2 Experimental details	28
2.2.1 Experimental setup of fs-ESHS	29

Table of Contents

2.2.2	Characterization of the fs-ESHS system	30
3	Non-specific Ion-water Interactions at Low Ionic Strengths	35
3.1	Introduction	37
3.2	Materials and methods	38
3.2.1	Sample preparation	38
3.2.2	Femtosecond elastic second harmonic scattering	39
3.2.3	Molecular dynamics simulations	40
3.2.4	Surface tension measurements	40
3.3	Results and discussion	41
3.3.1	Femtosecond snapshots of collective effects	41
3.3.2	Induction of structural orientational order by electrolytes	42
3.3.3	Estimate of the spatial range of the perturbation	43
3.3.4	Distortion of the H-bond network over nanoscopic distances . .	50
3.3.5	Origin of the nanoscopic distortions	51
3.3.6	Orientational order probed macroscopically	56
3.4	Conclusions	59
3.5	Appendix	61
3.5.1	Constants and properties of H ₂ O and D ₂ O	61
3.5.2	Mean-field models	61
4	Specific Ion-Water Interactions at High Ionic Strengths	69
4.1	Introduction	70
4.2	Materials and methods	72
4.2.1	Sample preparation	72
4.2.2	Femtosecond elastic second harmonic scattering	72
4.2.3	Molecular dynamics simulations	73
4.2.4	Fitting of the fs-ESHS data	73
4.3	Results and discussions	74
4.3.1	Theory: Expected fs-ESHS response from electrolyte solutions .	74
4.3.2	Experiments: fs-ESHS from electrolyte solutions	79
4.3.3	Macroscopic properties of aqueous solutions of electrolytes . .	83
4.4	Conclusions	87
II	Aqueous Nanoscale Interfaces	89
5	Methods to Probe Aqueous Nanoscale Interfaces	91
5.1	Introduction	92

5.2	Theoretical background	92
5.2.1	Vibrational sum frequency scattering	92
5.2.2	SHS from aqueous nanoscale interfaces	100
5.2.3	Dynamic light scattering	101
5.2.4	Electrokinetic mobility measurements	102
5.3	Experimental details	104
5.3.1	The SFS experimental setup	104
5.3.2	SFS spectra recording	107
5.3.3	SFS spectra analysis	108
5.3.4	SHS measurements of aqueous nanoscale interfaces	108
6	From Hydrophobic to Hydrophilic	111
6.1	Introduction	112
6.2	Materials and Methods	115
6.2.1	Sample preparation	115
6.2.2	Second harmonic scattering measurements	116
6.2.3	Vibrational sum frequency scattering measurements	116
6.3	Results and discussion	117
6.3.1	Surface structure of 1-dodecanol	117
6.3.2	Chain length dependence	122
6.3.3	Concentration dependence: Isotherm and water structure.	124
6.3.4	Interfacial water alignment	126
6.3.5	Full picture of the interfacial structure	128
6.3.6	A comparison to the alkanol/water and alkanol/air interfaces	130
6.4	Conclusions	132
7	Three Dimensional Nano “Langmuir Trough” for Lipid Studies	133
7.1	Introduction	134
7.2	Creation of 3D lipid monolayers on oil nanodroplets	135
7.2.1	Materials	135
7.2.2	3D monolayers on oil nanodroplets	135
7.3	Tunability of 3D lipid monolayers	136
7.4	Surface density and chain orientation of DPPC	138
7.5	The molecular structures of the interfacial oil and water	140
7.5.1	Oil structure	140
7.5.2	Water structure	142
7.6	Conclusions	144

Table of Contents

8 Summary and Outlook	147
8.1 Summary	147
8.2 Outlook	149
Bibliography	182
Curriculum Vitae	183

List of Figures

1.1	Schematic illustration of two hydrogen-bonded water molecules. . . .	1
1.2	Surface tension change as a function of NaCl concentration in water. .	3
1.3	Periodic table of elements, with ions studied in this thesis highlighted.	4
1.4	Structural formulas of alkanol and phospholipid molecules used in this thesis.	5
1.5	Schematic illustration of a Langmuir monolayer.	6
1.6	Schematic illustration of the optical processes in SHG and SFG.	7
2.1	Sketch of the SHS geometry.	16
2.2	Symmetry of the water and benzene molecule.	21
2.3	Illustration of the fs-ESHS experimental setup	29
2.4	Characterization of incident fs-laser pulses.	30
2.5	Elastic and inelastic SHS.	31
2.6	Response of the fs-ESHS system.	32
3.1	Snapshots of long-range perturbations in aqueous NaCl solutions. . . .	42
3.2	Sketch of the relevant parameters needed in the phenomenological discussion.	45
3.3	$\Delta I(2\omega)$ as a function of domain size and relative structural anisotropy.	49
3.4	Nonspecific long-range changes in the H-bond network of water. . . .	51
3.5	Nuclear quantum effects.	53
3.6	MD simulations of orientational order in the H-bond network of water.	55
3.7	Macroscopic manifestation of orientational order in the H-bond network of aqueous electrolyte solutions.	58
3.8	Mean-field models and temperature dependence.	66
4.1	Illustration of possible contributions to the fs-ESHS response of electrolyte solutions.	75
4.2	Computed SH intensities from electrolyte solutions.	79
4.3	Measured SSS fs-ESHS intensities of electrolyte solutions.	81

List of Figures

4.4	Measured PPP fs-ESHS intensities of electrolyte solutions.	82
4.5	Correlations between fs-ESHS intensity increase and viscosity B-coefficient.	84
4.6	Correlations between fs-ESHS intensity increase and hydration free energy of electrolytes.	86
5.1	Sketch (top view) of the SFS geometry.	93
5.2	Illustration of symmetric and antisymmetric stretch modes of the CH ₃ and CH ₂ groups.	99
5.3	Retrieval of the particle size from DLS measurements.	102
5.4	Schematic illustration of the electrical double layer.	103
5.5	Illustration of the SFS experimental setup.	105
5.6	Typical VIS and IR pulses used in the SFS experiment.	106
6.1	Thermodynamic data of solute transfer.	113
6.2	The surface structure of 1-dodecanol and hexadecane at the hexadecane nanodroplet/water interface.	117
6.3	Calculated SFS electrical field amplitude ratios	120
6.4	Calculated r^+/r^- amplitude ratio as a function of the average tilt angle ϕ of the end methyl group of the alkyl chain with respect to the surface normal.	121
6.5	The surface structure of alkanols of different lengths at the hexadecane nanodroplet/water interface.	122
6.6	The surface structure of hexadecane at the hexadecane nanodroplet/water interface with alkanols of different lengths.	123
6.7	Isotherm of hexanol.	124
6.8	Water alignment at the hexadecane/hexanol/water interface.	128
6.9	Possible surface structures of 1-hexanol and 1-dodecanol.	129
7.1	The surface structure of DPPC at the hexadecane nanodroplet/water interface.	137
7.2	Surface density and average tilt angle of the DPPC chains.	139
7.3	The molecular structure of interfacial oil covered with a DPPC monolayer.	141
7.4	Hydration of DPPC monolayers.	142

List of Tables

3.1	Domain radius (R), corresponding number of hydration shells, and anisotropy (η) in case the domain size is determined only by the average ion separation.	49
3.2	Constants and properties of H_2O and D_2O	61
4.1	Effective ionic radii used for calculations of the incoherent SH intensity from individual ions in Fig. 4.2A.	78
4.2	Empirical rate and onset of the increase of fs-ESHS intensities obtained from the linear fits to the fs-ESHS data in Figs. 4.3 and 4.4.	80
4.3	Viscosity B-coefficients and hydration free energy values of chloride salts for Figs. 4.5 and 4.6.	83
6.1	Fitted frequency, amplitude, and linewidth of the 1-dodecanol and hexadecane spectra of the hexadecane nanodroplet/1-dodecanol/water interface (Fig. 6.2).	118
6.2	Refractive index elements used for the calculation of the SFS electrical field.	119
7.1	Fitted frequency, amplitude, and linewidth for the DPPC spectra in the C-H stretch region of the hexadecane nanodroplet/DPPC/water interface of Fig. 7.1.	138
7.2	Fitted frequency, amplitude, and linewidth for the DPPC spectrum in the P-O stretch region of the hexadecane nanodroplet/DPPC/water interface with 1 mM DPPC in the solution.	143

1 Introduction

1.1 Water

“A colorless, transparent, odorless, liquid which forms the seas, lakes, rivers, and rain and is the basis of the fluids of living organisms” is the definition of water in the Oxford dictionary¹. Water is omnipresent in nature. It covers 71% of the Earth’s surface; it composes roughly 60% of the human body. One of the most important and indispensable functions of water in nature is to dissolve different substances and allow various biological processes as well as physical and chemical processes to occur. As the universal solvent on Earth, water provides an essential environment for the birth and evolution of life. There is no wonder that water is called the “matrix of life”.²

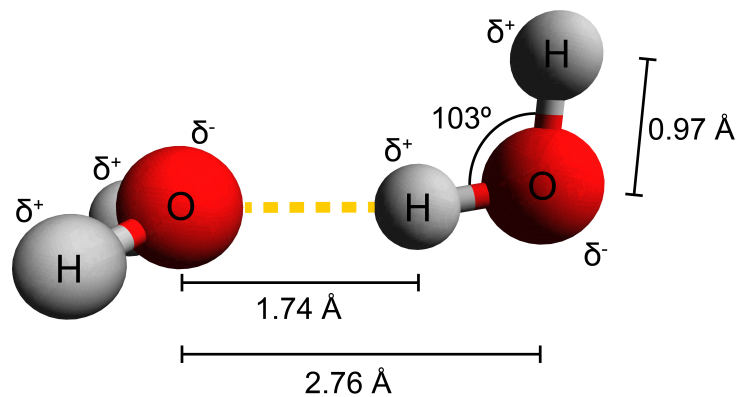


Figure 1.1 – Schematic illustration of two hydrogen bonded water molecules. The two water molecules are hydrogen bonded as indicated by the yellow dashed line. The properties of the water molecules noted in the figure are obtained from Ref.³.

Water is simple in molecular structure, composed of only one oxygen (O) and two hydrogen (H) atoms. Figure 1.1 shows a schematic illustration of two water

molecules connected by a hydrogen (H)-bond. Despite the simple three-atom structure, water presents extraordinarily complicated physical and chemical properties due to its ability to form H-bonds and its amphoteric nature.³ One example is that the density of ice is lower than that of liquid water at 0 °C and standard atmospheric pressure. As a consequence, ice can float on top of water. In contrast, the solid state of almost every other compound is heavier (denser) than its liquid state. The complicated properties of water make the solvation of different substances and their interactions in water intricate and elusive.

1.2 Electrolyte solutions

One of the most fundamental and long-standing questions about aqueous solutions is how electrolytes interact with water. Electrolyte solutions are ubiquitous and the basis of complicated biological aqueous systems, where ions are present in solutions and as functional groups on proteins, peptides, lipids, sugars and other macromolecules. The hydration of ionic groups is related to various physiologically, medically, and chemically relevant processes. Examples are protein folding and precipitation, enzyme, ion channel, or ion pump activity, the action potentials generation, the transport across membranes, self-assembly processes, interfacial charging, and aerosol formation.⁴⁻⁸ Physical properties of electrolyte solutions also depend on the electrolyte. Examples are the surface tension⁹, viscosity¹⁰, and hydration free energy^{11,12}. In this thesis, we will treat two open questions that are crucial for understanding the interaction between electrolytes and water:

1. What is the spatial range of the interaction of ions with liquid water?
2. What is the connection between the molecular structure and the macroscopic properties that are influenced by electrolytes, such as the surface tension, viscosity, and hydration free energy? Are these long-range or only short-range?

Many previous experiments^{13,14} and simulation studies^{13,15,16} of the molecular structure and dynamics in electrolyte solutions showed that ions induce a short-range perturbation in the structure and dynamics of water, up to the third hydration shell.[†] The underlying interaction is mainly the charge-dipole interaction between the ion and water molecules. Specific ion effects are observed at electrolyte concentrations above ~0.1 M.¹⁷ They constitute ion-specific changes in a physical or chemical property, such as the surface tension, solubility, aggregation, or reactivity. Specific

[†] We will refer to short-range when the interaction occurs within one nanometer, and refer that > 1 nm to long-range.

ion effects have been the topic of many recent studies^{5,18–21} and are important to understanding a multitude of biochemical processes.

Long-range ion induced effects are less well studied and are often shrouded in controversy. One effect that is of particular interest to this thesis is the Jones-Ray effect. Jones and Ray reported on the surface tension of 13 different aqueous electrolyte solutions at low ionic strengths.^{22–26} They measured, using the capillary rise method, that the surface tension gradually decreases, reaching a minimum at ~1 mM, after which it levels off and finally increases at ionic strengths above ~100 mM. The data of NaCl solutions measured by Jones and Ray²⁵ is plotted in Fig. 1.2.

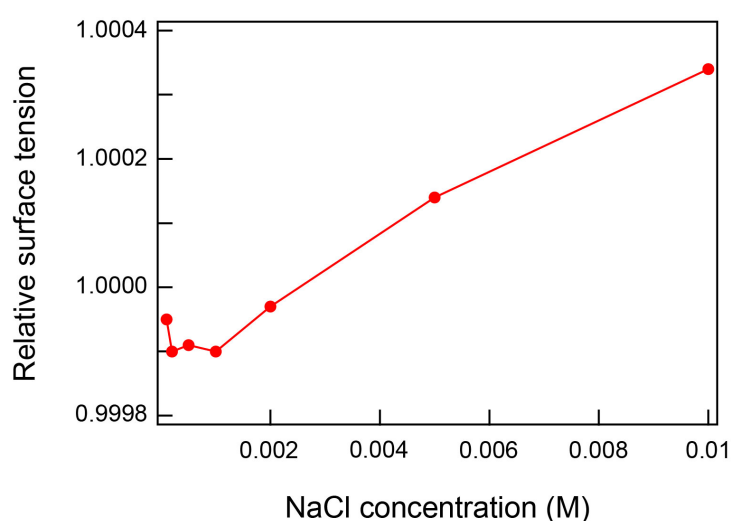


Figure 1.2 – Surface tension change as a function of NaCl concentration in water. The surface tension of NaCl solutions was measured by the capillary rise method by Jones and Ray. This data is adapted with permission from Ref.²⁵. Copyright 2017 American Chemical Society.

Surface tension reports on the free energy of an interface. As such, a lowering of the surface tension suggests that the excess of ions at the interface increases,²⁷ meaning that there is some kind of ion binding. The data measured by Jones and Ray is therefore controversial because it seems to suggest that there is some preferential unspecific concentration dependent binding of ions^{28,29} or ion pairs³⁰ at the interface. This behavior seemingly contradicts expectations: Ions are preferentially hydrated, and thus not surface active at low concentrations^{31,32}. In addition, as a confirmation of the previous statement, ions increase the surface tension at high salt concentrations.^{27,33} Currently, even though Jones and Ray made their first observation in 1935, and despite many studies on this topic,^{9,29,34–42} it is still controversial. Questions that are commonly asked revolve around the validity of the effect and its possible physical origin.

Periodic Table of Elements																	
IA																	
1	H ⁺																
3	Li ⁺															VIIA	
11	Na ⁺	12	Mg ²⁺													17	Cl ⁻
19	K ⁺	20	Ca ²⁺													35	Br ⁻
37	Rb ⁺	38	Sr ²⁺													53	I ⁻
55	Cs ⁺																

Polyatomic Ions

ammonium	NH ₄ ⁺	dihydrogen phosphate	H ₂ PO ₄ ⁻
hydroxide	OH ⁻	sulphate	SO ₄ ²⁻
nitrate	NO ₃ ⁻	thiocyanate	SCN ⁻
perchlorate	ClO ₄ ⁻	thiosulphate	S ₂ O ₃ ²⁻

Figure 1.3 – Periodic table of elements, with ions studied in this thesis highlighted.

In the first part of this thesis, we will present studies of the molecular structure of electrolyte solutions probed with femtosecond elastic second harmonic scattering (fs-ESHS), a second-order nonlinear optical method. Figure 1.3 shows a periodic table of elements, in which the ions that were studied in this thesis are highlighted. We will discuss the ion-water interactions based on our experimental observations and theoretical modeling and try to shed some new light on the above two fundamental questions concerning electrolyte solutions.

1.3 Aqueous nanoscale interfaces

Another aqueous system of great importance in nature is the aqueous nanoscale interface. An aqueous nanoscale interface is a boundary between water and an insoluble substance with a nanoscopic size. Transitions between the hydrophilic and hydrophobic environments take place at the interface. An aqueous nanoscale interface can be the membrane in a cell, mainly composed of various lipids,⁴³ and can also be the surface of nanoparticles/droplets dispersed in water⁴⁴. As interfaces are two dimensional and often exhibit different physical and chemical properties, they play important roles in structural transformations, transport phenomena and reactivities.^{4,27,45} Nanoscale droplets embedded in aqueous phases are important constituents of many systems. Examples are emulsions in food, agriculture and medical products, adiposomes (lipid droplets) in living cells and miniature vessels for synthesis and reactions.^{45,46} Since it has been demonstrated only recently that

such interfaces could be studied with molecular level precision⁴⁷, many aspects of the physico-chemical properties of these systems are unknown.

One system of great interest is that of hydrophobic oil droplets in water. Two topics are of particular interest in the frame of this thesis.

1. In such a system, how does the molecular structure evolve from the aqueous phase to the hydrophobic phase?
2. Can small droplets be used to develop a platform for more realistic molecular level membrane studies?

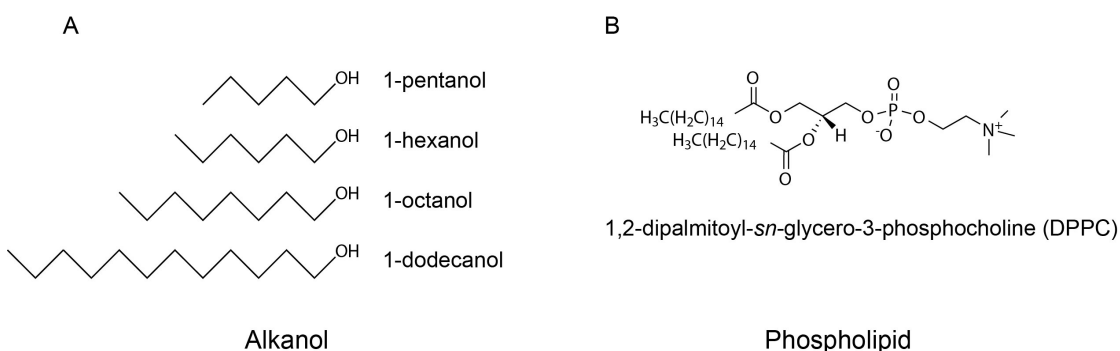


Figure 1.4 – Structural formulas of alkanol and phospholipid molecules used in this thesis. (A) Structural formulas of alkanols. (B) Structural formula of DPPC.

1.3.1 The transition from hydrophobic to hydrophilic bulk material

The quantitative study of the hydrophobe/water interface and related interactions started with interfacial tension studies on insoluble monolayers over a century ago.^{48–50} Based on these studies, it was suggested that amphiphilic molecules can lower the energy of the interface and thus are surface active. Alkanols are uncharged amphiphilic molecules consisting of a hydrophobic hydrocarbon chain and a hydrophilic hydroxyl (OH) group (see the structural formulas in Fig. 1.4A). As such, they are the simplest molecules to facilitate the formation of a hydrophobic/hydrophilic interface. Several studies have been performed at the water/alkanol/oil interface. These studies^{51–57} painted a picture of an alkanol layer that is highly structured, forming even crystalline domains that facilitate the transition from the water to the oil phase. It is not clear whether the exact same structures are found around small droplets.

In the second part of this thesis, we will present a molecular level in-situ study of the transition from a hydrophobic to an aqueous phase at the nanoscale

interface by using vibrational sum frequency scattering (SFS) and second harmonic scattering (SHS). A full molecular level insight into the molecular structural aspects of the transition will be provided.

1.3.2 Lipid monolayers

Another type of molecules that is often found in nature and plays a very important role in facilitating life is the phospholipid molecule. Phospholipid molecules (as illustrated in Fig. 1.4B) consist of, like alkanols, a hydrophilic headgroup and a hydrophobic tail. They form bilayer membranes in aqueous solutions and monolayer structures at aqueous hydrophobic interfaces. Membrane studies on the molecular level are often performed using Langmuir monolayers as a model system (as illustrated in Fig. 1.5). Despite their advantages, such as an easy access to the interface and phase tunability of the Langmuir monolayer, Langmuir troughs also have a number of drawbacks. One main drawback is the small surface area of Langmuir troughs relative to their large sample volume (e.g. the Microtrough XS from Kibron⁵⁸ has a surface area of 135.7 cm² and a sample volume of 145 mL). As a consequence, large amounts of often hard to come by biomolecules are needed. In addition, limitations on the available purity of biomolecules (lipids, > 99%; proteins, ~ 95%) results in unavoidable concerns regarding cleanliness and reproducibility/reliability. The presence of air as one of the contact media also leads to an environment that is not very close to most membrane environments. Meanwhile, in this environment, unsaturated lipids and compounds (such as cholesterol) are not stable in the Langmuir monolayer due to oxidation.⁵⁹

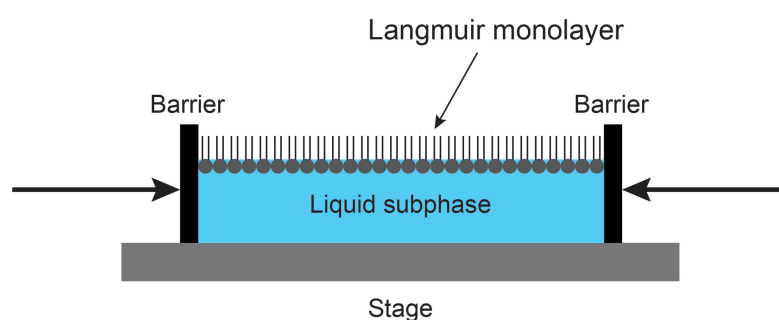


Figure 1.5 – Schematic illustration of a Langmuir monolayer.

In the last part of this thesis, we will present a new membrane model system for in-situ lipid studies: phospholipid monolayer on oil nanodroplets in water, which mimics the structure of a lipid droplet⁶⁰. We will use 1,2-dipalmitoyl-*sn*-glycero-3-phosphocholine (DPPC, see the structural formula in Fig. 1.4B) as a model lipid. This

membrane model system has a surface area of 18 cm^2 in a typical volume of $60 \text{ }\mu\text{L}$, is prepared in solution, and thus solves the above-mentioned issues.

1.4 Nonlinear optical methods

Second-order nonlinear optical methods are surface sensitive optical techniques that are used to probe the molecular level structure at interfaces. In the next section, we will introduce these methods in brief. Further information is provided in Ch. 2 and 5.

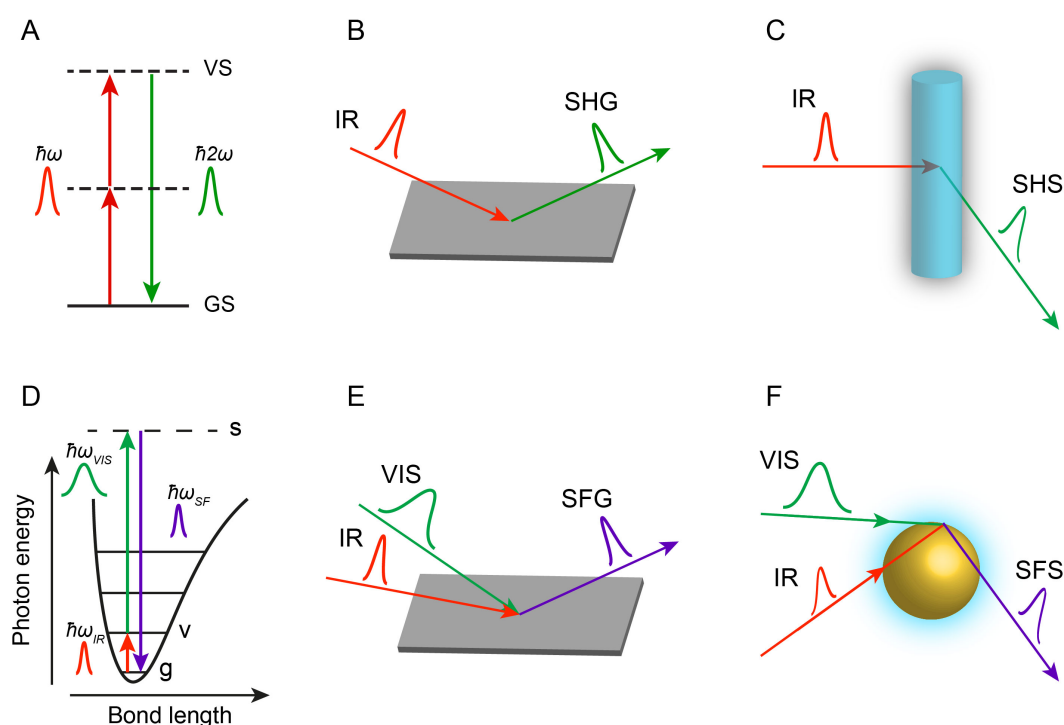


Figure 1.6 – Schematic illustration of the optical processes in SHG and SFG. (A) Illustration of the energy level transition in SHG. Two incident photons with the same frequency ω excite a molecule from the ground state GS to a virtual state VS (red arrows). Subsequently, the molecule returns (green arrow) to the ground state GS with an emission of a photon with the frequency 2ω . (B) The geometry of SHG at a planar surface. (C) The geometry of SHS in a bulk medium. (D) Illustration of the energy level transition in SFG. It shows the potential energy surface of a molecular vibrational mode. The incident infrared (IR) photon is resonant with the vibrational mode, resulting in an excitation (red arrow) of the molecular vibration. This molecular vibration is upconverted to a virtual state (green arrow) by a nonresonant interaction with the incident visible (VIS) photon. Subsequently, the molecule returns to the initial ground state (purple arrow) with an emission of a photon with the sum frequency of the IR and VIS photons. (E) The geometry of SFG at a planar surface. (F) The geometry of SFS at a nanoscale interface.

1.4.1 Second harmonic scattering

Second harmonic generation (SHG) is a second-order nonlinear optical process discovered by Franken and co-workers⁶¹ in 1961. Figure 1.6A shows a schematic illustration of the molecular transitions involved in the optical process. Two incident photons with the same frequency ω excite a molecule from the ground state GS to a virtual state VS. Subsequently, the molecule returns to the ground state with an emission of a photon with the second harmonic (SH) frequency 2ω . As a second-order nonlinear optical process, SHG is forbidden in a medium with centrosymmetry under the electric-dipole approximation.^{62,63} Therefore, SHG possesses a specific sensitivity to noncentrosymmetric spatial symmetry. SHG is used, for example, as a way to generate tunable femtosecond (fs) laser pulses^{64–66}, or to probe non-centrosymmetric structures in inorganic crystals⁶⁷, protein crystals⁶⁸, cells⁶⁹, tissues and organisms⁷⁰. Since the centrosymmetry is necessarily broken along the normal direction of an interface, SHG is a powerful surface-specific tool to characterize interfaces between isotropic media with molecular level details. Bloembergen and Pershan⁷¹ first considered and theoretically formulated surface SHG in 1962. Following this early work, the theory of surface SHG has been well developed.^{72–75} Since its first employment to probe surface molecular monolayers in 1969 by Brown and Matsuoka⁷⁶, SHG has been broadly used in studies of various planar surfaces/interfaces including solid/liquid and solid/gas^{77,78}, solid/solid⁷⁹, liquid/gas^{9,80}, liquid/liquid⁸⁰, and solid/liquid⁸⁰ interfaces. Figure 1.6B shows a schematic illustration of SHG at a planar surface.

SHG can also occur in a bulk medium, such as in pure water as illustrated in Fig. 1.6C. In this case, SH photons are generated and scattered by individual molecules that have a non-centrosymmetric electronic structure. Second harmonic scattering (SHS) was first observed in water by Terhune *et al.* in 1965.⁸¹ This type of SHS was explained to arise from isotropically distributed non-centrosymmetric water molecules. It is also commonly referred to as hyper-Rayleigh scattering (HRS).⁸² The theory of HRS was first proposed by Cyvin *et al.*⁸³ in 1965 and then generalized by Bersohn *et al.*⁸⁴ and Kauranen and Persoons⁸⁵. The SH light of HRS originates from molecules that are not correlated in their spatial (orientational) positions. Therefore, there is no fixed phase relationship between the generated SH photons and the HRS intensity is linearly proportional to the number density of the molecules.⁸⁶

HRS has been used in the optical characterization of minerals⁸⁷ and the determination of the hyperpolarizability of noncentrosymmetric molecules.^{86,88} The derivation of the HRS intensity from aqueous solutions will be presented in detail in Ch. 2.

In addition to SHS from uncorrelated molecules, SHS can also originate from correlated molecules.⁸⁴ Molecules are spatially correlated by, for example, being present at the same interface. In this case, the optical process is coherent and the SHS intensity depends quadratically on the number density of correlated molecules.⁸² The theory of SHS from nanoscale interfaces was first worked out for metal particles⁸⁹ as a nonlinear extension of the linear Mie scattering in 1980's. This theory was then developed extensively for dielectric particles.^{90–98} Experimentally, SHS from colloidal particles in water was first demonstrated in 1996 by Wang *et al.*,⁹⁹ in which the resonant SH light originated from malachite green molecules (a water-soluble dye) adsorbed to the particle surface. Since then, resonant coherent SHS has been widely used to probe the adsorption kinetics of molecules and to probe metallic nanoparticles (see the review articles Refs.^{82,98,100,101}). In 1998, Yan *et al.*¹⁰² first used nonresonant SHS to probe interfacial water molecules to obtain the surface potential and charge of polystyrene particles in water. Following that, several studies have been performed in which the orientational order of water at nano- and micro-particle surfaces was probed.^{103–113}

1.4.2 Vibrational sum frequency scattering

Vibrational sum frequency generation (SFG) is a second-order nonlinear optical process that involves the generation of a photon at the sum frequency (SF) of the two incident photons. Figure 1.6D shows an illustration of the optical transitions involved in an SFG process. An infrared (IR) beam and a visible (VIS) beam with frequency $\omega_{IR}, \omega_{VIS}$ and wavevectors $\mathbf{k}_{IR}, \mathbf{k}_{VIS}$ respectively are incident on a material. The incident IR photon is resonant with a vibrational mode of the molecule, resulting in an excitation (red arrow) of the molecular vibration. The molecule is upconverted to a virtual state (green arrow) by the incident nonresonant VIS photon. Subsequently, the molecule returns to the initial ground state (purple arrow) with an emission of a photon with the sum frequency of the IR and VIS photons. By tuning the wavelength of the incident IR beam, SFG can be used to selectively probe the vibrational modes of specific molecules. Similar with SHG, SFG can be used to probe surfaces/interfaces with a high sensitivity. To probe surfaces/interfaces, two geometries can be employed: reflection (Fig. 1.6E) or scattering (Fig. 1.6F). The development of the theory of surface SFG dates back to the early work by Bloembergen and Pershan⁷¹. Subsequently, the theory has been developed extensively in 1980's and 1990's.^{75,114–116} First SFG setups were built in the late 1980's and early 1990's to probe macroscopic planar surfaces by measuring the reflected or transmitted SF light.^{78,117–124} During

the last decades, surface SFG has been broadly applied in studies of various planar interfaces, such as the air/water interface^{9,125–132}, solid/liquid and liquid/liquid interfaces^{80,127,131,133,134}. However, these traditional methods in a reflection or transmission geometry cannot be applied to nanoscale interfaces for in-situ studies of particle and droplet interfaces.⁸² Vibrational sum frequency scattering (SFS) from a suspension of submicron particles was first demonstrated in 2003 by Roke *et al.*¹³⁵. SFS combines SFG with light scattering. In the experiment (Fig. 1.6F), an IR and VIS beam overlap in a dispersion of particles. SF photons are generated at the particle surface. These generated SF photons are scattered and detected. Using nonlinear light scattering theories^{94,95,136,137}, the molecular structure of the nanoscale interfaces and the morphology of the particles can be retrieved. SFS studies have been used to obtain molecular level insight into interfacial phenomena on nanoscopic oil droplets^{47,104,109,110,135,138}, colloidal particles^{139–141}, vesicles and liposomes^{111,142}. Fundamental differences between nanoscale interfaces and macroscopic planar interfaces were found.^{103,105,110,111,138,143}

1.5 This thesis

This thesis consists of two parts and is structured as follows:

Part I consists of 3 chapters (Ch. 2 - 4). In Part I, we focus on electrolyte solutions and try to address the aforementioned questions concerning ion-water interactions. We study ion-induced structural changes in the water network primarily using fs-ESHS supplemented with surface tension measurements and theoretical modeling.

In Ch. 2, we will provide a detailed description of the theoretical background and experimental details of fs-ESHS measurements of electrolyte solutions. The first section of the chapter introduces the fundamental concepts of SHS and theoretical calculations of the SHS intensity from liquids. The second section describes our fs-ESHS experimental setup along with a systematic characterization of the setup.

In Ch. 3, we will present a multi-scale investigation of the bulk and surface of aqueous electrolyte solutions at low ionic strengths (1 μ M-100 mM). This study extends from nanoscopic length scales, using bulk and interfacial femtosecond second harmonic measurements, to the macroscopic scale, using surface tension measurements. We find that electrolytes induce orientational order at concentrations starting at 10 μ M that causes nonspecific changes in the surface tension of dilute electrolyte solutions. Aside from ion-dipole interactions, collective hydrogen-bond interactions are crucial and explain the observed difference of a factor of 6 between light and heavy

water.

In Ch. 4, we will present our study of specific water ordering in extended hydration shells around cations in concentrated electrolyte solutions (0.1 - 4 M, or up to solubility limits). fs-ESHS is used to assess chemical effects at molecular and nanoscopic length scales, probing changes in the charge distribution around ions as well as the structural orientational order of water molecules in the extended hydration shells. The viscosity and free energy of hydration of electrolyte solutions are used to assess changes on the macroscopic level.

Part II consists of 3 chapters (Ch. 5 - 7). In Part II, we focus on molecular interactions at aqueous nanoscale interfaces. We study the molecular structure and interactions at various nanoscale interfaces with different chemical components, including alkanol and phospholipid molecules. SFS is employed to selectively probe the interfacial structure of the dissolved substances on the molecular level and SHS is used to probe the interfacial water ordering.

In Ch. 5, we will provide the theoretical background of the experimental methods employed in our research of aqueous nanoscale interfaces. Specifically, theories of SFS and SHS, dynamic light scattering and electrokinetic mobility measurements of aqueous nanoscale interfaces will be introduced in detail. Experimental details of SFS and SHS measurements of aqueous nanoscale interfaces will be provided.

In Ch. 6, we will present our study of the molecular structure of the hexadecane droplet/alkanol/water interface using SFS and SHS. This combination of methods allows us to investigate the interfacial alkyl chain conformation of the oil and alkanols, ranging from 1-pentanol to 1-dodecanol, the orientational distribution of the methyl groups, the surface density of the alkanols, as well as the orientational alignment of interfacial water molecules. The found interfacial structures differ significantly from those of the planar alkanol/water and alkanol/air interfaces and charged surfactant/oil/water interface.

In Ch. 7, we will present a new membrane model system: three-dimensional-phospholipid monolayer on oil nanodroplets, composed of hexadecane, DPPC, and water. This in-situ prepared membrane model system has controllable molecular surface properties and mimics lipid droplets in cells. We characterize the molecular interfacial structure of this nanoscopic system by using SFS and SHS.

Finally, in Ch. 8, we will provide a summary of this thesis as well as an outlook.

The work in Ch. 3 of this thesis represents a collaboration with the following people:

Dr. Halil I. Okur and Prof. Dr. Paul S. Cremer (Fig. 3.7C) *from the Laboratory for Biointerfaces at Pennsylvania State University, headed by Prof. Dr. Paul S. Cremer;*

Prof. Dr. Poul B. Petersen (Fig. 3.7B) *from the Petersen Group at Cornell University, headed by Prof. Dr. Poul B. Petersen;*

Dr. Gabriele Tocci, Dr. Chungwen Liang, and Prof. Dr. Michele Ceriotti (Figs. 3.6 and 3.8A) *from the Laboratory of Computational Science and Modeling at École Polytechnique Fédérale de Lausanne (EPFL), headed by Prof. Dr. Michele Ceriotti;*

Dr. David M. Wilkins (Fig. 3.8A) *from the Manolopoulos Group at University of Oxford, headed by Prof. Dr. David E. Manolopoulos.*

Electrolyte Solutions

Part I

2 Background of Second Harmonic Scattering

Second harmonic scattering is the key technique used in our studies of electrolyte solutions. In this chapter, we will provide the theoretical background representing the state of the art and experimental details of femtosecond elastic second harmonic scattering measurements of electrolyte solutions.

2.1 Theoretical background

2.1.1 Geometry of SHS

Figure 2.1 shows a sketch of the SHS geometry. An aqueous solution is illuminated with a fundamental beam with frequency ω and wavevector \mathbf{k}_1 . The fundamental beam propagates along the Z -axis. The XZ -plane defines the scattering plane. The generated SH beam with frequency 2ω and wavevector \mathbf{k}_0 is detected at a scattering angle θ in the scattering plane. The scattering vector \mathbf{q} is defined as $\mathbf{q} \equiv \mathbf{k}_0 - 2\mathbf{k}_1$. The polarization state of the fundamental/SH beam is described by the angle α/γ between the electrical field and the horizontal scattering plane. P/S refers to the light polarization direction parallel/perpendicular to the scattering plane. The probed molecules are described in a right-handed Cartesian coordinate system (a, b, c) as illustrated in Fig. 2.1.

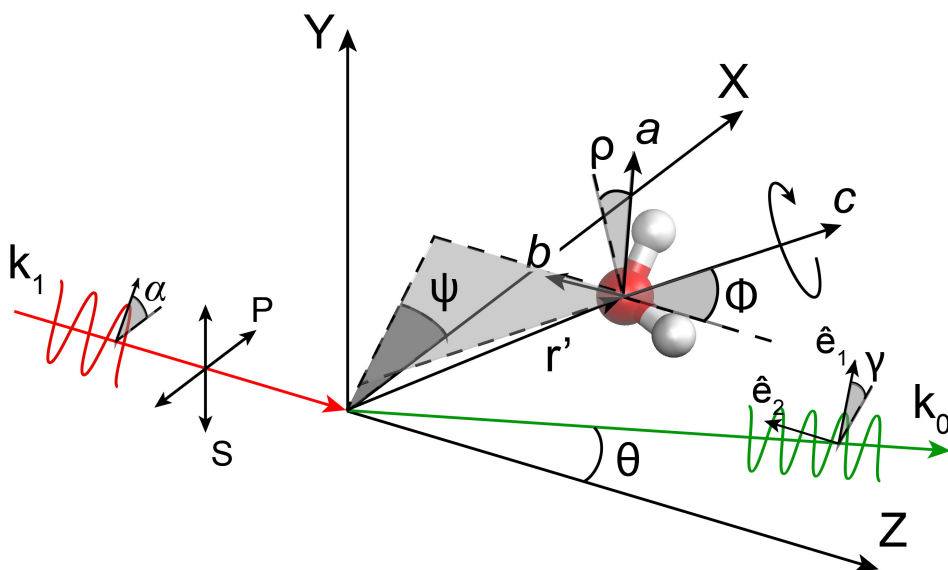


Figure 2.1 – Sketch of the SHS geometry. An aqueous solution is illustrated with a fundamental beam with the frequency ω and wavevector \mathbf{k}_1 . The generated SH beam with wavevector \mathbf{k}_0 is detected at a scattering angle of θ in the scattering plane (XZ -plane). (X, Y, Z) and (a, b, c) coordinate systems define the lab frame and molecular frame, respectively. P/S refers to the light polarization direction parallel/perpendicular to the scattering plane.

The relation between the lab frame (X, Y, Z) and the molecular frame (a, b, c)

is given by

$$\begin{aligned}
 \hat{\mathbf{X}} &= (\cos \phi \cos \psi \cos \varrho - \sin \psi \sin \varrho) \hat{\mathbf{a}} + (-\sin \psi \cos \varrho - \cos \phi \cos \psi \sin \varrho) \hat{\mathbf{b}} \\
 &\quad + \sin \phi \cos \psi \hat{\mathbf{c}} \\
 \hat{\mathbf{Y}} &= (\cos \phi \sin \psi \cos \varrho - \cos \psi \sin \varrho) \hat{\mathbf{a}} + (\cos \psi \cos \varrho - \cos \phi \sin \psi \sin \varrho) \hat{\mathbf{b}} \\
 &\quad + \sin \phi \sin \psi \hat{\mathbf{c}} \\
 \hat{\mathbf{Z}} &= -\sin \phi \cos \varrho \hat{\mathbf{a}} - \sin \phi \sin \varrho \hat{\mathbf{b}} + \cos \phi \hat{\mathbf{c}}
 \end{aligned} \tag{2.1}$$

ϕ , ψ , and ϱ are the three Euler angles as defined in Fig. 2.1. \mathbf{k}_0 , \mathbf{k}_1 , X - and Z -axis all lie in the same horizontal plane. $\hat{\mathbf{X}}$, $\hat{\mathbf{Y}}$, $\hat{\mathbf{Z}}$ represent the unit vectors along the X , Y , Z axes in the lab frame. $\hat{\mathbf{a}}$, $\hat{\mathbf{b}}$, $\hat{\mathbf{c}}$ represent the unit vectors along the a , b , c axes in the molecular frame.

2.1.2 SHS from aqueous solutions

In aqueous solutions, the SHS light originates from second-order molecular dipoles $\tilde{\mathbf{p}}^{(2)}$ that are induced by the electrical field $\tilde{\mathbf{E}}(\omega)$ of the incident fundamental beam. The general expression of $\tilde{\mathbf{p}}^{(2)}$ is given by

$$\tilde{\mathbf{p}}^{(2)} = \boldsymbol{\beta}^{(2)} : \tilde{\mathbf{E}}(\omega) \tilde{\mathbf{E}}(\omega) \tag{2.2}$$

where the second-order hyperpolarizability $\boldsymbol{\beta}^{(2)}$ is a rank-3 tensor that characterizes the SH response of the molecule. The detected SH field represents the sum of the SH fields emitted from individual induced molecular dipoles. In what follows, we present the theoretical derivation of the measured SHS intensity.

We define, in the frequency domain, the electrical field of a linearly polarized incident fundamental beam at the position of a molecule as

$$\tilde{\mathbf{E}}(\omega) = \mathbf{E}(\omega) e^{i\mathbf{k}_1 \cdot \mathbf{r}'} = E_0 (\cos \alpha \hat{\mathbf{x}} + \sin \alpha \hat{\mathbf{y}}) e^{i\mathbf{k}_1 \cdot \mathbf{r}'} \tag{2.3}$$

where α is the angle between $\tilde{\mathbf{E}}(\omega)$ and the X -axis (Fig. 2.1) that indicates the polarization state of the fundamental beam. The fundamental beam is propagating with a frequency ω and a wavevector \mathbf{k}_1 and has an amplitude of E_0 . \mathbf{r}' denotes the position of the molecule. $(\mathbf{k}_1 \cdot \mathbf{r}')$ in the exponential term of Eq. 2.3 represents the phase of the fundamental beam at the position of the molecule.

Inserting Eq. 2.3 into Eq. 2.2, we obtain the three orthogonal components of

the induced second-order molecular dipole, $\tilde{\mathbf{p}}^{(2)}$, in the lab frame (X, Y, Z) as

$$\begin{aligned}
 \tilde{p}_X^{(2)} &= p_X^{(2)} e^{i2\mathbf{k}_1 \cdot \mathbf{r}'} \\
 &= E_0^2 e^{i2\mathbf{k}_1 \cdot \mathbf{r}'} \left(\beta_{XYY}^{(2)} \sin^2 \alpha + \beta_{XXX}^{(2)} \cos^2 \alpha + \beta_{XYX}^{(2)} \sin \alpha \cos \alpha + \beta_{XXY}^{(2)} \sin \alpha \cos \alpha \right) \\
 \tilde{p}_Y^{(2)} &= p_Y^{(2)} e^{i2\mathbf{k}_1 \cdot \mathbf{r}'} \\
 &= E_0^2 e^{i2\mathbf{k}_1 \cdot \mathbf{r}'} \left(\beta_{YY Y}^{(2)} \sin^2 \alpha + \beta_{YXX}^{(2)} \cos^2 \alpha + \beta_{YYX}^{(2)} \sin \alpha \cos \alpha + \beta_{YXY}^{(2)} \sin \alpha \cos \alpha \right) \\
 \tilde{p}_Z^{(2)} &= p_Z^{(2)} e^{i2\mathbf{k}_1 \cdot \mathbf{r}'} \\
 &= E_0^2 e^{i2\mathbf{k}_1 \cdot \mathbf{r}'} \left(\beta_{ZYY}^{(2)} \sin^2 \alpha + \beta_{ZXX}^{(2)} \cos^2 \alpha + \beta_{Z Y X}^{(2)} \sin \alpha \cos \alpha + \beta_{Z X Y}^{(2)} \sin \alpha \cos \alpha \right)
 \end{aligned} \tag{2.4}$$

Here, the molecular hyperpolarizability $\boldsymbol{\beta}^{(2)}$ is given with respect to the lab frame (X, Y, Z) . The conversion of $\boldsymbol{\beta}^{(2)}$ from the molecular frame (a, b, c) into the lab frame (X, Y, Z) can be done by using Eq. 2.1.

At the detection position \mathbf{R} in the scattering plane (the XZ -plane in Fig. 2.1), the electrical field of the emitted light from the induced molecular second-order dipole (labeled by ν) is given by:¹⁴⁴

$$\tilde{\mathbf{E}}_\nu(2\omega) = \frac{k_0^2 e^{i\mathbf{k}_0 \cdot (\mathbf{R} - \mathbf{r}')}}{4\pi\epsilon_0 R} (\hat{\mathbf{R}} \times \tilde{\mathbf{p}}^{(2)}) \times \hat{\mathbf{R}} \tag{2.5}$$

where k_0 is the magnitude of \mathbf{k}_0 , the wavevector of the emitted SH beam. $\hat{\mathbf{R}}$ is the unit vector in the direction of \mathbf{R} and is given by

$$\hat{\mathbf{R}} = \sin \theta \hat{\mathbf{X}} + 0 \hat{\mathbf{Y}} + \cos \theta \hat{\mathbf{Z}}$$

where θ is the scattering angle as defined in Fig. 2.1. Extracting the exponential term related to the position of the molecule, we can expand Eq. 2.5 as

$$\begin{aligned}
 \tilde{\mathbf{E}}_\nu(2\omega) &= \mathbf{E}_\nu(2\omega) e^{i\mathbf{k}_0 \cdot (\mathbf{R} - \mathbf{r}') + i2\mathbf{k}_1 \cdot \mathbf{r}'} \\
 &= \frac{k_0^2 e^{i\mathbf{k}_0 \cdot (\mathbf{R} - \mathbf{r}') + i2\mathbf{k}_1 \cdot \mathbf{r}'}}{4\pi\epsilon_0 R} \left\{ \left(p_X^{(2)} \cos^2 \theta - p_Z^{(2)} \sin \theta \cos \theta \right) \hat{\mathbf{X}} + p_Y^{(2)} \hat{\mathbf{Y}} \right. \\
 &\quad \left. + \left(p_Z^{(2)} \sin^2 \theta - p_X^{(2)} \sin \theta \cos \theta \right) \hat{\mathbf{Z}} \right\}.
 \end{aligned} \tag{2.6}$$

At the point of detection, the polarization state of the SH light, i.e. the oscillating direction of the electrical field, can be analyzed by decomposing the electrical field into two specified orthogonal directions. These two directions both are perpendicular

to $\hat{\mathbf{k}}_0$ as the SH light is a transverse wave. As illustrated in Fig. 2.1, we can express a specified direction $\hat{\mathbf{e}}_1$ and the corresponding orthogonal direction $\hat{\mathbf{e}}_2$ as:

$$\begin{aligned}\hat{\mathbf{e}}_1 &= \cos \gamma \cos \theta \hat{\mathbf{X}} + \sin \gamma \hat{\mathbf{Y}} - \cos \gamma \sin \theta \hat{\mathbf{Z}} \\ \hat{\mathbf{e}}_2 &= -\sin \gamma \cos \theta \hat{\mathbf{X}} + \cos \gamma \hat{\mathbf{Y}} + \sin \gamma \sin \theta \hat{\mathbf{Z}}.\end{aligned}$$

γ is defined as the angle between the direction $\hat{\mathbf{e}}_1$ and the XZ -plane. Thus, for the polarization analysis, we can write the SH field (Eq. 2.6) as a combination of the two orthogonal components:

$$\begin{aligned}\mathbf{E}_v(2\omega) &= \frac{k_0^2}{4\pi\epsilon_0 R} \left\{ \left(p_X^{(2)} \cos \gamma \cos \theta + p_Y^{(2)} \sin \gamma - p_Z^{(2)} \cos \gamma \sin \theta \right) \hat{\mathbf{e}}_1 \right. \\ &\quad \left. + \left(-p_X^{(2)} \sin \gamma \cos \theta + p_Y^{(2)} \cos \gamma + p_Z^{(2)} \sin \gamma \sin \theta \right) \hat{\mathbf{e}}_2 \right\}.\end{aligned}\quad (2.7)$$

Each of the two components, in the directions of $\hat{\mathbf{e}}_1$ or $\hat{\mathbf{e}}_2$, can be measured independently.

Treating all molecules as individual scatterers, we can sum up the emitted SH fields from all molecules and obtain the total SH intensity as

$$I(2\omega) = \frac{cn\epsilon_0}{2} \left| \sum_v \tilde{\mathbf{E}}_v(2\omega) \right|^2 \quad (2.8a)$$

$$= \frac{cn\epsilon_0}{2} \left\{ \underbrace{\sum_v \left| \mathbf{E}_v(2\omega) \right|^2}_{\text{self-correlations, incoherent}} + \underbrace{\sum_{v \neq v'} \mathbf{E}_v(2\omega) \mathbf{E}_{v'}^*(2\omega) e^{i\mathbf{q} \cdot (\mathbf{r} - \mathbf{r}')}}_{\text{cross-correlations, coherent}} \right\} \quad (2.8b)$$

where c is the velocity of light in vacuum, n is the refractive index of air. \mathbf{r} and \mathbf{r}' are the positions of the molecules v and v' , respectively. $\mathbf{q} \equiv \mathbf{k}_0 - 2\mathbf{k}_1$ is the scattering wavevector. In the far field, that is, $r \ll R$, the difference in \mathbf{k}_0 of the SH light emitted from molecules at different positions is negligible and the unit vector $\hat{\mathbf{k}}_0 \sim \hat{\mathbf{R}}$. $\mathbf{E}_v^*(2\omega)$ is the complex conjugate of $\mathbf{E}_v(2\omega)$. Combining Eq. 2.4, Eq. 2.7, and Eq. 2.8b, we obtain the expression of the measured SHS intensity as a function of the molecular hyperpolarizability $\beta^{(2)}$ in the lab frame.

It is worth noting that the first term in Eq. 2.8b represents self correlations of individual molecules and is thus an incoherent contribution to the total SH intensity. The second term in Eq. 2.8b, i.e. the double summation over v and v' , represents cross-correlations between molecules that result in a coherent contribution to the total SH intensity.⁸⁴ For the coherent term, the correlation between two molecules is described by $e^{i\mathbf{q} \cdot (\mathbf{r} - \mathbf{r}')}$, in which $\mathbf{q} \cdot (\mathbf{r} - \mathbf{r}')$ is the phase difference between the SH fields

of the two molecules. Before going into detailed discussion of incoherent and coherent SHS, we first look at the symmetry properties of the molecular hyperpolarizability $\boldsymbol{\beta}^{(2)}$, which can significantly reduce the complexity of the calculation of the SHS intensity.

2.1.3 Symmetry properties of $\boldsymbol{\beta}^{(2)}$

$\boldsymbol{\beta}^{(2)}$ is a three dimensional tensor with 27 Cartesian elements. The symmetry properties of $\boldsymbol{\beta}^{(2)}$ are determined by the nature of the second-order optical process and reflect the spatial symmetry of the molecule (assuming the molecule can be considered static). The total number of independent tensor elements is reduced by the symmetry properties of $\boldsymbol{\beta}^{(2)}$. In the following, we will first examine the symmetry properties originating from the nature of the light-matter interaction process involved in SHS. Then, we will present the influence of the spatial symmetry of the molecule on the values of the $\boldsymbol{\beta}^{(2)}$ elements.

For SHS, following Eq. 2.2, we can express the second-order molecular dipole moment $\tilde{\mathbf{p}}^{(2)}$ in terms of the tensor element $\beta_{ijk}^{(2)}(2\omega, \omega, \omega)$ as

$$\tilde{p}_i^{(2)} = \sum_{j,k} \beta_{ijk}^{(2)}(2\omega, \omega, \omega) \tilde{E}_j(\omega) \tilde{E}_k(\omega), \quad (2.9)$$

where the subscripts i, j, k denote the polarization states of $\tilde{\mathbf{p}}^{(2)}$ and the two incident electrical fields $\tilde{\mathbf{E}}(\omega)$, respectively. Regardless of the used coordinate system, as i, j, k are dummy indices, we can interchange j with k together with the related frequencies and electrical field in Eq. 2.9 and have

$$\beta_{ijk}^{(2)}(2\omega, \omega, \omega) \tilde{E}_j(\omega) \tilde{E}_k(\omega) = \beta_{ikj}^{(2)}(2\omega, \omega, \omega) \tilde{E}_k(\omega) \tilde{E}_j(\omega). \quad (2.10)$$

Canceling the product $\tilde{E}_j(\omega) \tilde{E}_k(\omega)$ on both sides, we obtain:

$$\beta_{ijk}^{(2)}(2\omega, \omega, \omega) = \beta_{ikj}^{(2)}(2\omega, \omega, \omega). \quad (2.11)$$

This property of $\boldsymbol{\beta}^{(2)}$ is known as intrinsic permutation symmetry.¹⁴⁵

For lossless media, the values of the $\boldsymbol{\beta}^{(2)}$ elements are real. In addition, if the dispersion of the medium is negligible, the indices i, j, k of $\beta_{ijk}^{(2)}(2\omega, \omega, \omega)$ are fully

permutable regardless of the frequency.¹⁴⁵ In this case, we have:

$$\begin{aligned}
 \beta_{ijk}^{(2)}(2\omega, \omega, \omega) &= \beta_{ikj}^{(2)}(2\omega, \omega, \omega) = \beta_{jki}^{(2)}(2\omega, \omega, \omega) \\
 &= \beta_{jik}^{(2)}(2\omega, \omega, \omega) = \beta_{kji}^{(2)}(2\omega, \omega, \omega) \\
 &= \beta_{kij}^{(2)}(2\omega, \omega, \omega).
 \end{aligned}
 \tag{2.12}$$

$\beta^{(2)}$ for nonresonant SHS is independent on the frequency, which is a significant difference with $\beta^{(2)}$ for SFG that will be discussed in Ch. 5. Without loss of generality, we will abbreviate $\beta_{ijk}^{(2)}(2\omega, \omega, \omega)$ as $\beta_{ijk}^{(2)}$ hereafter in this chapter.

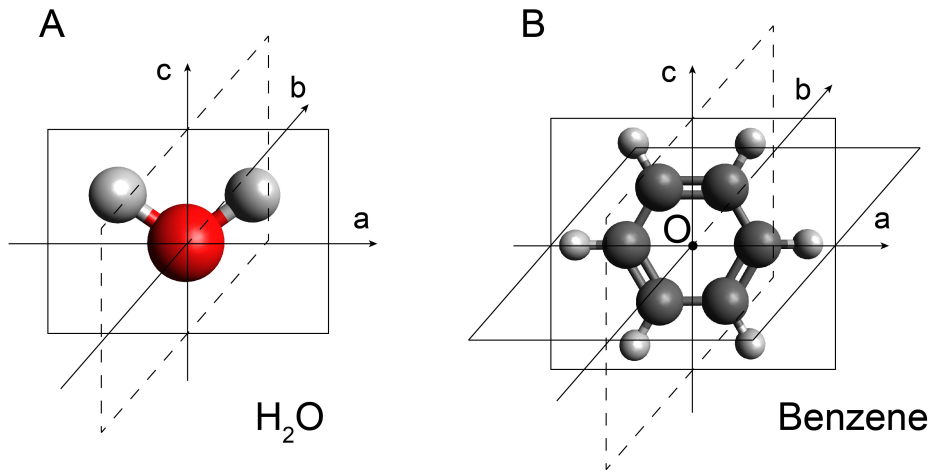


Figure 2.2 – Symmetry of the water and benzene molecule. (A) The water molecule belongs to the C_{2v} point group with two mirror symmetry planes, the ac - and bc -planes, and a 2-fold axis of symmetry, the c -axis. (B) The benzene molecule belongs to the D_{6h} point group and is centrosymmetric. The centrosymmetry center is the geometric center of the benzene molecule, i.e the origin point O in the figure.

In addition to these intrinsic symmetry properties of $\beta^{(2)}$ for SHS, the value of $\beta_{ijk}^{(2)}$ depends on the molecular structure. The spatial symmetry of the molecule determines the nonzero $\beta_{ijk}^{(2)}$ elements. For nonresonant SHS, the spatial symmetry refers to the symmetry of the molecular structure. As the water molecule is the primary source of SHS light in aqueous solutions, we firstly take the water molecule for example.

As illustrated in Fig. 2.2A, under static conditions, the water molecule belongs to the point group C_{2v} with two planes of symmetry, the ac - and bc -planes, and a 2-fold axis of symmetry, the c -axis, as symmetry elements. The coordinate system (a, b, c) defines the molecular frame. As a molecular property, $\beta^{(2)}$ of water possesses the same symmetry.^{145,146} By a symmetry operation, the water molecule is moved in such a way that its final position is physically indistinguishable from its initial position.¹⁴⁶

Accordingly, the value of $\beta_{ijk}^{(2)}$ is unchanged by the same symmetry operation. To illustrate, we discuss the reflection operation about the bc -plane in the following.

With the fundamental electrical field $E_c(\omega)$, the a -component of the induced second-order water dipole moment is given by

$$\tilde{p}_a^{(2)} = \beta_{acc}^{(2)} \tilde{E}_c(\omega) \tilde{E}_c(\omega) \quad (2.13)$$

Applying a reflection operation about the bc -plane to the water molecule, we invert the a -component of vectorial quantities while the b - and c -components are unchanged. $\beta_{acc}^{(2)}$ is unchanged under the reflection operation. Therefore, Eq. 2.13 is equivalent to

$$-\tilde{p}_a^{(2)} = \beta_{acc}^{(2)} \tilde{E}_c(\omega) \tilde{E}_c(\omega) \quad (2.14)$$

Equations 2.13 and 2.14 hold simultaneously only if $\beta_{acc}^{(2)} = 0$. More generally, we can find in a similar way that for the bc -plane of symmetry, $\beta_{ijk}^{(2)}$ with an odd number of a in the subscripts is zero. The same consideration can be extended to all the other symmetry of the molecule. As a consequence, there are only 7 nonzero $\beta^{(2)}$ elements out of 27 possible ones, which are $\beta_{aac}^{(2)}$, $\beta_{aca}^{(2)}$, $\beta_{caa}^{(2)}$, $\beta_{bbc}^{(2)}$, $\beta_{bcb}^{(2)}$, $\beta_{cbb}^{(2)}$, and $\beta_{ccc}^{(2)}$.

For the elastic SHS measurements of electrolyte solutions presented in Ch. 3 and Ch. 4, the dispersion between the fundamental and SH beams is negligible. The full permutation symmetry of $\beta_{ijk}^{(2)}$ is thus valid (Eq. 2.12). The nonzero $\beta^{(2)}$ elements of the water molecule are further related as follows

$$\begin{aligned} \beta_{aac}^{(2)} &= \beta_{aca}^{(2)} = \beta_{caa}^{(2)} \\ \beta_{bbc}^{(2)} &= \beta_{bcb}^{(2)} = \beta_{cbb}^{(2)} \\ \beta_{ccc}^{(2)} \end{aligned} \quad (2.15)$$

A special group of molecules worth noting is the molecules with centrosymmetry, for which all $\beta^{(2)}$ elements are vanishing. We take the benzene molecule as an example. The benzene molecule (as shown in Fig. 2.2B) belongs to the D_{6h} point group with a center of centrosymmetry (inverse symmetry) O. With the fundamental electrical field $E_j(\omega)$ and $E_k(\omega)$, the i -component of the induced molecular dipole moment is given by

$$\tilde{p}_i^{(2)} = \beta_{ijk}^{(2)} \tilde{E}_j(\omega) \tilde{E}_k(\omega) \quad (2.16)$$

Applying the inverse operation about the center O to the benzene molecule, we invert all the components of vectorial quantities while $\beta_{ijk}^{(2)}$ is unchanged. Equation 2.16 is

equivalent to

$$-\tilde{p}_i^{(2)} = \beta_{ijk}^{(2)} [-\tilde{E}_j(\omega)] [-\tilde{E}_k(\omega)] \quad (2.17)$$

Only if $\beta_{ijk}^{(2)} = 0$, Eqs. 2.16 and 2.17 hold simultaneously. As i, j, k are dummy indices, all $\beta_{ijk}^{(2)}$ elements vanish. Thus, there is no SH light generated by centrosymmetric molecules. For electrolyte solutions studied in this part of the thesis, simple centrosymmetric ions will have vanishing $\beta_{ijk}^{(2)}$ elements. The water molecules are, therefore, responsible for the SHS response.

In the next section, we will present calculations of the SHS intensity generated by uncorrelated water molecules. The complexity of these calculations will be greatly reduced by the use of the above discussed symmetry properties of $\beta^{(2)}$.

2.1.4 Calculation of the incoherent SHS intensity

Incoherent SHS from noncentrosymmetric molecules with an isotropic distribution is commonly referred to as hyper-Rayleigh scattering (HRS). HRS has been widely used to measure the SH response of various solutions, especially that of pure liquids (see the review articles Refs.^{82,101} and references therein). Pure liquids are usually assumed to be isotropic, in which molecules are uncorrelated. The SH signal thus solely originates from incoherent contributions,⁸⁶ represented by the first term in Eq. 2.8b. The basic equations for HRS have been worked out by Bersohn *et al.*⁸⁴ and Kauranen and Persoons⁸⁵. Here, we reproduce them for arbitrary polarization states of beams and in SI units.

Given a large number of molecules contributing to the SH signal, the incoherent contributions can be represented by a statistical average over all the molecules, that is:

$$I(2\omega) = \frac{cn\epsilon_0}{2} N_m V \left\langle \left| \mathbf{E}_v(2\omega) \right|^2 \right\rangle, \quad (2.18)$$

where $\langle \rangle$ denotes an ensemble orientational average over all contributing molecules that randomly orient and distribute in space, N_m is the number density of molecules, and V is the volume in which molecules contribute to the SH intensity. V typically corresponds to the focal volume of the incident laser beam. For the SH intensity that is analyzed in a linear polarization described by the polarization angle γ (i.e., in the direction of $\hat{\mathbf{e}}_1$, Fig. 2.1), we obtain the detected SH intensity by inserting Eq. 2.7 into

Eq. 2.18:

$$\begin{aligned}
 I(2\omega) &= \frac{\text{cn}k_0^4}{32\pi^2\epsilon_0 R^2} N_m V \left\langle \left(p_X^{(2)} \cos \gamma \cos \theta + p_Y^{(2)} \sin \gamma - p_Z^{(2)} \cos \gamma \sin \theta \right)^2 \right\rangle \\
 &= \frac{\text{cn}k_0^4}{32\pi^2\epsilon_0 R^2} N_m V \left\langle \left[p_X^{(2)} \right]^2 \cos^2 \gamma \cos^2 \theta + 2 p_X^{(2)} p_Y^{(2)} \cos \gamma \cos \theta \sin \gamma \right. \\
 &\quad + \left[p_Y^{(2)} \right]^2 \sin^2 \gamma - 2 p_X^{(2)} p_Z^{(2)} \cos^2 \gamma \cos \theta \sin \theta + \left[p_Z^{(2)} \right]^2 \cos^2 \gamma \sin^2 \theta \\
 &\quad \left. - 2 p_Y^{(2)} p_Z^{(2)} \cos \gamma \sin \gamma \sin \theta \right\rangle, \quad (2.19)
 \end{aligned}$$

where the second-order molecular dipole moments are given in the lab frame (X, Y, Z) . To obtain the SH intensity, it is essential to calculate the ensemble averages of the respective products of $\mathbf{p}^{(2)}$ components in Eq. 2.19. The $\mathbf{p}^{(2)}$ components are given by Eq. 2.4. The product of two $\mathbf{p}^{(2)}$ components translates into a set of products of two $\beta^{(2)}$ tensor elements, i.e. $\beta_{IJK}^{(2)} \beta_{I'J'K'}^{(2)}$. Because in isotropic media the molecules orient randomly with an even probability in all directions, $\langle \beta_{IJK}^{(2)} \beta_{I'J'K'}^{(2)} \rangle$ has spatial centrosymmetry. Similar to the spatial symmetry discussion for $\beta_{ijk}^{(2)}$ in Sec. 2.1.3, we can find that an even number of X, Y , and Z subscripts are required for nonzero $\langle \beta_{IJK}^{(2)} \beta_{I'J'K'}^{(2)} \rangle$. Using Eq. 2.4 and the symmetry property of the ensemble average, we have

$$\begin{aligned}
 \left\langle \left[p_X^{(2)} \right]^2 \right\rangle &= E_0^4 \left\{ \left\langle \left[\beta_{XYX}^{(2)} \right]^2 \right\rangle \sin^4 \alpha + \left\langle \left[\beta_{XXX}^{(2)} \right]^2 \right\rangle \cos^4 \alpha + \left\langle \left[\beta_{XXY}^{(2)} \right]^2 \right\rangle \sin^2 \alpha \cos^2 \alpha \right. \\
 &\quad + \left\langle \left[\beta_{XXY}^{(2)} \right]^2 \right\rangle \sin^2 \alpha \cos^2 \alpha + 2 \left\langle \beta_{XXY}^{(2)} \beta_{XXY}^{(2)} \right\rangle \sin^2 \alpha \cos^2 \alpha \\
 &\quad \left. + 2 \left\langle \beta_{XXY}^{(2)} \beta_{XXY}^{(2)} \right\rangle \sin^2 \alpha \cos^2 \alpha \right\} \\
 \left\langle \left[p_Y^{(2)} \right]^2 \right\rangle &= E_0^4 \left\{ \left\langle \left[\beta_{YYX}^{(2)} \right]^2 \right\rangle \sin^4 \alpha + \left\langle \left[\beta_{YXX}^{(2)} \right]^2 \right\rangle \cos^4 \alpha + \left\langle \left[\beta_{YYX}^{(2)} \right]^2 \right\rangle \sin^2 \alpha \cos^2 \alpha \right. \\
 &\quad + \left\langle \left[\beta_{YXX}^{(2)} \right]^2 \right\rangle \sin^2 \alpha \cos^2 \alpha + 2 \left\langle \beta_{YXX}^{(2)} \beta_{YXX}^{(2)} \right\rangle \sin^2 \alpha \cos^2 \alpha \\
 &\quad \left. + 2 \left\langle \beta_{YXX}^{(2)} \beta_{YXX}^{(2)} \right\rangle \sin^2 \alpha \cos^2 \alpha \right\} \\
 \left\langle \left[p_Z^{(2)} \right]^2 \right\rangle &= E_0^4 \left\{ \left\langle \left[\beta_{ZYY}^{(2)} \right]^2 \right\rangle \sin^4 \alpha + \left\langle \left[\beta_{ZXX}^{(2)} \right]^2 \right\rangle \cos^4 \alpha + \left\langle \left[\beta_{ZYY}^{(2)} \right]^2 \right\rangle \sin^2 \alpha \cos^2 \alpha \right. \\
 &\quad + \left\langle \left[\beta_{ZXX}^{(2)} \right]^2 \right\rangle \sin^2 \alpha \cos^2 \alpha + 2 \left\langle \beta_{ZYY}^{(2)} \beta_{ZXX}^{(2)} \right\rangle \sin^2 \alpha \cos^2 \alpha \\
 &\quad \left. + 2 \left\langle \beta_{ZYY}^{(2)} \beta_{ZXX}^{(2)} \right\rangle \sin^2 \alpha \cos^2 \alpha \right\} \\
 \left\langle p_X^{(2)} p_Y^{(2)} \right\rangle &= E_0^4 \left\{ \left\langle \beta_{XYX}^{(2)} \beta_{YXX}^{(2)} \right\rangle \sin^3 \alpha \cos \alpha + \left\langle \beta_{XXY}^{(2)} \beta_{YXX}^{(2)} \right\rangle \sin^3 \alpha \cos \alpha \right.
 \end{aligned}$$

$$\begin{aligned}
 & + \langle \beta_{XXX}^{(2)} \beta_{YYX}^{(2)} \rangle \sin \alpha \cos^3 \alpha + \langle \beta_{XXX}^{(2)} \beta_{YXY}^{(2)} \rangle \sin \alpha \cos^3 \alpha \\
 & + \langle \beta_{XYX}^{(2)} \beta_{YYX}^{(2)} \rangle \sin^3 \alpha \cos \alpha + \langle \beta_{XYX}^{(2)} \beta_{YXX}^{(2)} \rangle \sin \alpha \cos^3 \alpha \\
 & + \langle \beta_{XXY}^{(2)} \beta_{YYX}^{(2)} \rangle \sin^3 \alpha \cos \alpha + \langle \beta_{XXY}^{(2)} \beta_{YXX}^{(2)} \rangle \sin \alpha \cos^3 \alpha \} \\
 \langle p_X^{(2)} p_Z^{(2)} \rangle & = \langle p_Y^{(2)} p_Z^{(2)} \rangle = 0.
 \end{aligned} \tag{2.20}$$

For an isotropic medium, the lab frame indices X , Y , and Z for the subscripts of $\langle \beta_{IJK}^{(2)} \beta_{I'J'K'}^{(2)} \rangle$ can be mutually permuted. There are 5 permutation ways in total:

$$\begin{aligned}
 & \begin{cases} X \rightarrow Y \\ Y \rightarrow Z, \\ Z \rightarrow X \end{cases} \quad \begin{cases} X \rightarrow Y \\ Y \rightarrow X, \\ Z \rightarrow Z \end{cases} \quad \begin{cases} X \rightarrow Z \\ Y \rightarrow X, \\ Z \rightarrow Y \end{cases} \quad \begin{cases} X \rightarrow Z \\ Y \rightarrow Y, \\ Z \rightarrow X \end{cases} \quad \begin{cases} X \rightarrow X \\ Y \rightarrow Z. \\ Z \rightarrow Y \end{cases}
 \end{aligned}$$

and the remaining 6 independent $\langle \beta_{IJK}^{(2)} \beta_{I'J'K'}^{(2)} \rangle$ are as follows as given by Bersohn *et al.*⁸⁴

$$\begin{aligned}
 \langle [\beta_{YYY}^{(2)}]^2 \rangle & = \frac{1}{7}h + \frac{2}{35}b_1 + \frac{2}{35}b_2 + \frac{1}{35}b_3 + \frac{2}{35}b_4 + \frac{1}{35}b_5 + \frac{1}{105}c_1 \\
 & \quad + \frac{1}{105}c_2 + \frac{2}{105}c_3 + \frac{1}{210}d_1 + \frac{1}{105}d_2; \\
 \langle [\beta_{ZXX}^{(2)}]^2 \rangle & = \frac{1}{7}h + \frac{4}{105}b_1 - \frac{1}{35}b_2 + \frac{3}{35}b_3 - \frac{1}{35}b_4 + \frac{2}{105}b_5 + \frac{1}{35}c_1 \\
 & \quad - \frac{1}{215}c_2 - \frac{1}{105}c_3 + \frac{1}{70}d_1 - \frac{1}{210}d_2; \\
 \langle \beta_{ZXX}^{(2)} \beta_{ZYY}^{(2)} \rangle & = \frac{1}{105}h + \frac{2}{35}b_1 - \frac{1}{105}b_2 + \frac{1}{35}b_3 - \frac{1}{105}b_4 - \frac{1}{105}b_5 + \frac{8}{105}c_1 \\
 & \quad + \frac{1}{105}c_2 - \frac{1}{21}c_3 - \frac{1}{84}d_1 + \frac{1}{105}d_2; \\
 \langle \beta_{YYY}^{(2)} \beta_{YXX}^{(2)} \rangle & = \frac{1}{35}h + \frac{11}{105}b_1 + \frac{1}{210}b_2 + \frac{2}{105}b_3 + \frac{1}{210}b_4 - \frac{1}{70}b_5 + \frac{1}{35}c_1 \\
 & \quad - \frac{1}{210}c_2 + \frac{1}{42}c_3 - \frac{1}{420}d_1 - \frac{1}{210}d_2; \\
 \langle [\beta_{YYZ}^{(2)} + \beta_{ZZY}^{(2)}]^2 \rangle & = \frac{4}{35}h - \frac{4}{35}b_1 + \frac{2}{105}b_2 + \frac{8}{105}b_3 + \frac{2}{105}b_4 + \frac{8}{105}b_5 - \frac{2}{105}c_1 \\
 & \quad + \frac{1}{70}c_2 - \frac{4}{105}c_3 + \frac{1}{42}d_1 + \frac{1}{70}d_2; \\
 \langle [\beta_{XYZ}^{(2)} + \beta_{XZY}^{(2)}]^2 \rangle & = \frac{4}{105}h - \frac{4}{105}b_1 - \frac{4}{105}b_2 + \frac{4}{35}b_3 - \frac{4}{105}b_4 + \frac{1}{21}b_5 - \frac{2}{21}c_1 \\
 & \quad - \frac{1}{35}c_2 + \frac{8}{105}c_3 + \frac{11}{210}d_1 - \frac{1}{35}d_2;
 \end{aligned} \tag{2.21}$$

where the parameters h, b, c , and d are defined by

$$\begin{aligned}
 h &= \sum_i \left[\beta_{iii}^{(2)} \right]^2 \\
 b_1 &= \sum_{i,j} \beta_{iii}^{(2)} \beta_{ijj}^{(2)} \\
 b_2 &= \sum_{i,j} \beta_{iii}^{(2)} \left(\beta_{jij}^{(2)} + \beta_{jji}^{(2)} \right) \\
 b_3 &= \sum_{i,j} \left[\beta_{ijj}^{(2)} \right]^2 \\
 b_4 &= \sum_{i,j} \beta_{ijj}^{(2)} \left(\beta_{jij}^{(2)} + \beta_{jji}^{(2)} \right) \\
 b_5 &= \sum_{i,j} \left(\beta_{jij}^{(2)} + \beta_{jji}^{(2)} \right)^2 \\
 c_1 &= \sum_{i,j,k} \beta_{ijj}^{(2)} \beta_{ikk}^{(2)} \\
 c_2 &= \sum_{i,j,k} \left(\beta_{jij}^{(2)} + \beta_{jji}^{(2)} \right) \left(\beta_{kik}^{(2)} + \beta_{kki}^{(2)} \right) \\
 c_3 &= \sum_{i,j,k} \beta_{ijj}^{(2)} \left(\beta_{kik}^{(2)} + \beta_{kki}^{(2)} \right) \\
 d_1 &= \sum_{i,j,k} \left(\beta_{ijk}^{(2)} + \beta_{ikj}^{(2)} \right)^2 \\
 d_2 &= \sum_{i,j,k} \left(\beta_{ijk}^{(2)} + \beta_{ikj}^{(2)} \right) \left(\beta_{jik}^{(2)} + \beta_{jki}^{(2)} \right). \tag{2.22}
 \end{aligned}$$

The subscripts i (j, k) refer to a, b or c of the molecular coordinate system (Fig. 2.1). The conversion of $\beta^{(2)}$ tensor elements from the molecular frame to the lab frame follows the rules given by Eq. 2.1 and result in the fractional numbers in Eq. 2.21. For example, $\frac{1}{7}h$ in the expression of $\left\langle \left[\beta_{YYY}^{(2)} \right]^2 \right\rangle$ results from the following integral:

$$\begin{aligned}
 \frac{1}{7}h &= \frac{1}{8\pi^2} \int_0^\pi \sin \phi \, d\phi \int_0^{2\pi} d\psi \int_0^{2\pi} d\varrho \left\{ \left(\cos \phi \sin \psi \cos \varrho - \cos \psi \sin \varrho \right)^6 \left[\beta_{aaa}^{(2)} \right]^2 \right. \\
 &\quad \left. + \left(\cos \psi \cos \varrho - \cos \phi \sin \psi \sin \varrho \right)^6 \left[\beta_{bbb}^{(2)} \right]^2 + \sin^6 \phi \sin^6 \psi \left[\beta_{ccc}^{(2)} \right]^2 \right\}.
 \end{aligned}$$

For SHS in a lossless and dispersionless medium, the full permutation symmetry is valid. As discussed in Sec. 2.1.3, the subscripts of $\beta_{IJK}^{(2)}$ can be mutually permuted as shown in Eq. 2.12. We thus have $\beta_{YZY}^{(2)} = \beta_{ZZY}^{(2)}$ and $\beta_{XYZ}^{(2)} = \beta_{XZY}^{(2)}$ that further simplify Eq. 2.21 and also the calculation of the parameters in Eq. 2.22. Applying these permutation symmetries, we obtain a simplified general expression for

$I(2\omega)$ in terms of the $\beta^{(2)}$ tensor elements for nonresonant SHS and arbitrary linear polarization states:

$$\begin{aligned}
 I(2\omega) = & \frac{\text{cn}k_0^4 E_0^4}{32\pi^2 \epsilon_0 R^2} N_m V \left\{ \left\langle \left[\beta_{XY Y}^{(2)} \right]^2 \right\rangle [\cos^2 \alpha \sin^2 \gamma (1 + 3 \sin^2 \alpha) \right. \\
 & + \cos \theta \sin 2\alpha \sin 2\gamma + \frac{1}{4} \cos^2 \gamma (2(5 + 3 \cos 2\alpha) \cos^2 \theta \sin^2 \alpha \\
 & + (3 + \cos 4\alpha) \sin^2 \theta)] + \left\langle \left[\beta_{XY Z}^{(2)} \right]^2 \right\rangle \sin^2 2\alpha \cos^2 \gamma \sin^2 \theta \\
 & + \left\langle \left[\beta_{YY Y}^{(2)} \right]^2 \right\rangle [\cos^4 \alpha \cos^2 \gamma \cos^2 \theta + \sin^4 \alpha \sin^2 \gamma] \\
 & + \left\langle \beta_{XY Y}^{(2)} \beta_{XX X}^{(2)} \right\rangle \left[\sin 2\alpha \left(\frac{1}{2} \sin 2\alpha (\cos^2 \theta \cos^2 \gamma + \sin^2 \gamma) + \cos \theta \sin 2\gamma \right) \right] \\
 & \left. + \frac{1}{2} \left\langle \beta_{ZY Y}^{(2)} \beta_{ZX X}^{(2)} \right\rangle \sin^2 2\alpha \cos^2 \gamma \sin^2 \theta \right\}.
 \end{aligned} \tag{2.23}$$

The SHS intensity of the beams with specified polarization states can be deduced from Eq. 2.23. Defining P/S polarization in the direction parallel/perpendicular to the scattering plane (Fig. 2.1), $\alpha = \gamma = 0$ for P polarized light and $\alpha = \gamma = 90^\circ$ for S polarized light. The expressions of SH intensities measured at different scattering angle θ for the four nonzero polarization combinations are then:

$$\begin{aligned}
 I_{SSS}(2\omega) &= \frac{\text{cn}k_0^4 E_0^4 N_m V}{32\pi^2 \epsilon_0 R^2} \left\langle \left[\beta_{YY Y}^{(2)} \right]^2 \right\rangle \\
 I_{PPP}(2\omega) &= \frac{\text{cn}k_0^4 E_0^4 N_m V}{32\pi^2 \epsilon_0 R^2} \left\{ \left\langle \left[\beta_{YY Y}^{(2)} \right]^2 \right\rangle \cos^2 \theta + \left\langle \left[\beta_{XY Y}^{(2)} \right]^2 \right\rangle \sin^2 \theta \right\} \\
 I_{PSS}(2\omega) &= \frac{\text{cn}k_0^4 E_0^4 N_m V}{32\pi^2 \epsilon_0 R^2} \left\langle \left[\beta_{XY Y}^{(2)} \right]^2 \right\rangle \\
 I_{SPP}(2\omega) &= \frac{\text{cn}k_0^4 E_0^4 N_m V}{32\pi^2 \epsilon_0 R^2} \left\langle \left[\beta_{XY Y}^{(2)} \right]^2 \right\rangle
 \end{aligned} \tag{2.24}$$

The subscripts of $I(2\omega)$, from left to right, denote the polarizations of the involved beams from the high frequency (SH) to the low frequency (fundamental), respectively. In the example of $I_{SPP}(2\omega)$, the subscripts SPP indicate that the SH light is S polarized and the incident fundamental light is P polarized. Knowing values of the $\beta_{ijk}^{(2)}$ elements, such as those calculated for water molecules by *ab initio* calculations¹⁴⁷, we can calculate SHS patterns from a liquid in different polarization combinations by combining Eqs. 2.20-2.24. Any significant deviation between the calculation and experimental data may indicate the presence of coherent SHS and thus cross-correlations between

the noncentrosymmetric molecules in the liquid.

2.1.5 Coherent SHS

Coherent SHS originates from correlated noncentrosymmetric molecules. These correlations pertain to the orientational order of molecules in the liquid. For electrolyte solutions, the SHS light originates mainly from water molecules. To calculate the coherent contribution to the SHS intensity (the second term in Eq. 2.8b), knowledge of the molecular correlations are necessary. These correlations depend on the molecular level details of the system. In Ch. 3 and Ch. 4, we will model electrolyte solutions in several ways in which the correlations may be taken into account.

Once the molecular correlations are known, the spatial symmetry consideration discussed in Sec. 2.1.3 can be extended to the correlated molecules to determine the polarization combinations for which the coherent SH intensity is nonzero. These selection rules will help to attribute observed scattering contributions to either incoherent self-correlations or coherent cross-correlations. An example can be given for molecular correlations with spherical symmetry. As illustrated in Fig. 2.1, the SHS geometry has a plane of symmetry, the scattering plane. As a result of the combination of the spherical symmetry of the molecular correlations and the reflection symmetry of the SHS geometry, the coherent SHS process should be symmetric with respect to the scattering plane. Thus, an even number of S polarized (perpendicular to the scattering plane) beams are required for nonvanishing coherent SHS. Accordingly, we can only measure nonzero coherent SHS contributions using the polarization combinations of PPP and PSS but not SPP or SSS.

More detailed discussions of coherent SHS from electrolyte solutions are presented in Ch. 3 and Ch. 4.

2.2 Experimental details

Ultrashort laser pulses with high intensities are needed to perform SHS measurements in liquids and other non-crystalline media. In this thesis, we utilize femtosecond (fs)-laser pulses to measure elastic non-resonant SHS responses from aqueous solutions. Since fs-laser pulses are much shorter than the orientational relaxation time of the H-bond network of water (~ 1 ps)^{148,149}, snapshots of the self- and cross-correlations of water molecules are obtained. As this method is different from the commonly employed SHS/HRS using nanosecond laser pulses^{81,150–152} (which may involve an

inelastic scattering process¹⁵³), we refer to this method as femtosecond elastic second harmonic scattering (fs-ESHS). A detailed description of the fs-ESHS experiment is given in the following section.

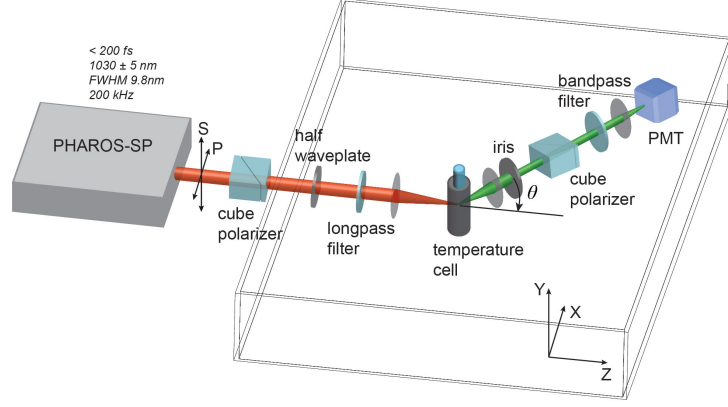


Figure 2.3 – Illustration of the fs-ESHS experimental setup. Same with Fig. 2.1, the XZ -plane defines the scattering plane.

2.2.1 Experimental setup of fs-ESHS

Figure 2.3 shows an illustration of our fs-ESHS experiment setup¹⁵⁴. 1030 ± 5 nm, < 200 fs laser (PHAROS-SP, Light conversion) with a 200 kHz repetition rate is utilized as the source of the input fundamental beam. The polarization of the input beam is controlled by a Glan-Taylor polarizer (GT10-B, Thorlabs) and a zero-order half wave plate (WPH05M-1030). The polarized input beam with a $0.3 \mu\text{J}$ pulse energy is filtered (with a FEL0750 filter, Thorlabs) and then focused by a plano-convex lens ($f = 7.5$ cm) into a cylindrical glass cuvette (LS instruments) with an inner diameter of 4.2 mm. The focused beam has a waist diameter of $\sim 35 \mu\text{m}$ at the focus and a Rayleigh length of 0.94 mm. The sample cuvette is placed in a customized temperature controller (Quantum Northwest) that provides a local environment with the controlled temperature in a range of -20 °C to 150 °C with a precision of ± 0.1 °C. The scattered SH beam is collected and collimated with a plano-convex lens ($f = 5$ cm). The angle of acceptance for the scattered SH beam is controlled by an iris sitting behind the collimating lens. The collimated SH beam is then analyzed (GT10-A, Thorlabs), filtered with a notch filter (ET525/50, Chroma), and finally focused by a plano-convex lens ($f = 1.5$ cm) into a gated PMT (H7421-40, Hamamatsu). The signal from the PMT is amplified by a GHz wide band amplifier (HFAC-26dB, Becker & Hickl) and is then read out by a two channel gated photon counter (SR400, Stanford research systems).

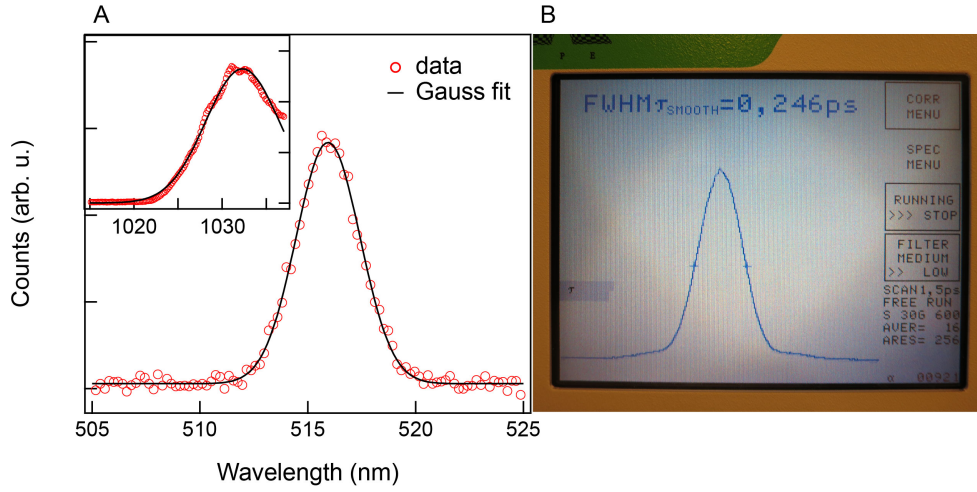


Figure 2.4 – Characterization of incident fs-laser pulses. (A) SH transmission spectrum of the incident fs-laser pulses from a BBO crystal. The inset shows the spectrum of the near IR fundamental beam. The spectra are fitted with Gaussian functions. (B) Pulse duration measured with an autocorrelator.

2.2.2 Characterization of the fs-ESHS system

Specifications of incident fs-laser pulses

We characterized the spectral and temporal profiles of the incident fs-laser pulses using a USB spectrometer (USB4000, Ocean Optics) and an autocorrelator (PulseCheck, A.P.E.). The USB spectrometer has a detection range of 345-1037 nm and a spectral resolution of 0.2 nm. As such, a part of the red side of the spectrum could not be measured. To check the complete spectral shape of the fs-laser pulse, we measured also the non-resonant SH signal from a type-I beta barium borate (BBO) crystal that was illuminated by the fs-laser beam. Figure 2.4A shows the measured spectra (circles) of both the incident fs-laser beam and the SH signal from the crystal. The data was fitted with Gaussian functions (solid line). The incident fs-laser beam has a symmetric spectral shape close to a Gaussian-shape, as indicated by the SH spectrum. The central frequency and the bandwidth of the incident fs-laser beam from the fit are 1032.3 nm and 9.8 nm (FWHM; 2.76×10^{12} Hz in frequency space), respectively. Figure 2.4B shows a screenshot of the measured pulse autocorrelation of the incident fs-laser beam. The autocorrelation has an FWHM of 246 fs, which translates to a pulse duration (FWHM) of $246/\sqrt{2} = 174$ fs. The time-bandwidth product of the incident fs-laser beam is thus $174 \text{ fs} \times 2.76 \times 10^{12} \text{ Hz} = 0.48$, which is not far from the theoretical minimum time-bandwidth product of bandwidth-limited Gaussian-shaped pulses (~ 0.44)¹⁵⁵. The incident fs-laser beam is thus of good quality.

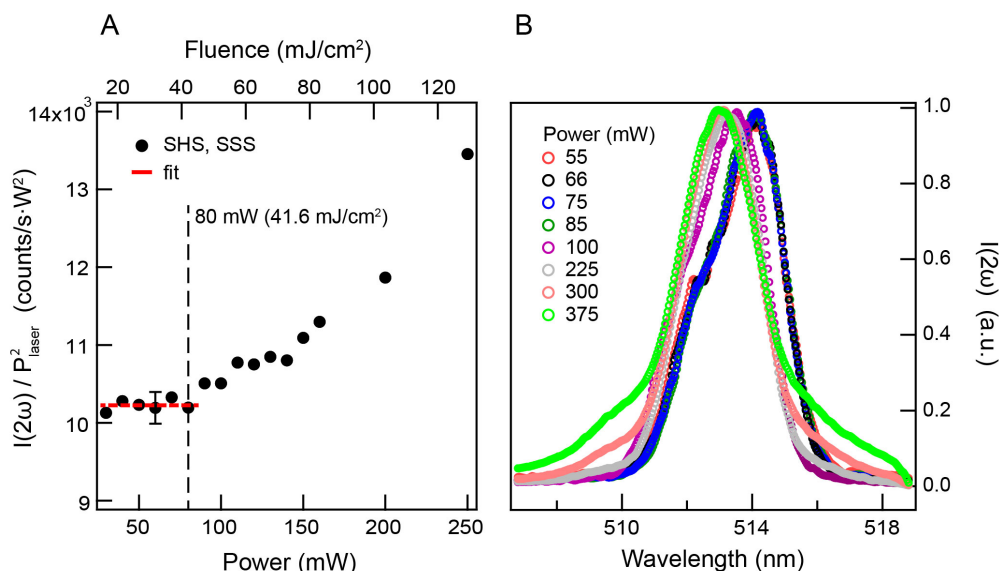


Figure 2.5 – Elastic and inelastic SHS. (A) Plot of the SH intensity divided by the square of the incident laser power as a function of the incident laser power (bottom axis) and fluence (top axis). The red line indicates the quadratic dependence of the SH intensity on the incident power. (B) Normalized SH spectra of pure H₂O at different incident powers.

Power dependence of the fs-ESHS response of water

Although neither the fundamental nor the SH beam is at resonance with any transitions of the studied molecule species, it is important to verify that the measured SH response results from elastic scattering. To do this, we recorded the scattered SH intensity as well as the spectrum of the scattered light as a function of the incident laser power (P_{laser}). If any perturbing effects (e.g. realignment of water molecules by the laser field¹⁵⁶ or higher order processes¹⁴⁵) occur, the ratio of the SH intensity to the square of the incident laser power ($I(2\omega)/P_{laser}^2$) will no longer be power independent. With energy transfer between the laser pulses and water, inelastic scattering will lead to changes in the spectral shape. Figure 2.5A shows the measured SH intensity from pure H₂O, plotted as $I(2\omega)/P_{laser}^2$ versus the incident laser power P_{laser} (bottom axis) and the pulse fluence (top axis). Figure 2.5B shows SH spectra recorded with different incident laser powers. Both recordings were done in the SSS polarization combination (where the incoherent electronic single molecule response of water is maximum) and at a scattering angle of 90°. The data shows that the SH intensity depends quadratically on the incident power up to 80 mW, and that up to this incident power the SH spectrum does not display any changes. At higher powers, it can be seen that the power dependence of the SH intensity starts to deviate from quadratic behavior and that the SH spectra become blue-shifted and broadened with increasing intensities on

the wings. fs-ESHS measurements of electrolyte solutions were performed at 60 mW.

Polarization response of the system and influence of the sample cuvette geometry

To test that the experimental system is equally sensitive to S and P polarizations, we performed angle resolved scattering measurements of a 40 μ M trypan blue (Sigma-Aldrich) solution. Upon excitation with the 1030 nm laser beam, the trypan blue molecules undergo a 2-photon fluorescence process. This process results in an isotropic scattering pattern that does not depend on the polarization state of the light. Figure 2.6A shows the recorded patterns for the SSS and PPP polarization combinations. In these 2-photon fluorescence measurements, the gate delay of the PMT for detection was increased by 19 ns to detect only the fluorescence signal. With such a gate delay, the detected SH signal was reduced to zero. Other experimental settings were kept the same with routine fs-ESHS measurements. It can be seen that both patterns are identical within the experimental errors. The experimental system is thus equally responsive to both S and P polarization states.

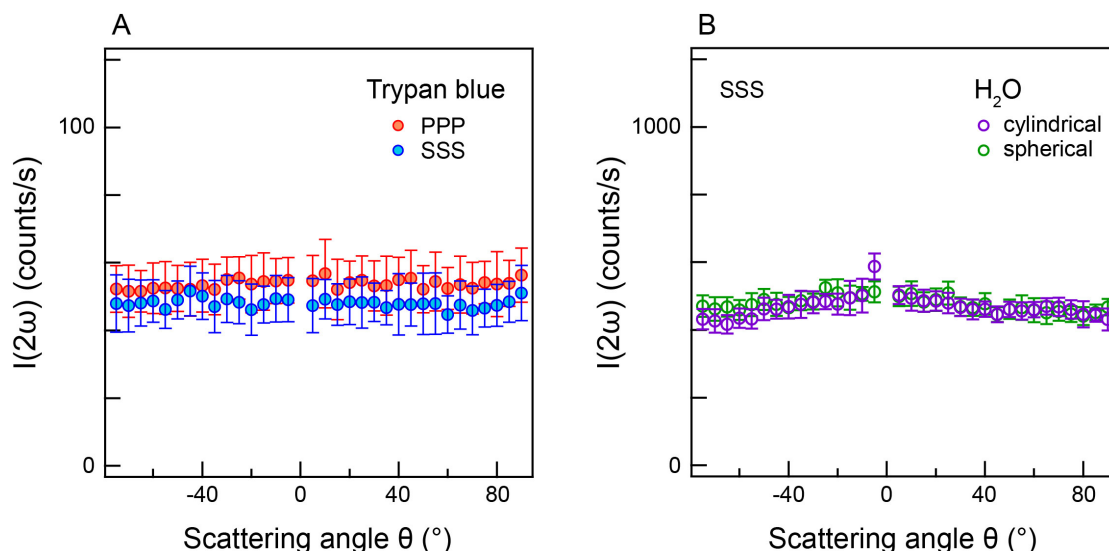


Figure 2.6 – Response of the fs-ESHS system. (A) Fluorescence from a 40 μ M trypan blue solution measured in the SSS and PPP polarization configurations. (B) SSS fs-ESHS patterns of pure water using a cylindrical and a spherical sample cuvette.

We use cylindrical glass sample cuvettes in the fs-ESHS measurements of aqueous solutions as illustrated in Fig. 2.3. The spot diameter of the fundamental laser beam on the wall of the glass cuvette is ~ 100 μ m (Gaussian width), much smaller than the inner diameter of the cylindrical cuvette (4.2 mm). For such a small spot of the laser beam, the difference in the transmitted beam spot between the horizontal

and vertical dimensions is expected to be negligible. To verify that the geometry of the sample cell does not influence the polarization dependent scattering, we compared experiments performed in the cylindrical sample cuvette to those performed in a spherical sample cuvette (25 mL round bottom flask, Duran). A spherical sample cuvette does not induce a distortion in the scattering patterns because of its spherical symmetry. To compare these two cuvettes, we measured fs-ESHS from pure water in the SSS polarization configuration. As can be seen in Fig. 2.6B, the data for both cuvettes is indistinguishable. The geometry of the cylindrical cuvette thus has no influence, in agreement with the above expectation.

3 Non-specific Ion-water Interactions at Low Ionic Strengths

Electrolytes interact with water in many ways: changing dipole orientation, inducing charge transfer, and distorting the hydrogen-bond network in the bulk and at interfaces. Numerous experiments and computations have detected short-range perturbations that extend up to three hydration shells around individual ions. We report a multi-scale investigation of the bulk and surface of aqueous electrolyte solutions that extends from the atomic scale (using atomistic modeling) to nanoscopic length scales (using bulk and interfacial femtosecond second harmonic measurements) to the macroscopic scale (using surface tension experiments). Electrolytes induce orientational order at concentrations starting at 10 μM that causes nonspecific changes in the surface tension of dilute electrolyte solutions. Aside from ion-dipole interactions, collective hydrogen-bond interactions are crucial and explain the observed difference of a factor of 6 between light and heavy water.

For the work in this chapter, Yixing Chen performed the fs-ESHS measurements, data analysis, and phenomenological, analytical nonlinear light scattering modeling. This work also represents a collaboration with the following people:

Dr. Halil I. Okur and Prof. Dr. Paul S. Cremer (*from the Laboratory for Biointerfaces at Pennsylvania State University, headed by Prof. Dr. Paul S. Cremer*) performed the surface tension measurements and related data analysis (Fig. 3.7C);

Prof. Dr. Poul B. Petersen (*from the Petersen Group at Cornell University, headed by Prof. Dr. Poul B. Petersen*) performed the surface resonant SH measurements and related data analysis (Fig. 3.7B) as part of his PhD work in the lab of Prof. Richard J. Saykally at University of California, Berkeley;

Dr. Gabriele Tocci, Dr. Chungwen Liang, and Prof. Dr. Michele Ceriotti (*from the Laboratory of Computational Science and Modeling at École Polytechnique Fédérale de Lausanne (EPFL), headed by Prof. Dr. Michele Ceriotti*) and Dr. David M. Wilkins (*from the Manolopoulos Group at University of*

Chapter 3. Non-specific Ion-water Interactions at Low Ionic Strengths

Oxford, headed by Prof. Dr. David E. Manolopoulos) performed the MD simulations and mean-field modeling using Debye-Hückel theory (Figs. 3.6 and 3.8A);

3.1 Introduction

The hydration of ions is related to physiologically, medically, and chemically relevant processes such as protein folding/precipitation, enzyme/ion channel/ion pump activity, action potentials generation, transport across membranes, self-assembly, interfacial charging, and aerosol formation.^{4–8,14} Ions interact with dipolar water molecules mainly through ion-dipole interactions. The electrostatic potential around an ion decays with $1/R$ (with R being the distance away from the ion) and is damped by the high dielectric constant of water and the presence of other ions. The orientation-averaged interaction energy of a dipole and an ion decays with $1/R^4$. The structure and dynamics of water around ions have been studied with neutron scattering^{157–159}, X-ray diffraction^{160,161}, X-ray absorption spectroscopy^{162,163}, Raman spectroscopy¹⁶⁴, dielectric spectroscopy^{165,166}, solvent relaxation measurements¹⁶⁷, vibrational dynamics measurements^{168–172}, infrared photodissociation spectroscopy of small gas clusters^{173,174}, and molecular dynamics (MD) simulation studies^{12,13,172,175,176}. In these studies, a significant perturbation in the structure and dynamics of liquid water by ions is observed only at high ionic strengths (e.g. > 0.1 M for univalent ions) and not beyond the third hydration shell. While the perturbation is found to depend primarily on the valency of the ions, specific effects of chemical structure, size, and polarizability are clearly present^{19,20}. Ion pairing becomes relevant at the same ionic strengths¹⁶⁶. In general, there is an agreement that the ions' influence on the water network is mainly dictated by behavior that can be described with mean-field models, in which water is treated as an ideal gas of dipoles and ion-dipole interactions are the sole driving force. However, water is a structured liquid in which complex collective H-bond interactions account for many of its unusual properties (such as the high melting and boiling points, the large viscosity, and the high surface tension). In addition, most experiment methods in previous studies rely on either using local probes or determining differences in an average property. Local probes include, for example, the O-H stretch frequency, which can be used as an indicator of either chemical interactions¹⁶⁴ or molecular reorientation¹⁶⁹, or the structure factor of O atoms in the first solvation shell, which only changes significantly for water molecules in the first few hydration shells. High electrolyte concentrations are needed to detect a difference in the average distribution of such a property (the O-H stretch frequency, the orientational relaxation, or the structure factor). Similarly, computer simulation methods are typically limited to a relatively small number of molecules¹², applicable to either “infinite dilution” or high concentrations (~ 1 M), making it impractical to simulate the dilute electrolyte solutions (< 0.1 M).

In this chapter, we report a multi-scale investigation of the bulk and surface of dilute aqueous electrolyte solutions. fs-ESHS is used to detect changes in the orientational order of water molecules in bulk electrolyte solutions over nanoscopic length scales. Snapshots of changes in the orientational distribution of water molecules in different polarization combinations of the incoming and outgoing light reveal that electrolytes induce a perturbation in the orientational order of bulk water. The orientational order, recorded for 21 different electrolytes, starts to change at ionic strengths $< 10 \mu\text{M}$. This seemingly long-range and universal effect is independent of the chemical structure, polarizability, and size of the ions. H_2O (hydrogen oxide, light water) and D_2O (deuterium oxide, heavy water) show remarkably different responses: the absolute fs-ESHS intensity of pure H_2O is 40% lower than that of D_2O , whereas a 6 \times higher ionic strength is needed to perturb D_2O compared to H_2O . The amount of orientational order induced by the electrolytes is also a factor of 3 lower for D_2O . A mean-field model that exclusively incorporates ion-dipole interactions cannot describe the experimental data. MD simulations that include both ion-dipole and dipole-dipole interactions show that ions induce long-range changes in the orientational order of the bulk water network, modulating the intrinsic H-bond correlations. That the H-bond is somewhat shorter and stronger for D_2O than for H_2O (a nuclear quantum effect) qualitatively explains the observed difference between neat light water and heavy water and their respective electrolyte solutions. The resultant orientational order can be detected macroscopically. Macroscopic surface tension measurements display changes at ionic strengths that match the saturated values for H_2O and D_2O , as well as the phenomenological differences observed between them. A comparison with surface- and ion-specific resonant reflection SH measurements shows that the nanoscopic restructuring of the bulk H-bond network is responsible for the non-ion-specific changes in the surface tension.

3.2 Materials and methods

3.2.1 Sample preparation

CCl_4 (99.9%, Sigma-Aldrich), LiCl (99.999%, Sigma-Aldrich), NaCl [(99.999%, Acros) for fs-ESHS measurements and (99.999%, Sigma-Aldrich) for surface tension measurements], KCl (99.999%, Acros), MgCl_2 (99.99%, Sigma-Aldrich), CaCl_2 (99.99%, Sigma-Aldrich), SrCl_2 (99.99%, Sigma-Aldrich), $\text{BaCl}_2 \cdot 2\text{H}_2\text{O}$ (99.9999%, Alfa Aesar), NaNO_3 (99.999%, Fluka), NaBr (99.995%, Fluka), NaI (99.999%, Sigma-Aldrich), NaH_2PO_4

(99.999%, Fluka), NH_4Cl (99.9995%, Fluka), NaSCN (99.99%, Sigma-Aldrich), $\text{Na}_2\text{S}_2\text{O}_3$ (99.99%, Sigma-Aldrich), Na_2SO_4 (99.99%, Sigma-Aldrich), $\text{BeSO}_4 \cdot 4\text{H}_2\text{O}$ (99.99%, Sigma-Aldrich), MgSO_4 (99.99%, Sigma-Aldrich), CaSO_4 (99.99%, Sigma-Aldrich), NaClO_4 (99.0%, Acros), NaOH (99.99%, Sigma-Aldrich), and HCl (Ultrapur, Merck) were used as received without further purification. All samples were made by dissolving the electrolytes in degassed ultrapure water to obtain a stock solution with a high concentration. The stock solutions were filtered (Millipore Millex-VV 0.1 μm polyvinylidene difluoride membrane filters) and diluted to the desired concentrations. To purify H_2O , we used a Milli-Q UF-Plus instrument (Millipore Inc.) for the fs-ESHS measurements and a NANOpure Ultrapure Water System (Barnstead) for the surface tension measurements. The purified H_2O has an electrical resistance of 18.2 megohm $\cdot\text{cm}$. For the experiments with heavy water, degassed D_2O was used: D_2O (99.8% d, > 2 megohm $\cdot\text{cm}$, Armar) for the fs-ESHS measurements and D_2O (99.9% d, Cambridge Isotope Laboratories) for the surface tension measurements.

3.2.2 Femtosecond elastic second harmonic scattering

fs-ESHS measurements were performed with the fs-ESHS experimental setup described in Ch. 2. For fixed angle measurements of concentration series of electrolyte solutions, the detection angle was set to 90° with an acceptance angle of 11.4° . Data points were acquired with an acquisition time of $50 \times 1 \text{ s}$ [that is, using $50 \times (2 \times 10^5)$ pulses in total]. For scattering pattern measurements, the detection angle was set from -90° to 90° with a step of 5° and an acceptance angle of 3.4° . Data points were acquired with an acquisition time of $20 \times 1 \text{ s}$ [that is, using $20 \times (2 \times 10^5)$ pulses in total]. For the signal detection, the gate width of PMT was set to 10 ns. The fs-ESHS signal of pure H_2O or D_2O was measured between every two samples and was used as a reference. The reproducibility error of the fs-ESHS measurements was 1 to 3%. Samples were stored and measured in sealed glass sample cells. All measurements were performed in a temperature- and humidity-controlled room ($T = 297 \text{ K}$; relative humidity, 26.0%). The obtained relative intensities as a function of the ionic strength were fitted with a Langmuir equation, whose functional form is given by

$$\Delta I(2\omega) = C \frac{\rho/A}{1 + \rho/A}, \quad (3.1)$$

where ρ is the ion concentration and A and C are constants. For temperature-dependent measurements, the temperature of the sample was changed by a temperature controller (Quantum Northwest) and was kept for 5 minutes to reach equilibrium

before fs-ESHS measurements. More details about fs-ESHS measurements can be found in Ref.¹⁵⁴.

3.2.3 Molecular dynamics simulations

Fully atomistic MD simulations were performed using the GROMACS 5.0.4 package¹⁷⁷ and making extensive use of GPU acceleration. The TIP4P-2005 model¹⁷⁸ was chosen to model water, and the CHARMM36 parameters¹⁷⁹ for the Na⁺ and Cl⁻ ions. The SETTLE algorithm¹⁸⁰ was applied to constrain the bond lengths and angles of the water molecules, allowing an integration time step of 2 fs. Long-range electrostatic interactions were calculated by the Particle-Mesh-Ewald (PME) method¹⁸¹ with a grid spacing of 0.12 nm. Short-range repulsive and attractive dispersion interactions were described with the Lennard-Jones potentials, using 0.9 nm for the cut off length. The simulation systems were constructed in the following steps. First, a box was filled with pre-equilibrium water molecules, and several ion pairs were randomly added to the systems to reach the desired concentrations. Second, after steepest descent energy minimization, the systems were equilibrated for 2 ns in the NPT ensemble simulations using the Berendsen thermostat and barostat¹⁸² to reach a target temperature of 298 K and pressure of 1 bar, respectively. The ion concentration was 8 mM (40 ion pairs), the number of water molecules was 264,443 (0 mM) and 264,363 (8 mM), and the length of the cubic simulation box was 19.94 nm. After equilibration, 50 ns long MD simulations were performed in the NVT ensemble. The target temperature of 298 K was kept constant using the canonical velocity rescaling thermostat¹⁸³, with a coupling time of 1 ps. The analysis of the water-water correlations has been performed over the full duration of the simulations, sampling every 2 ps.

3.2.4 Surface tension measurements

Surface tension measurements were performed using the Wilhelmy plate method²⁷. The Wilhelmy plate method uses a vertically suspended Pt plate with a perimeter l , which is pulled out of the electrolyte solution towards air. The force (F) acting on this plate is correlated to the surface tension γ by the following equation

$$\gamma = \frac{F}{l \cos \varphi}, \quad (3.2)$$

where φ is the contact angle between Pt and water, which has a value of $\varphi = 0$.¹⁸⁴ The measurement error of this method is 0.1%.²⁷

The surface tension measurements were performed using an Attension Sigma 701 force tensiometer (Biolin Scientific), which was equipped with an Attension Pt Wilhelmy plate (Biolin Scientific). This instrument was placed on a Micro-g lab table (TMC), located in an ISO class 6 (1000 p/ft³) clean room (Clean Air Products) to minimize environmental noise and reduce atmospheric dust. All solutions were kept and measured in glassware, which was previously treated with a standard Piranha glass cleaning procedure. Namely, the glassware was first treated for a minimum of 5 minutes with a 3:1 mixture of concentrated sulfuric acid (95-98%, Sigma-Aldrich) and hydrogen peroxide solution (30%, Macron fine chemicals). After this process, the glassware was washed with copious amounts of water. Each sample solution has been scanned a minimum of 40 times, and every surface tension value has been reproduced independently at least 5 times.

3.3 Results and discussion

3.3.1 Femtosecond snapshots of collective effects

In our fs-ESHS experiments (illustrated in Fig. 3.1B), S- or P-polarized femtosecond laser pulses interact with an aqueous electrolyte solution and induce a second-order polarization ($\mathbf{P}^{(2)}(2\omega)$, Eq. 3.3) that instantaneously emits polarized SH photons. This second-order polarization originates from two main sources⁸⁴: electronic anisotropy within an individual non-centrosymmetric molecule^{84,85,150} and structural anisotropy, which reports on the combined structural electronic anisotropy of many molecules. The first term is an incoherent contribution and can be understood as a measure of charge asymmetry within a molecule (and is also known as the self-correlation term; Eqs. 3.10 and 3.12). The second term is a coherent contribution and reports on the total sum of static positional orientational correlations between any pair of molecules (Eq. 3.13). A randomly distributed set of water molecules (as in an ideal gas) contains electronic anisotropy but no orientational correlations. For this reason, femtosecond second harmonic scattering is used routinely to probe particle and droplet surfaces^{82,91}: Water molecules aligned by a surface through H-bonding, by an electrostatic field, or by other interactions have orientational correlations. As an example, the orientational correlation of a pair of water molecules (as illustrated in Fig. 3.1A) can be changed by breaking an H-bond through a rotational or bending/libration

motion, but not by stretching the H-bond. Femtosecond laser pulses that are shorter than the orientational relaxation time of water are necessary to take snapshots of the static collective orientational correlations in water^{148,156}. In what follows, we refer to the structural collective orientational correlations as orientational order.

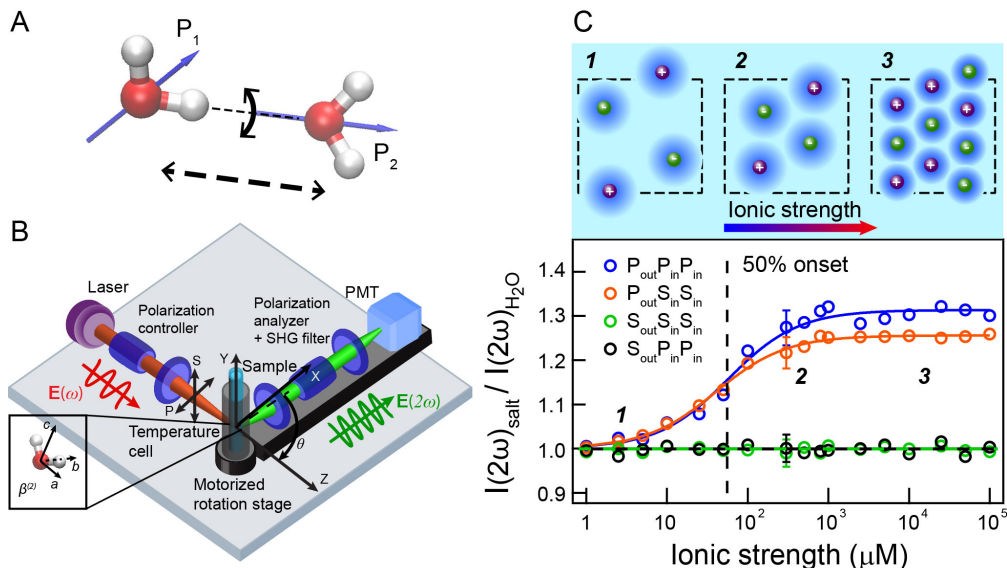


Figure 3.1 – Snapshots of long-range perturbations in aqueous NaCl solutions. (A) Illustration of two H-bonded water molecules that are orientationally correlated. The black arrows represent different axes along which H-bonds can be broken. fs-ESHS is only sensitive to the breaking of this H-bond via rotation (black curved arrow). Nuclear quantum effects predict that the H-bond bending mode is stronger, whereas the H-bond stretching mode is weaker, for D₂O compared to H₂O. (B) Sketch of the fs-ESHS experiment. fs-ESHS intensities are recorded at a scattering angle (θ) of 90°. P/S refers to a polarization direction parallel/perpendicular to the scattering plane. (C) Top: Illustration of the different regimes probed in the experiment. At low ionic strengths (1), each ion induces long-range structural water correlations in its vicinity, forming a water-ordered domain. At higher ionic strengths, more domains appear. These domains (2) start to overlap and (3) interfere with one another, leading to a saturation of the detected fs-ESHS signal. Bottom: fs-ESHS intensities of NaCl solutions, relative to that of H₂O. Four different polarization combinations were measured: PPP, PSS, SPP, and SSS. Only the PPP and PSS intensities change with increasing NaCl concentrations.

3.3.2 Induction of structural orientational order by electrolytes

The polarization combination of the exciting and emitted beams can be used to obtain information about the nature of the induced second-order polarization. Electronic anisotropy can be found in all eight possible polarization combinations. Orientational order (structural correlation) that is, on average, spherically symmetric, appears only in four polarization combinations: PPP, SSP, PSS, and SPS^{82,95}. If centrosymmetric ions induce changes in the orientational order of water, we expect these changes to

appear only in the abovementioned polarization combinations, and not in the combinations SSS, PPS, SPP, and PSP. The latter combinations report on translational/dipolar order as found in noncentrosymmetric crystals¹⁸⁵. By examining the polarization dependence of the fs-ESHS intensities of aqueous solutions of NaCl from 1 μ M to 0.1 M, we can determine whether the ions induce changes in the orientational order of the water network. Figure 3.1C (bottom) shows the change in the fs-ESHS intensity relative to that of pure H₂O (at $\theta = 90^\circ$) for 1 μ M to 0.1 M NaCl solutions for four different polarization combinations: PPP, SSS, SPP, and PSS, reporting on the collective orientational order (PPP and PSS)⁹⁵ and the electronic structure of individual molecules (SSS and SPP)¹⁸⁵. The polarization combinations SSS and SPP do not display any concentration-dependent intensity change with respect to the signal of pure H₂O. This excludes a change in the ion-induced electronic anisotropy of molecules. However, the PPP and PSS intensities increase by $30 \pm 3\%$ and $25 \pm 3\%$, respectively, before reaching a plateau at ~ 1 mM. Despite being a bulk phenomenon, the dependence of the intensity on concentration is well captured by the functional form of the Langmuir equation. The Langmuir equation is most commonly used to describe surface adsorption processes. Figure 3.1C is concerned with a bulk measurement and we note that this correlation is purely empirical. The observed changes in these polarization combinations alone indicate that the orientational order of water^{85,95} is changing, in qualitative agreement with the inelastic nanosecond HRS study conducted by Shelton¹⁵³.

3.3.3 Estimate of the spatial range of the perturbation

To make an estimate of the spatial range and magnitude of the ion-induced orientational order in water, we simplistically place each ion at the center of a spherical domain that is surrounded by a monomolecular shell of water at a distance R and is distorted in its structure by a tunable phenomenological parameter η , in analogy with nonlinear light scattering models^{82,91,186}. In detail, we consider two contributions that can be used to explain the change in fs-ESHS intensity observed in Fig. 3.1C:

1. The short-lived structural perturbations as arising from an unknown structural correlation, which we represented by spherical shells with a certain adjustable anisotropy (η) that surround domains with a radius R around a central ion. These shells with structurally correlated water molecules generate SH photons.
2. The single molecule electronic response of water as described by the third-order hyperpolarizability elements $\beta^{(3)}$, that couples to the electromagnetic fields of the incoming laser pulses and the screened electrostatic field of the ions in

solution.

To model these contributions, we use a nonlinear Rayleigh-Gans-Debye (RGD) light scattering model, which assumes that the linear refractive index is perturbed minimally by the presence of ions^{135,187} and is valid for domain sizes $R < 250$ nm.¹⁴¹ In this model we make use of the following coordinate systems (from large to small length scale):

- The right-handed Cartesian coordinate system of the laboratory frame (x,y,z). Here, x,z determines the horizontal plane of scattering, with z being directed along the SH $2\mathbf{k}_1$ vector, and y indicates the vertical direction out of the scattering plane. The polarization of light is indicated with P or S and labeled with u_i (as well as the electrical field components). In the frame \mathbf{q} is defined as the scattering wave vector, such that $\mathbf{q} \equiv \mathbf{k}_0 - 2\mathbf{k}_1$, and the scattering angle θ is defined as the angle between the scattered wave and the incoming beam.
- The right-handed Cartesian coordinate system of the effective susceptibility $\Gamma^{(2)}$, which is needed to calculate scattering integrals analytically and allows easy predictions of symmetry selection rules.¹³⁶ This frame is rotated with respect to the lab frame (and depends on the scattering geometry), with the principal axis lying along the scattering vector \mathbf{q} . In coordinate transformations, we label these indices with a_i .
- The spherical coordinate system of the nanoparticle surface or a monomolecular shell, which is indicated by (r', θ', ϕ') . In coordinate transformations, we label these indices with b_i .
- The Cartesian molecular coordinates, designated by (a, b, c) , where c represents the direction of the dipole moment of water. In coordinate transformations, we label these indices with c_i .

These coordinate systems are illustrated in Fig. 3.2.

The response from structural correlations

The total SH polarization of a single spherical domain originating from structural perturbations of water is given by¹⁸⁸

$$P_{u_0 u_1 u_2}^{(2)}(2\omega) \propto \sum_{a_0 a_1 a_2} \Gamma_{a_0 a_1 a_2}^{(2)} \prod_{i=0}^2 (\mathbf{q}_{a_i} \cdot \mathbf{e}_{u_i}) E_{u_1}(\omega) E_{u_2}(\omega), \quad (3.3)$$

where $E_{u_i}(\omega)$ is the amplitude of the incoming electrical field (the subscript u_i refers to the polarization state and here $u_1 = u_2$ for fs-ESHS), $\Gamma_{a_0 a_1 a_2}^{(2)}$ is an effective suscepti-

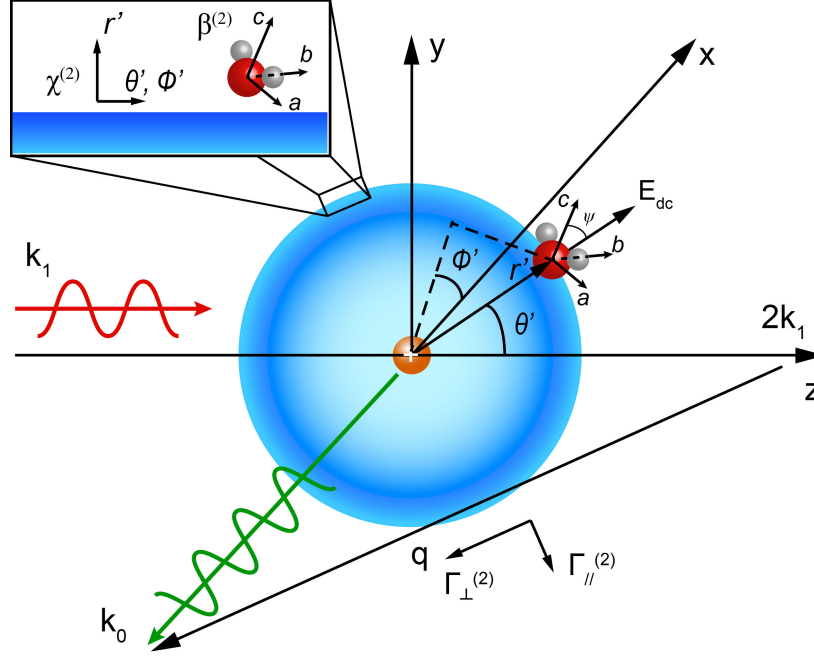


Figure 3.2 – Sketch of the relevant parameters needed in the phenomenological discussion. The illustration shows an ion and its extended hydration shell that are illuminated by fundamental laser pulses with a wave vector \mathbf{k}_1 . The fs-ESHS intensity is measured at a scattering angle (θ) of 90° . The scattering vector, \mathbf{q} , is defined as the difference, $\mathbf{k}_0 - 2\mathbf{k}_1$. The scattering vector defines the direction of the orthonormal coordinate system used for calculating the effective susceptibility ($\Gamma^{(2)}$) elements. The inset shows a close-up of the water shell, relative to which the $\chi^{(2)}$ elements are defined. The principal coordinate system of the water molecule is (a, b, c). The molecular hyperpolarizability $\beta^{(2)}$ is defined with respect to that system.

bility element (which is further described below), and \mathbf{e}_{u_i} denotes the polarization state unit vector of the electrical field. The effective susceptibility $\Gamma_{a_0 a_1 a_2}^{(2)}$ elements can be calculated using^{136,187}

$$\Gamma_{a_0 a_1 a_2}^{(2)} = \sum_{b_0 b_1 b_2} \int_{V_0} \chi_{b_0 b_1 b_2}^{(2)}(\mathbf{r}') f(\mathbf{r}') e^{i\mathbf{q} \cdot \mathbf{r}'} \prod_{i=0}^2 (\mathbf{q}_{a_i} \cdot \mathbf{e}_{b_i}) d^3 \mathbf{r}', \quad (3.4)$$

where V_0 denotes the volume of the domain in which molecules are correlated. The structural correlations of water molecules are represented by $\chi_{b_0 b_1 b_2}^{(2)}$, which is the angle averaged susceptibility of correlated water molecules at position \mathbf{r}' with a phase factor $e^{i\mathbf{q} \cdot \mathbf{r}'}$. For SHS from correlated molecules with spherical symmetry, e.g. molecules at a particle surface or in a monomolecular shell around a point center, $f(\mathbf{r}') = \delta(|\mathbf{r}'| - R\hat{\mathbf{r}})$. The results of the integrals in Eq. 3.4, as reported in Ref.¹⁸⁷, can be expanded as a power series of the radius R of the spherical domain (or the monomolec-

ular shell). The power series is given by

$$\Gamma^{(2)} \sim \chi^{(2)} R^2 (g_1(qR) + g_3(qR)^3 + O[(qR)^7]) \quad (3.5)$$

with g_i the expansion coefficients. For the present case, $qR \ll 1$, so the effective susceptibility $\Gamma^{(2)}$ is mainly determined by the first term in the above expansion. Therefore, the total SH polarization $P_{u_0 u_1 u_2}^{(2)}(2\omega)$ has a cubic dependence on the radius of the spherical domain (i.e., $P_{u_0 u_1 u_2}^{(2)}(2\omega) \propto R^3$) for nanometer length scales. The relation between $\chi_{b_0 b_1 b_2}^{(2)}$ and the second-order molecular hyperpolarizability $\beta_{c_0 c_1 c_2}^{(2)}$ is given by a coordinate transform

$$\chi_{b_0 b_1 b_2}^{(2)} = \frac{N_m}{\epsilon_0} \langle T_{b_0 c_0}(\mathbf{r}') T_{b_1 c_1}(\mathbf{r}') T_{b_2 c_2}(\mathbf{r}') \rangle \beta_{c_0 c_1 c_2}^{(2)}, \quad (3.6)$$

where $\langle T_{b_0 c_0}(\mathbf{r}') T_{b_1 c_1}(\mathbf{r}') T_{b_2 c_2}(\mathbf{r}') \rangle$ is the averaged transformation from the molecular coordinate system (c_0, c_1, c_2) to the monomolecular shell coordinate system (b_0, b_1, b_2) . The averaged transformation is determined by the orientational distribution function (ODF) of water molecules, and reflects molecular structural correlations. If the water molecules exhibit no structural correlation and thus are completely isotropic, the average of Eq. 3.6 equals zero and no coherent fs-ESHS signal is generated. Note that in order to introduce the effective susceptibility we assumed that the orientation of molecules is correlated with the center of the spherical domain, but not with the orientation of neighboring molecules.

The extent of the structural correlation is described by an average angle Ψ between the water dipole and the radial direction (assuming azimuthal isotropy). The product $\langle T_{b_0 c_0}(\mathbf{r}') T_{b_1 c_1}(\mathbf{r}') T_{b_2 c_2}(\mathbf{r}') \rangle$ can be calculated as a function of this average angle Ψ . The solutions for the expression $\langle T_{b_0 c_0}(\mathbf{r}') T_{b_1 c_1}(\mathbf{r}') T_{b_2 c_2}(\mathbf{r}') \rangle$ can be found in Ref.¹³⁷. Changes of the water structure, which result from all possible interactions in the system, are included in this relation. Since we do not have any information on the precise molecular structures, we introduce a relative structural anisotropy parameter η to capture the ion induced structural changes in the nonlinear susceptibility. Our definition of the relative structural anisotropy is $\eta = \epsilon_0 \chi_{r' r' r'}^{(2)} / (N_m \beta_{ccc}^{(2)})$, where r' is the shell normal/radial direction, and c is the direction of the dipole moment of the water molecule. Since a non-zero $\chi_{b_0 b_1 b_2}^{(2)}$ results from changes in the structural correlation between molecules, η reports on the ion induced water structuring that results in changes in the fs-ESHS intensity.

The response from third-order single molecule interactions

In addition to structural correlations between water molecules, there is also a contribution to the fs-ESHS response from a pure third-order electronic single-molecule interaction. Here, the intensity of the scattered light is determined by the third-order hyperpolarizability $\beta^{(3)}$. Following Ref.¹⁸⁸, the induced SH polarization of a single water molecule at position \mathbf{r}' is given by

$$p_i^{(3)}(2\omega, \mathbf{r}') = \beta_{ijk}^{(3)}(\mathbf{r}') E_j(\omega, \mathbf{r}') E_k(\omega, \mathbf{r}') E_{DC}(0, \mathbf{r}'), \quad (3.7)$$

in which $E_{DC}(0, \mathbf{r}')$ is the magnitude of the electrostatic field. Since the electrostatic field $\mathbf{E}_{DC}(0, \mathbf{r}')$ is directed in the radial direction, the rotational average of this induced SH polarization has the same symmetry properties as $\chi_{b_0 b_1 b_2}^{(2)}$. A similar quantity $\chi_{b_0 b_1 b_2 r'}^{(3)}$ (arising from $\beta_{ijk}^{(3)}$) can thus be calculated in the same way with Eq. 3.6. An effective susceptibility, $\Gamma_{a_0 a_1 a_2 r}^{(3)}$, can be calculated as well if we include $\mathbf{E}_{DC}(0, \mathbf{r}')$ in the integral of Eq. 3.4. The total $\beta^{(3)}$ -related SH polarization of water molecules within an extended water domain around an ion is then given by

$$P_{u_0 u_1 u_2}^{(3)}(2\omega) \propto \sum_{a_0 a_1 a_2} \Gamma_{a_0 a_1 a_2 r}^{(3)} \prod_{i=0}^2 (\mathbf{q}_{a_i} \cdot \mathbf{e}_{u_i}) E_{u_i}(\omega) E_{u_2}(\omega), \quad (3.8)$$

which is a function of the volume in which water molecules are contributing to the SH polarization. The effective size of the volume is determined by the strength of $\mathbf{E}_{DC}(0, \mathbf{r}')$. Combining both second- and third-order effects, the intensity of the scattered SH light of structurally correlated water molecules in a single domain is now given by

$$I_{corr, u_0 u_1 u_2}(2\omega) = C^2 \frac{k_0^4 \epsilon_0^2}{r_0^2} E_{u_1}^2(\omega) E_{u_2}^2(\omega) \left| \sum_{a_0 a_1 a_2} (\Gamma_{a_0 a_1 a_2}^{(2)} + \Gamma_{a_0 a_1 a_2 r}^{(3)}) \prod_{i=0}^2 (\mathbf{q}_{a_i} \cdot \mathbf{e}_{u_i}) \right|^2, \quad (3.9)$$

where C is a constant (which depends on the chosen system of units), r_0 is the detector position (in the far field), k_0 is the magnitude of the scattered SH wavevector.

The fs-ESHS intensity from uncorrelated water molecules in an isotropic liquid is given by¹⁸⁹

$$I_{uncorr, u_0 u_1 u_2}(2\omega) = C^2 \frac{k_0^4}{r_0^2} E_{u_1}^2(\omega) E_{u_2}^2(\omega) \langle [\beta_{u_0 u_1 u_2}^{(2)}]^2 \rangle N_m \int_{V_0} d^3 \mathbf{r}', \quad (3.10)$$

where N_m is again the number density of water molecules and \int_{V_0} denotes a volume integral over the water volume that is associated with one ion.

Spherical domain size dependence of the fs-ESHS signal

To estimate the length scale that contributes most to relative changes in the fs-ESHS intensity (as plotted in Fig. 3.1C), we calculate the response of all extended hydration shells in the solution by dividing the intensity of a single ion domain (arising from single molecule responses (Eq. 3.10) as well as structural correlations and third-order interactions (Eq. 3.9)) by the intensity from uncorrelated water molecules in the same volume (Eq. 3.10), i.e.

$$\Delta I(2\omega) = \frac{I_{corr}(2\omega) + I_{uncorr}(2\omega)}{I_{uncorr}(2\omega)} = \frac{I_{corr}(2\omega)}{I_{uncorr}(2\omega)} + 1. \quad (3.11)$$

We use the values of Table 3.2 as input. The domain size (R) and the relative structural anisotropy (η) are adjustable parameters. By adjusting these we can find a (R , η) parameter space which is compatible with the measured intensity change. At very low electrolyte concentrations, we can assume the position of the ions to be largely uncorrelated, so the intensity will increase linearly with the concentration of ions. The change in the total fs-ESHS signal can then be taken as the linear sum of the intensities from all ions. At higher electrolyte concentrations (when the intensity curve in Fig. 3.1C is no longer linear), ions or their domains become correlated. We will discuss the implications of ion correlations in the next section.

Figure 3.3 shows the computational results for dilute electrolyte solutions for four different fs-ESHS intensity changes that correspond to four different electrolyte concentrations. We assume for simplicity that only a mono-molecular shell of radius R contributes to the signal, so that the intensity that arises from a single ion can be obtained from the absolute square of Eq. 3.3. This treatment differs from the description of bulk water in Ref. ¹⁹⁰ where entire bulk domains are used. Both methods, however, do not provide any information about the structure of water and serve to assess length scales only.

We can now investigate which combinations of domain size and relative anisotropy are compatible with the measurements. The red curve represents the parameter space of (R , η) for which an intensity change of $\Delta I(2\omega) = 1.05$ is calculated, which corresponds to the measured value at a NaCl concentration of 10 μ M. Such a response can be achieved with a monomolecular shell with a domain radius of 21.8 nm and a relative structural anisotropy of 0.0245. In this case, each water molecule has an additional radial alignment that corresponds to 2.45% of the electronic anisotropy of a single water molecule. Smaller domain radii but with larger relative anisotropies that lie on the red curve can also lead to $\Delta I(2\omega) = 1.05$. The orange, green and

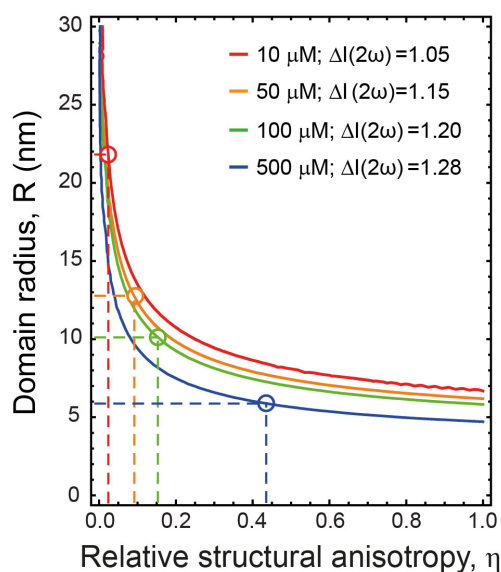


Figure 3.3 – $\Delta I(2\omega)$ as a function of domain size and relative structural anisotropy. The solid curves represent calculated relative intensities that match the relative intensities for 10, 50, 100 and 500 μM NaCl solutions, respectively, as a function of the amount of structural anisotropy (η , X-axis) and domain size (R , Y-axis). The dashed lines indicate half of the average separation of ions for each electrolyte concentration. The corresponding relative structural anisotropy that is needed to obtain the measured $\Delta I(2\omega)$ is also indicated.

blue curves represent $\Delta I(2\omega)$ for different values that correspond to different NaCl concentrations (50, 100, and 500 μM). The horizontal dashed lines indicate the domain radius that corresponds to half the average distance between the ions, here calculated from simple cubic packing of ions. Table 3.1 summarizes the relevant domain sizes, corresponding number of hydration shells, and anisotropy in case that the domain size is only determined by the average ion separation.

c (μM)	R (nm)	Number of water layers (hydration shells)	η
10	21.8	70.3	0.0245
50	12.8	41.3	0.0901
100	10.1	32.6	0.1512
500	5.9	19.0	0.4321

Table 3.1 – Domain radius (R), corresponding number of hydration shells, and anisotropy (η) in case the domain size is determined only by the average ion separation.

Figure 3.3 shows that if the structural anisotropy matches the electronic anisotropy in magnitude ($\eta = 1$), a minimum domain radius of ~ 5 nm is needed to reach the observed increase of the fs-ESHS intensity. Alternatively, from Fig. 3.1C we see that the ion positions become correlated at ~ 55 μM , which requires a domain

radius of 6.1-12.4 nm and a relative anisotropy of 1-0.097, which corresponds to the range of values that are permissible by taking either the domain radius as being determined by the average separation or the relative anisotropy ($\eta = 1$) as limiting parameters. Furthermore, the domains become structurally intertwined when the data in Fig. 3.1C levels off at $\sim 500 \mu\text{M}$, which requires a maximum radius of 5.9 nm and a structural anisotropy of 0.43. If the observed effect would be short-range and the increase of signal of electrolyte solutions from 0 to $10 \mu\text{M}$ would originate from a monomolecular shell of ~ 1 nm size, then a relative anisotropy of $\sim 8.4 \times 10^6$ would be needed, which is physically unreasonable.

The importance of the single molecule third-order contribution can also be estimated. Using the average separation of ions as an indicator for the effective size of the volume for the calculation of the $\beta^{(3)}$ contribution to the SH polarization, we see that this contribution to the signal is minor: At an electrolyte concentration of $50 \mu\text{M}$, the pure $\beta^{(3)}$ contribution to the relative increase of the SH intensity is only 0.014%, which is negligible compared to the total increase of 15%.

Summarizing what we have seen so far, in measurements of up to $\sim 55 \mu\text{M}$ (Fig. 3.1C), the spherical domains do not overlap and the measured intensity increases linearly with concentration. At higher concentrations, the fs-ESHS intensity levels off. As more ions are added, the volumes associated with different ions begin to overlap, to interfere with one another, and to exhibit spatial correlations. The preceding analysis that considers water molecules as organized in concentric shells is not a physically meaningful representation of water and should not be interpreted as such. However, this oversimplified representation does serve to show that within this model (i) the length scale over which the orientational order extends is > 5 nm and (ii) short-range (< 1 nm) structural changes cannot account for the observed changes. From the preceding analysis, it is easy to see that the collective orientational order could extend as far as 19 to 70 hydration shells (Table 3.1).

3.3.4 Distortion of the H-bond network over nanoscopic distances

Next, we want to determine whether the observed increase in orientational order depends on the chemical structure and charge of the ions. We addressed this question by repeating the fs-ESHS measurements for 20 other electrolytes together with a nonpolar neutral molecule (CCl_4) as a control. Figure 3.4 shows the PPP fs-ESHS intensity in the same ionic strength range for a monovalent Cl^- cation series (NH_4Cl , KCl , NaCl , LiCl , and HCl) and for a monovalent Na^+ anion series (NaH_2PO_4 , NaOH , NaCl , NaBr , NaI , NaNO_3 , NaClO_4 , and NaSCN). The divalent cationic–monovalent

anionic pairs (MgCl_2 , CaCl_2 , SrCl_2 , and BaCl_2), the monovalent cationic–divalent anionic pairs ($\text{Na}_2\text{S}_2\text{O}_3$ and Na_2SO_4), and the divalent cationic–anionic pairs (BeSO_4 , MgSO_4 , and CaSO_4) are also shown. For all electrolyte solutions, the same trend is observed: a rise in intensity up to a plateau. In contrast, for nonionic CCl_4 , the fs-ESHS intensity remains unchanged. Note that the ionic strengths at which the curves change slope, as well as the relative intensity of the plateau, are independent of the electrolyte used. Thus, there is no dependence on the ionic radius, the polarizability, or the chemical structure of the ions. This absence of ion specificity is consistent with the notion that the fs-ESHS signal generated by the immediate neighborhood of the ion is negligible (see Fig. 3.3).

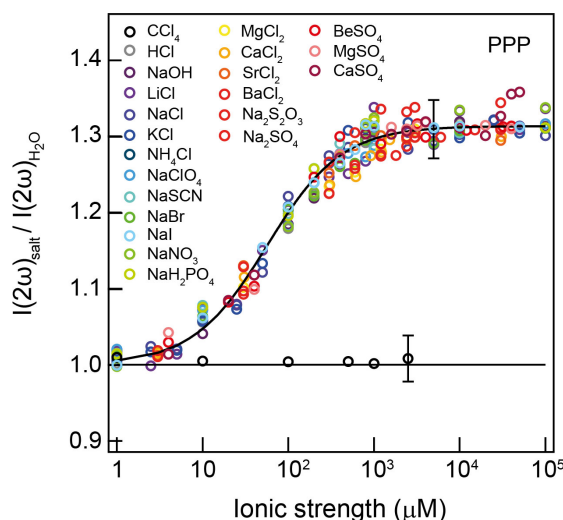


Figure 3.4 – Nonspecific long-range changes in the H-bond network of water. fs-ESHS intensities, relative to that of pure water, of 21 different electrolyte solutions obtained at a scattering angle of 90° (PPP polarization combination). The relative intensities of all electrolyte solutions can be fitted with the same Langmuir type equation. The dashed line indicates the concentration of half saturation. fs-ESHS intensities of aqueous CCl_4 solutions are also plotted for comparison (the X-axis should be read here as “Concentration (μM)”).

3.3.5 Origin of the nanoscopic distortions

Thus far, the origin of the increase in orientational order observed in Figs. 3.1C and 3.4 has not been attributed to any specific type of interactions. Ion-dipole interactions as captured by a mean-field description are a candidate, but so are collective H-bond interactions between water molecules that are distorted by electrolytes. In the appendix (Sec. 3.5.2), we consider a Debye-Hückel (DH) model that treats water as an ideal gas of dipoles, in which ions interact by means of ion-dipole interactions.

This model predicts that the fs-ESHS response saturates as a function of the ionic strength. The fs-ESHS response is also expected to scale as $1/\text{temperature}$. Light water and heavy water have comparable dipole moments and dielectric constants (1.8546 D/1.8558 D and 78.45/78.08 for $\text{H}_2\text{O}/\text{D}_2\text{O}$; Table 3.2) and thus generate identical fs-ESHS responses within this framework. However, we observed that the temperature-dependent fs-ESHS response (Fig. 3.8B) does not follow the trend found by the DH model.

Isotope experiments

In order to further investigate the validity of the DH model, we measured the fs-ESHS response of pure light and heavy water. Figure 3.5A shows fs-ESHS scattering patterns of bulk H_2O and D_2O . It can be seen that the scattering patterns are isotropic for the SSS polarization combination and peaked towards the forward direction in the PPP polarization combination. The straight lines represent a calculation of the fs-ESHS response assuming that only the incoherent electronic single molecule response gives rise to fs-ESHS signal. According to this assumption, the curves should obey Eq. 2.24, that is (Ref.⁸⁴, Eq. 50, only the first term)

$$\begin{aligned} I_{SSS}(2\omega) &= A \left\langle \left[\beta_{YYY}^{(2)} \right]^2 \right\rangle \\ I_{PPP}(2\omega) &= A \left\langle \left[\beta_{XXX}^{(2)} \right]^2 \right\rangle \cos^2 \theta + A \left\langle \left[\beta_{ZXX}^{(2)} \right]^2 \right\rangle \sin^2 \theta, \end{aligned} \quad (3.12)$$

in which A is the scaling constant, θ is the scattering angle as defined in Fig. 3.1B, and $\beta_{IJK}^{(2)}$ is the effective hyperpolarizability in the laboratory frame coordinates (Fig. 3.2). $\langle \rangle$ represents an orientational and temporal average over a large number of molecules. $\left\langle \left[\beta_{YYY}^{(2)} \right]^2 \right\rangle = \left\langle \left[\beta_{XXX}^{(2)} \right]^2 \right\rangle = 282.1 \left[\times (3.20 \times 10^{-53} \text{C}^3 \text{m}^3 \text{J}^{-2})^2 \right]$ and $\left\langle \left[\beta_{ZXX}^{(2)} \right]^2 \right\rangle = 33.2 \left[\times (3.20 \times 10^{-53} \text{C}^3 \text{m}^3 \text{J}^{-2})^2 \right]$, for isolated water molecules in an isotropic environment. These values are calculated based on the hyperpolarizability values given in Table 3.2 in combination with the response for molecules of the C_{2v} point group (Appendix B of Ref.⁸⁴).

Based on the ideal gas model that underlies the DH theory and the assumption of isotropy, we should not expect a difference between the fs-ESHS patterns of H_2O and D_2O . Furthermore, the shape of the data would follow the calculated lines. Figure 3.5A shows fs-ESHS patterns of bulk H_2O and D_2O . The SSS data can be seen to follow the trend of the predicted line shape of Eq. 3.12, while the PPP data does

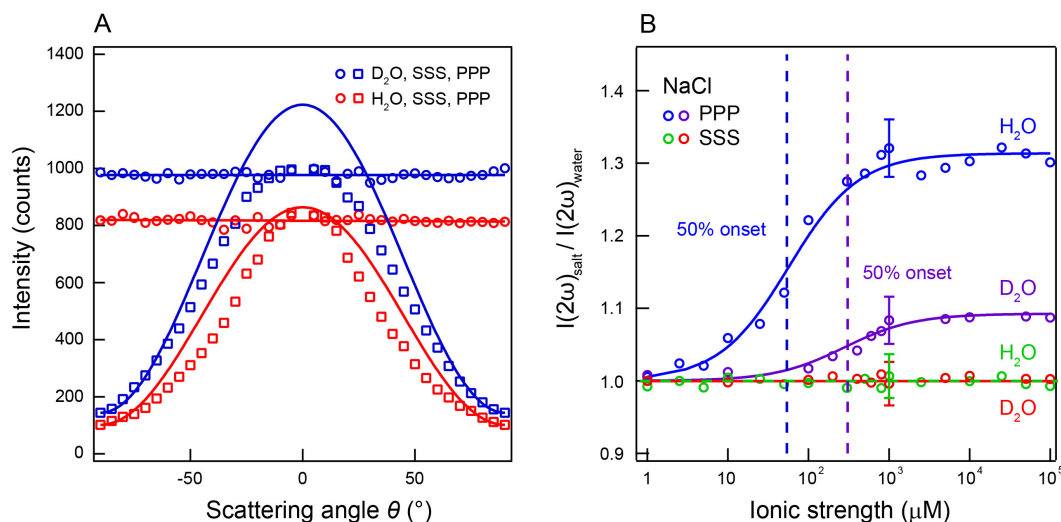


Figure 3.5 – Nuclear quantum effects. (A) fs-ESHS patterns for pure H_2O and pure D_2O . Both the SSS (circles, red for H_2O and blue for D_2O) and the PPP fs-ESHS patterns (squares, red for H_2O and blue for D_2O) are plotted. The solid lines correspond to an incoherent averaged single molecule response. It can be seen that such a response does not fully capture the shape of the data. Note that the computed single molecule responses are here scaled to coincide with the experimental data at the scattering angle of $\theta = \pm 90^\circ$. (B) Relative fs-ESHS intensities of NaCl in H_2O and D_2O (PPP and SSS polarization combinations).

not. Additionally, the D_2O response is significantly more intense than the H_2O response (e.g. 40% bigger for PPP at $\theta = 90^\circ$; or 20% for SSS). The intensity ratios of $I_{PPP}(0^\circ) / I_{PPP}(90^\circ)$ are 7.8 ± 0.3 for H_2O and 6.9 ± 0.3 for D_2O , whereas a purely incoherent ideal gas response would have a ratio of 8.5 for both H_2O and D_2O (using the values and formulas of Refs.^{84,191}). The above deviations (deviations in the magnitude of the polarization ratios and in the scattering pattern, the isotope effect) suggest that structural correlations/collective H-bond interactions play a significant role here. Only by including these interactions we can account for the differences between the data and the ideal gas model. Incorporating collective H-bond interactions in the explanation, a direct relationship between H-bond properties and fs-ESHS response is expected: As D_2O has stronger H-bonds than H_2O , there is more orientational order, which translates into a stronger fs-ESHS response. In addition, in agreement with the observation, the polarization ratios for D_2O are expected to deviate further from ideal gas behavior than those of H_2O .

In addition to pure light and heavy water, we also investigated electrolyte solutions with D_2O at different ionic strengths compared to those with H_2O . Figure 3.5B compares the fs-ESHS measurements of NaCl dissolved in H_2O and D_2O (PPP and SSS polarization combinations). The PPP intensity change up to the plateau for D_2O solutions is $9 \pm 3\%$ (instead of $30 \pm 3\%$ for H_2O , a factor of ~ 3.3). The ionic strength

at half saturation is $310 \pm 71 \mu\text{M}$ for D_2O (instead of $55 \pm 5 \mu\text{M}$ for H_2O , a factor of 6 ± 1.9). In contrast, the DH model predicts a saturated fs-ESHS response that is a factor of 20 (for D_2O) or a factor of 6 (for H_2O) larger than the measurement. The predicted onset of the increase is either on the order of the observed value (H_2O) or off by a factor of 7 (D_2O). Within the DH framework, there are no adjustable parameters that can account for any of these effects.

Molecular dynamics simulations

Orientational order arising from H-bond interactions has not been considered relevant in the interpretation of SH data from bulk water^{190,192}. However, experiments of SHS from surfaces of oil nanodroplets in aqueous solutions^{104,110} hint at the importance of H-bonding. Including H-bond interactions here will likely modulate the fs-ESHS signal and may reduce the orientational order found from the DH model. Indeed, liquid water derives its unique properties from its three-dimensional H-bond network, which ensures that some degree of structural orientational order is present. This can be demonstrated with an MD simulation of 264,000 (TIP4P 2005) water molecules that includes both ion-dipole and dipole-dipole interactions. Such a large simulation box (or an even larger one) is necessary to approach the low concentration limit that is probed by the experiments and to reduce finite-size artefacts in the electrostatic potential. Figure 3.6A shows the orientational order in water (that is, the water-water orientational correlations among all pairs of water molecules) as a function of distance. At water-water distances of $R < 1 \text{ nm}$, water molecules experience changes in their orientational distribution on the order of 10° to 20° per molecule. Ions will distort this distribution by means of ion-dipole interactions and by changing the H-bond network of water, which are both probed in the fs-ESHS measurements.

We computed the ion-induced changes in the water-water orientational correlations for a NaCl solution with a concentration of 8 mM (Fig. 3.6B) by calculating the difference in orientational correlations between the ionic solution and the pure water. This can be related to the fs-ESHS response as follows: The coherent contribution to the fs-ESHS response involves a quadratic distance dependent term, which is written for a pair of molecules as

$$\int_0^\infty dR \frac{\sin(qR)}{qR} R^2 \int d\Omega_1 \int d\Omega_2 g(R, \Omega_1, \Omega_2) \beta_{ijk}^{(2)}(\Omega_1) \beta_{ijk}^{*(2)}(\Omega_2), \quad (3.13)$$

see Bersohn et al.⁸⁴, Eq. 55. Here, R is the separation between two water molecules (labeled 1 and 2), with orientational angles Ω . The orientational correlations that enter

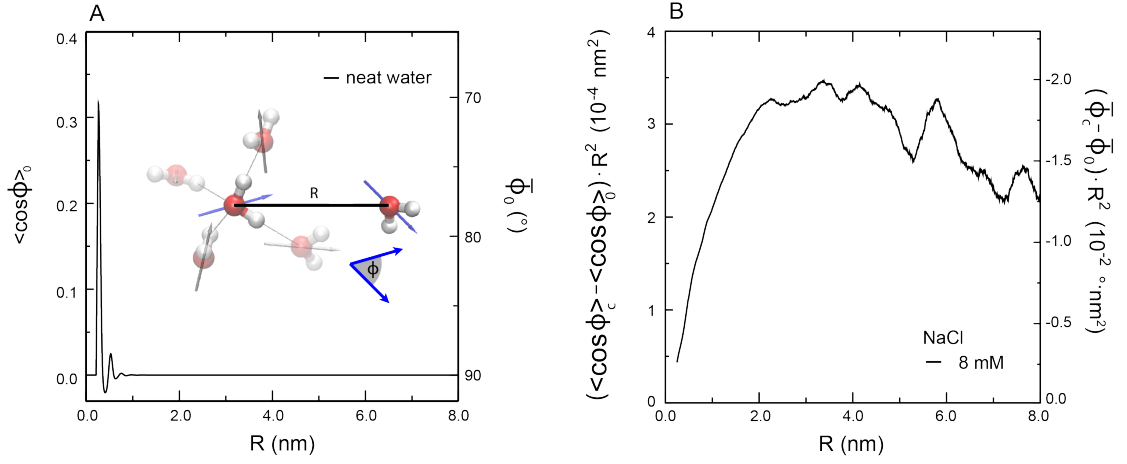


Figure 3.6 – MD simulations of orientational order in the H-bond network of water. (A) Water-water orientational correlations (left) and corresponding changes in average tilt angles (right) obtained from an MD simulation of pure water. (B) Ion-induced change in the orientational order for an 8 mM NaCl solution. Changes in the distance-weighted water-water orientational correlations are shown (left axis), as well as the corresponding changes in the distance-weighted average tilt angle per water molecule (right axis).

the definition of $g(R, \Omega_1, \Omega_2)$ are contained in the MD simulations. To express clearly the effect of ions on such correlations, we focus only on the angle ϕ between the dipoles of a pair of water molecules (as sketched in the inset of Fig. 3.6A). Considering that for the experiment $\frac{\sin(qR)}{qR} \rightarrow 1$, the contribution to the fs-ESHS response (Eq. 3.13) can be represented by

$$\int_0^\infty dR R^2 \langle \cos \phi \rangle. \quad (3.14)$$

Figure 3.6B shows the distance dependence of the ion induced change in the fs-ESHS response, i.e. it shows the difference in the average orientational distribution with and without 8 mM NaCl, $(\langle \cos \phi \rangle_c - \langle \cos \phi \rangle_0)$ multiplied by R^2 . The resulting distance-weighted angular distortion is plotted on the right axis. Perturbations with a magnitude of $\sim 0.02 \text{ }^\circ \cdot \text{nm}^2$ are induced by the presence of ions and persist over a length scale $> 8 \text{ nm}$ (here limited by the size of the simulation box).

Possible role of nuclear quantum effects

The contribution of H-bond interactions offers an explanation for the phenomenological differences between light water and heavy water observed in Figs. 3.5A and 3.5B. The strengths of the H-bond in H_2O and in D_2O are different and are modulated by nuclear quantum effects. The bending mode of the H-bond (illustrated in Fig. 3.1A) in

D₂O is stronger than that in H₂O, whereas the stretching mode of the H-bond displays the opposite behavior. Isotope effects are usually not more than a few percentages in magnitude because of the competition of these opposite quantum effects along the two different molecular axes illustrated in Fig. 3.1A.^{182,193,194} In the data of Fig. 3.5B, a much bigger difference between H₂O and D₂O is found because only one of the two modes (the bending motion of H-bond) modulates the fs-ESHS response. A stronger H-bond in D₂O (along the bend axis) consistently implies a higher fs-ESHS intensity of pure D₂O, a higher ionic strength for the half saturation, and a smaller relative saturation intensity.

3.3.6 Orientational order probed macroscopically

We have seen thus far that electrolyte concentrations as low as 10 μ M induce orientational order in water that amounts to a fraction of a degree. At such concentrations, each ion is surrounded by 2.75 ± 10^6 water molecules. Therefore, although the magnitude of the change in orientation order is small, the total cooperative effect can be significant. Macroscopic properties might be influenced, too, if they report on changes in orientational order. We will explore macroscopic changes next. The method that we used for that was surface tension measurements, which may seem to be an unusual method for probing ion-solute interactions.

Surface tension (γ) measures the work needed to create a unit surface area of liquid-vapor interface. Adding electrolytes to water leads to a change in the surface tension $\Delta\gamma$. The change in $\Delta\gamma$ is in turn linked to a change in the net surface excess or depletion of the electrolyte at the interface by the Gibbs adsorption equation. The surface excess (Γ_i) of component i is defined as

$$\Gamma_i = \left(\frac{\partial \gamma}{\partial \mu_i} \right)_T. \quad (3.15)$$

The chemical potential (μ_i) of component i is given by

$$\mu_i = \mu_i^0 + 2k_B T \ln f_i x_i \quad (3.16)$$

for a 1:1 electrolyte, where f_i refers to the activity coefficient, x_i to the partial concentration, and μ_i^0 to the standard chemical potential. Since μ_i contains both bulk (first term) and surface (second term) properties, a measurement of $\Delta\gamma$ as a function of the ionic strength reports on both bulk and surface properties of an electrolyte solution.¹⁹⁵ Another way of understanding this is that the surface tension is also defined

as the change in the free energy when the surface area is increased by a unit area.²⁷ For an air (a)/water (w) interface it can be expressed by:

$$\gamma = \frac{1}{2}W_w + \frac{1}{2}W_a - W_{wa}, \quad (3.17)$$

where W_w and W_a are the reversible work needed to separate two unit areas of two surfaces from contact with each other to infinite spacing in vacuum for water and for air, respectively. W_{wa} refers to the work of adhesion due to the interfacial interaction energy per unit area of air and water (see Fig. 3.7A for a sketch). Since molecules in an ideal gas are non-interacting, $W_a \rightarrow 0$. $W_{wa} \rightarrow 0$ as well because of the low concentration of gas molecules compared to the concentration of water molecules (about a factor of 1000 lower). The change in the surface tension $\Delta\gamma$ ($\Delta\gamma = \gamma_{\text{solution}} - \gamma_{\text{water}}$) as a function of electrolyte concentration c can be expressed as

$$\frac{\partial\Delta\gamma}{\partial c} = \frac{1}{2}\frac{\partial\Delta W_w}{\partial c} + \frac{1}{2}\frac{\partial\Delta W_a}{\partial c} - \frac{\partial\Delta W_{wa}}{\partial c} = \frac{1}{2}\frac{\partial\Delta W_w}{\partial c}. \quad (3.18)$$

Since $W_a \rightarrow 0$ and $W_{wa} \rightarrow 0$, $\frac{\partial\Delta W_a}{\partial c} = \frac{\partial\Delta W_{wa}}{\partial c} = 0$. Thus $\frac{\partial\Delta\gamma}{\partial c}$ reports on breaking H-bonds.

For electrolytes at molar concentrations, the surface is depleted relative to the bulk, leading to an increase in surface tension (that is, $\Delta\gamma > 0$)¹⁵. At concentrations < 1 mM, which are much smaller than those at which depletion effects become measurable, Jones and Ray²³ measured a decreasing $\Delta\gamma$ that reaches a minimum at a concentration of ~ 1 mM, using the capillary rise method. A possible explanation for this observation is that, at such low concentrations, the decrease in $\Delta\gamma$ does not stem from the surface segregation of the bare ions, but rather from the relative stability of the weakly oriented water that surrounds the ions. An increase in the orientational order of the water H-bond network entails an entropic penalty that is greater in the bulk than at the surface, leading to a net favorable interaction with the surface and, hence, to a decrease in $\Delta\gamma$.

To verify this hypothesis, we measured (i) the concentration-dependent surface adsorption of ions by means of resonant SH measurements in reflection mode (Fig. 3.7B) and (ii) compared the $\Delta\gamma$ values of electrolyte solutions for light water and heavy water at different ionic strengths up to 100 mM (Fig. 3.7C). Starting with the first set of experiments, SH measurements in reflection mode were recorded under resonant conditions, probing the charge-transfer-to-solvent (CTTS) transition of I^- present in NaI and KI solutions. The surface activity of I^- is found from spectral decomposition and is plotted for NaI and KI solutions as $|\chi^{(2)}|^2$ in Fig. 3.7B (black and red

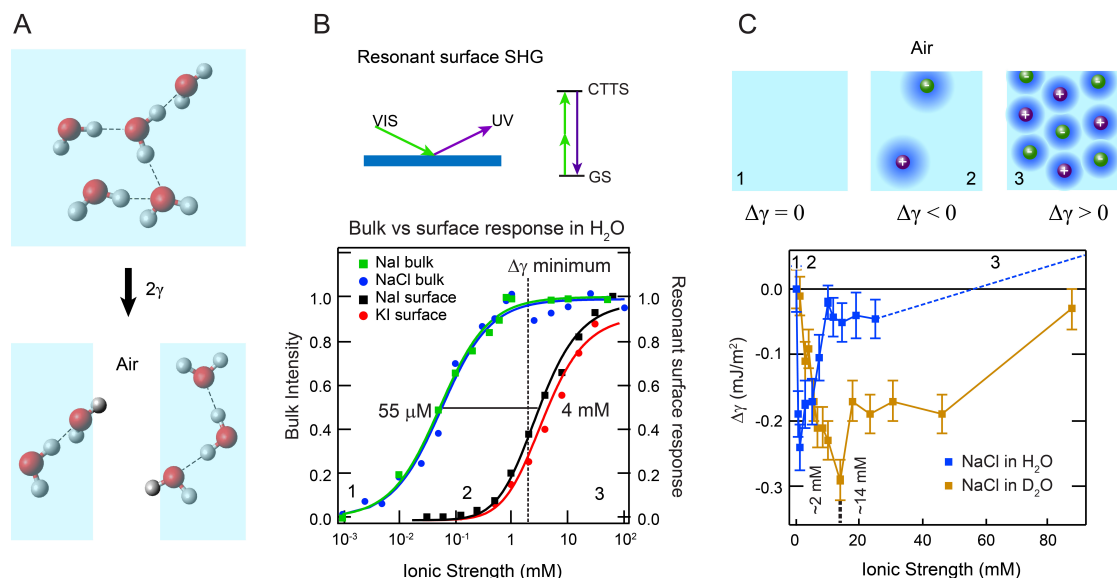


Figure 3.7 – Macroscopic manifestation of orientational order in the H-bond network of aqueous electrolyte solutions. (A) An illustration of the concept of surface tension. (B) Normalized resonant I[−] surface SHG signal of NaI and KI ($|\chi^2|^2$; black and red data)¹⁹⁶ and normalized fs-ESHS (bulk) intensity change originating from constraints in the orientational order of bulk water (blue and green data). Ion-induced changes in the H-bond network of bulk water occur at lower concentrations (55 μ M) than the surface adsorption (4 mM). The saturation of the bulk structural changes coincides with the minimum in $\Delta\gamma$ (dashed line). The top panel shows an illustration of resonant surface SHG. VIS, visible; UV, ultraviolet; GS, ground state. (C) Measured surface tension difference ($\Delta\gamma$) for NaCl solutions of H₂O (blue data) and D₂O (brown data). Above 20 mM, $\Delta\gamma$ increases, as indicated by the dashed line (see Jarvis and Scheiman³³). A cartoon illustrating the structural changes in the electrolyte solution is shown on top. The numbers correspond to the different regimes of ionic strength and are also indicated in (B).

data). The I[−] surface SHG signal increases at micro-molar concentrations close to the minimum of the surface tension measurements and then saturates at ~ 100 mM. Other salts that have an optically accessible CTTS transition, such as K₄Fe(CN)₆, also lead to changes in the surface SH signal. The smaller halide ions have CTTS transitions at shorter wavelengths that are not optically accessible. The changes in the surface SHG signal were nonetheless interpreted as non-specific.^{29,196} The bulk fs-ESHS responses of NaCl and NaI solutions are also shown (blue and green data). As discussed, it shows that the orientational order of bulk water is changed at ~ 1 mM. The ionic strength for the half saturation of both curves (55 μ M and 4 mM) is different by ~ 2 orders of magnitude.

Figure 3.7C shows the second set of experiments: $\Delta\gamma$ recorded for NaCl solutions in H₂O and D₂O using the Wilhelmy plate method²⁷. As worked out in detail in the above, here, $\Delta\gamma$ reports on the ion-induced free-energy change involved in creating a water-air surface, with an accuracy of 0.1% (0.072 mJ/m²). It can be seen in Fig.

3.7C that $\Delta\gamma$ reaches a minimum at 2 ± 1 mM for NaCl in H₂O and at 14 ± 0.5 mM for D₂O (that is, at an $\sim 7\times$ higher ionic strength than for H₂O). Beyond ~ 20 mM (H₂O), $\Delta\gamma$ increases.^{15,23} Within the error of the measurements, the concentrations for which the minima are reached are the same as the ones for which the fs-ESHS signal saturates for both H₂O and D₂O (Fig. 3.5B). The difference equals the phenomenological factor of ~ 6 observed in the fs-ESHS measurements (Fig. 3.5B). Because surface tension measurements cannot distinguish between the different axes along which H-bonds can be formed/broken (Fig. 3.1A), the magnitude of $\Delta\gamma$ is expected, and observed, to be the same for H₂O and D₂O. In agreement with this observation, interfacial isotope effects are small: Sum frequency experiments on isotopic mixtures at the air-water interface indicate no substantial isotope effect¹⁹⁷ or, at most, a 4% isotope effect¹⁹⁸.

Thus, although the change in the orientational order of a single water molecule is small, the collective effect appears to be linked to macroscopically detectable distortions in the H-bond network of water. This is a remarkable manifestation of how an accumulation of small distortions may result in macroscopic effects. Water plays an omnipresent role in physics, chemistry, biology, and medicine, and subtle effects can have significant consequences for equilibrium and non-equilibrium processes. The observed effects may well be relevant to a wide variety of phenomena, and the sizable difference observed between H₂O and D₂O provides us with a handle to understand and verify models aimed at understanding nuclear quantum effects in aqueous systems.

3.4 Conclusions

In summary, we observe electrolyte-induced perturbations in the H-bond network of liquid water that start to appear at ionic strengths $< 10 \mu\text{M}$. The changes level off at ~ 1 mM, are constant up to ~ 0.1 M, and can be explained as an increase in orientational order in the H-bond network of water. The observed perturbations are independent of the chemical nature of the 21 ion pairs used, indicating a universal effect that is also present at physiological electrolyte concentrations. The observed constraint in the orientational order of water molecules is also detectable macroscopically: The decrease in surface tension measured at micromolar concentrations points to a qualitative change in the surface propensity of ions that can be explained in terms of the collective interaction between nanoscopic "ordered domains" of water around ions and the interface. The H-bond restructuring observed in the fs-ESHS measurements occurs in both H₂O and D₂O, but the comparative response of D₂O is a factor of

~3 lower in relative fs-ESHS intensity than that of H₂O, and occurs at an ~6× higher electrolyte concentration. This is consistent with H-bonds being stronger in D₂O than in H₂O as a result of nuclear quantum effects, which leads to smaller perturbations in heavy water than in light water. This large difference in the onset concentration is also observed in surface tension measurements, suggesting a further link between nanoscopic and macroscopic length scales.

3.5 Appendix

3.5.1 Constants and properties of H₂O and D₂O

Property		H ₂ O	D ₂ O
Refractive index, ¹⁹⁹ 298 K	514 nm	1.3363	1.3308
	1028 nm	1.3245	1.3215
Dipole moment (D)	gas phase ²⁰⁰	1.8546	1.8558
	liquid phase ¹⁴⁷ , 300 K	2.95	–
Permittivity at infinite frequency ²⁰¹		4.49	–
Static dielectric constant ²⁰² , 298 K		78.45	78.08
$\beta^{(2)}$ in gas phase ^{146,203–206} ($3.206361 \times 10^{-53} \text{C}^3 \text{m}^3 \text{J}^{-2}$)	$\beta_{aac}^{(2)}$	-11.064	-10.83
	$\beta_{caa}^{(2)}$	-11.244	-10.98
	$\beta_{bbc}^{(2)}$	-5.873	-5.89
	$\beta_{cbb}^{(2)}$	-5.343	-5.36
	$\beta_{ccc}^{(2)}$	-15.240	-15.07
$\beta^{(2)}$ in liquid phase ¹⁹¹ ($3.206361 \times 10^{-53} \text{C}^3 \text{m}^3 \text{J}^{-2}$)	$\beta_{caa}^{(2)}$	5.7	–
	$\beta_{cbb}^{(2)}$	10.9	–
	$\beta_{ccc}^{(2)}$	31.6	–
$\beta^{(3)}$ in liquid phase ¹⁹¹ ($6.235378 \times 10^{-65} \text{C}^4 \text{m}^4 \text{J}^{-3}$)	$\beta_{aaaa}^{(3)}$	768	–
	$\beta_{bbbb}^{(3)}$	4936	–
	$\beta_{cccc}^{(3)}$	2504	–
	$\beta_{aabb}^{(3)}$	902	–
	$\beta_{ccbb}^{(3)}$	1197	–
	$\beta_{ccaa}^{(3)}$	490	–

Table 3.2 – Constants and properties of H₂O and D₂O.

3.5.2 Mean-field models

Here we obtain an analytical expression for the intensity of scattered SH light using mean-field models that describe water as a dipolar gas that interacts with ions. Water-water correlations are here neglected, and the electrolyte solution is modeled as a gas of non-interacting dipoles, for which the statistical mechanics is well known. The structural correlations of water molecules are here solely determined by the interaction potential that each water molecule has with a single ion, and are described by an ionic form factor (F), while the ion-ion correlations are later included

by means of a structure factor (S). The derivation borrows concepts from different studies^{88,188,207–209}. From the analysis we find that a mean-field model does not capture the essence of the experimental observations. As can be seen from the below analysis (Fig. 3.8) we find that:

1. The outcome of a mean-field model critically depends on the shape of the chosen interaction potential and specifically on how it is decaying at nanoscopic distances. Values for the saturated intensity deviate by a factor of 10^3 .
2. Models can either under or over represent the found intensities, and the half saturation concentration and the saturated intensity cannot be predicted simultaneously for either H_2O or D_2O solutions.
3. Differences between H_2O and D_2O electrolyte solutions cannot be accounted for.
4. Temperature dependent measurements do not agree to the predicted $(1/T)$ trend by the mean field theory.

Ordering of dipoles around a single central ion

Considering first the water molecules surrounding a single monovalent ion, and referring to the $P_{u_0 u_1 u_2}^{(2)}(2\omega)$ term, inserting Eqs. 3.4 and 3.6 into Eq. 3.3 and using the fact that $T_{b_i c_i}(\mathbf{r}') = (\mathbf{e}_{b_i} \cdot \mathbf{e}_{c_i}(\mathbf{r}'))$ gives the average polarization

$$P_{u_0 u_1 u_2}^{(2)}(2\omega) \propto N_m \int \langle (\mathbf{e}_{b_0} \cdot \mathbf{e}_{c_0}(\mathbf{r}')) (\mathbf{e}_{b_1} \cdot \mathbf{e}_{c_1}(\mathbf{r}')) (\mathbf{e}_{b_2} \cdot \mathbf{e}_{c_2}(\mathbf{r}')) \rangle_T \beta_{c_0 c_1 c_2}^{(2)} e^{i\mathbf{q} \cdot \mathbf{r}'} d^3 \mathbf{r}', \quad (3.19)$$

where the average is weighted by a Boltzmann factor. Next, we take a Boltzmann average of the non-observable quantity $P_{u_0 u_1 u_2}^{(2)}(2\omega)$ because we are assuming that water molecules, while correlated by the ion, are not orientationally correlated with each other. The energy of a dipole at \mathbf{r}' is $-\boldsymbol{\mu} \cdot \mathbf{E}_{DC}(0, \mathbf{r}') = -\mu E_{DC}(0, \mathbf{r}') \cos \psi$, where ψ is the angle between the dipole and the electrical field $\mathbf{E}_{DC}(0, \mathbf{r}')$, and μ is the static dipole moment. The ensemble-average can be written as an average over all orientations

$$\begin{aligned} & \langle (\mathbf{e}_{b_0} \cdot \mathbf{e}_{c_0}(\mathbf{r}')) (\mathbf{e}_{b_1} \cdot \mathbf{e}_{c_1}(\mathbf{r}')) (\mathbf{e}_{b_2} \cdot \mathbf{e}_{c_2}(\mathbf{r}')) \rangle \\ &= \left\langle (\mathbf{e}_{b_0} \cdot \mathbf{e}_{c_0}(\mathbf{r}')) (\mathbf{e}_{b_1} \cdot \mathbf{e}_{c_1}(\mathbf{r}')) (\mathbf{e}_{b_2} \cdot \mathbf{e}_{c_2}(\mathbf{r}')) e^{\boldsymbol{\mu} \cdot \mathbf{E}_{DC}(0, \mathbf{r}') / k_B T} \right\rangle, \quad (3.20) \end{aligned}$$

which, expanded to first order, is (with the constant term giving an average over three direction cosines and thus zero average)

$$\frac{\mu E_{\text{DC}}(0, \mathbf{r}')}{k_B T} \langle (\mathbf{e}_{b_0} \cdot \mathbf{e}_{c_0}(\mathbf{r}')) (\mathbf{e}_{b_1} \cdot \mathbf{e}_{c_1}(\mathbf{r}')) (\mathbf{e}_{b_2} \cdot \mathbf{e}_{c_2}(\mathbf{r}')) \cos \psi \rangle. \quad (3.21)$$

Carrying out the averages and taking the sum in Eqs. 3.3 and 3.4 give

$$P_{u_0 u_1 u_2}^{(2)}(2\omega) \propto N_m E_{u_1}(\omega) E_{u_2}(\omega) \frac{\mu \beta^{(2)}}{3 k_B T} \int E_{\text{DC}}(0, \mathbf{r}') \frac{\mathbf{r}' \cdot \mathbf{e}_{u_0}}{|\mathbf{r}'|} e^{i \mathbf{q} \cdot \mathbf{r}'} d^3 \mathbf{r}' \quad (3.22)$$

with

$$\beta^{(2)} = \delta_{u_0 u_1} \beta_{\parallel}^{(2)} + (1 - \delta_{u_0 u_1}) \beta_{\perp}^{(2)}, \quad (3.23)$$

where $\beta_{\parallel}^{(2)}$ and $\beta_{\perp}^{(2)}$ are defined by Ref.⁸⁴, in which c is the molecular dipole axis. A similar analysis can be carried out for the third-order hyperpolarizability $\beta^{(3)}$ to give

$$P_{u_0 u_1 u_2}^{(3)}(2\omega) \propto N_m E_{u_1}(\omega) E_{u_2}(\omega) \beta^{(3)} \int E_{\text{DC}}(0, \mathbf{r}') \frac{\mathbf{r}' \cdot \mathbf{e}_{u_0}}{|\mathbf{r}'|} e^{i \mathbf{q} \cdot \mathbf{r}'} d^3 \mathbf{r}' \quad (3.24)$$

with $\beta^{(3)} = \delta_{u_0 u_1} \beta_{\parallel}^{(3)} + (1 - \delta_{u_0 u_1}) \beta_{\perp}^{(3)}$.

The final expression for the intensity of generated SH light due to ion-dipole correlations around a single ion is thus

$$I_{coh, u_0 u_1 u_2}(2\omega) = C^2 \frac{k_0^4}{r_0^2} E_{u_1}^2(\omega) E_{u_2}^2(\omega) N_m^2 \left| \frac{\mu \beta^{(2)}}{3 k_B T} + \beta^{(3)} \right|^2 \left| \int E_{\text{DC}}(0, \mathbf{r}') \frac{\mathbf{r}' \cdot \mathbf{e}_{u_0}}{|\mathbf{r}'|} e^{i \mathbf{q} \cdot \mathbf{r}'} d^3 \mathbf{r}' \right|^2, \quad (3.25)$$

where $E_{\text{DC}}(0, \mathbf{r}')$ stands for the radial electrostatic field originating from the ion. We will consider various possible expressions for $E_{\text{DC}}(0, \mathbf{r}')$ at a later stage.

In the experiment the relative change in fs-ESHS intensity, $\Delta I(2\omega)$ (Eq. 3.11), is reported. For a solution with ion number density ρ , it becomes

$$\Delta I(2\omega, q, \rho) = K \rho |F(q, \rho)|^2 S(q, \rho) + 1. \quad (3.26)$$

Here, K is a constant depending on the experimental setup and the molecular proper-

ties of pure water. For the PPP polarization combination, it reads

$$K = \left(\frac{\mu \beta_{\perp}^{(2)}}{3k_B T} \right)^2 \frac{N_m f(0)^2 Z^2 e^2}{\epsilon_0 \epsilon \left\langle \left[\beta_{ZXX}^{(2)} \right]^2 \right\rangle}, \quad (3.27)$$

where μ is the dipole moment of a water molecule in gas phase, N_m is the solvent number density, $f(0)$ is the Lorentz local field factor, Z is the ion's valence, e is the elementary charge, and $\frac{[\beta_{\perp}^{(2)}]^2}{\langle [\beta_{ZXX}^{(2)}]^2 \rangle} = 2.8$ (see Ref. ¹⁹¹). $F(q, \rho)$, is the ionic form factor, i.e., the amplitude scattered by each ion that can be written as the Fourier transform of the electrical field. Contrary to what is usually seen in other scattering experiments, $F(q, \rho)$ can have a pronounced concentration dependence, which is related to the decay of $E_{DC}(0, \mathbf{r}')$ as we will discuss in the following paragraphs. Finally, $S(q, \rho)$ is the structure factor, which accounts for the correlations between the ions, and for liquids can be written in terms of the Fourier transform of the radial distribution function.

Different mean-field models

Next, we describe the scattered intensity $\Delta I(2\omega, q, \rho)$ (Eq. 3.26) for different scenarios involving different choices of the form and structure factors. For the form factor, we have compared three possibilities with three slightly different but very similar electrostatic potentials.

1. A dielectrically but otherwise unscreened Coulomb potential $V(r)$, and corresponding form factor F_C

$$V(r) = \frac{Ze}{4\pi\epsilon_0\epsilon r} \quad (3.28)$$

$$F_C = 1/q$$

2. The same Coulomb potential that is truncated at the position where the next ionic domain starts (estimating this mean domain radius from a simple-cubic packing of ions). We obtain for the form factor (F_{TC})

$$F_{TC}(q, \rho) = \frac{\sin(qR) - qR}{q^2 R}, \quad R = \frac{1}{2\sqrt[3]{2\rho}} \quad (3.29)$$

3. An exponentially-screened potential as obtained from DH theory and the corre-

spending form factor F_{DH}

$$\begin{aligned} V(r) &= \frac{e^{-\kappa_D(\rho)r} Ze}{4\pi\epsilon_0\epsilon r} \\ F_{DH} &= \frac{q}{q^2 + \kappa_D(\rho)^2} \\ \kappa_D(\rho)^2 &= \frac{2I(\rho)e^2}{\epsilon_0\epsilon k_B T} \end{aligned} \quad (3.30)$$

where $1/\kappa_D(\rho)$ is the Debye screening length and $I(\rho)$ is the ionic strength.

These form factors can be compared with different structure factors. At very low concentrations (when the ions are not correlated in position), the contributions from individual ions can reasonably be represented by summing them incoherently. The structure factor takes the form: $S(q, \rho) \rightarrow 1$. We refer to this structure factor as S_1 . $\Delta I(2\omega, q, \rho)$ would then be determined solely by the ionic form factor. At intermediate and larger concentrations, the distribution of ions will not anymore be random, and ion-ion correlations exist. Both positively and negatively charged ions contribute to the signal, and so one has to combine the structure factors of same-sign and opposite-sign species. If one calculates the appropriate combination within DH theory, one obtains for the structure factor²¹⁰

$$S_{DH}(q, \rho) = \frac{q^2}{q^2 + \kappa_D(\rho)^2}. \quad (3.31)$$

Monovalent electrolytes are used in the calculation as a representative, for which $I(\rho) = \rho Z^2$.

Experimental data vs mean-field models: Dependence on the ionic strength and temperature

Figure 3.8A shows incoherent combinations ($S(q, \rho) = S_I = 1$) of the different form factors F_C (green curve) and F_{DH} (red curve). The computed incoherent response for a truncated potential (F_T) does not generate a $\Delta I(2\omega)$ bigger than 10^{-3} and is omitted from the graph. If neither screening nor ion correlations are included ($F_C + S_1$, green curve), the intensity increases linearly with concentration. Clearly this overshoots the experimental data (black lines). On the other hand, if one considers the Coulomb field to be abruptly truncated at half the mean ion separation ($F_{TC} + S_1$, not shown) the predicted signal is orders of magnitude smaller than what is observed. A DH screened potential agrees somewhat with an increasing signal at low concentration ($F_{DH} + S_1$,

red curve), and has a maximum that agrees with the 50% saturation point of the H₂O data (indicated by the black vertical line), but not that of D₂O. At higher ionic strengths, $\Delta I(2\omega)$ returns to the level of the neat water intensity without saturating. Thus, even though the electrostatic potential of the ions ($V(r)$) are almost indistinguishable up to several tens of nanometers away from the ion, the three implemented potentials result in curves for $\Delta I(2\omega)$ that differ by orders of magnitude. Already for the very low ionic strengths, where ion-ion correlations are absent, the curves are remarkably different. Thus, due to the long-range nature of fs-ESHS experiments, minute changes in the long-range screening of the potential result in dramatic changes of the predicted signal.

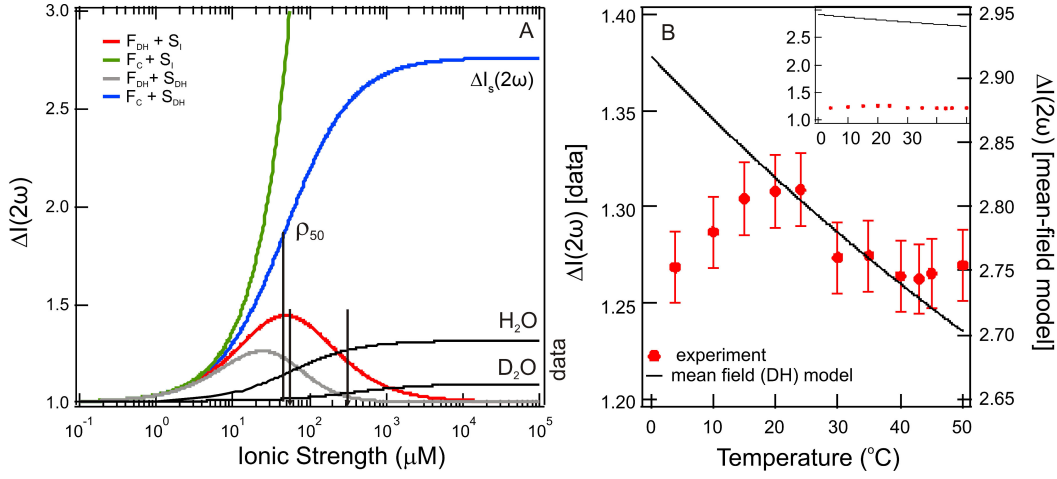


Figure 3.8 – Mean-field models and temperature dependence. (A) fs-ESHS response relative to that of pure water computed for a solution of monovalent ions in water. Plotted are the combination of a form factor arising from a Coulombic potential (F_C) with a structure factor of uncorrelated ions (S_1 , green line), a form factor arising from a DH potential (F_{DH}) with a structure factor of uncorrelated ions (S_1 , red line), a form factor arising from a DH potential (F_{DH}) with a DH structure factor of correlated ions (S_{DH} , grey line), and a form factor arising from a Coulombic potential (F_C) with a DH structure factor of correlated ions (S_{DH} , blue line). The black lines indicate the data for NaCl in H₂O and D₂O, and the vertical lines mark the ionic strengths of half saturation. (B) Temperature dependence of the saturated fs-ESHS intensity. fs-ESHS intensities were recorded for a 10 mM NaCl solution in H₂O at different temperatures (red markers, left axis). The computed saturation value obtained from the combination of F_C and S_{DH} is plotted as a black line (right axis). The inset shows both curves on the same scale.

Including ion-ion correlations, by combining F_{DH} with S_{DH} (grey curve) or F_C with S_{DH} (blue curve) we find that big differences between those two models remain: The gray curve is seen to reach a maximum, while the blue curve saturates. Interestingly the blue curve, a combination of an unscreened Coulomb potential and a DH structure factor, captures the shape of the experimental data. This combination, which corresponds to the linear superposition of the effect of ions on dipolar water molecules with correlated (ionic) positions, is arguably the most consistent

application of DH theory, and we will focus on it in what follows.

The 50% saturation point (45 μM) is close to that found for H_2O , but not for the one found for D_2O (310 μM). The saturated value for $\Delta I(2\omega)$ is reached at 2.8, which is an over representation of the experimental data (1.3/1.09 for $\text{H}_2\text{O}/\text{D}_2\text{O}$, respectively). The ionic strength at the point of 50% saturation (ρ_{50}) and the saturation intensity ($\Delta I_s(2\omega)$) are given by the following expressions

$$\begin{aligned} \rho_{50} &= \frac{q^2 \epsilon_0 \epsilon k_B T}{2(Ze)^2} \\ \Delta I_s(2\omega) &= \left(\frac{\mu \beta_{\perp}^{(2)}}{3k_B T} \right)^2 \frac{\rho_s f(0)^2 k_B T}{2\epsilon_0 \epsilon \left\langle \left[\beta_{ZX}^{(2)} \right]^2 \right\rangle} + 1. \end{aligned} \quad (3.32)$$

It can be seen that ρ_{50} does not contain any parameters that would generate a different curve for H_2O and D_2O . Similarly $\Delta I_s(2\omega)$ does not contain parameters that allow for a downward adjustment by a factor of 6 (H_2O) or 20 (D_2O), in order for it to agree to the experimental result.

Both expressions do allow for a further check in terms of the broader validity of the model. By performing temperature dependent measurements, we can check the validity of Eq. 3.32, and hence determine how well this particular mean field model describes the experimental findings. Figure 3.8B shows the measured intensity of saturation $\Delta I_s(2\omega)$ for a 10 mM NaCl solution in H_2O (red data points, left axis). The computed value for $\Delta I_s(2\omega)$ is plotted as well (black line, right axis). The inset shows both traces on the same scale. It can be seen that the experimental data does not change much in magnitude in the temperature range from 4 $^{\circ}\text{C}$ to 50 $^{\circ}\text{C}$. There is a slight reduction in $\Delta I_s(2\omega)$ at both high and low temperatures. The mean-field model predicts a decrease in $\Delta I_s(2\omega)$ going from low to high temperatures. It therefore seems that the combination of an F_C form factor and an S_{DH} structure factor are not well suited to predict the trends that are experimentally observed.

Thus, several approaches for mean-field models that treat the water as an ideal gas that interacts with a cloud of ions using electrostatic potentials that differ only marginally have been considered. We observe that the computed fs-ESHS signal of a monovalent electrolyte solution relative to that of pure water varies from a negligible contribution to the fs-ESHS response to a fs-ESHS response twice that of pure water. The models do not allow for the prediction of a difference between H_2O and D_2O , nor can they capture the temperature dependence. Since small differences in the interaction potentials lead to large differences in the fs-ESHS response, it is necessary to consider the fs-ESHS response using a molecular dynamics simulation, which

contains not only the ion-dipole interactions, but also other water-water interactions. These interactions may modify the interaction potentials and lead to additional cooperative effects that are not included in any of the mean field models considered here. To capture also the observed difference between light water and heavy water, more sophisticated models (that are still to be developed) are needed.

4 Specific Ion-Water Interactions at High Ionic Strengths

Specific ion effects in aqueous solutions are investigated on the molecular, nanoscopic and macroscopic level. Femtosecond elastic second harmonic scattering is used in this chapter to assess chemical effects on molecular and nanoscopic length scales, probing changes in the charge distribution around ions as well as structural orientational order of water molecules in the extended hydration shells. We measured a series of > 0.05 M chloride salt solutions (LiCl, NaCl, KCl, CsCl, RbCl, NH_4Cl , MgCl_2 , CaCl_2 , and SrCl_2). Ion specificity is observed in both the local electronic anisotropy and the nanoscopic orientational ordering of water. Both observables are influenced more by cations with larger valencies and smaller sizes and follow a direct Hofmeister trend. These ion-induced structural changes in the hydrogen-bond network of water are strongly correlated with the viscosity B-coefficient and the hydration free energy. Such a connection between the nanoscopic and macroscopic changes provides a possibility to construct a better molecular model for specific ion effects in aqueous solutions.

4.1 Introduction

Inorganic ions play specific and irreplaceable roles in various physical, chemical, and biological processes in aqueous solutions, from colloid assembly and bubble coalescence to protein folding and enzyme activities.^{7,15,17,18,21,211} Specific ion effects are shown to be present in various macroscopic properties of bulk aqueous solutions, such as viscosity of electrolyte solutions and hydration free energy of ions, typically observed above the physiological concentration of electrolytes (~ 0.1 M).^{10,11,212} Recent work also reports observations of changes that occur on the molecular level.^{12,13,213} Neutron and X-ray diffraction studies that measure the structure factor of ionic hydration shells report ion-specific coordination numbers of alkali ions.^{157,158,160,214} The electronic state of ion hydrating water molecules can, for example, be probed with X-ray absorption. It was found that cations with a low charge density weaken the H-bonds of hydrating water molecules whereas cations with a high charge density cause the formation of strong H-bonds.^{162,215} Raman spectroscopy,^{164,216} vibrational dynamics measurements,^{168,169,171,172} and ensemble infrared photodissociation spectroscopy^{173,174} probe the O-H stretch modes of hydrating water molecules in the vicinity of ions. These studies show that different ions perturb the water network and restrain the dynamics of water molecules to different extents, which lead to ion-specific changes in the spectra of O-H stretch regions. Changes in the complex permittivity of electrolyte solutions as probed by dielectric spectroscopy measurements indicate that small and highly charged cations align and irrotationally bind water in the first hydration shell.²¹⁷ Auger electron spectroscopy studies of ultrafast charge delocalization phenomena in electrolyte solutions show that cations with bigger charges slow down the electron-hopping in the oxygen atoms of hydrating water molecules.^{218,219} Computer simulations that calculate the radial distribution and orientation of water molecules in the ionic hydration shells^{14,15,164,172,176,220,221} show that ions induce distinct changes in the water network that involve changing the number of H-bonds per water molecule and affect the reorientation of individual water molecules.

All the above studies report specific ion effects on the structure and dynamics of water molecules in the first few hydration shells of ions in aqueous solutions. However, there is still a lack of an overarching molecular model that explains how specific ion effects extend from the first few hydration shells of ions to the bulk water network and lead to macroscopic effects in the bulk properties of electrolyte solutions. To help with this issue, a technique that is able to probe the hydrating water on the molecular level with a sensitivity to longer range structural changes in extended hydration shells

is needed. fs-ESHS has been shown to access molecular level properties of electrolyte solutions up to nanoscopic distances (Ch. 3 and Ref.²²²). Specifically, fs-ESHS studies on electrolyte solutions with ionic strengths in the range of 1 μ M to 100 mM found a universal long-range (~ 20 nm) influence of ions on the H-bond network of water molecules. As a second-order nonlinear optical process, fs-ESHS selectively probes both local electronic anisotropy of individual molecules and nanoscopic structural anisotropy (i.e. orientational order) in liquids. The electronic anisotropy gives rise to an incoherent response and the structural anisotropy gives rise to a coherent response that reflects the orientational order of molecules, whereas no SH signal is generated in a centrosymmetric environment composed of centrosymmetric molecules. The coherent and incoherent contributions can be investigated separately using different polarization combinations of the incoming and outgoing light. The sensitivity to the orientational order as well as the electronic charge distribution suggests that fs-ESHS could also provide molecular level insights into specific ion effects in concentrated aqueous solutions. As the orientational order in the H-bond network relates directly to the forming and breaking of H-bonds, its connection with macroscopic properties of electrolyte solutions, such as viscosity and the Gibbs free energy of hydration, may also be worth investigating.

In this chapter, we probe aqueous solutions, with ionic strengths > 0.05 M, of a series of chloride salts (LiCl, NaCl, KCl, CsCl, RbCl, NH_4Cl , MgCl_2 , CaCl_2 , and SrCl_2) with fs-ESHS. We observe ion specificity in both the local electronic anisotropy and the nanoscopic orientational ordering of water in extended hydration shells. Both observables are influenced more by cations with larger valencies and smaller sizes that follow a direct Hofmeister trend. We also find that the ion-induced orientational ordering in the water network, revealed by a linear increase in the fs-ESHS intensity of the coherent response as a function of the electrolyte concentration, strongly correlates with the viscosity B-coefficient and the hydration free energy of electrolytes. These findings are of particular interest, given that cations play critical roles in biologically relevant aqueous systems. The mechanism of specific cation effects is not yet fully understood.⁷ A well-known example is the high selectivity of ion channels for either K^+ or Na^+ ions, which cannot be understood simply by a difference in size alone.^{223,224} Another example is that Na^+ is essential to regulate blood pressure but toxic with a high intracellular concentration, whereas K^+ is not toxic and serves as the major intracellular monovalent ion.²²⁵ The observed connection between the molecular (electronic anisotropy), nanoscopic (orientational ordering of water) and macroscopic (viscosity/hydration free energy) observables will undoubtedly further our understanding of the hydration of ions as well as specific ion effects in aqueous

solutions.

This chapter is structured as follows: We first present theoretical calculations of the SH intensity of aqueous solutions of a series of chloride salts. The incoherent SH responses from single spherical ions with different radii and single water molecules are considered first. The coherent SH intensity is calculated for electrolyte solutions based on the DH theory, in which a dielectric continuum, a gas of water dipoles, and statistical distributions of ions that follow the linearized Boltzmann distribution are assumed. Then, we compare these relatively simplistic theoretical results with the data of fs-ESHS measurements of electrolyte solutions for the incoherent and coherent responses separately. We find that the experiments contain many details about the intricate relationship of water and ions that are not captured by the models (that consider only ion-ion and ion-dipole interactions). Finally, we correlate the fs-ESHS responses with the viscosity B-coefficient and hydration free energy to show a connection between the nanoscopic and the macroscopic observations. Such a connection evidently warrants further investigation into the atomistic details that underlie the presented experiments.

4.2 Materials and methods

4.2.1 Sample preparation

MgCl₂ (99.99%, Sigma-Aldrich), CaCl₂ (99.99%, Sigma-Aldrich), SrCl₂ (99.99%, Sigma-Aldrich), LiCl (99.999%, Sigma-Aldrich), NaCl (99.999%, Acros), NH₄Cl (99.9995%, Fluka), RbCl (99.95%, Sigma-Aldrich), CsCl (99.9995%, Fluka), and KCl (99.999%, Acros) were used as received without further purification. All samples were made by dissolving the electrolytes in degassed ultra-pure water (18.2 megohm·cm, Millipore, Inc.) to obtain a 5 ml stock solution with a high concentration by using a 5 ± 0.025 ml volumetric flask (Duran) at room temperature. The stock solutions were filtered (0.1 μ m PVDF membrane filters, Millex-VV, Millipore) and then diluted to the desired concentrations.

4.2.2 Femtosecond elastic second harmonic scattering

As previously described in Sec. 3.2.2, fs-ESHS measurements of electrolyte solutions were performed at a fixed scattering angle of 90° with an acceptance angle of 11.4°. Data points were acquired with an acquisition time of 50×1 s [that is, using $50 \times (2$

$\times 10^5$) pulses in total]. The fs-ESHS signal of pure H₂O was measured between every two samples and was used as a reference. The reproducibility error of the fs-ESHS measurements was 1 to 3%. Samples were stored and measured in sealed glass sample cells. All measurements were performed in a temperature- and humidity-controlled room ($T = 297$ K; relative humidity, 26.0%). A detailed description of the fs-ESHS experimental setup can be found in Ch. 2 and in Ref.¹⁵⁴.

4.2.3 Molecular dynamics simulations

Polarizable MD simulations were performed using the TINKER 7.1 package²²⁶ to calculate the electrostatic field $E_{DC}(0)$ on an ion. The AmoeBa14 model²²⁷ was chosen for the water molecules, and the AmoeBa ion parameters²²⁸ for the sodium and chloride ions. Cubic simulation boxes, with a side size of 5 nm, were prepared by combining ~4,000 water molecules with randomly distributed pairs of ions, up to the concentration of 2 M. After initial equilibration of 100 ps, simulations were run for 500 ps, and snapshots of the instantaneous configurations of water and ions were saved for every 100 fs. During equilibration in the NPT ensemble, the velocity Verlet method was used with 1.0 fs integration time steps. The system temperature was kept at 298 K using Andersen thermostat with a coupling time of 0.1 ps. The system pressure was kept at 1.0 atm using Berendsen barostat with a coupling time of 2.0 ps. The particle mesh Ewald method¹⁸¹ was used to evaluate the long-range electrostatic interaction, and the real space cutoff for Ewald summation as well as for van der Waals interactions was set to 12.0 Å. The convergence threshold of 10^{-5} D was applied during calculation of self-consistent induced dipoles. During production runs in the NVT ensemble, Langevin dynamics with velocity Verlet integrator were employed. The Langevin dynamics used a friction coefficient of 1.0 ps^{-1} . The system pressure was kept at 1.0 atm using the Nosé-Hoover thermostat²²⁹ with a coupling time of 0.1 ps.

4.2.4 Fitting of the fs-ESHS data

The fs-ESHS data of Figs. 4.3 and 4.4 was fitted with a linear function:

$$y = kx + b \quad (4.1)$$

where y and x are fitted to the relative SH intensity and electrolyte concentration, k is the fitted slope, and b is the intersect of the Y-axis of the linear curve. Linear fittings with this given equation were performed for the fs-ESHS data shown in Figs. 4.3 and

4.4 by using the built-in fitting function “Line” in IGOR Pro 6 (WaveMetrics), in which the singular value decomposition algorithm²³⁰ is employed for this non-iterative curve fitting. The coefficient of determination R^2 , indicating the quality of the linear fit, can be calculated by²³¹

$$R^2 \equiv 1 - \frac{\sum_i (y_i - f_i)^2}{\sum_i (y_i - \bar{y})^2} \quad (4.2)$$

where y_i is the data and \bar{y} is the mean value of y_i , and f_i is the corresponding predicted value. When a value of R^2 close to 1 is obtained, the regression line well fits the data.

The fitted k values of the SH intensity data in Figs. 4.3 and 4.4 are shown in Table 4.2. Note that the relative error in the electrolyte concentration is ~0.5%, which is much smaller than the 1-3% error in the measured SH intensity. For the obtained k values of the SH intensity in Figs. 4.5 and 4.6, the reported error bar of k is given by the 95% confidence interval of the fitted k from the linear fittings of the SH intensity.

4.3 Results and discussions

4.3.1 Theory: Expected fs-ESHS response from electrolyte solutions

For an ionic solution, incoherent SH intensity from electronic anisotropy within individual water molecules or ions may be expected. We can also consider whether there are coherent contributions from structural orientational order between water molecules or ions to the fs-ESHS response. Both contributions are illustrated in Figs. 4.1B and 4.1C and will be described below. In what follows, we will first calculate the incoherent SH intensity from individual ions by using the results from a MD simulation in combination with the scaling law for $\beta^{(3)}$ (which is used for describing non-resonant nonlinear optical interactions)¹⁴⁵. Single spherical ions with different radii will be considered. The incoherent SH intensity from water molecules will be discussed briefly as well. Then, we will focus on the expected coherent SH intensity from water molecules as induced by ions. To estimate this coherent SH intensity from electrolyte solutions, we make use of the mean-field DH model that was described in the appendix of Ch. 3.²²² In this model, the medium is considered as a dielectric continuum. It is also assumed that the statistical distribution of ions follows the linearized Boltzmann distribution. Water molecules are considered as a non-interacting gas of dipoles.

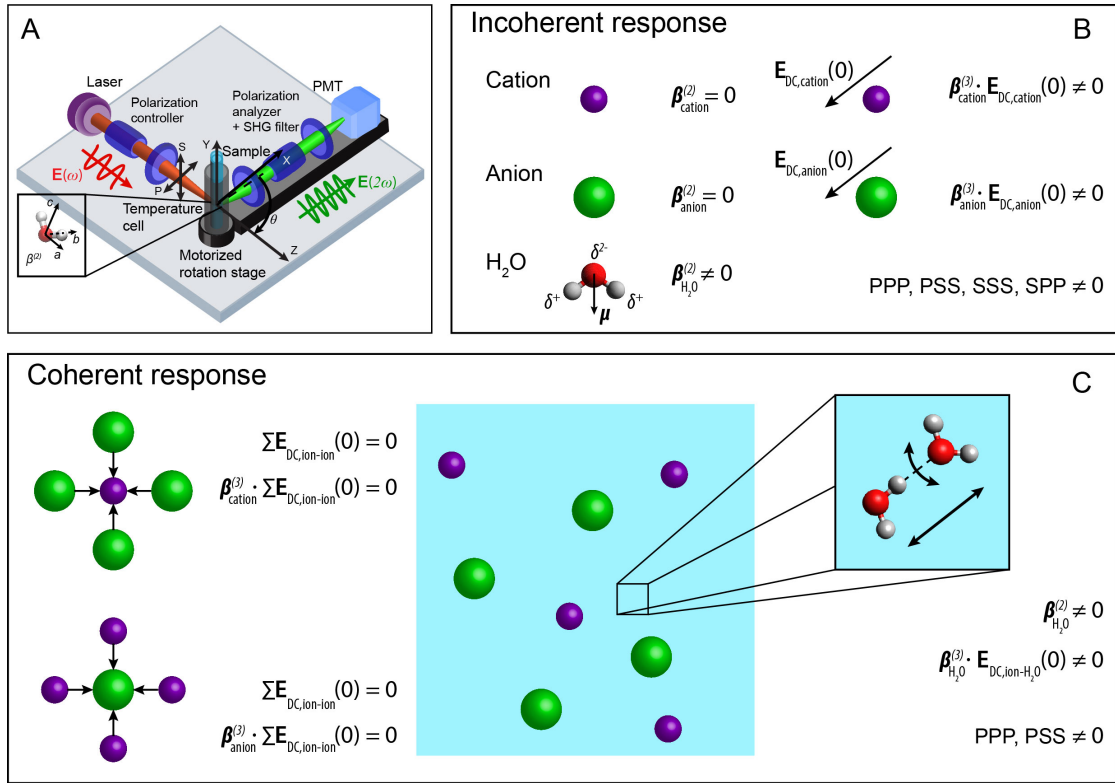


Figure 4.1 – Illustration of possible contributions to the fs-ESHS response of electrolyte solutions. (A) Sketch of the fs-ESHS experiment and the different coordinate systems. (B) Illustration of possible incoherent contributions to the fs-ESHS responses of spherical ions (row 1 and 2) and water molecules (row 3) in an electrolyte solution. (C) Illustration of possible coherent contributions to the fs-ESHS responses of ions (left) and water molecules (right). These responses correspond to changes in the structural orientational correlations in the solution and can only be probed in the PPP and PSS polarization combinations. The inset illustrates two correlated water molecules with an H-bond. The black arrows represent two directions along which the H-bond can be broken (via bending and stretching). fs-ESHS is only sensitive to the bending motion of the H-bond.²²² $E_{\text{DC,ion-ion}}(0)$ and $E_{\text{DC,ion-H}_2\text{O}}(0)$ represent the electrostatic field from ions on a central ion or on water molecules, respectively.

Incoherent response: Local electronic anisotropy

As shown in Fig. 4.1B, for centrosymmetric ions, the absence of molecular electronic anisotropy results in a vanishing $\beta^{(2)}$ tensor. Spherical ions will, therefore, contribute primarily through the third-order response ($\beta^{(3)}$ -related) that requires an interaction with two optical photons and an electrostatic field component. The electrostatic field originates from surrounding water molecules and ions in the solution. A value for this electrostatic field $E_{\text{DC}}(0)$ is obtained from atomistic polarizable MD simulations using Amoeba models^{227,228}. These computations show that the electrostatic field $E_{\text{DC}}(0)$ that is felt by the ions originates primarily from the surrounding water molecules. We find concentration-independent values of $|E_{\text{DC,anion}}(0)| \sim (12.2 \pm 4.2) \times 10^9$ V/m on the

anions and $|\mathbf{E}_{\text{DC,cation}}(0)| \sim (4.9 \pm 2.0) \times 10^9 \text{ V/m}$ on the cations, for aqueous solutions of 13 mM, 40 mM, and 2 M NaCl. The contribution of other ions to $\mathbf{E}_{\text{DC}}(0)$ is found to be negligible compared to that of neighboring water molecules, probably due to an on average, symmetric arrangement of ions around the central one as illustrated in Fig. 4.1C. In addition, these surrounding ions are further away than the surrounding water molecules.

The average magnitude of $\beta^{(3)}$ of the chloride ion was calculated previously using quantum chemistry calculations:²³² $|\tilde{\beta}_{\text{Cl}^-}^{(3)}| \sim 1.86 \pm 10^{-60} \text{ C}^4 \cdot \text{m}^4 / \text{J}^3$. Knowing this value, we can compute $\beta^{(3)}$ for other spherical ions by using the following scaling law for non-resonant nonlinear optical processes:¹⁴⁵

$$|\tilde{\beta}_{\text{ion}}^{(3)}| = |\tilde{\beta}_{\text{Cl}^-}^{(3)}| \left(\frac{R_{\text{ion}}}{R_{\text{Cl}^-}} \right)^7 \quad (4.3)$$

where R_{ion} is the ionic radius. The incoherent fs-ESHS intensity from individual ions in water of an AB_j electrolyte is thus given by

$$I_{\text{ion}}(2\omega) \propto c \left\{ \left(|\tilde{\beta}_{\text{cation}}^{(3)}| |\mathbf{E}_{\text{DC,cation}}(0)| \right)^2 + j \left(|\tilde{\beta}_{\text{anion}}^{(3)}| |\mathbf{E}_{\text{DC,anion}}(0)| \right)^2 \right\} \quad (4.4)$$

where c is the concentration of electrolytes in M. $j = 1$ for chloride salts with monovalent cations and $j = 2$ for divalent cations.

In contrast to spherical ions, $\beta^{(2)}$ is nonzero for dipolar water molecules, which thus gives rise to the leading-order contribution to the incoherent SH emission. Values of $\beta^{(2)}$ of liquid water are obtained from an ab-initio study by Gubskaya and Kusalik¹⁹¹. The incoherent response is expected to contribute to all four accessible polarization states (PPP, PSS, SPP, and SSS, with collinear illumination).

Coherent response: Orientational order of water

In addition to an incoherent contribution to the fs-ESHS intensity, there is also a coherent contribution to $I(2\omega)$ that reports on orientational correlations between water molecules. As illustrated in Fig. 4.1C the coherent contribution from ions is expected to vanish according to symmetry considerations. Structural correlations or orientational order is represented by the second term in Eq. 2.8b. This orientational order gives rise to ion-induced coherent SH water signals in two (PPP, PSS) of the four accessible polarization states. The orientational order that is probed in this way reports, for a significant part, on the breaking and forming of H-bonds. As illustrated in the inset of Fig. 4.1C, coherent fs-ESHS is only sensitive to bending of the H-bond

(rotational motion of water), but not to stretching of the H-bond (translational motion of water).

The orientational order of water can be qualitatively (not quantitatively as shown in Ch. 3 and Ref.²²²) described by the DH model. The coherent fs-ESHS intensity is found to relate to the structure factor $S(q, c)$ of a gas of water dipoles in contact with ions:²²²

$$I_{coh,J}(2\omega) \propto c \left| P_{i-w,J}^{(2)}(2\omega) \right|^2 S(q, c) \quad (4.5)$$

where $P_{i-w,J}^{(2)}(2\omega)$ is the second-order polarization induced in the water molecules by a single ion. $S(q, c)$ reflects the relative positions of ions in an aqueous solution that is modeled as a uniform dielectric material. $S(q, c)$ is given by

$$S(q, c) = \frac{q^2}{q^2 + \kappa_D(c)^2} \quad (4.6)$$

$$\kappa_D(c) = \sqrt{\frac{(z_{\text{cation}}^2 + j z_{\text{anion}}^2) c N_A e^2}{\epsilon_0 \epsilon k_B T}}$$

where $\kappa_D(c)$ is the DH screening parameter, z_{cation} (z_{anion}) is the valency of cations (anions), N_A is the Avogadro's number, e is the elementary charge, ϵ_0 is the vacuum permittivity, ϵ is the static relative permittivity of water (at 293 K), k_B is the Boltzmann constant, and T is the temperature in K. $j = 1$ for chloride salts with monovalent cations and $j = 2$ for divalent cations. For the coherent PPP fs-ESHS intensity measured at a scattering angle θ of 90° , the orientational distribution of water dipoles can be computed in terms of the ion-dipole interactions and thermal fluctuations. Using the linearized Boltzmann distribution, we find the second-order polarization that is induced in the water molecules:^{88,222}

$$P_{i-w}^{(2)}(2\omega)_Z \sim N_m \left(\tilde{\beta}_{ZXX}^{(3)} + \frac{\mu \tilde{\beta}_{ZXX}^{(2)}}{3k_B T} \right) E_X(\omega)^2 \int E_{DC}(0, \mathbf{r}') \frac{\mathbf{r}' \cdot \mathbf{e}_Z}{|\mathbf{r}'|} e^{i\mathbf{q}_{90} \cdot \mathbf{r}'} d^3 \mathbf{r}' \quad (4.7)$$

$$\tilde{\beta}_{ZXX}^{(2)} = \frac{1}{5} \sum_a \left(2\beta_{Zaa}^{(2)} - \beta_{aaZ}^{(2)} \right), \quad \tilde{\beta}_{ZXX}^{(3)} = \frac{1}{15} \sum_{a,b} \left(\beta_{abba}^{(3)} + 2\beta_{aabb}^{(3)} \right)$$

where N_m is the number density of water molecules, μ is the permanent dipole moment of a water molecule, \mathbf{e}_Z is the unit vector in the Z direction in which the P polarized SH light is at the scattering angle of 90° , and $|\mathbf{q}_{90}| = \sqrt{2}|\mathbf{k}_0|$. With $E_{DC}(0; \mathbf{r}')$

from a single ion given by the Coulomb equation, the integral

$$\int E_{\text{DC}}(0, \mathbf{r}') \frac{\mathbf{r}' \cdot \mathbf{e}_Z}{|\mathbf{r}'|} e^{i\mathbf{q}_{90} \cdot \mathbf{r}'} d^3\mathbf{r}' = \frac{Zef(0)}{q\epsilon_0\epsilon}, \quad (4.8)$$

in which $f(0)$ is the local field factor for the ionic electrostatic field. Note that the linearization of the Boltzmann distribution to obtain $\frac{\mu\tilde{\beta}_{ZZX}^{(2)}}{3k_B T}$ in Eq. 4.7 is typically valid for ion-dipole distances exceeding 1 nm, i.e. $|\mathbf{r}'| \geq 1$ nm, at which the ion-induced interaction energy is much weaker than the thermal energy $k_B T$. As mentioned, in this calculation, water molecules are approximated as an ideal gas, for which water-water interactions are neglected. Using Eqs. 4.5-4.8 we can then compute the coherent SH response of water molecules in an electrolyte solution within this model.

Computational results

Figure 4.2A shows the calculated incoherent SH intensity $I_{\text{ion}}(2\omega)$ from individual ions in aqueous solutions of chloride salts with different cations. It can be seen that according to the computation (Eqs. 4.3 and 4.4) $I_{\text{ion}}(2\omega)$ increases linearly with the electrolyte concentration. There is no distinguishable difference in $I_{\text{ion}}(2\omega)$ for different monovalent cations and different divalent cations. The absence of ion specificity in $I_{\text{ion}}(2\omega)$ is probably caused by the facts that the intensity scales with R^{14} ($|\tilde{\beta}_{\text{ion}}^{(3)}| \propto R^7$, Eq. 4.3) and that the Cl^- ion ($R_{\text{Cl}^-} = 0.181$ nm) is much bigger in size than any of the studied cations ($0.065 \text{ nm} < R_{\text{cation}} < 0.169$ nm, see Table 4.1). In addition, $|\mathbf{E}_{\text{DC,anion}}(0)|$ is more than twice larger than $|\mathbf{E}_{\text{DC,cation}}(0)|$. The contribution from cations to $I_{\text{ion}}(2\omega)$ is thus negligible. The difference between the divalent and monovalent series is caused by the different number of Cl^- in solution; when the curves are corrected for the number difference of Cl^- , this difference vanishes.

Cations	Mg^{2+}	Ca^{2+}	Sr^{2+}	Li^+	Na^+	NH_4^+	Rb^+	Cs^+	K^+	Cl^-
R (nm)	0.065	0.099	0.116	0.068	0.095	0.148	0.149	0.169	0.133	0.181

Table 4.1 – Effective ionic radii^{233,234} used for calculations of the incoherent SH intensity from individual ions in Fig. 4.2A.

The computed coherent, concentration-dependent response of bulk water is shown in Fig. 4.2B. The intensity increases at very low electrolyte concentrations. As will be discussed in the next chapter, this increase is caused by ions inducing a small amount of orientational order in water molecules. In the electrolyte concentration range from 1 μM to 100 mM, the actual observed increase in the orientational order

is 6 times smaller and displays a large isotope effect. The difference between the experimental data and theoretical curve is probably caused by neglecting H-bonding in the DH model. For the present study at high electrolyte concentrations, we note that the DH model does not predict any ion specificity, and the SH intensity remains constant up to 4 M.

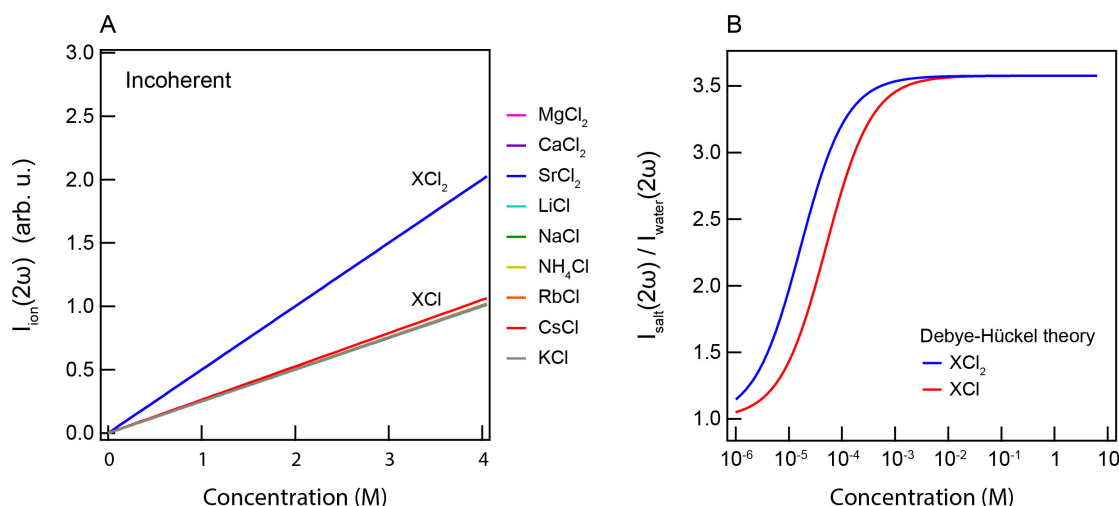


Figure 4.2 – Computed SH intensities from electrolyte solutions. (A) The incoherent SHS intensities from individual ions are calculated based on Eqs. 4.3 and 4.4 for a cation series of chloride salts. All monovalent and divalent cations behave approximately in the same way so that the curves overlap. (B) The coherent SHS intensities of electrolyte solutions are calculated based on the DH theory (Eqs. 4.5-4.8) for monovalent and divalent cations. There is no ion specificity in the calculated SH intensity.

4.3.2 Experiments: fs-ESHS from electrolyte solutions

The fs-ESHS intensities ($I_{\text{salt}}(2\omega)$) from aqueous electrolyte solutions were measured in the SSS (Fig. 4.3) and PPP (Fig. 4.4) polarization combinations at a scattering angle of $\theta = 90^\circ$ for electrolyte concentrations up to 4 M (or approaching the solubility limits of SrCl_2 , RbCl , and KCl). The SSS signal contains only incoherent responses, whereas the PPP signal contains both coherent and incoherent responses. The plotted $I_{\text{salt}}(2\omega)$ is normalized by that of pure water ($I_{\text{water}}(2\omega)$) measured in the same polarization combination. In both cases the curves were fitted with a linear function (Eq. 4.1). The linear increase rate of PPP (SSS) $I_{\text{salt}}(2\omega) / I_{\text{water}}(2\omega)$ is labelled as k_{PPP} (SSS). Fit values are listed in Table 4.2.

As shown in Fig. 4.3, the measured incoherent response differs from ion to ion, and k_{SSS} changes from negative (K^+) to almost zero (Cs^+) and to positive (other cations). The linear increase is observed to start at $c > 0.8$ M (Mg^{2+}) or higher

Cation series		MgCl ₂	CaCl ₂	SrCl ₂	LiCl	NaCl	NH ₄ Cl	RbCl	CsCl	KCl
k_{PPP} (M ⁻¹)		0.45	0.36	0.34	0.22	0.20	0.18	0.17	0.16	0.14
k_{SSS} (M ⁻¹)		0.111	0.064	0.001	0.068	0.054	0.035	0.020	0.001	-0.013
Onset (M)	PPP	0.21	0.36	0.49	0.42	0.47	0.47	0.15	0.59	0.15
	SSS	0.79	0.94	-	2.00	1.90	0.75	1.12	-	-

Table 4.2 – Empirical rate and onset of the increase of fs-ESHS intensities obtained from the linear fits to the fs-ESHS data in Figs. 4.3 and 4.4.

concentrations ($c > 2$ M, Na⁺ and Li⁺). Comparing Fig. 4.2A to Fig. 4.3, we observe differences between the computation and the measurement: The presence of ion specificity is not predicted by the theory nor is the large onset concentration of the intensity increase in Fig. 4.3. Instead of incoherent single ion contributions that mainly arise from Cl⁻ anions, there must be another effect that dominates the SSS fs-ESHS intensity. As we have seen in Eq. 2.8b, the incoherent response of water is the other origin of the fs-ESHS intensity. This response, which depends on the electronic structure of water, can possibly be influenced by ions in highly concentrated electrolyte solutions.^{218,219,235,236} The measured intensity changes start to appear at ion : water ratios of about 1:14 (NaCl) or 1:23 (MgCl₂). At such concentrations, ion-induced changes in the electronic structure of the hydration shells may be playing a role that could comprise charge transfer effects or ion pairing. Within this explanation, a decreasing intensity then implies that K⁺ ions reduce the electronic anisotropy to a more spherical distribution of electron density, whereas an increase in intensity implies an increase in the amount of electronic anisotropy in the hydration shells. Cs⁺ and Sr²⁺ do not or hardly influence the response of water, which means that the electronic structure of the closely associated water molecules is not different from that of bulk water. MgCl₂ and CaCl₂ do influence the electronic anisotropy in the neighboring water molecules, with Mg²⁺ having a bigger influence than Ca²⁺. This is expected because of the double valency and smaller size of Mg²⁺ compared to Ca²⁺. For the ions Li⁺, Na⁺, NH₄⁺, Rb⁺, and Cs⁺ the amount of distortion is governed by the size of the ion.^{237,238} Why K⁺ has an opposite effect on the electronic structure of water cannot be explained by the size and charge difference with respect to the other ions. In fact, in order to reduce the electronic anisotropy of the first hydration shell, the lone pair electrons of water oxygen need to shift towards the hydrogen of the same hydrating water molecule. The distribution of the lone pair electrons of water oxygen highly depends on the local environment, which can be changed by H-bonding or the presence of ions as indicated by previous oxygen K-edge X-ray emission spectroscopy

measurements on liquid water.²³⁹

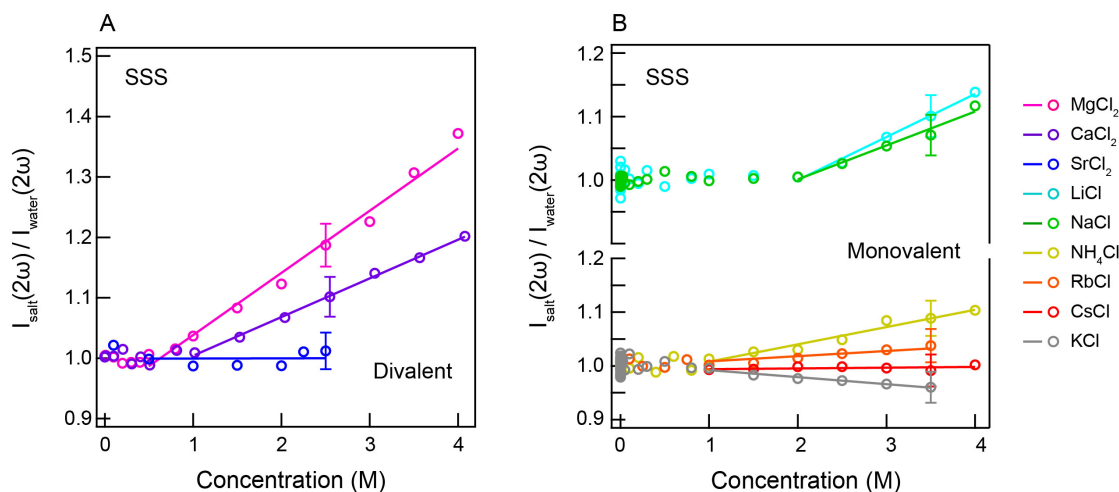


Figure 4.3 – Measured SSS fs-ESHS intensities of electrolyte solutions. The fs-ESHS intensities ($I_{\text{salt}}(2\omega)$) of electrolyte solutions for the chloride salt series were measured in the SSS polarization combination. $I_{\text{salt}}(2\omega)$ is normalized by that of pure water ($I_{\text{water}}(2\omega)$) measured in the same polarization combination. The solid lines represent a linear fit of the fs-ESHS intensity. Note that the computed Y-scale in Fig. 4.2A cannot be compared to the measured Y-scale in Fig. 4.3.

Turning now to the combined coherent and incoherent responses (Fig. 4.4), we observe that in the PPP polarization combination the fs-ESHS intensities show the same type of behavior: The fs-ESHS intensity increases linearly with electrolyte concentration. There are, however, two notable differences: Figure 4.4 displays an increase of a larger magnitude (from 1.3 to 3 instead of from 1 to 1.3 for MgCl_2) as well as an onset concentration that is roughly a factor of 5 lower, bringing the ion : water ratios to hundreds of water molecules per ion. It is unlikely that at such low concentrations ions already induce a significant perturbation in the distribution of electronic charges of the hydration shell that is necessary to change $\beta^{(2)}$.¹⁶² For such low onset concentrations, and to generate a bigger change in the PPP fs-ESHS intensity, ion-induced orientational correlations between water molecules are needed.

Figure 4.4 shows that for increasing salt concentrations the normalized intensities start to diverge, which may be a consequence of the hydration shells becoming smaller and being influenced by the charge, electronic structure, shape, and size of the ions. It can be seen in Fig. 4.4 that all the slopes are positive and that k_{PPP} follows the order: $\text{K}^+ < \text{Cs}^+ < \text{Rb}^+ < \text{NH}_4^+ < \text{Na}^+ < \text{Li}^+ < \text{Sr}^{2+} < \text{Ca}^{2+} < \text{Mg}^{2+}$, which resembles a direct cationic Hofmeister series (with K^+ and NH_4^+ as exceptions).^{17,240} The exception of NH_4^+ is likely due to H-bonding with water molecules, which induces changes in the orientational order of hydrating water molecules. A possible reason for the special behavior of K^+ might be that the water network becomes more disordered

and the hydration shell becomes looser, as indicated by the larger ion-water oxygen distance than the oxygen-oxygen distance as well as the large ion-hydrogen distance measured by neutron diffraction.^{214,241} It can be seen that small divalent ions have the biggest influence on k_{PPP} and thus the most restricting influences on the rotational motion (or H-bond bending mode) of water molecules. In contrast, larger monovalent ions have a smaller influence on restricting the H-bond bending mode and lead to a lesser increase in the orientational order of water as represented by the PPP fs-ESHS intensity.

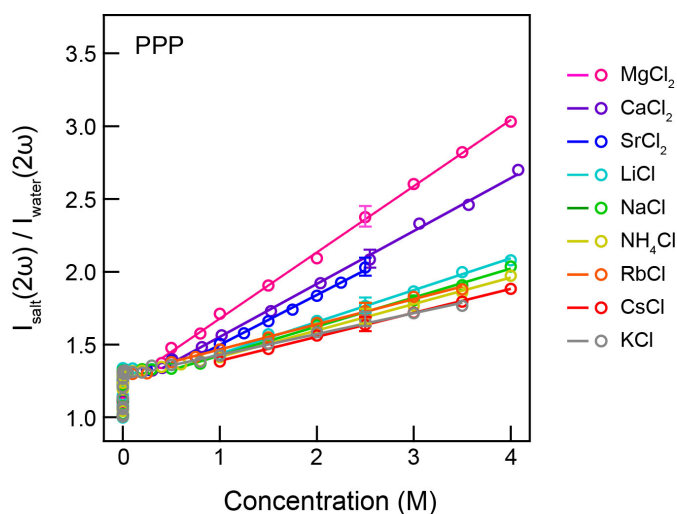


Figure 4.4 – Measured fs-ESHS PPP intensities of electrolyte solutions. The fs-ESHS intensities ($I_{\text{salt}}(2\omega)$) of electrolyte solutions for the chloride salt series were measured in the PPP polarization combination. $I_{\text{salt}}(2\omega)$ is normalized by that of pure water ($I_{\text{water}}(2\omega)$) measured in the same polarization combination. The solid lines represent a linear fit of the fs-ESHS intensity.

Figure 4.2B shows the computed coherent relative SH intensity based on the DH theory. This curve reflects the ion-induced orientational order in a dipolar gas of water molecules. This model does not describe the experimental data well. It can be seen that the DH model fails to capture the observed ion specificity. It does, however, show the extent over which ions could influence the orientational order of water if all water-water interactions would be turned off. As can be seen, at 4 M, the MgCl_2 curve reaches a relative intensity of $I_{\text{salt}}(2\omega) / I_{\text{water}}(2\omega) = 3$, which is close to the limiting value of the DH theory, namely ~ 3.5 (assuming the values for $\beta^{(2)}$ reported by Gubskaya and Kusalik¹⁹¹). This suggests that, at such high salt concentrations, the Mg^{2+} -water interactions strongly contribute to the orientational order of water molecules. In previous X-ray Raman and small angle X-ray scattering studies by Nilsson and coworkers,²¹⁵ Mg^{2+} has also been shown to have strong interactions with water molecules and form tightly bound hydration shells.

With the structure of the water network being changed specifically by cations, we might expect similar changes to occur as well on macroscopic properties of bulk water that are sensitive to water-water interactions. Two of the most well-known candidates are the viscosity of electrolyte solutions and the Gibbs free energy change on hydration of electrolytes, both bulk properties that display ion specificity.^{10–12,242,243}

4.3.3 Macroscopic properties of aqueous solutions of electrolytes

Viscosity B-coefficients

The resistance of a fluid to deformation by an external stress is described by the viscosity, which is a measure of intermolecular interactions, such as H-bonding in water. The dynamic viscosity of an aqueous electrolyte solution can be described by the empirical Jones-Dole equation^{10,242} as a power series of the electrolyte concentration c in the solution:

$$\eta/\eta_0 = 1 + Ac^{1/2} + Bc \quad (4.9)$$

where η is the dynamic viscosity of the solution, η_0 the viscosity of pure water, A the viscosity A-coefficient, and B the viscosity B-coefficient. The A-coefficient is thought to be related to ion-ion interactions and influences the value of η/η_0 for $c < 0.05$ M. The B-coefficient displays ion specificity, and is thought to reflect ion-water interactions influencing the value of η/η_0 for $c > 0.05$ M.¹⁰ In a traditional view, weakly hydrated ions with negative B-coefficients are referred to as “structure breakers” and strongly hydrated ions with positive B-coefficients are referred to as “structure makers”.^{10,14,244} Even though this idea has been challenged,¹⁴ it is widely accepted that the B-coefficient is pertinent to the hydration of ions and ion-induced structural changes in the water network.

Cation series	MgCl ₂	CaCl ₂	SrCl ₂	LiCl	NaCl	NH ₄ Cl	RbCl	CsCl	KCl
B-coefficient (M ⁻¹)	0.375	0.274	0.251	0.141	0.080	-0.013	-0.038	-0.052	-0.014
−ΔG _{hydr} (kJ·mol ⁻¹)	2532	2209	2080	828	722	639	628	605	651

Table 4.3 – Viscosity B-coefficients¹⁰ and hydration free energy¹¹ values of chloride salts for Figs. 4.5 and 4.6.

Ion-induced orientational order of water molecules can be understood as a restriction of the motion of water molecules. This restriction may influence the fluidity of the liquid and the motion of other objects in the water and thus is related to changes

in the viscosity. From Fig. 4.4 we observe that the onset electrolyte concentration of the linear increase of the PPP fs-ESHS intensity coincides with the concentration range where the B-coefficient starts to dominate (i.e. 0.05-0.1 M). As we have seen that the PPP fs-ESHS intensity is a measure of the ion-induced orientational order of water molecules, a correlation between the electrolyte-induced PPP fs-ESHS intensity increase and the viscosity B-coefficient may be expected. In Fig. 4.5A, we correlate k_{PPP} of the linear fit of the fs-ESHS intensity (Fig. 4.4) with literature values (see Table 4.3)¹⁰ of the viscosity B-coefficient for different electrolytes. The quality of the correlation is indicated by R^2 , the coefficient of determination. A perfect correlation is achieved with $R^2 = 1$.²³¹ It can be seen that there exists a very good correlation ($R^2 = 0.97$) between the B-coefficient and k_{PPP} . This correlation can be qualitatively explained by noting that viscosity is determined by the rate at which H-bonds are broken and formed, which is what the fs-ESHS experiment probes (as illustrated in Fig. 4.1C).

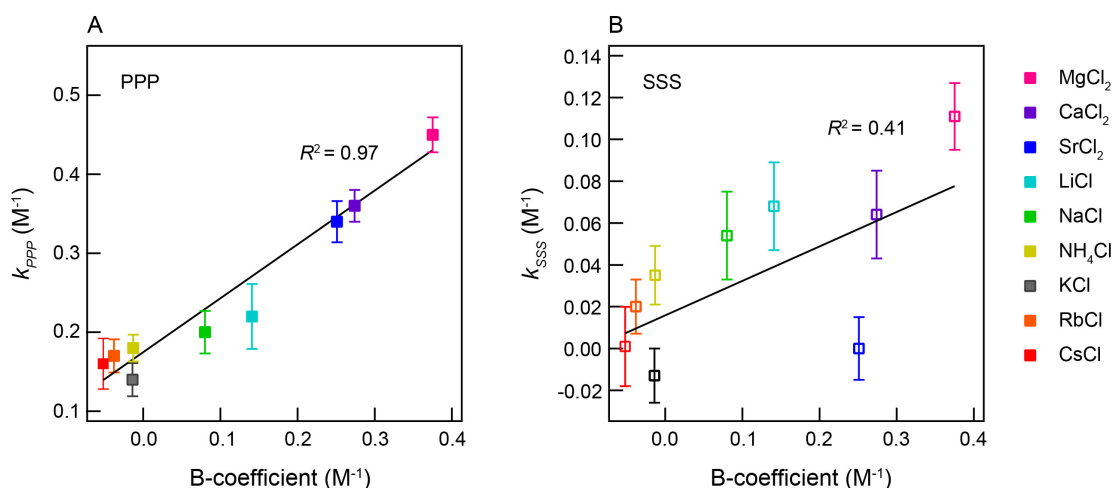


Figure 4.5 – Correlations between fs-ESHS intensity increase and viscosity B-coefficient. (A) k_{PPP} vs. the viscosity B-coefficient for the monovalent and divalent cation series of chloride salts in Fig. 4.4. (B) k_{SSS} vs. the viscosity B-coefficient for the monovalent and divalent cation series of chloride salts in Fig. 4.3. The error bar in k represents the 95% confidence interval of the linear fit of the fs-ESHS intensity to Eq. 4.1. The values for the viscosity B-coefficient are taken from Ref.¹⁰.

In contrast, as can be seen in Fig. 4.5B, no clear correlation between k_{SSS} and the viscosity B-coefficient can be observed ($R^2 = 0.41$). The linear change of the SSS fs-ESHS intensity starts at electrolyte concentrations much higher than 0.05 M (e.g., 2 M for LiCl). Thus the electronic structural changes in the hydrating water molecules do not correlate with the B-coefficient. This is not entirely unexpected: Viscosity is a property that depends more on intermolecular interactions than on changes in the molecular electronic structure.²³³

The viscosity B-coefficient of electrolyte solutions dominates the influence of ions on the structure of water for electrolyte concentrations > 0.05 M.¹⁰ A recent neutron diffraction study²⁴¹ reasons that ion induced viscosity changes are not caused by changes in the H-bond network of water as the viscosity B-coefficient correlates with the difference between the oxygen-oxygen distance in pure water and the ion-oxygen distance in an electrolyte solution. The experimental data supporting this argument is, however, incomplete since neutron diffraction is only sensitive to up to the first two hydration shells. Here, we observe a strong correlation between the viscosity B-coefficient and ion-induced orientational order in water as measured by fs-ESHS, which reports on changes in hundreds of water molecules (i.e. the extended hydration shell). Qualitatively, this correlation can be understood since the ions impose a restriction to the degrees of freedom in the H-bond network. As the resistance of water to objects moving through it is determined by the breaking and forming of H-bonds, it is clear that there can indeed be a connection. The viscosity of electrolyte solutions is thus highly related to the ion-induced distortions in the H-bond network of water.

Gibbs free energy change on electrolyte hydration

The hydration free energy (Gibbs free energy change on the hydration of electrolytes, ΔG_{hydr}) describes the total free energy change during the formation of hydrated individual ions (cations and anions) from pure liquid water and ions in the gas phase. The free energy change of water molecules in the ionic hydration shells dominates ΔG_{hydr} since ΔG_{hydr} is given in the limit of infinite dilution and thus ion-ion interactions are excluded.¹² Thus, ΔG_{hydr} directly reflects the ion-induced energy changes in the extended hydration shells of ions.

In Figs. 4.6A and 4.6B, we correlate the rates of changes in the fs-ESHS intensity (Figs. 4.3 and 4.4) - k_{PPP} and k_{SSS} - with literature values (see Table 4.3)¹¹ of $-\Delta G_{\text{hydr}}$, respectively. As Fig. 4.6A shows, a strong correlation exists between ΔG_{hydr} and k_{PPP} for the cation series of chloride salts, with $R^2 = 0.96$. Cations that induce larger orientational order in the water network, characterized by a larger k_{PPP} , correlate to larger values of $-\Delta G_{\text{hydr}}$. This means that ions which constrain more water molecules generate a bigger (negative) increase in the free energy of hydration. For example, Mg^{2+} induces a larger constraint on water molecules than Cs^+ and the hydration of Mg^{2+} is energetically more favorable. As such, smaller ions with larger valencies induce larger structural changes in the water network that lead to a larger reduction in the Gibbs free energy of the water network for the ion hydration. ΔG_{hydr} is thus highly related to the ion-induced distortions in the H-bond network of water. In contrast,

there is no clear correlation ($R^2 = 0.29$) between k_{SSS} and $-\Delta G_{\text{hydr}}$, as shown in Fig. 4.6B. The ion-induced electronic changes, in the hydrating water molecules, do not correlate with the changes in the total free energy of the solution. We can explain the correlation by noting that ΔG_{hydr} mainly results from the ion-water and water-water interactions related to the orientational order of water molecules.

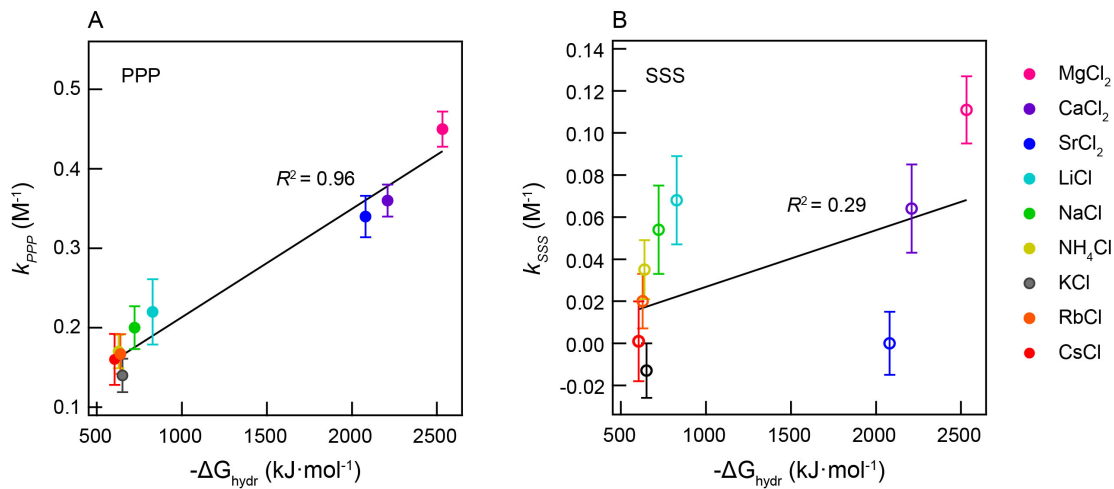


Figure 4.6 – Correlations between fs-ESHS intensity increase and hydration free energy of electrolytes. (A) k_{PPP} vs the hydration free energy of electrolytes ($-\Delta G_{\text{hydr}}$) for the monovalent and divalent cation series of chloride salts in Fig. 4.4. (B) k_{SSS} vs. $-\Delta G_{\text{hydr}}$ for the monovalent and divalent cation series of chloride salts in Fig. 4.3. The error bar in k represents the 95% confidence interval of the linear fit of the fs-ESHS intensity to Eq. 4.1. The values for the hydration free energy are taken from Ref. ¹¹.

Thus, we find that the viscosity B-coefficient, $-\Delta G_{\text{hydr}}$, and k_{PPP} increase in magnitude following a direct cation Hofmeister series.^{17,240} It is also evident that for these three observables changes in the H-bond network play an important role. Recent MD simulations performed by Thomas and Elcock²²⁰ show that the influence of ions on the relative number of H-bonds per water molecule in electrolyte solutions is ion specific and follows a direct Hofmeister series. Connecting both aspects, there is a qualitative explanation for the observed correlations. What the exact molecular mechanism is for the observed increase in the fs-ESHS response and what the exact mechanism is behind the correlations observed in Figs. 4.5 and 4.6 need to be investigated in more detail. More sophisticated atomistic simulations that calculate the electronic anisotropy as well as the induced orientational order will be useful.

4.4 Conclusions

We have probed ion-induced electronic and structural changes in water for a cation series of chloride salts using fs-ESHS. For both the incoherent and coherent responses, specific ion effects are observed above concentrations of ~ 1 M and ~ 0.1 M, respectively. Comparing the changes in the molecular electronic anisotropy (incoherent response) as measured with fs-ESHS in the SSS polarization combination to theoretical considerations, we conclude that the spherical cations themselves do not significantly contribute to the measured fs-ESHS response. An ion-specific SSS response is rather originating from ion-induced changes in the electronic structure of water molecules adjacent to the ion. Positive changes as much as 37% (Mg^{2+} , 4 M) and negative changes of -4% (K^+ , 4 M) indicate the extent of the impact of the ions on the electronic structure of hydrating water molecules. The increased responses are stronger for smaller ions with larger valencies. The K^+ -induced reduction in the fs-ESHS response is, however, anomalous. It means that K^+ reduces the overall electronic anisotropy of water, for example via a redistribution of charge in an H-bonding event. The difference in hydration between K^+ and Na^+ is particularly interesting in light of the unusual sensitivity of ion channels to either one of the species,^{223,224} and our experimental data might prove to be useful in elucidating the molecular cause of the functional difference.

The coherent PPP fs-ESHS response reports mainly on ion-induced changes in the structural orientational order of water in the extended hydration shells of the ions. Specific effects that follow a Hofmeister trend are observed. Smaller ions lead to a larger increase in the fs-ESHS response, and an increasing valency also results in a higher fs-ESHS intensity. The measured trend shows how cations restrict the orientational freedom of water, which is more effectively achieved for smaller ions with larger valencies.

Such a reduction in the orientational freedom of water molecules also influences macroscopic properties of bulk water. Both the viscosity B-coefficient and hydration free energy ΔG_{hydr} correlate well with the linear increase in the PPP fs-ESHS response. These observations open up a possible connection between these three observables, among which the first two observables report on ion-water interactions on a macroscopic scale and the last observable on a molecular scale. This connection would make it possible to connect molecular and macroscopic properties of water with atomistic details and undoubtedly further our understanding of the ion hydration. Given the omnipresent role that ions and water play in physics, chemistry, biology, and medicine, this study is relevant for a wide variety of phenomena. The observed

specific cation effects in both the electronic structure and the orientational ordering of water molecules provide us with a handle to understand and verify models aimed at understanding specific ion effects in water on both the molecular and macroscopic levels.

Aqueous Nanoscale Interfaces **Part II**

5 Methods to Probe Aqueous Nanoscale Interfaces

In this chapter, we will provide the theoretical background and experimental details of the techniques employed to probe aqueous nanoscale interfaces. In particular, vibrational sum frequency scattering will be discussed in detail. We will also give a brief introduction to second harmonic scattering from nanoscale interfaces, dynamic light scattering, and electrokinetic mobility measurements.

5.1 Introduction

Vibrational sum frequency scattering (SFS) and second harmonic scattering (SHS) are noninvasive second-order nonlinear optical techniques that can access buried droplet/particle surfaces with molecular specificity. In this chapter, we will present the theoretical background of SFS and SHS as well as the used instrumentations. In addition, we will provide a brief introduction of dynamic light scattering (DLS) and electrokinetic mobility measurements for further characterizations of the dispersed nanodroplets.

5.2 Theoretical background

5.2.1 Vibrational sum frequency scattering

Geometry of SFS

Figure. 5.1 shows a sketch of the SFS geometry. A spherical nanodroplet with a radius of R is illuminated with two laser beams with the wavevectors of \mathbf{k}_1 (for VIS) and \mathbf{k}_2 (for IR). The XZ -plane defines the scattering plane. The direction of the P/S polarization is parallel/perpendicular to the scattering plane. The opening angle between the VIS and IR beams is β and the angle between the IR beam and the direction of $\mathbf{k}_1 + \mathbf{k}_2$ (Z -axis) is α as shown in the figure. The scattering angle between the scattered SF wavevector \mathbf{k}_0 and the sum of the two incident wavevectors, $\mathbf{k}_1 + \mathbf{k}_2$, is labeled by θ . The scattering vector \mathbf{q} is defined as $\mathbf{k}_0 - (\mathbf{k}_1 + \mathbf{k}_2)$ and $q \equiv |\mathbf{q}| = 2k_0 \sin(\theta/2)$. The four related coordinate systems are thus, the lab frame (X, Y, Z), the rotated lab frame (x, y, z) defined by the scattering wavevector \mathbf{q} , the interface frame (r', θ', ϕ'), and the molecular frame (a, b, c) as illustrated in Fig. 5.1.

In the lab frame, the \mathbf{k} -vectors are given by

$$\begin{aligned}
 \mathbf{k}_0 &= k_0 \sin \theta \hat{\mathbf{X}} + 0 \hat{\mathbf{Y}} + k_0 \cos \theta \hat{\mathbf{Z}} \\
 \mathbf{k}_1 &= -k_1 \sin(\beta - \alpha) \hat{\mathbf{X}} + 0 \hat{\mathbf{Y}} + k_1 \cos(\beta - \alpha) \hat{\mathbf{Z}} \\
 \mathbf{k}_2 &= k_2 \sin \alpha \hat{\mathbf{X}} + 0 \hat{\mathbf{Y}} + k_2 \cos \alpha \hat{\mathbf{Z}} \\
 \mathbf{k}_1 + \mathbf{k}_2 &= 0 \hat{\mathbf{X}} + 0 \hat{\mathbf{Y}} + |\mathbf{k}_1 + \mathbf{k}_2| \hat{\mathbf{Z}}
 \end{aligned} \tag{5.1}$$

where $\hat{\mathbf{X}}, \hat{\mathbf{Y}}, \hat{\mathbf{Z}}$ represent the unit vectors along the X, Y, Z axes. The unit polarization

vectors of the scattered and incoming beams are given by

$$\begin{aligned}
 \mathbf{u}_{0,P} &= \cos\theta \hat{\mathbf{X}} + 0 \hat{\mathbf{Y}} - \sin\theta \hat{\mathbf{Z}} \\
 \mathbf{u}_{1,P} &= -\cos(\beta - \alpha) \hat{\mathbf{X}} + 0 \hat{\mathbf{Y}} + \sin(\beta - \alpha) \hat{\mathbf{Z}} \\
 \mathbf{u}_{2,P} &= \sin\alpha \hat{\mathbf{X}} + 0 \hat{\mathbf{Y}} + \cos\alpha \hat{\mathbf{Z}} \\
 \mathbf{u}_{0,S} = \mathbf{u}_{1,S} = \mathbf{u}_{2,S} &= 0 \hat{\mathbf{X}} + \hat{\mathbf{Y}} + 0 \hat{\mathbf{Z}}
 \end{aligned} \tag{5.2}$$

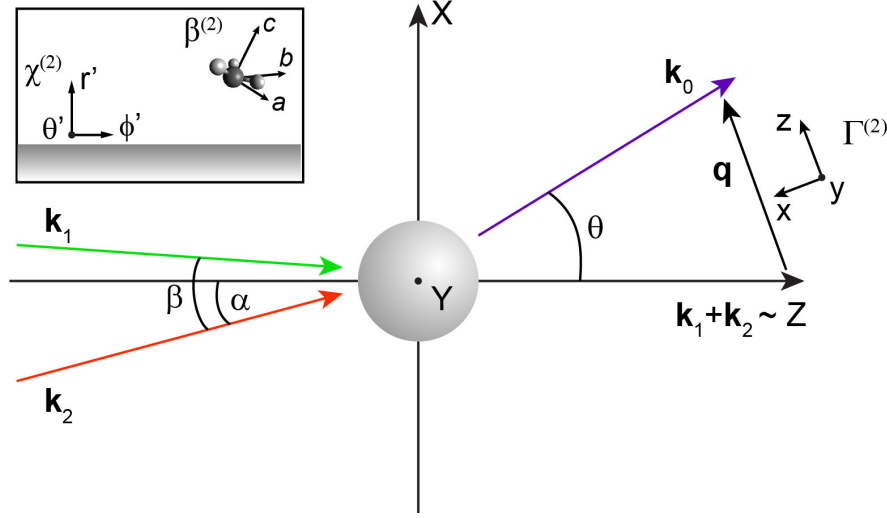


Figure 5.1 – Sketch (top view) of the SFS geometry. A spherical nanodroplet is illuminated with two pulses of different frequencies and wavevectors \mathbf{k}_1 (for VIS) and \mathbf{k}_2 (for IR). The generated SF light is detected at a scattering angle of θ with a wavevector of \mathbf{k}_0 . The scattering vector \mathbf{q} is defined as $\mathbf{k}_0 - (\mathbf{k}_1 + \mathbf{k}_2)$. The effective particle susceptibility $\Gamma^{(2)}$ is defined in the rotated lab frame defined by \mathbf{q} . $\mathbf{u}_{\perp(\parallel)}$ indicate the parallel (perpendicular) directions with respect to \mathbf{q} . The inset shows a close-up of the nanodroplet surface, relative to which the surface susceptibility $\chi_s^{(2)}$ is defined. The hyperpolarizability $\beta^{(2)}$ is defined in the molecular coordinate system (a, b, c) .

The relation between the rotated lab frame (x, y, z) and the lab frame (X, Y, Z) can be given by

$$\begin{aligned}
 \hat{\mathbf{x}} &= -\sin(\theta/2) \hat{\mathbf{X}} + 0 \hat{\mathbf{Y}} - \cos(\theta/2) \hat{\mathbf{Z}} \\
 \hat{\mathbf{y}} &= 0 \hat{\mathbf{X}} + \hat{\mathbf{Y}} + 0 \hat{\mathbf{Z}} \\
 \hat{\mathbf{z}} &= \cos(\theta/2) \hat{\mathbf{X}} + 0 \hat{\mathbf{Y}} - \sin(\theta/2) \hat{\mathbf{Z}}
 \end{aligned} \tag{5.3}$$

where $\hat{\mathbf{x}}, \hat{\mathbf{y}}, \hat{\mathbf{z}}$ represent the unit vectors along the x, y, z axes.

The spherical coordinate system (r', θ', ϕ') defines the interface frame. The polar axis is along the z -axis of the rotated lab frame. \mathbf{r}' represents the position of the interface and is along the radial direction emanating from the center of the droplet.

The relation between the interface frame and the rotated lab frame can be given by

$$\begin{aligned}\hat{\mathbf{r}}' &= \sin\theta' \cos\phi' \hat{\mathbf{x}} + \sin\theta' \sin\phi' \hat{\mathbf{y}} - \cos\theta' \hat{\mathbf{z}} \\ \hat{\boldsymbol{\theta}}' &= \cos\theta' \cos\phi' \hat{\mathbf{x}} + \cos\theta' \sin\phi' \hat{\mathbf{y}} - \sin\theta' \hat{\mathbf{z}} \\ \hat{\boldsymbol{\phi}}' &= -\sin\phi' \hat{\mathbf{x}} + \cos\phi' \hat{\mathbf{y}} + 0 \hat{\mathbf{z}}\end{aligned}\quad (5.4)$$

where $\hat{\mathbf{r}}', \hat{\boldsymbol{\theta}}', \hat{\boldsymbol{\phi}}'$ are the unit vectors along the r', θ', ϕ' axes.

The conversion of the molecular frame (a, b, c) into the interface frame can be performed as follows

$$\begin{aligned}\hat{\mathbf{a}} &= (\cos\phi \cos\psi \cos\varphi - \sin\psi \sin\varphi) \hat{\mathbf{r}}' + (-\sin\psi \cos\varphi - \cos\phi \cos\psi \sin\varphi) \hat{\boldsymbol{\theta}}' \\ &\quad + \sin\phi \cos\psi \hat{\boldsymbol{\phi}}' \\ \hat{\mathbf{b}} &= (\cos\phi \sin\psi \cos\varphi + \cos\psi \sin\varphi) \hat{\mathbf{r}}' + (\cos\psi \cos\varphi - \cos\phi \sin\psi \sin\varphi) \hat{\boldsymbol{\theta}}' \\ &\quad + \sin\phi \sin\psi \hat{\boldsymbol{\phi}}' \\ \hat{\mathbf{c}} &= \sin\phi \cos\varphi \hat{\mathbf{r}}' + \sin\phi \sin\varphi \hat{\boldsymbol{\theta}}' + \cos\phi \hat{\boldsymbol{\phi}}'\end{aligned}\quad (5.5)$$

where $\hat{\mathbf{a}}, \hat{\mathbf{b}}, \hat{\mathbf{c}}$ are the unit vectors along the a, b, c axes.

SFS from nanoscale interfaces

The local interface SF response, characterized by the surface susceptibility $\chi_s^{(2)}$, is an orientation-weighted sum of the molecular response, characterized by the molecular hyperpolarizability $\boldsymbol{\beta}^{(2)}$. The measured SFS intensity thus contains information of the interfacial structure of molecules. To retrieve this information, we need to first convert the scattered SF light intensity measured in the lab frame to parameters that relate to the local interfacial structure and molecular orientation. The effective particle susceptibility $\boldsymbol{\Gamma}^{(2)}$ has been developed for this purpose.¹³⁶ $\boldsymbol{\Gamma}^{(2)}$ is defined in the rotated lab frame (Fig. 5.1) as the susceptibility that describes the integral SF response of the surface of a nanodroplet. The electrical field of the detected SFS light can be expressed as a function of $\boldsymbol{\Gamma}^{(2)}$ by

$$\mathbf{E}_0(\omega_{SF}) \propto \mathbf{E}_1(\omega_{VIS}) \mathbf{E}_2(\omega_{IR}) \sum_{a_0, a_1, a_2} \Gamma_{a_0 a_1 a_2}^{(2)}(\omega_{SF}) \prod_{i=0}^2 (\mathbf{a}_i \cdot \mathbf{u}_{i,l}) \quad (5.6)$$

where the SF, VIS, and IR beams are labeled with 0, 1, and 2, respectively. The subscript $a_0 a_1 a_2$ of $\Gamma^{(2)}$ denotes the tensor element in the rotated lab frame (x, y, z). \mathbf{a}_i can be $\hat{\mathbf{x}}$, $\hat{\mathbf{y}}$, or $\hat{\mathbf{z}}$. The index l denotes the polarization state of the beam and can be either P or S.

Achiral droplet interfaces between isotropic liquid media can be probed with four polarization combinations: PPP, SPP, SPS, and PSS. This is similar to the coherent fs-ESHS intensity emitted by spherically correlated water molecules as discussed in Sec. 3.3.2. For these four polarization combinations, the SFS electrical field amplitudes can be given by¹³⁷

$$\begin{aligned}
 E_{PPP} &\propto \cos \frac{\theta}{2} \cos \left(\frac{\theta}{2} - \alpha \right) \cos \left(\frac{\theta}{2} - \alpha + \beta \right) \Gamma_1^{(2)} + \cos (\theta - \alpha + \beta) \cos \left(\frac{\theta}{2} - \alpha \right) \Gamma_2^{(2)} \\
 &\quad + \cos (\theta - \alpha) \cos \left(\frac{\theta}{2} - \alpha + \beta \right) \Gamma_3^{(2)} + \cos \beta \cos \frac{\theta}{2} \Gamma_4^{(2)}, \\
 E_{SPP} &\propto \cos \left(\frac{\theta}{2} - \alpha \right) \Gamma_2^{(2)}, \\
 E_{SPS} &\propto \cos \left(\frac{\theta}{2} - \alpha + \beta \right) \Gamma_3^{(2)}, \\
 E_{PSS} &\propto \cos \frac{\theta}{2} \Gamma_4^{(2)}
 \end{aligned} \tag{5.7}$$

where $\Gamma_1^{(2)} = \Gamma_{\perp\perp\perp}^{(2)} - \Gamma_{\parallel\parallel\perp}^{(2)} - \Gamma_{\parallel\perp\parallel}^{(2)} - \Gamma_{\perp\parallel\parallel}^{(2)}$, $\Gamma_2^{(2)} = \Gamma_{\parallel\parallel\perp}^{(2)}$, $\Gamma_3^{(2)} = \Gamma_{\parallel\perp\parallel}^{(2)}$, and $\Gamma_4^{(2)} = \Gamma_{\perp\parallel\parallel}^{(2)}$. The subscripts \perp (\parallel) denotes the direction parallel (perpendicular) to the scattering wavevector \mathbf{q} . The measured intensity is $I \propto |E|^2$.

For a spherical nanodroplet, $\Gamma^{(2)}$ is given by an integral of $\chi_s^{(2)}$, the surface second-order susceptibility, over the interface where $\chi_s^{(2)}(\mathbf{r}') = \chi^{(2)}(\mathbf{r}')\delta(|\mathbf{r}'| - R)$ as

$$\Gamma_{IJK}^{(2)} = \sum_{ijk} \chi_{ijk,s}^{(2)} \oint (T_{Ii} T_{Jj} T_{Kk}) e^{i\mathbf{q}\cdot\mathbf{r}} d^2\mathbf{r} \tag{5.8}$$

where $(T_{Ii} T_{Jj} T_{Kk})$ represents a coordinate transformation from the interface frame to the lab frame. For achiral interfacial molecules, Eq. 5.8 becomes

$$\begin{pmatrix} \Gamma_1^{(2)} \\ \Gamma_2^{(2)} \\ \Gamma_3^{(2)} \\ \Gamma_4^{(2)} \end{pmatrix} = \begin{pmatrix} 2F_1 - 5F_2 & 0 & 0 & 0 \\ F_2 & 2F_1 & 0 & 0 \\ F_2 & 0 & 2F_1 & 0 \\ F_2 & 0 & 0 & 2F_1 \end{pmatrix} \begin{pmatrix} \chi_1^{(2)} \\ \chi_2^{(2)} \\ \chi_3^{(2)} \\ \chi_4^{(2)} \end{pmatrix} \tag{5.9}$$

where $\chi_1^{(2)} = \chi_{\perp\perp\perp}^{(2)} - \chi_{\parallel\parallel\perp}^{(2)} - \chi_{\parallel\perp\parallel}^{(2)} - \chi_{\perp\parallel\parallel}^{(2)}$, $\chi_2^{(2)} = \chi_{\parallel\parallel\perp}^{(2)}$, $\chi_3^{(2)} = \chi_{\parallel\perp\parallel}^{(2)}$, and $\chi_4^{(2)} = \chi_{\perp\parallel\parallel}^{(2)}$. The subscripts \perp (\parallel) denote the direction perpendicular (parallel) to the particle surface plane. F_1 and F_2 are the two scattering form factors for second-order scattering from

spherical nanodroplets and are given by

$$\begin{aligned} F_1(qR) &= 2\pi R^2 i \left(\frac{\sin(qR)}{(qR)^2} - \frac{\cos(qR)}{qR} \right), \\ F_2(qR) &= 4\pi R^2 i \left(3 \frac{\sin(qR)}{(qR)^4} - 3 \frac{\cos(qR)}{(qR)^3} - \frac{\sin(qR)}{(qR)^2} \right) \end{aligned} \quad (5.10)$$

The RGD approximation is used in the derivation of the expressions of these two form factor functions.^{136,188} The RGD approximation assumes that the refractive index difference between the two media is negligible. For scattering from spherical particles and droplets, the RGD approximation is valid if $qR(1-m) \ll 1$, where m is the relative refractive index of the scatterer with respect to the solvent.²⁴⁵ For the samples (hexadecane nanodroplets dispersed in water) studied in this thesis, this condition holds.^{141,188}

For an azimuthally isotropic interface, the relation between $\chi^{(2)}$ and $\beta^{(2)}$ can be given based on Eq. 5.5 by^{119,137}

$$\begin{pmatrix} \chi_1^{(2)} \\ \chi_2^{(2)} \\ \chi_3^{(2)} \\ \chi_4^{(2)} \end{pmatrix} = \frac{N_s \langle \cos \phi \rangle}{2\epsilon_0} \begin{pmatrix} 5D-3 & 0 & 0 & 0 \\ 1-D & 2 & 0 & 0 \\ 1-D & 0 & 2 & 0 \\ 1-D & 0 & 0 & 2 \end{pmatrix} \begin{pmatrix} \beta_1^{(2)} \\ \beta_2^{(2)} \\ \beta_3^{(2)} \\ \beta_4^{(2)} \end{pmatrix} \quad (5.11)$$

where $\beta_1^{(2)} = \beta_{ccc}^{(2)} - \beta_2^{(2)} - \beta_3^{(2)} - \beta_4^{(2)}$, $\beta_2^{(2)} = (\beta_{aac}^{(2)} + \beta_{bbc}^{(2)})/2$, $\beta_3^{(2)} = (\beta_{aca}^{(2)} + \beta_{bcb}^{(2)})/2$, and $\beta_4^{(2)} = (\beta_{caa}^{(2)} + \beta_{cbb}^{(2)})/2$. N_s is the interfacial number density of the probed chemical groups. $\langle \cos \phi \rangle$ denotes the average cosine of the tilt angle ϕ of the studied chemical group relative to the interface normal. $D = \langle \cos^3 \phi \rangle / \langle \cos \phi \rangle$.

It is worth noting that the nanodroplets dispersed in water are uncorrelated, so are the SF photons generated from each nanodroplet. For the dispersions of oil droplets in water studied in Ch. 6 and Ch. 7, no multiple scattering occurs.⁴⁷ Therefore, the total SFS intensity is proportional to the product of the volume fraction of the oil droplets and R^3 . Combining Eqs. 5.7-5.11, we can express the relative amplitude of the SFS signal (i.e. the ratio of SFS amplitudes in different polarization combinations) as a function of solely ϕ and $\beta^{(2)}$. The $\beta^{(2)}$ values can be calculated using the bond polarizability derivative model^{115,246} with measured Raman depolarization ratio ρ , as is shown next. Thus, we can retrieve the orientation (i.e. the average tilt angle ϕ) of the chemical group of interest from the measured SFS amplitudes.

SF response of a single molecule: $\beta^{(2)}$

The SH response of a single molecule and the molecular hyperpolarizability were discussed in Ch. 2. Here, we describe the molecular response in an SFS experiment. The SH/SF response of a molecule is characterized by the second-order hyperpolarizability, $\beta^{(2)}$, as for all second-order nonlinear optical processes as introduced in Ch. 2. The SF intensity is given by $\beta^{(2)}$ as $I_{SF} \propto |\beta^{(2)}|^2$. For SFS, the quantum mechanical expression of $\beta^{(2)}$ is derived from the electric dipole approximation for the light-molecule interaction using perturbation theory. The result is as follows^{62,115,247}

$$\beta_{ijk}^{(2)}(\omega_{SF}, \omega_{VIS}, \omega_{IR}) = -\frac{1}{\hbar} \sum_v \frac{\langle g | \alpha_{ij} | v \rangle \langle v | \mu_k | g \rangle}{\omega_{IR} - \omega_v + i\gamma_v} (\rho_g^{(0)} - \rho_v^{(0)}) \quad (5.12a)$$

$$\langle g | \alpha_{ij} | v \rangle = \sum_s \left(\frac{\langle g | \mu_i | s \rangle \langle s | \mu_j | v \rangle}{\omega_{SF} - \omega_{sg}} + \frac{\langle g | \mu_j | s \rangle \langle s | \mu_i | v \rangle}{\omega_{SF} + \omega_{sv}} \right) \quad (5.12b)$$

where μ is the electric dipole operator. $\langle g | \mu_i | s \rangle$ represents the dipole transition from the (quantum) energy state s to g . α_{ij} represents the $(i j)$ component of the Raman polarizability tensor α for the $v \rightarrow g$ transition and μ_k represents the k component of the IR transition moment for the $g \rightarrow v$ transition. As illustrated in Fig. 1.6D, g denotes the ground energy state, v denotes the excited vibrational state, and s denotes the virtual higher energy state. ω_v is the frequency of the vibrational transition from state g to v , i.e. the transition energy is equal to $\hbar\omega_v$. ω_{sg} and ω_{sv} are the transition frequencies between state s and g and between state s and v , respectively. γ_v is the damping rate of the vibrational transition from state g to v . γ_v^{-1} is the dephasing time of the molecular polarization.¹⁴⁵ $\rho_g^{(0)}$ and $\rho_v^{(0)}$ are the fractional population of state g and v , respectively. The indices i , j , and k denote the polarization states of the SF, VIS, and IR beams, respectively.

Symmetry properties of $\beta^{(2)}$

The value of $\beta^{(2)}$ is determined by the nature of the underlying molecular transition and the molecular symmetry. The symmetry properties of $\beta^{(2)}$ determine the relations between tensor elements and reduce the number of nonzero elements. In Sec. 2.1.3, we have discussed the symmetry properties of $\beta^{(2)}$ for nonresonant SHS, including the permutation symmetry and spatial symmetry. In this section, we will discuss additional symmetry properties of $\beta^{(2)}$ for SFS due to the vibrational resonance and the molecular spatial symmetry.

The full permutation symmetry in nonresonant SHS of lossless and disper-

sionless media discussed in Sec. 2.1.3 is not valid in SFG since the value of $\beta_{ijk}^{(2)}$ is complex as indicated in Eq. 5.12a. Instead, a permutation between i and j together with ω_{SF} and ω_{VIS} for the SF and VIS light is valid as the SF and VIS photons are off resonance. This permutation is independent of the frequency if the dispersion of the medium for ω_{SF} and ω_{VIS} can be neglected. This permutation symmetry can be described as

$$\beta_{ijk}^{(2)}(\omega_{SF}, \omega_{VIS}, \omega_{IR}) = \beta_{jik}^{(2)}(\omega_{SF}, \omega_{VIS}, \omega_{IR}). \quad (5.13)$$

Without loss of generality, we will always refer the subscripts of $\beta_{ijk}^{(2)}$, from left to right, to the SF, VIS, and IR beams, respectively, and abbreviate $\beta_{ijk}^{(2)}(\omega_{SF}, \omega_{VIS}, \omega_{IR})$ as $\beta_{ijk}^{(2)}$ hereafter.

The spatial symmetry relates to both the geometric symmetry of the molecule and the symmetry of the vibrational mode. We have discussed the influence of the molecular geometric symmetry on spatial symmetry properties of $\beta^{(2)}$ in Sec. 2.1.3. The symmetry of the vibrational mode relates to the IR and Raman transitions. The molecular dipole vibration determines the nonzero component μ_k of the IR transition moment. The symmetry of the Raman transition determines the nonzero Raman tensor component α_{ij} . The $\beta_{ijk}^{(2)}$ elements are nonzero only when both μ_k and α_{ij} are nonzero (Eq. 5.12a).

To illustrate, we discuss the nonzero $\beta_{ijk}^{(2)}$ elements for the symmetric and antisymmetric stretch modes of the CH_3 and CH_2 groups in the following. These two molecular groups are studied in Ch. 6 and Ch. 7 and these symmetric and antisymmetric stretch modes are probed. Figure 5.2 illustrates the symmetric and antisymmetric stretching of the CH_3 and CH_2 groups. The blue arrows indicate the motions of atoms in each vibrational mode. The red arrows indicate the vibration directions of the molecular dipoles.

The CH_3 group belongs to the C_{3v} point group with a C_3 symmetry axis along the c -axis as shown Fig. 5.2. For the symmetric stretch mode (s- CH_3), all the three H atoms vibrate symmetrically (as indicated by the blue arrows in Fig. 5.2). The ac -plane is a plane of symmetry. The molecular dipole vibrates along the c -axis (the red arrow in Fig. 5.2), leading to a nonzero μ_c . The nonvanishing Raman tensor components are $\alpha_{aa} = \alpha_{bb}$ and α_{cc} . Inserting μ_c and the nonzero Raman tensor elements into Eq. 5.12a, we have the nonzero $\beta^{(2)}$ elements for the s- CH_3 mode as²⁴⁶

$$\beta_{aac}^{(2)} = \beta_{bbc}^{(2)}, \quad \beta_{ccc}^{(2)}. \quad (5.14)$$

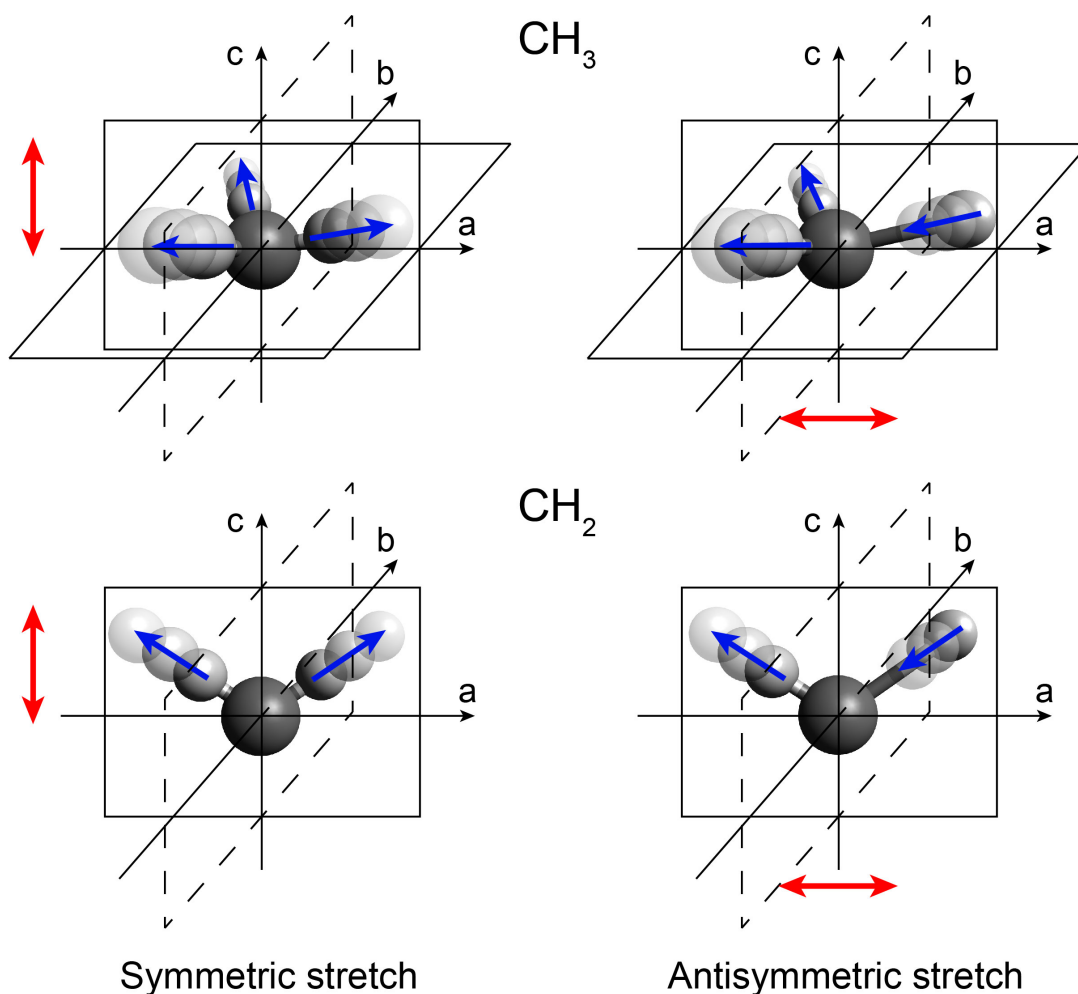


Figure 5.2 – Illustration of symmetric and antisymmetric stretch modes of the CH_3 and CH_2 groups. The principle symmetry axis of the molecular group is directed along the c -axis of the molecular coordinate system (a, b, c). For the CH_3 group, the ac -plane bisects two C-H bonds. The third C-H bond is in the ac -plane. For the CH_2 group, the two C-H bonds are in the ac -plane. The blue arrows indicate the motions of the atoms in the stretch. The red arrows indicate the vibration directions of the molecular dipoles.

For the antisymmetric stretch mode (as- CH_3), as illustrated in Fig. 5.2, two H atoms move synchronously away from the central C atom while the third H atom moves towards the C atom. The two H atoms that move synchronously are switching among the three H atoms. The vibration direction of the molecular dipole is parallel to the ab -plane. The nonvanishing Raman tensor components are $\alpha_{aa} = -\alpha_{bb}$, $\alpha_{bb} = \alpha_{ab} = \alpha_{ba}$, $\alpha_{ac} = \alpha_{bc}$, and $\alpha_{ca} = \alpha_{cb}$. Correspondingly, the nonzero $\beta^{(2)}$ elements for the as- CH_3 mode are²⁴⁶

$$\beta_{aaa}^{(2)} = -\beta_{bba}^{(2)}, \quad \beta_{bba}^{(2)} = \beta_{abb}^{(2)} = \beta_{bab}^{(2)} \quad (5.15a)$$

$$\beta_{aca}^{(2)} = \beta_{bcb}^{(2)}, \quad \beta_{caa}^{(2)} = \beta_{cbb}^{(2)} \quad (5.15b)$$

As the SF and VIS photons are both off resonance, the Raman tensor elements have the relationships that $\alpha_{ac} = \alpha_{ca}$, $\alpha_{bc} = \alpha_{cb}$. Equation 5.15b is changed as

$$\beta_{aca}^{(2)} = \beta_{bcb}^{(2)} = \beta_{caa}^{(2)} = \beta_{cbb}^{(2)} \quad (5.16)$$

The CH₂ group belongs to the C_{2v} point group with a C₂ symmetry axis along the *c*-axis as shown in Fig. 5.2. The *ac*-plane is a plane of symmetry. All the atoms of the CH₂ group are in the *ac*-plane. For the symmetric stretch mode (s-CH₂), all the two H atoms vibrate symmetrically in the *ac*-plane. The molecular dipole vibrates along the *c*-axis, leading to a nonzero μ_c . The nonvanishing Raman tensor components are α_{aa} , α_{bb} , and α_{cc} . Correspondingly, the nonvanishing $\beta^{(2)}$ elements for the s-CH₂ mode are²⁴⁶

$$\beta_{aac}^{(2)}, \quad \beta_{bbc}^{(2)}, \quad \beta_{ccc}^{(2)}. \quad (5.17)$$

For the antisymmetric stretch mode (as-CH₂), as illustrated in Fig. 5.2, one H atom moves away from the central C atom while the other H atom moves towards the C atom. The vibration direction of the molecular dipole is parallel to the *a*-axis, leading to a nonzero μ_a . The nonvanishing Raman tensor components are $\alpha_{ac} = \alpha_{ca}$ with the SF and VIS photons off-resonance. Correspondingly, the nonzero $\beta^{(2)}$ elements for the as-CH₂ mode are²⁴⁶

$$\beta_{aca}^{(2)} = \beta_{caa}^{(2)} \quad (5.18)$$

The above-discussed symmetry properties of $\beta^{(2)}$ govern the SF response of a single molecule and are reflected in the measured SFS intensity through Eqs. 5.7-5.11.

5.2.2 SHS from aqueous nanoscale interfaces

The geometry of SHS is similar with that of SFS shown in Fig. 5.1. The difference is that the particle is illuminated by only one incident beam propagating along the *Z*-axis in SHS. The scattering vector \mathbf{q} is defined as $\mathbf{k}_0 - 2\mathbf{k}_1$. The angles α and β are zero. For

the case of non-resonant SHS from particles, the expressions of Eq. 5.7 thus reduce to

$$\begin{aligned}
 E_{PPP} &\propto \cos^3 \frac{\theta}{2} \Gamma_1^{(2)} + \cos \theta \cos \frac{\theta}{2} \Gamma_2^{(2)} + \cos \theta \cos \frac{\theta}{2} \Gamma_3^{(2)} + \cos \frac{\theta}{2} \Gamma_4^{(2)}, \\
 E_{SPP} &\propto \cos \frac{\theta}{2} \Gamma_2^{(2)}, \\
 E_{SPS} &\propto \cos \frac{\theta}{2} \Gamma_3^{(2)}, \\
 E_{PSS} &\propto \cos \frac{\theta}{2} \Gamma_4^{(2)}
 \end{aligned} \tag{5.19}$$

The $\beta^{(2)}$ elements are the same as discussed previously in Ch. 2.

5.2.3 Dynamic light scattering

DLS measurements are used to determine the size distribution of the nanodroplets used in this thesis. DLS, also known as photon correlation spectroscopy, measures the linear light scattering (Rayleigh scattering) intensity from small particles in suspension as a function of time. The scattered light intensity fluctuates due to the Brownian motion of the particles. An intensity-intensity autocorrelation function, $g^2(\tau)$, can be obtained directly from this measurement, which can be converted to an electrical field autocorrelation function $g(q, \tau)$. This is illustrated in Fig. 5.3A for a suspension of 2 vol. % hexadecane nanodroplets in water with 10 mM sodium dodecylsulfate. For a mono-dispersive sample, $g(q, \tau)$ decays exponentially with respect to the time-lag τ

$$\begin{aligned}
 g(\tau) &\propto \exp(-Dq^2\tau) \\
 q &= \frac{4\pi}{\lambda} \sin(\theta/2)
 \end{aligned} \tag{5.20}$$

where q is the wavevector of the linear scattering and θ is the scattering angle. The diffusion constant D is related to the hydrodynamic radius R of the particle by the Stokes-Einstein relation²⁴⁸

$$D = \frac{k_B T}{6\pi\eta R} \tag{5.21}$$

where η is the solvent dynamic viscosity. Therefore, the size distribution of particles can be retrieved from the measured linear scattering intensity fluctuations. Figure 5.3B shows the size distribution of the droplets retrieved from the intensity autocorrelation function shown in the panel A.

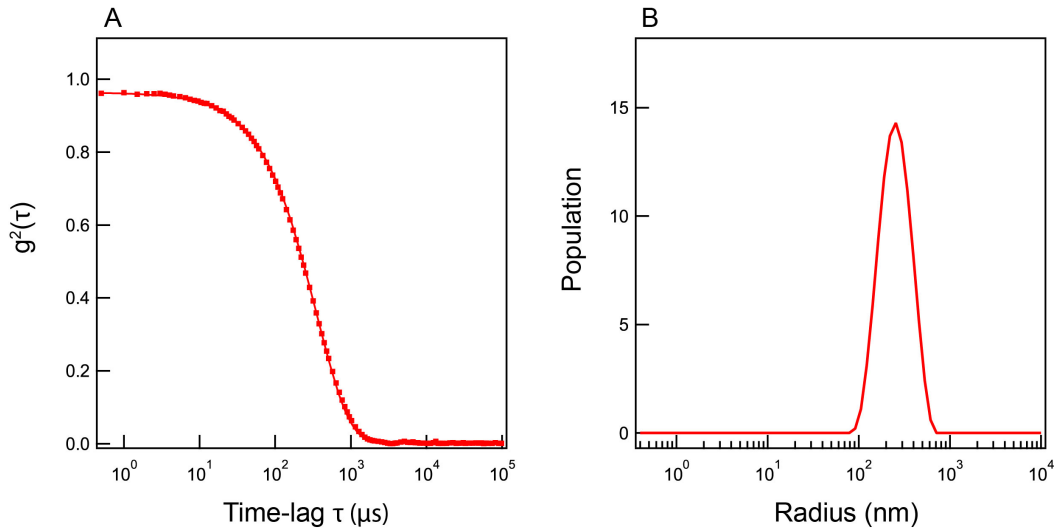


Figure 5.3 – Retrieval of the particle size from DLS. (A) The intensity autocorrelation function, $g^2(\tau)$, as a function of the time-lag τ . $g^2(\tau)$ is calculated from the measured linear scattering intensity fluctuations. (B) The size distribution of the measured nanodroplets. The measured sample is a nanoemulsion consisting of 10 mM sodium dodecylsulfate and 2 vol. % hexadecane in water.

5.2.4 Electrokinetic mobility measurements

A charged particle dispersed in water is surrounded by an electrical double layer. This double layer is illustrated in Fig. 5.4 and originates from the interaction of ions with the particle's electrostatic field. The ions close to the particle are immobilized. Further into the solution, ions become mobile. The plane that divides these regions is called the slipping plane. The electrostatic potential at the slipping plane is referred to as the zeta (ζ)-potential.²⁴⁹ The ζ -potential is a common indicator of the colloidal stability. A ζ -potential magnitude larger than 30 mV normally indicates a stable colloid.²⁵⁰

The ζ -potential of dispersed small particles can be determined using electrokinetic mobility measurements. Electrokinetic mobility is the phenomenon of the movement of dispersed charged particles driven by an external electrical field. The velocity v_e of the particle can be measured by Laser Doppler velocimetry. The particle mobility μ_e can be given by the measured quantity

$$\mu_e = \frac{v_e}{E_{ext}} \quad (5.22)$$

where E_{ext} is the applied external electrical field. μ_e can be expressed as follows

$$\mu_e = \frac{2\epsilon\zeta f(\kappa_D R)}{3\eta} \quad (5.23)$$

where, ϵ is the dielectric constant. $f(\kappa_D R)$ is Henry's function that depends on the particle size R and the Debye length $1/\kappa_D$ (Equation 3.30). When the particle size is much smaller than the Debye length, i.e. $R \ll 1/\kappa_D$, the Smoluchowski theory is applicable, resulting in $f(\kappa_D R) = 1.5$, which corresponds to a thin double layer. This condition usually holds for aqueous solutions of particles with radii ~ 100 nm.

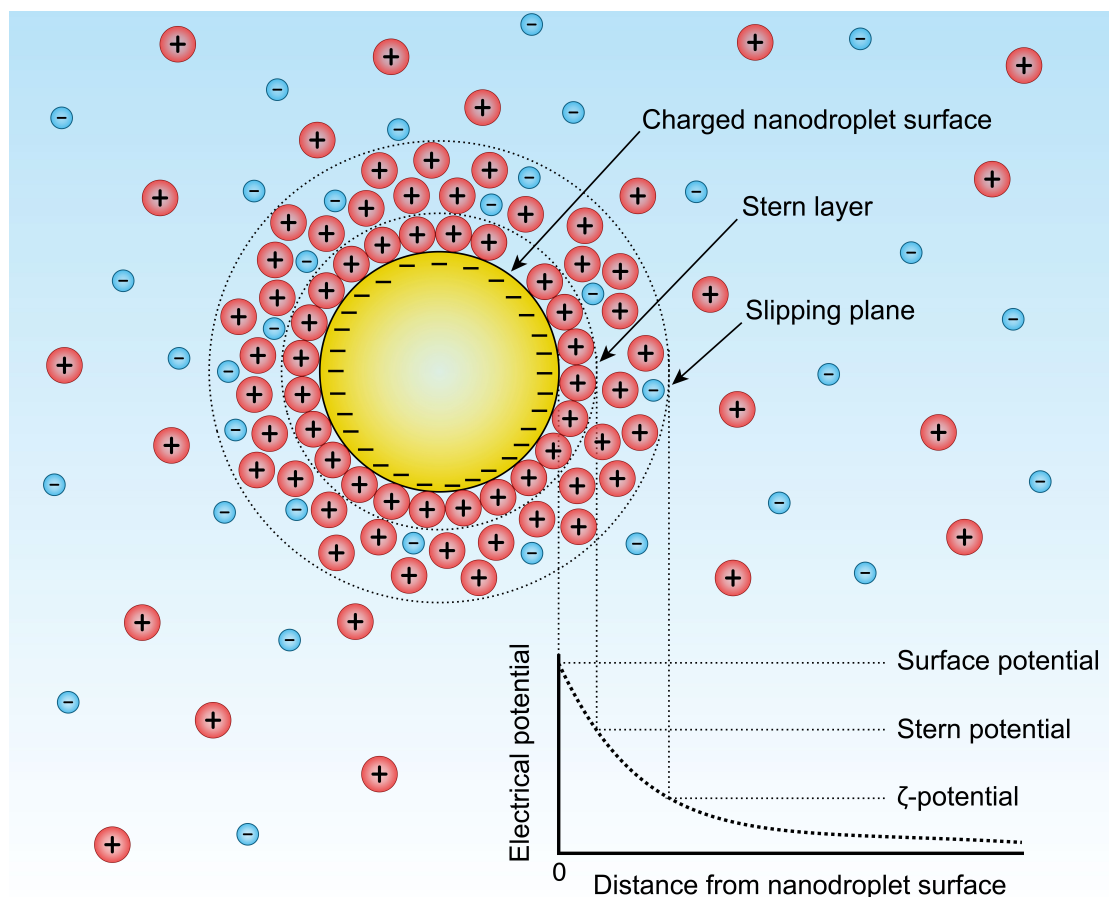


Figure 5.4 – Schematic illustration of the electrical double layer.[†] The ζ -potential, stern potential, and surface potential are defined as the electrical potentials at the slipping plane, stern layer, and the nanodroplet surface, respectively.

A more detailed description of DLS and electrokinetic mobility measurements of the particle's size and ζ -potential can be found in Ref.^{249,251}.

[†] This diagram is modified and adapted from the image: http://en.wikipedia.org/wiki/File:Zeta_Potential_for_a_particle_in_dispersion_medium.png by Mjones1984 and Larryisgood.

5.3 Experimental details

In this section, we will present our SFS experimental setup as well as the SFS spectrum acquisition and analysis. Following that, experimental details of SHS measurements of the interfacial water structure will be presented.

5.3.1 The SFS experimental setup

Our SFS experimental setup is composed of a laser system, an SFS stage, and a detection unit. Figure 5.5 shows an illustration of the SFS experimental setup. In what follows, each component will be described in detail.

The laser system

The laser system consists of 4 units: an fs oscillator (Integral 50, Femtolasers), a chirped pulse amplifier (Spitfire, Spectra-Physics), an IR generator (HE-Topas, Light conversion), and a home-built pulse shaper. The fs oscillator generates 3 nJ, 800 nm, 50 fs laser pulses with an 18 nm spectral FWHM. These laser pulses are directed into the Spitfire as the seed pulses. The incident seed pulses are first stretched in time to ~200 ps by a stretcher to reduce the peak power. Then the stretched seed pulses are amplified sequentially by a regenerative amplifier (RGA) and a double pass amplifier (DPA). The final pulse energy is ~6 mJ. The gain media of the amplifiers are Ti:Sapphire crystals, pumped by Nd:YLF pump lasers (527 nm, 150 ns, 1 kHz, 20 mJ). In the last step, the amplified laser pulses are re-compressed by a compressor to their specified duration of ~100 fs. The output pulses have a repetition rate of 1 kHz and are centered at 800 nm. 90% of the power of the output from the amplifier is directed into the Topas. IR pulses with tunable wavelengths from 2.5 to 15 μm are generated using white-light-continuum generation, optical parametric amplification, and difference frequency generation. The rest of the 800 nm output pulses are directed into a home-built pulse shaper. In the pulse shaper, the pulses are horizontally dispersed by a blazed diffraction grating for 800 nm (PC 1800 50 \times 50 \times 10 NIR, Spectrogon) and then propagate through a lens and a vertical slit. After that, the cut pulses travel back through the same path via a reflection mirror. In this way, the spectral content of the pulses can be reduced down to ~5 cm^{-1} . We refer to these pulses as the VIS pulses. The time delay of the VIS pulses relative to the generated IR pulses is adjusted by a retroreflecting mirror on a motorized translation stage. The generated pulses of this laser system thus consist of broadband IR pulses and narrowband VIS pulses as

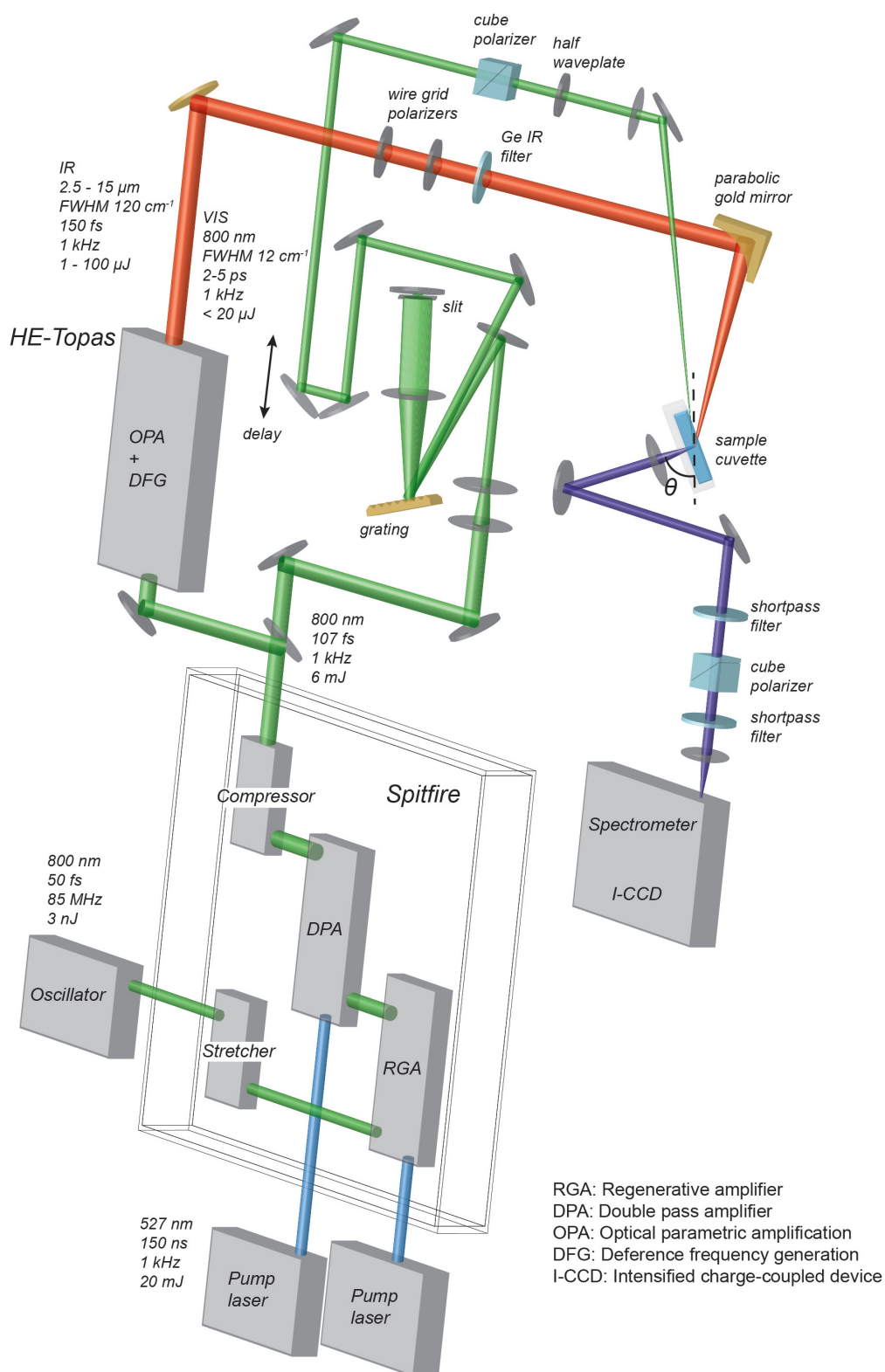


Figure 5.5 – Illustration of the SFS experimental setup. The SFS experimental setup consists of a laser system providing a VIS and a tunable IR beam, an SFS stage, and a detection unit.

illustrated in Fig. 5.6.

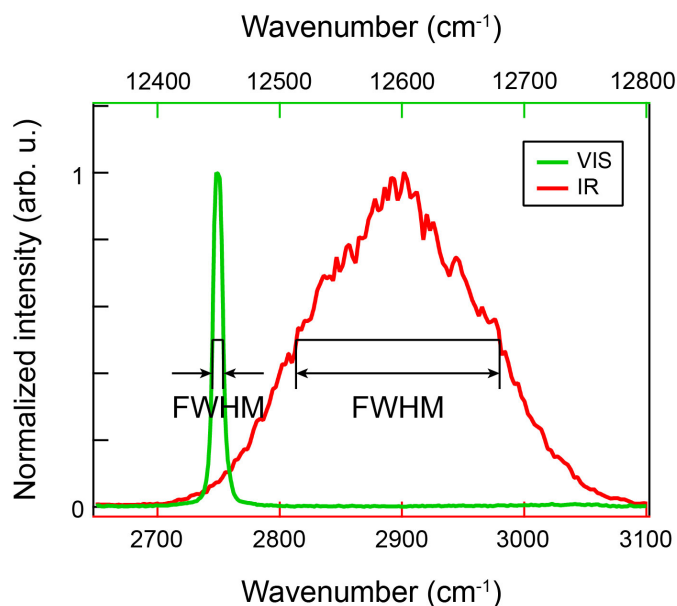


Figure 5.6 – Typical VIS and IR pulses used in the SFS experiment. The VIS pulse is centered at 12450 cm^{-1} (~ 803 nm) and the IR pulse is centered at 2900 cm^{-1} (~ 3448 nm). The FWHM of each pulse is ~ 9 cm^{-1} (VIS) and ~ 165 cm^{-1} (IR).

The SFS stage

The SFS stage consists of optical paths for the IR and VIS pulses and a sample stage. The IR pulses from the Topas propagate through two BaF₂ wire grid polarizers (WP25H-B, Thorlabs). The first polarizer controls the transmitted energy and the second controls the polarization state. The frequency content of the IR beam is then cleaned by a Germanium longpass IR filter (704024001, 50% at 2.4 μm , Laser Components GmbH) and focused by a 90° off-axis parabolic bare gold mirror with an effective focal length of 101.6 mm (84-625, Edmund optics). The polarization of the VIS beam is controlled by a polarizing beam splitter cube (PBS-800-050, CVI) and a half-wave plate (460-4215, EKSMa). The polarized VIS beam is focused by a plano-convex lens with a focal length of 125 mm (LA1986-B, Thorlabs). The focused IR and VIS beams are overlapped under an angle of 15° (measured in air). This angle corresponds to an open angle of $\beta = 5^\circ$ in the sample cuvette (Fig. 5.5). The optical path length inside the sample cuvette is ~ 200 μm . The angle between the IR beam and the normal direction of the incident window of the sample cuvette is 45°. The IR and VIS pulses are also temporally overlapped by adjusting the delay of the VIS pulses using the retroreflector

stage. The sample cuvette consists of a 1.3 mm thick CaF_2 window (CeNing optics) facing the incident IR and VIS beam and a Quartz cell with a 0.2 mm depth (106-QS, Hellma analytics). The sample cuvette is mounted on a platform of two stacked translation stages to ensure a two-dimensional precise positioning. The cuvette is mounted in such a way that the outgoing window is perpendicular to the scattered SF beam.

The detection unit

The scattered SF light from the sample is collected and collimated by a plano-convex lens with a focal length of 15 mm (LA1540-B, Thorlabs) at a scattering angle of 57° (measured in air). This angle corresponds to a scattering angle of 35° inside the cuvette. The reported scattering angles in Ch. 6 and Ch. 7 refer to the scattering angles in solution samples. Two shortpass filters (3RD770SP, 3rd Millennium) are used to clean the collimated SF beam and its polarization is analyzed by a Glan-Taylor polarizer (GT15-B, Thorlabs). Then, the SF beam is focused into a spectrometer (SpectraPro 2300i, Acton) by a plano-convex lens with a focal length of 50 mm (LA1131-B, Thorlabs). The spectrum of the SF beam is recorded with an intensified charge-coupled device camera (I-CCD, PI-Max3, Princeton instruments).

5.3.2 SFS spectra recording

SFS spectra were recorded in four polarization combinations -PPP, SSP, SPS, and PSS- for which the interfacial coherent SFS signal is nonzero. The SFS spectrum of a reference -a nanoemulsion containing 2 vol % d_{34} -hexadecane (~ 100 nm radius) in D_2O with 10 mM sodium dodecyl sulfate (SDS)- was measured between every other measurement to detect and correct for possible fluctuations during the course of the experiment. The acquisition time for a single spectrum was set to either 150 or 300 s with a gate width of 10 ns of the I-CCD. The spectrum of the incident IR pulses was obtained by measuring the reflected SFG spectrum from a flat z-cut quartz window in the IR frequency range $\geq 2000 \text{ cm}^{-1}$. For the IR frequency range $< 2000 \text{ cm}^{-1}$ a bare gold mirror was used in a reflection geometry. The spectrum of the incident VIS pulses was measured directly in the reflection geometry with the two shortpass filter in the detection unit removed. The background noise was recorded by removing the temporal overlapping of the incident IR and VIS pulses.

5.3.3 SFS spectra analysis

The measured SFS spectra were processed and analyzed using IGOR PRO 6 (WaveMetrics). First, the narrow spectrum of the VIS pulses was fitted with a Gaussian function. The SF data was then rescaled using the central frequency of the VIS pulse. The spectra were corrected for noise by subtracting the background spectra. After that, the sample spectra were normalized by the normalized IR spectrum, the acquisition time, and incident IR and VIS pulse energies.

The SFS spectra were fitted using Levenberg-Marquadt iterations^{252,253} by the following expression

$$I_{SFS}(\omega_{IR}, \theta) \propto \left| A_{NR}(\theta) f(\omega_{IR}) e^{i\varphi_{NR}} + \sum_v \frac{A_v(\theta) \gamma_v}{\omega_{IR} - \omega_v + i\gamma_v} \right|^2. \quad (5.24)$$

From the fits, the following parameters were retrieved: the amplitudes of the resonant ($A_v(\theta)$) and nonresonant ($A_{NR}(\theta)$) responses, the linewidth γ_v , and the phase difference φ_{NR} between the resonant and nonresonant responses.

The amplitudes of the vibrational modes report on the amplitude of these modes in the SFS pattern at the scattering angle θ . Using the relative values of the amplitudes of, for example, the s-CH₃ and as-CH₃ modes, it is possible to determine the molecular tilt angle as discussed in Sec. 5.2.1.

5.3.4 SHS measurements of aqueous nanoscale interfaces

SHS measurements of aqueous nanoscale interfaces were performed with the fs-ESHS experimental setup as introduced in Sec. 2.2.1 and under the same experimental conditions. The SHS intensity, $I_{emulsion}(2\omega, \theta)$, of the dispersion of nanodroplets (nanoemulsion) was measured at different scattering angles from -90° to 90° . The HRS intensity, $I_{solution}(2\omega, \theta)$, of the corresponding aqueous solution (without the dispersed nanodroplets) was measured at the same scattering angles for the correction of the background signal from the bulk water phase in the nanoemulsion. In addition, the HRS intensity, $I_{water}(2\omega, \theta)$, of pure water was measured as a reference. All SHS signals were recorded in both PPP and SSS polarization combinations. The SHS pattern from nanodroplets was obtained by subtracting the PPP SHS intensity of the solution, $I_{solution,PPP}(2\omega, \theta)$, from that of the nanoemulsion, $I_{emulsion,PPP}(2\omega, \theta)$. The obtained SHS intensity was normalized by the SSS SHS intensity of pure water

$I_{water,SSS}(2\omega, \theta)$:

$$\frac{I_{emulsion,PPP}(2\omega, \theta) - I_{solution,PPP}(2\omega, \theta)}{I_{water,SSS}(2\omega, \theta)} \quad (5.25)$$

The normalization by $I_{water,SSS}(2\omega, \theta)$ was done both to correct for possible experimental aberrations between measurements and to rescale for the different overlapping focal volumes at different scattering angles.

6 From Hydrophobic to Hydrophilic

The molecular structure of the hexadecane droplet/alkanol/water interface has been investigated using vibrational sum frequency scattering and second harmonic scattering. This combination of methods allows us to investigate the interfacial alkyl chain conformation of the oil and several alkanols, ranging from 1-pentanol to 1-dodecanol, the orientational distribution of the methyl groups, the surface density of the alkanols, as well as the orientational alignment of water. For the hexadecane/1-dodecanol/water interface, dodecanol alkyl chains form a fluid layer with a wide distribution of tilt angles of the terminal CH₃ groups. Indistinguishable spectra are recorded for the alkanol alkyl chains of 1-pentanol, 1-hexanol, 1-octanol, and 1-dodecanol. Alkanols with chain length longer than 6 carbon atoms all form films with similar densities. In contrast, the alkyl chains of the oil phase are relatively more distorted with respect to the pure oil/water interface for alkanols with shorter chain lengths. The projected surface area of a saturated film of hexanol is $29 \pm 5 \text{ \AA}^2$, which requires a free energy of adsorption of $\Delta G = -26.3 \pm 0.7 \text{ kJ/mol}$. In addition, with increasing alkanol density the interfacial water structure loses its initial orientational alignment, which matches with the added number of interfacial 1-hexanol molecules. The found structures differ significantly from those reported on the planar alkanol/water and alkanol/air interfaces and charged surfactant/oil/water interface.

6.1 Introduction

The structural elements that form the building blocks of life are composed of aqueous regions that are in contact with hydrophobic domains or cores, such as the structures found in membranes, peptides, and proteins. The transition from a hydrophilic to a hydrophobic environment is, therefore, essential for understanding fundamental aspects of living systems. The quantitative study of this type of structures and the related interactions started over a century ago when interfacial tension studies were performed on insoluble monolayers.^{48–50} It was suggested that molecules are surface active when they lower the energy of the interface. This lowering of the interfacial energy was explained in terms of solubility: When a molecule has parts that dissolve better in a polar/nonpolar solvent it will orient itself in a configuration of lowest energy, that is, partially dissolved in oil and partially dissolved in water. Alkanols are uncharged amphiphilic molecules with a hydrophobic part and a hydrophilic part that dissolve well in an oil phase and a water phase, respectively. They form essential building blocks that provide a transition between hydrophobic and hydrophilic environments. Depending on the chain length, the partitioning of alkanols between water and oil as described by the partitioning coefficient changes, as well as the free energy of transfer from the oil to the water phase. Figure 6.1 shows the partitioning coefficient derived from the Ostwald solubility (A) and the free energy of transfer (B) for several 1-alkanols in the hexadecane/water system, which is exemplary of a true hydrophobic liquid in contact with water (used, for example, to estimate the activity of pharmaceuticals²⁵⁴). Here, the partitioning coefficient is the ratio of the concentration of 1-alkanols in hexadecane to that in water at equilibrium. It can be seen that 1-propanol, 1-butanol, and 1-pentanol are more soluble in water than in oil, while for 1-hexanol, 1-heptanol, 1-octanol, and 1-decanol the reverse applies. The free energy of transfer from water to hexadecane shows a similar trend, but here only 1-propanol has a positive free energy of transfer to the oil phase. This difference is possibly due to the lower molar concentration of hexadecane relative to that of water. At the same concentration where the partitioning coefficient equals 1, the mole fraction of alkanols in hexadecane ($\{x_{\text{oil}}\}$) is larger than that in water ($\{x_{\text{water}}\}$). This leads to a negative free energy of transfer since $\Delta G = -RT \ln \frac{\{x_{\text{oil}}\}}{\{x_{\text{water}}\}}$, in which R is the gas constant and T is the temperature. How the transition from oil to water occurs on the molecular level, whether this transition requires a particular structure of the alkanol, the water or the oil, and whether it depends critically on chain length is not conveyed by the data in Fig. 6.1.

Molecular level information about the electronic order present in the inter-

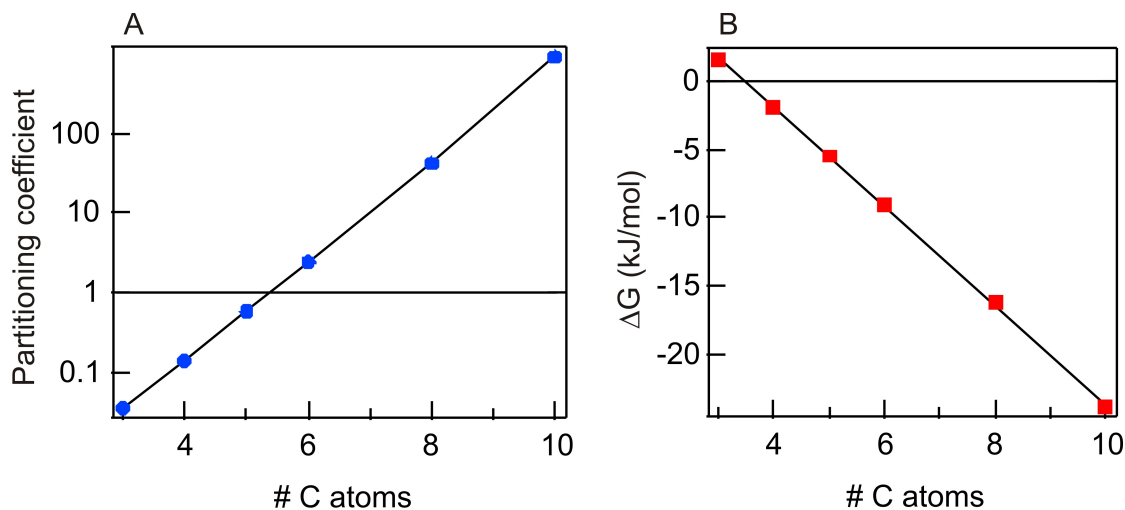


Figure 6.1 – Thermodynamic data of solute transfer. (A) Partitioning coefficient of several 1-alkanols with chain lengths from C₃-C₁₀, derived by dividing the Ostwald solubilities of the respective 1-alkanol in hexadecane by that of water. (B) Free energies of transfer from water to hexadecane. The data was adapted from Ref. ²⁵⁴.

facial layer can be obtained from X-ray reflection measurements in combination with appropriate modeling of ordered monolayers of alkanols on water (see, for example, Refs. ^{255,256}). Molecular level insight combined with intrinsic interfacial sensitivity can also be obtained by means of SFG, a vibrational coherent interface spectroscopy that measures the combined IR and Raman spectrum of molecules in non-centrosymmetric environments such as interfaces.^{126,138,257} The majority of the vibrational SFG studies have been performed on the air/alkanol interface with a focus on the alkyl chain conformation^{51,52}, and on the water/alkanol/air interface^{53–55} with a focus on both the alkyl chain conformation and the effects of hydration^{56,57}. The choice of these systems is likely determined by the experimental geometry, which permits unhindered access to the interface. Studies of the liquid/liquid oil/water interface are more challenging for several reasons: The optical beams need to pass through one of the often absorptive phases,²⁵⁸ the formation of a planar oil/water interface is non-trivial, and it often consists of a heterogeneous structure²⁵⁹ made up of nano- and micro-scopic islands, which are critically influenced by the tiniest amount of intrinsic impurities that might be present.²⁶⁰ Therefore, the focus is often on one aspect, namely the water structure^{261–264} or the alkyl chain conformation²⁵⁸. The latter can be probed by measuring SFG spectra in the C-H stretch region. The amplitude ratio (referred to as d^+/r^+ ratio) of the symmetric methylene (d^+ at ~ 2850 cm⁻¹) and the symmetric methyl (r^+ at ~ 2876 cm⁻¹) stretch modes is a common empirical indicator for the conformation of alkyl chains.^{119,265,266} A value of $d^+/r^+ \ll 1$ is

associated with a stretched all-trans chain conformation, whereas a value of $d^+/r^+ > 1$ indicates that gauche defects dominate the measured SFG spectrum. Using selective deuteration it is possible to independently probe the surfactant and the oil molecules since C-D and C-H modes vibrate at different frequencies.²⁶⁶

In order to obtain full molecular level insight into the molecular structural aspects of the transition from a hydrophobic to an aqueous phase without being hindered by the above restrictions, we use a dispersion of ~ 100 nm (radius) hexadecane droplets in water that also contains 1-pentanol, 1-hexanol, 1-octanol, or 1-dodecanol. We study the transition from the hydrophobic to aqueous phase and the role of hydrophobic interactions by determining the alkyl chain conformation of the alkanols and the oil, the surface density of the alkanols, and the structural changes imposed on the water using a combination of SHS^{82,99,100} and SFS^{82,135}. Second harmonic²⁰⁷ scattering^{99,102,107,154} is a process that occurs only in non-centrosymmetric materials. The SHS signal can be used as a probe for the interfacial water around nanoscopic droplets and reports on the difference in dynamic orientational directionality of the water molecules in the interfacial region compared to the orientational directionality in the bulk solution.^{103,207,267,268} At the same time, the SFS signal can be used to probe the chemical composition, alkyl chain conformation, and density of molecules at the droplet/water interface.^{82,137,143} Using selective deuteration and probing the C-H stretch mode region we have measured the conformation of the alkyl chains present on the 1-pentanol, 1-hexanol, 1-octanol, and 1-dodecanol/ d_{34} -hexadecane interface and the d_{11} -1-pentanol, d_{13} -1-hexanol, d_{17} -1-octanol, and d_{25} -1-dodecanol/hexadecane interface. Starting with the hexadecane/1-dodecanol/water interface, we find that the relative chain conformation represents that of a fluid layer with a wide distribution of tilt angles of the terminal CH_3 groups. Changing the chain lengths of the alkanol, the alkanol alkyl chains adopt a conformation that generates indistinguishable SF spectra. Comparing the amplitude of the spectra it appears that the alkanols with chain lengths longer than 6 carbon (C) atoms all form films with comparable chain densities. In contrast, the alkyl chains of the oil phase are relatively more distorted with respect to the pure oil/water interface for shorter alkanol alkyl chains. For 1-hexanol, we determined the surface density more accurately by means of an adsorption isotherm measured with SFS. We found a projected surface density of $29 \pm 5 \text{ \AA}^2$ and a free energy of adsorption of $\Delta G = -26.3 \pm 0.7 \text{ kJ/mol}$. SHS measurements of the same system show that with increasing 1-hexanol density the interfacial water structure loses its initial orientational alignment in a way that matches with the added number of interfacial 1-hexanol molecules. The found conformations differ significantly from that reported at the planar alkanol/water and alkanol/air interfaces.

In what follows, we will first present and analyze SFS spectra of the hexadecane/1-dodecanol/water interface. Then we will change the chain length and investigate the isotherm of 1-hexanol. Finally, we will turn to the water structure and discuss our findings in a broader scope.

6.2 Materials and Methods

6.2.1 Sample preparation

Hexadecane ($C_{16}H_{34}$, 99.8%, Sigma-Aldrich), d_{34} -hexadecane ($C_{16}D_{34}$, 98% d, Cambridge Isotope), 1-pentanol ($CH_3(CH_2)_4OH$, 99%, Acros), 1-pentan- d_{11} -ol ($CD_3(CD_2)_4OH$, 98% d, Sigma-Aldrich), 1-hexanol ($CH_3(CH_2)_5OH$, 99.5%, Sigma-Aldrich), 1-hexan- d_{13} -ol ($CD_3(CD_2)_5OH$, 98% d, Sigma-Aldrich), 1-octanol ($CH_3(CH_2)_7OH$, 99%, Sigma-Aldrich), 1-octan- d_{17} -ol ($CD_3(CD_2)_7OH$, 98% d, Sigma-Aldrich), 1-dodecanol ($CH_3(CH_2)_{11}OH$, 98%, Sigma-Aldrich), and 1-dodecan- d_{25} -ol ($CD_3(CD_2)_{11}OH$, 98% d, Sigma-Aldrich) were used as received. All aqueous solutions were made with ultrapure water (H_2O , Milli-Q UF plus, Millipore, Inc., electrical resistance of 18.2 megohm·cm; D_2O 99.8% Armar, > 2 megohm·cm). Glassware was cleaned with a 3:1 mixture of concentrated sulfuric acid (95-98%, Sigma Aldrich) and hydrogen peroxide solution (30%, Reactolab SA), after which it was thoroughly rinsed with ultrapure water (H_2O , Milli-Q UF plus, Millipore, Inc., electrical resistance of 18.2 megohm·cm).

Dispersions of oil nanodroplets in water were prepared with 1 vol % (Figs. 6.2, and 3) or 2 vol % (Fig. 6.8) of *n*-hexadecane or d_{34} -hexadecane in D_2O for SFS and in H_2O for SHS. The solutions were mixed with 5 mM alkanols for 4 min with a hand-held homogenizer (TH, OMNI International) and subsequently placed in an ultrasonic bath (35 kHz, 400 W, Bandelin) for the same duration. The resultant emulsions of alkanols except hexanol were directly used for SFS. An alkanol concentration of 5 mM was used in the study of the interfacial structures of alkanols and oil. The resultant stock emulsion of hexanol was diluted to an oil concentration of 1 vol % for SFS (0.1 vol % for SHS) with a solution of alkanol in water to yield the desired hexanol concentration. The size distribution and ζ -potential of the nanodroplets were measured with DLS and electrokinetic mobility measurements (Malvern ZS Nanosizer) as previously described. The nanodroplets were consistently found to have a mean hydrodynamic diameter in the range of 220-300 nm with a polydispersity index (PDI) of less than 0.3. All samples were stable for at least several weeks. All measurements were performed at 24 °C.

6.2.2 Second harmonic scattering measurements

SHS measurements were performed, as previously described in Sec. 3.2.2 and Ref.¹⁵⁴, using the experimental setup as described in Ch. 2. The input pulse energy at the sample was set 0.25 μJ (incident laser power $P_{\text{laser}} = 50 \text{ mW}$). The detection angle was set $\theta = 35^\circ$, where the SHS intensity from nanodroplets with radii of $\sim 100 \text{ nm}$ is maximum. The acceptance angle of the SHS signal was set 11.4° . Data points were acquired with $20 \times 1 \text{ s}$ acquisition time and a gate width of 10 ns. The plotted data points represent the SHS signal corrected for the background HRS and normalized by the PPP signal of neat water

$$\frac{I_{\text{SHS,emulsions,PPP}}(\theta = 35^\circ) - I_{\text{HRS,solutions,PPP}}(\theta = 35^\circ)}{I_{\text{HRS,water,PPP}}(\theta = 35^\circ)} \quad (6.1)$$

The reproducibility of the SHS measurements is in the range of 1-3%. Samples were stored and measured in sealed glass sample cells. All measurements were performed in a temperature- and humidity-controlled room ($T = 297 \text{ K}$; relative humidity, 26.0%).

6.2.3 Vibrational sum frequency scattering measurements

SFS spectra were measured using the experimental setup as previously described in Ch. 5 and Refs.^{47,269}. The SFS light was spectrally dispersed with a monochromator (Acton, SpectraPro 2300i) and detected with an I-CCD (Princeton Instruments, PI-Max3) using a gate width of 10 ns. The acquisition time for a single spectrum was 150 s. The SFG spectrum obtained in the reflection geometry from a z-cut quartz crystal was used to normalize all the SFS spectra of tested samples. Concentration series were measured against a reference sample that was inserted between every other measurement to detect and correct for possible fluctuations during the course of the experiment. The d^+/r^+ and r^+/r^- amplitude ratios were obtained from a global fitting applied to the SFS spectra in which the weak nonresonant background was taken into account by using a measured SFS signal from an all-deuterated sample. This was done because the nonresonant background varied per sample and polarization combination. More details can be found in Ref.²⁷⁰.

6.3 Results and discussion

6.3.1 Surface structure of 1-dodecanol

By deuterating hexadecane or 1-dodecanol, we can selectively probe the C-H stretch modes of interfacial 1-dodecanol or hexadecane molecules in the respective SFS measurements and thus deduce the interfacial molecular structures. Figure 6.2 shows SFS spectra of the C-H stretch modes of the 1-dodecanol/ d_{34} -hexadecane droplet interface (A) and the d_{25} -1-dodecanol/hexadecane droplet interface (B) in D_2O . The spectra were recorded in three different polarization combinations: SSP, PPP, and SPS. Here the three letter code represents the polarization of each beam from high frequency to low frequency, with P(S) referring to light polarized parallel (perpendicular) to the scattering plane. The spectra were fitted according to the procedure described in the Sec. 5.3.3.

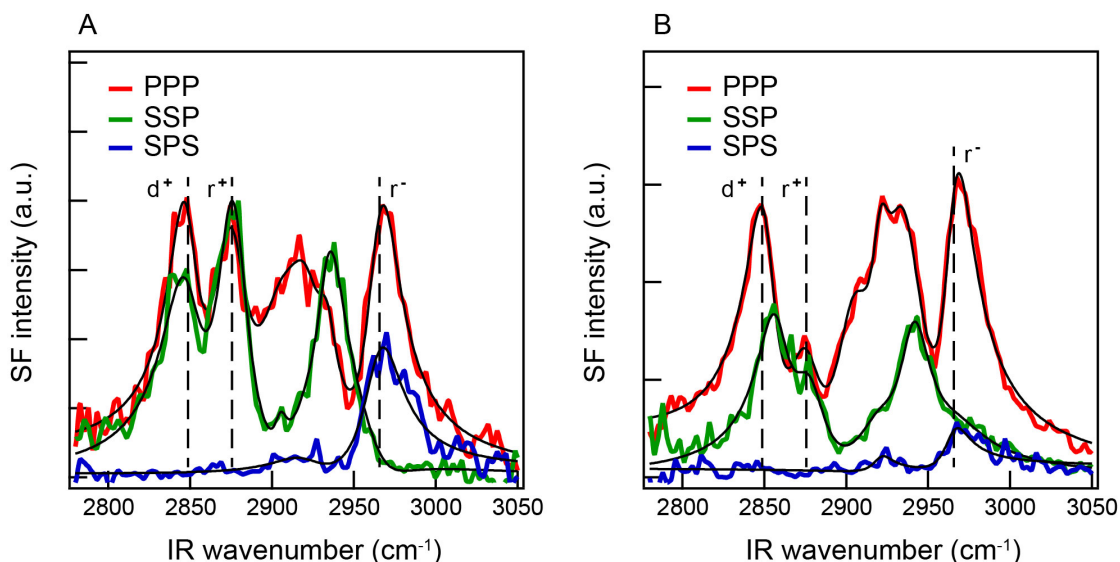


Figure 6.2 – The surface structure of 1-dodecanol and hexadecane at the hexadecane nanodroplet/water interface. SFS spectra of the C-H stretch modes of the 1-dodecanol/ d_{34} -hexadecane droplet interface (A) and the d_{25} -1-dodecanol/hexadecane droplet interface (B) in D_2O . The spectra are recorded in three different polarization combinations, PPP (red), SSP (green), and SPS (blue). The black lines are fits to the spectra.

Starting with the SSP spectrum of 1-dodecanol and hexadecane (green lines in Fig. 6.2), it can be seen that the following peaks are present:⁵² The symmetric (s) CH_2 stretch mode ($\sim 2850\text{ cm}^{-1}$, d^+), the s- CH_3 stretch mode ($\sim 2876\text{ cm}^{-1}$, r^+), the antisymmetric (as) CH_3 stretch mode ($\sim 2965\text{ cm}^{-1}$, r^-), the s- CH_2 -Fermi resonance ($\sim 2905\text{ cm}^{-1}$, d^+_{FR}), the s- CH_3 -Fermi resonance ($\sim 2933\text{ cm}^{-1}$, r^+_{FR}), and the as- CH_2

stretch mode ($\sim 2920 \text{ cm}^{-1}$, d^-). The latter three modes are broad and overlap.^{57,271} Fitted values to Eq. 5.24 can be found in Table 6.1. The obtained d^+/r^+ amplitude ratio for 1-dodecanol is 0.7 ± 0.2 , while that for hexadecane is 1.1 ± 0.2 . This shows that there are fewer visible gauche defects in the spectra of the alkyl chains of the 1-dodecanol than in the alkyl chains of the hexadecane.

mode	1-dodecanol					hexadecane				
	$\omega_i (\text{cm}^{-1})$	$\gamma_i (\text{cm}^{-1})$	SSP A_i	PPP A_i	SPS A_i	$\omega_i (\text{cm}^{-1})$	$\gamma_i (\text{cm}^{-1})$	SSP A_i	PPP A_i	SPS A_i
d^+	2848	13	1.2	1.1	0	2855	12	1.2	1.8	0
d_{FR}^+	2905	12	0.3	0.8	0	2905	15	0	1.4	0
d^-	2920	16	0.7	0.8	0.8	2920	12	0.7	0.8	0.3
r^+	2876	12	1.7	1.1	0	2877	14	0.9	1.2	0
r_{FR}^+	2933	9	1.2	0.4	0	2936	13	1.1	1.7	0
r^-	2965	16	-0.6	1.4	-1.6	2965	13	0.3	1.7	0.6
A_{NR}			0	0.2	0.3			0	0.3	0.5
φ_{NR}			0	274°	224°			0	84°	325°
d^+/r^+			0.7	1.0	-			1.3	1.5	-

Table 6.1 – Fitted frequency, amplitude, and linewidth of the 1-dodecanol and hexadecane spectra of the hexadecane nanodroplet/1-dodecanol/water interface (Fig. 6.2).

Comparing the three polarization combinations, we observe that the spectra are different. Specifically, it can be seen that the SSP spectra in Fig. 6.2 show less antisymmetric character and have a smaller relative d^+/r^+ ratio than the PPP spectra. The relative phase of the r^- mode is also different for the SSP and PPP polarization combinations. On the other hand, the SPS spectra display only the d^- and r^- mode. These differences are not a consequence of a different relative tilt angle of the alkyl chains with respect to the surface normal as it would be for SFG in the reflection geometry,⁶³ but are a consequence of the nonlinear light scattering geometry. Nonlinear light scattering theory predicts that for SFS each polarization combination has a different number of surface susceptibility elements that contribute to the SFS spectra with different weights (represented by form factor functions that are determined by scattering angle and droplet size¹³⁷). As a result, the PPP spectra are often the most intense ones because this polarization combination reports on all tensor elements of the surface susceptibility, which also appear with a larger magnitude.^{137,272} They are also subject to some weakly dispersive interaction from D_2O as we observed before.²⁷⁰ In contrast, here only the antisymmetric modes are visible in the SPS spectra, which is expected because SPS is the only polarization combination for which the $\beta_{aca}^{(2)}$ element of the hyperpolarizability tensor is dominant. A molecular tilt angle ϕ away from the surface

normal does reduce the overall intensity because SFS is only reporting on molecular groups that have some kind of preferential alignment along the surface normal of an isotropic surface (see Eq. 5.11 in Sec. 5.2.1, just like in reflection mode SFG). We found previously¹³⁷ that the r^- mode is sensitive to the tilt angle of the methyl group, while the r^+ mode is less sensitive, and the d^+ mode is not sensitive at all to the tilt angle. Thus, by calculating the different amplitude ratios¹³⁷ we can determine the average tilt angle ϕ of the terminal CH_3 group with respect to the droplet surface normal.

Orientation of terminal methyl groups

With its unique molecular symmetry and polarization selection rules, SFS is an effective tool for investigating the conformation of the interfacial alkyl chains. The molecular orientation of the terminal CH_3 groups can be retrieved by measuring the relative electrical field amplitudes of different vibrational modes of the same moiety.^{82,137} In the following, we will compare SFS amplitudes of different polarization combinations to determine the average tilt angle (ϕ) of the terminal CH_3 groups with respect to the droplet surface normal (i.e., the radial direction).

As previously described in Sec. 5.2.1, the relative amplitude of the SFS signal is seen to be determined only by the average tilt angle ϕ and molecular hyperpolarizability $\beta^{(2)}$ by combining Eqs. 5.7-5.11. For the vibrational modes of the CH_3 group, we use a bond polarizability derivative model²⁴⁶ from the single C-H bond polarizability derivative to calculate $\beta^{(2)}$. The single bond polarizability derivative ratio r can be obtained from the measured Raman depolarization ratio ρ . $\rho = 0.053$ and so $r = 0.026$ were obtained for the CH_3 group in ethanol and are used for 1-alkanols with longer chains. The corresponding hyperpolarizability ratio β_{aac}/β_{bbc} equals 3.4.²⁴⁶ To make the modeling more accurate, we employ a correction term to Eq. 5.9, which accounts for the small jump that the amplitude of the radial part of the electrical field experiences when it crosses the interface.²⁷³ The correction factor consists of multiplying the radial $\chi^{(2)}$ elements with n^2 , i.e. $\chi_{\parallel\parallel}^{(2)} \rightarrow n^2(\omega_{\text{IR}})\chi_{\parallel\parallel}^{(2)}$. Introducing such a factor generates a very good agreement with results from nonlinear Mie theory.⁹⁴ The values used for the refractive index are given in Table 6.2. All amplitude ratios were

	SF (650 nm)	VIS (800 nm)	IR (3450 nm)
hexadecane (Re, Im) ^{258,274}	(1.43, 0)	(1.43, 0)	(1.40, 0)
D ₂ O (Re, Im)	(1.32, 0) ²⁷⁵	(1.32, 0) ²⁷⁵	(1.23, 0.0023) ²⁷⁶

Table 6.2 – Refractive index elements used for the calculation of the SFS electrical field.

simulated for nanodroplets with a radius of $R = 115$ nm. A δ -function distribution was used for the tilt angle ϕ . The opening angle $\beta = 15^\circ$ and scattering angle $\theta = 57^\circ$ that were used in experiments were measured in air. When the beams travel through the cuvette, which is placed perpendicular to the outgoing scattered SF wavevector (see Fig. 5.1 and 5.5), these angles change. The opening angle β is reduced to 5° in D_2O and the scattering angle θ is also reduced to 35° . These values are then inserted in Equations 5.7-5.11. Figure 6.3 shows the computed SFS electrical field amplitude ratios for different tilt angles of the CH_3 group. The r^-/r^+ amplitude ratio of the SSP spectrum is plotted whereas the opposite amplitude ratio (r^+/r^-) is plotted for the other three polarization combinations. This is done to keep the ratio values in the same range for a clear comparison. Results of the simulations with (A) and without (B) the correction for the small jump in the amplitude of the radial part of the electrical field at the interface are both shown in Fig. 6.3. The difference between Figs. 6.3A and 6.3B shows the necessity of including the correction. Compared to other possible

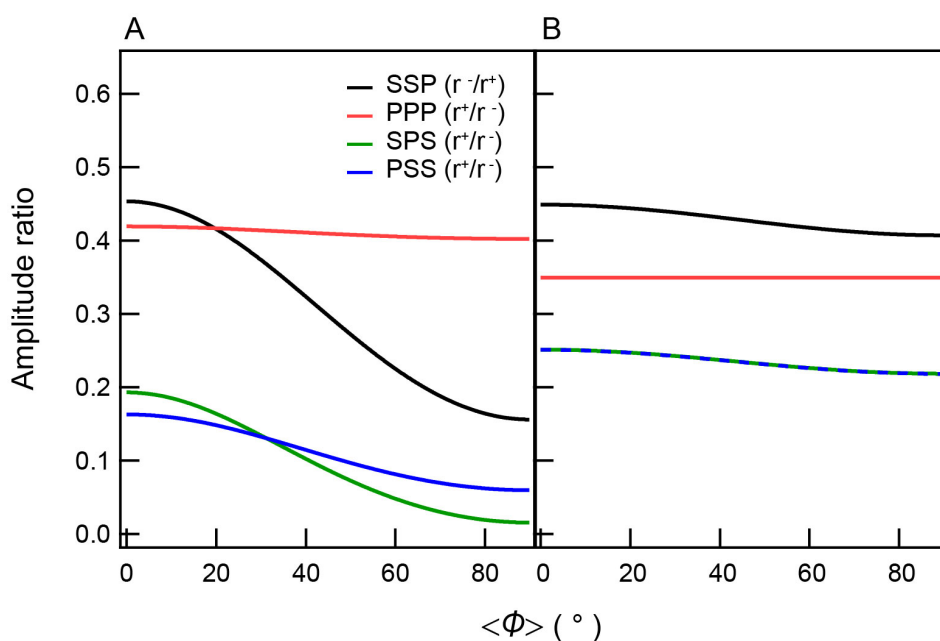


Figure 6.3 – Calculated SFS electrical field amplitude ratios. Equations 5.7-5.11 with the first order correction for the change in refractive index along the radial direction (A) and without this correction (B) were used for the calculation. All amplitude ratios were calculated using $R = 115$ nm, $\beta = 5^\circ$, $\theta = 35^\circ$ (values inside the cuvette). For simplicity and without bias to the result, a δ -function distribution of the tilt angle ϕ was used.

peak ratios, the r^+/r^- amplitude ratio of the SSP spectrum shows the highest sensitivity to the change of the tilt angle of the CH_3 group.

Figure 6.4 shows a computation of the r^+/r^- amplitude ratio as a function of ϕ assuming a hyperpolarizability ratio²⁴⁶ of 3.4 and a δ -distribution (blue line),

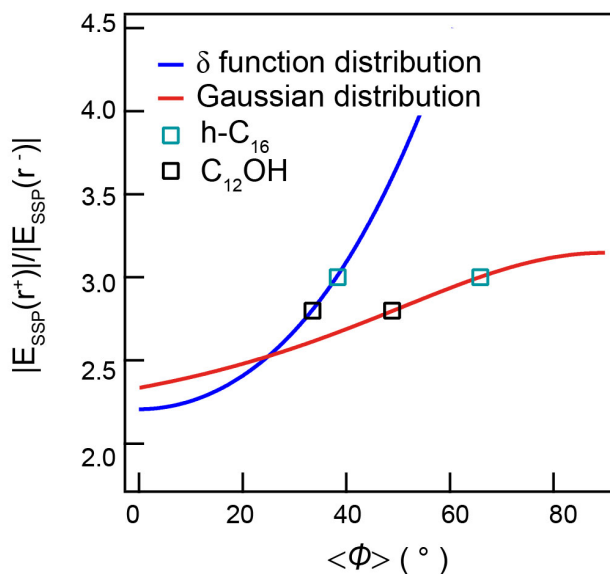


Figure 6.4 – Calculated r^+/r^- amplitude ratio as a function of the average tilt angle ϕ of the end methyl group of the alkyl chain with respect to the surface normal. The distribution of tilt angles is represented by both a δ -function and a Gaussian function (assuming an angular FWHM of 70°). For the hyperpolarizability ratio β_{aac}/β_{ccc} , we used the value 3.4.²⁴⁶ The average radius R of the nanodroplets is 115 nm (1 vol. %). For the opening (β) and scattering (θ) angle, we used $\beta = 5^\circ$ and $\theta = 35^\circ$ (which represent the values inside the cuvette), and appropriate refractive index values are given in Table 6.2.

as well as a broad Gaussian distribution (assuming an angular FWHM of 70°) of the tilt angles (red line). Both functions for the orientational distribution thus represent two extremes of a surface structure: a highly ordered one and a highly disordered one in terms of the tilt angle. The experimental values found for the r^+/r^- amplitude ratio from the fits in Fig. 6.2 are 2.8 for 1-dodecanol (C₁₂OH) and 3.0 for hexadecane (C₁₆). Comparing these values to the calculated lines, we find (assuming a δ -function) that $\phi_{C_{12}OH} = 33 \pm 5^\circ$ and $\phi_{C_{16}} = 38 \pm 5^\circ$. These values are both not far away from the values reported for a random distribution of tilt angles and do not necessarily report on an actual narrow tilt angle distribution.²⁷⁷ For the broad Gaussian distribution, we find $\phi_{C_{12}OH} = 49 \pm 17^\circ$ and $\phi_{C_{16}} = 66 \pm 17^\circ$. Because both tilt angle scenarios can describe the spectral data, it is likely that there is a broad distribution of tilt angles, as would be the case in a liquid phase. This agrees with the shape of spectra of Fig. 6.2, which are clearly not representative of a crystalline-like film (which would have a negligible amount of d^+ signal, as found for the 1-dodecanol/water interface⁵⁵). The d^+/r^+ ratios and the tilt angle analysis thus both indicate a broad distribution, which is in agreement with the interfacial layer being liquid-like. To further investigate the interaction of oil and alkanols, we vary the chain length of the alkanols and compare their alkyl structures as well as the oil chain structure using selective deuteration and

make a comparison to the pure oil droplet/water interface.

6.3.2 Chain length dependence

Figure 6.5A shows SFS spectra of the C-H stretch modes of different alkanols that are present at the interfaces of d_{34} -hexadecane droplets dispersed in D_2O with 1-dodecanol, 1-octanol, 1-hexanol, or 1-pentanol added to it. The spectra were recorded in the SSP polarization combination and normalized to the symmetric methyl stretch mode. Figure 6.5B shows the corresponding SF amplitudes, which were obtained by taking the square root of the integrated C-H spectra. The corresponding spectral changes for the hexadecane are shown in Fig. 6.6. These spectra were obtained by using deuterated alkanols and recorded in the PPP polarization combination. It can be seen that both the spectral shape and the intensity change with respect to pure *n*-hexadecane droplets in pure water (black line).

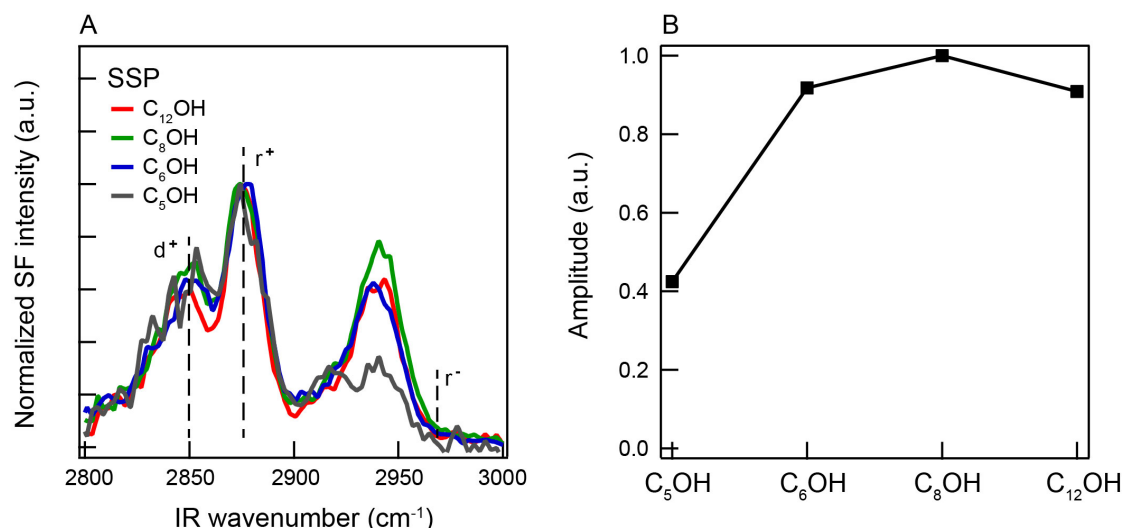


Figure 6.5 – The surface structure of alkanols of different lengths at the hexadecane nanodroplet/water interface. (A) Normalized spectra in SSP polarization for 1-pentanol, 1-hexanol, 1-octanol, and 1-dodecanol at the interface of d_{34} -hexadecane droplets in water (see the Materials and Methods for details on droplet size and concentrations). The spectra were normalized to the s-CH₃ stretch mode. (B) Spectral amplitude corresponding to the data in panel A.

Figure 6.5 shows that the spectral shape (A) and amplitude (B) for 1-hexanol, 1-octanol, and 1-dodecanol are not changing much. Both results combined suggest that the interfacial density of the three longest chain alkanols is constant and adding CH₂ pairs to the backbone of the alkyl chain does not contribute to the SFS signal. The spectrum of 1-pentanol has a reduced amplitude but an identical shape, which

indicates a reduced surface coverage. In theory, it could also indicate an identical surface density but with a molecular orientation that is more parallel to the interface. This explanation of the lower amplitude does not agree with the fact that 1-pentanol is the most hydrophilic of the alkanols studied here (see Fig. 6.1). We have also tried to measure the 1-butanol spectrum but we were not able to detect any SF signal in the C-H stretch region. This agrees with earlier studies^{103,278} that showed that at least 4 C atoms are needed to render a molecule hydrophobic and SFS visible.

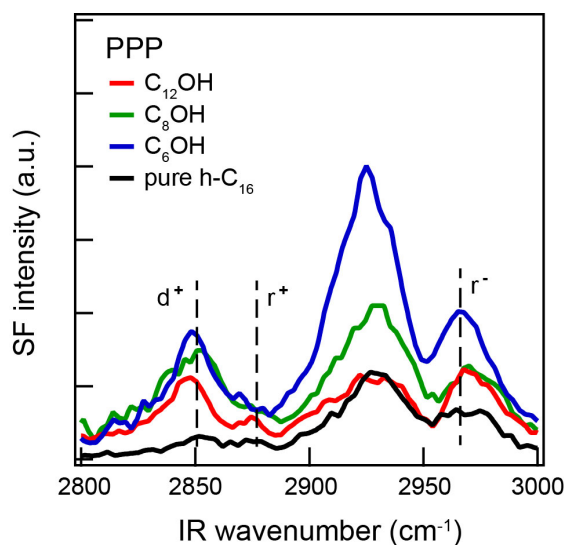


Figure 6.6 – The surface structure of hexadecane at the hexadecane nanodroplet/water interface with alkanols of different lengths. Hexadecane spectra for the same concentration of deuterated alkanols recorded in PPP polarization.

Figure 6.6 shows that in contrast to the alkanols, the hexadecane does have a different SF spectrum for each different interface. The spectrum of pure oil droplets in pure D₂O contains spectral features that match with alkane chains that are predominantly oriented along the interfacial plane and not with alkane chains that are perpendicularly oriented.^{270,272} MD simulations point to a similar conclusion.²⁷⁹ We see from Fig. 6.6 that the shorter alkanols lead to a bigger change in the oil structure: The overall intensity increases, the d⁺/r⁺ ratio becomes bigger and more antisymmetric stretch mode character is observed in the spectra (which is why we chose to plot the PPP polarization combination). Thus, it is likely that for a bigger mismatch in chain length more defects appear in the alkane chains, which results in a larger overall number of chain segments that are tilted toward the surface normal. That the 1-dodecanol covered hexadecane droplets differ less from the pure oil spectra than the 1-hexanol covered droplets indicates that the oil phase is shielded better by longer

chain alkanols than by shorter chain alkanols as expected. This implies that some part of the longer alkanol chains will have to follow the parallel structure of the oil chains.

6.3.3 Concentration dependence: Isotherm and water structure.

Having thus determined that the alkanols seem to form a liquid-like layer on the surface of the oil droplets and that they induce structural changes in the oil phase, we now turn to estimating the surface density in a more precise way. To this end, we use 1-hexanol, which is soluble in both water and hexadecane.

In order to determine the interfacial density of 1-hexanol, we collected SFS spectra of d_{34} -hexadecane droplets in water that were all prepared in the same emulsification procedure, and to which different amounts of aqueous 1-hexanol solution were added (following the procedure described in Sec. 6.2.1 and in Ref. ¹⁴³). Using this procedure, the droplet concentration and average radius remain constant.

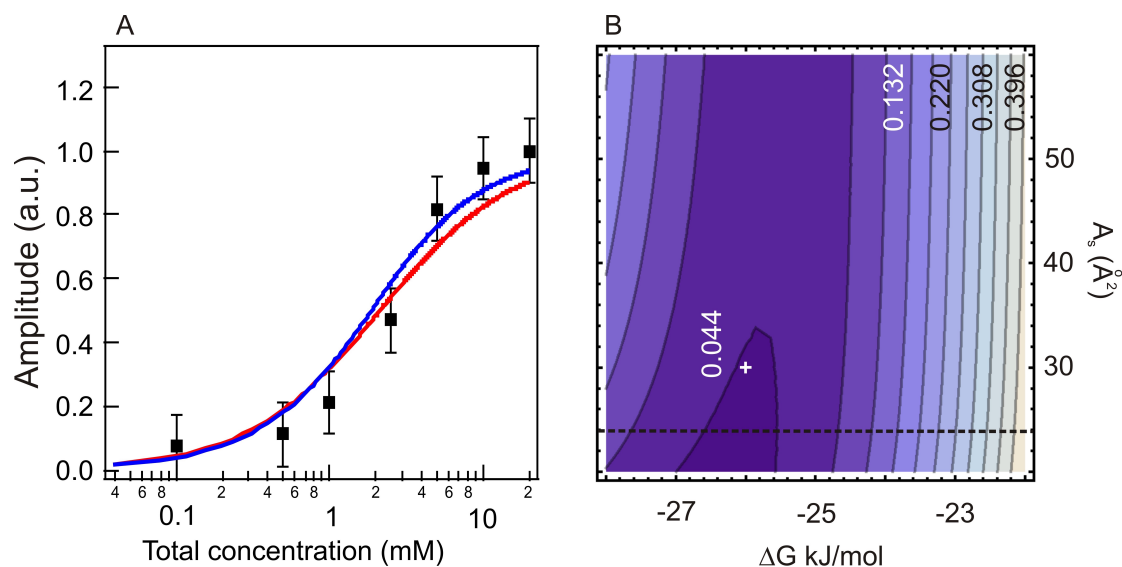


Figure 6.7 – Isotherm of hexanol. (A) Amplitude of the C-H stretch modes of 1-hexanol that is adsorbed at the surface of d_{34} -hexadecane droplets ($R = 163 \pm 24$ nm). The SFS spectra were recorded in the PPP polarization combination and with a scattering angle of $\theta = 57^\circ$ (measured in air). Two different fits are shown: a fit to the Langmuir equation (red) and a fit to the modified Langmuir equation (blue).²⁸⁰ The fit parameters are $\Delta G = -24.7$ kJ/mol (Langmuir model, red) and $\Delta G = -26.3$ kJ/mol; $R = 139$ nm; $A_s = 30 \text{ \AA}^2$ (modified Langmuir model, blue). (B) Contour plot of the squares of the difference between the modified Langmuir fit and the experiment data for $R = 139$ nm. The white plus sign indicates the parameters of the blue curve in (A). The dashed line indicates the limiting surface area based on the increase in SFS amplitude.

Figure 6.7 shows the amplitude of the total C-H stretch mode signal of 1-hexanol that is adsorbed at the surface of d_{34} -hexadecane droplets (black squares)

in water. The spectra from which these points are derived were recorded in the PPP polarization (as the relative error is the smallest) and they did not change much in spectral shape. Because of this, the SF amplitude can be considered proportional to the surface density of adsorbed molecules (N), which can be described using the Langmuir adsorption equation and Eisenthal's modified Langmuir equation.²⁸⁰ Taking the maximum achievable surface density as N_{\max} , we can then describe the amplitude as being proportional to the ratio N/N_{\max} . If the maximum surface site concentration is much smaller than the total concentration c of 1-hexanol, we can express the fraction of occupied adsorption sites as

$$\frac{N}{N_{\max}} = \frac{Kc}{c^{\ominus} + Kc} \quad \text{with} \quad K = e^{-\Delta G/R_g T}. \quad (6.2)$$

It should be noted that N and N_{\max} are given in the unit of mol/L here, which are to be interpreted as the equivalent bulk concentration of adsorbed molecules and the equivalent maximum achievable bulk concentration of adsorbed molecules, respectively, that is, N (N_{\max}) represents the (maximum) number of surface molecules divided by the total bulk volume of the sample.²⁸⁰ K is the equilibrium constant, R_g is the gas constant ($R_g = 8.31$ J/mol·K with a subscript g to distinguish it from the radius of the droplet R), T is the temperature in K, ΔG is the free energy of surface adsorption in kJ/mol, and c^{\ominus} is the molar concentration of water (55.5 mol/L). In this case, ΔG is the only fitting parameter. For the case that a significant number of 1-hexanol molecules are depleted from the solution, we can use Eisenthal's modified Langmuir model. This model is expected to be closer to reality since a 1 vol % solution of 163 nm radius droplets can accommodate ~1.5 mM of 1-hexanol on its surface, using a projected surface area per molecule of 20 \AA^2 , which is close to the projected area of an alkanol molecule in a packed alkanol layer ($18.7\text{-}21.0 \text{ \AA}^2$)²⁸¹. We then use

$$\frac{N}{N_{\max}} = \frac{1}{2N_{\max}} \left(c + N_{\max} + \frac{c^{\ominus}}{K} - \sqrt{\left(c + N_{\max} + \frac{c^{\ominus}}{K} \right)^2 - 4cN_{\max}} \right), \quad (6.3)$$

which uses the same parameters as Equation 6.2. For this case, N_{\max} and ΔG are both fitting parameters. N_{\max} can further be expressed as $N_{\max} = (3\phi V_{\text{tot}} 10^{-3}) / (RN_{\text{av}} A_s)$ where ϕ is the volume fraction of oil droplets, V_{tot} is the total volume of the emulsion, and R is the average (hydrodynamic) droplet radius. We used $R = 163 \pm 24$ nm, which was the range of values obtained from DLS measurements. In the fitting procedure, we let R free to vary between 139 and 187 nm. N_{av} is Avogadro's number ($6.02 \times 10^{23} \text{ mol}^{-1}$) and A_s is the projected minimum surface area per 1-hexanol molecule. Note

that for both models, it was assumed that the probability for adsorption or desorption energy is independent of the surface occupation or structure, that is, it was assumed to be an ideal gas. Figure 6.7A shows the obtained fits for both models. The fit values are $\Delta G = -24.7$ kJ/mol (Langmuir model, red curve) and $R = 139$ nm, $\Delta G = -26.3$ kJ/mol, and $A_s = 30$ Å² (modified Langmuir model, blue curve). Figure 6.7B shows a contour plot of the square of the difference between the modified Langmuir fit (using $R = 139$ nm) and the data points. The white plus sign indicates the parameters of the blue curve. It can be seen that there is a greater relative sensitivity to ΔG than to A_s . Nevertheless, the data does show that it is reasonable to expect that the projected area per 1-hexanol molecule is in the range of 20-34 Å², with ΔG values in the range of $-25.6 > \Delta G > -27.0$ kJ/mol. In addition, the range of A_s can be narrowed down by noting that the SFS amplitude (and hence the surface density) cannot exceed the maximum amount that could be present at the surface for the lowest concentration (i.e., all hexanol molecules present in the system) multiplied by the relative amplitude increase (13.6) in going from the lowest (100 μM) to the highest concentration (20 mM). For the experimental average of $R = 163$ nm, we arrive at a lower limit of 24 Å² for A_s , such that $A_s = 29 \pm 5$ Å². The projected areas agree qualitatively with the SFS spectrum of the alkyl chains of 1-hexanol, which shows a fairly ordered alkyl chain ($d^+/r^+ = 0.7$) that is also close to what is found with SFG studies on the planar interface of 1-hexanol liquid in contact with air,^{52,57} and temperature-dependent surface tension measurements on the 1-hexanol/hexadecane/water interface²⁸² that reported areas of 28-70 Å² per molecule with a ΔG value of -23.3 kJ/mol. In addition, the value found for ΔG is much larger than that found for the transfer of 1-hexanol from water to hexadecane which is -9.08 kJ/mol.²⁵⁴ Also, because the SF spectra for the alkanols are very similar in both shape and intensity based on Fig. 6.5, we can expect that the surface densities of 1-octanol and 1-dodecanol are comparable.

We thus see that the alkanols form liquid-like films at the hexadecane droplet interface that influence the oil structure. Shorter alkanol chains lead to bigger changes in the oil structure. Next, we determine if the water structure is also influenced by the alkanols. To investigate this, we used again 1-hexanol and probed the water structure with SHS.¹⁰⁴

6.3.4 Interfacial water alignment

The interfacial water around nanoscopic droplets can be measured with SHS, a process that occurs only in noncentrosymmetric materials. As shown by Eisenthal and co-workers,²⁰⁷ the SH signal reports on the difference in dynamic orientational direc-

tionality of the water molecules in the interfacial region compared to the orientational directionality in the bulk solution.^{103,207,267,268} The reason for this is that for a nonresonant SHS process the SH intensity depends quadratically on the number density of each component that is both dipolar and present in the noncentrosymmetric interfacial region. Because water has the largest hyperpolarizability (which also contributes quadratically) and because it greatly outnumbers the other species, the SHS signal reports primarily on the water orientation. Here, the change in directionality is induced only by interactions between the water and the 1-hexanol molecules. Charge effects on the water reordering can be excluded because the adsorbed 1-hexanol molecules are neutral and the ζ -potential of the droplets is verified to be constant. For a discussion about the origin of the large electrokinetic mobility and our explanation as originating from charge transfer effects in water, we refer to Ref.²⁷³. Figure 6.8A displays the SHS intensity obtained at a scattering angle (θ) of 35° using the PPP polarization combination (i.e., all beams are polarized in the horizontal scattering plane), and around the angle of maximum intensity¹⁸⁸ for emulsions containing different concentrations of 1-hexanol. The above derived projected average surface area for each hexanol molecule is plotted on the top axis. The measured intensity was corrected for HRS from the same solution without droplets and then divided by the HRS intensity in the PPP polarization of pure water for normalization purposes (following Ref.¹⁰⁶).

It can be seen that the interfacial SHS intensity of hexadecane droplets in water is approximately three times of the value of the SHS signal from pure water. That means that in absence of 1-hexanol orientational directionality of water is increased by the presence of oil droplets. This oriented water has a small majority of H atoms pointing toward the surface.^{264,283} Upon adding 1-hexanol to the emulsion, a reduction of the directionality of water along the surface normal is observed. This reduction can be explained by the additional H-bonding interaction that occurs between the hydroxyl group of the added hexanol molecule and the water. The $-\text{CH}_2\text{OH}$ group is sticking into the water phase and only H-bonds with a water molecule that has its O atom pointing toward the interfacial plane (see Fig. 6.8B; note that this illustration purely serves to highlight the changing directionality of H-bonding). When the concentration is increased and more 1-hexanol molecules are present at the interface, a larger number of water molecules will be reoriented, which means that the net orientational directionality of water molecules will be reduced, thereby decreasing the SHS signal. Because one 1-hexanol molecule forms only one H-bond, there should be a linear relationship between the number of 1-hexanol molecules that are present at the interface and the reduction in the number of water molecules that contribute to the

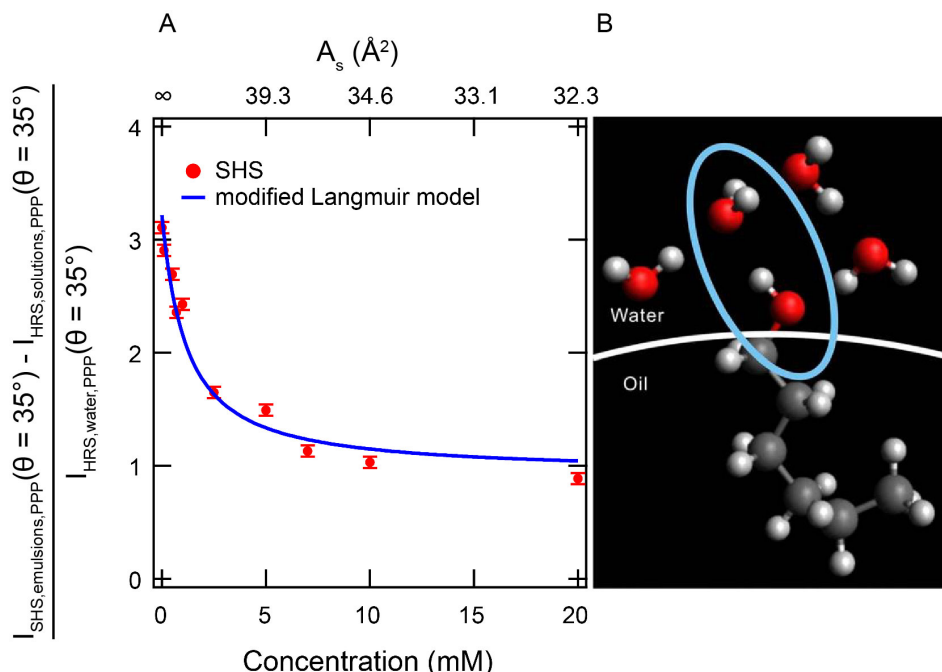


Figure 6.8 – Water alignment at the hexadecane/hexanol/water interface. (A) SHS intensities for hexadecane droplets in water prepared with different amounts of 1-hexanol. The PPP intensity was measured at the maximum scattering angle ($\theta = 35^\circ$), corrected for HRS and normalized by the PPP signal of pure water. It can be seen that relative to a pure oil droplet/water interface the orientational directionality of water is reduced when more 1-hexanol is present at the interface. The blue line represents a fit to the function $(A - B(N/N_{\text{max}}))^2$ with $A = 1.79$ and $B = 0.83$. The values used for (N/N_{max}) originate from the fit of the data in Fig. 6.7A. (B) Illustration of the effect of the hexanol hydroxyl group on the interfacial water structure. The ζ -potential of all droplets is the same, -60 ± 6 mV.

SHS signal. If this is the case, we can use the outcome of the modified Langmuir model fitting of the SFS data in Fig. 6.7A to fit the data in Fig. 6.8. N/N_{max} should also represent the number of water molecules that have been reoriented by H-bonding. The SHS intensity should then be described by a function of the form $(A - B(N/N_{\text{max}}))^2$, which, as can be seen from Fig. 6.8A, is indeed the case. The parameters A and B have no physical meaning other than to represent the geometry of the experiment. Thus, the SHS measurement of water and the SFS measurement of 1-hexanol are in good agreement with each other.

6.3.5 Full picture of the interfacial structure

Here we will first discuss the interfacial structure of the hexadecane/alkanol/water interface and then make a comparison to the planar alkanol/air and water/alkanol/air interfaces. The alkanols studied in the oil droplet/water system form a transition

layer between a relatively ordered structure on the water side of the interface, which is determined by the H-bonding network of water that allows only certain configurations of the -OH groups to a relatively ordered structure of mostly parallel oriented oil molecules, as present at the pure hexadecane/water interface.^{270,272,279} The longer chain 1-dodecanol forms liquid-like films with a fairly high degree of chain order that is visible in the SFS spectra ($d^+/r^+ < 1$). Shortening the alkyl chain length, we observed that the SFS spectra for C₆-C₁₂ are identical in shape and amplitude. Thus, the surface density for C₆-C₁₂ is comparable. In contrast, 1-pentanol is much less surface active and 1-butanol was not detected in the SFS experiments. We also observed that the hexadecane alkyl chains are strongly influenced by the alkanol monolayer. The oil alkyl chains appear to intercalate with the alkanol alkyl chains, as their SF spectra change when alkanols are added to the interfacial region and they become more distorted in their conformation by shorter alkanols than by the longer ones. SFS measurements and subsequent fitting with the modified Langmuir model on a concentration series of 1-hexanol show that 1-hexanol films with a projected molecular area of $29 \pm 5 \text{ \AA}^2$ are formed. The corresponding free energy of adsorption is in the range of $-25.7 > \Delta G > -27.0 \text{ kJ/mol}$. SHS measurements that report on the directionality of interfacial water show that the interfacial water restructures as well, whereby it is seen that the orientational directionality of the interfacial water is reduced. The reduction of SHS signal is proportional to the formation of one H-bond per 1-hexanol molecule.

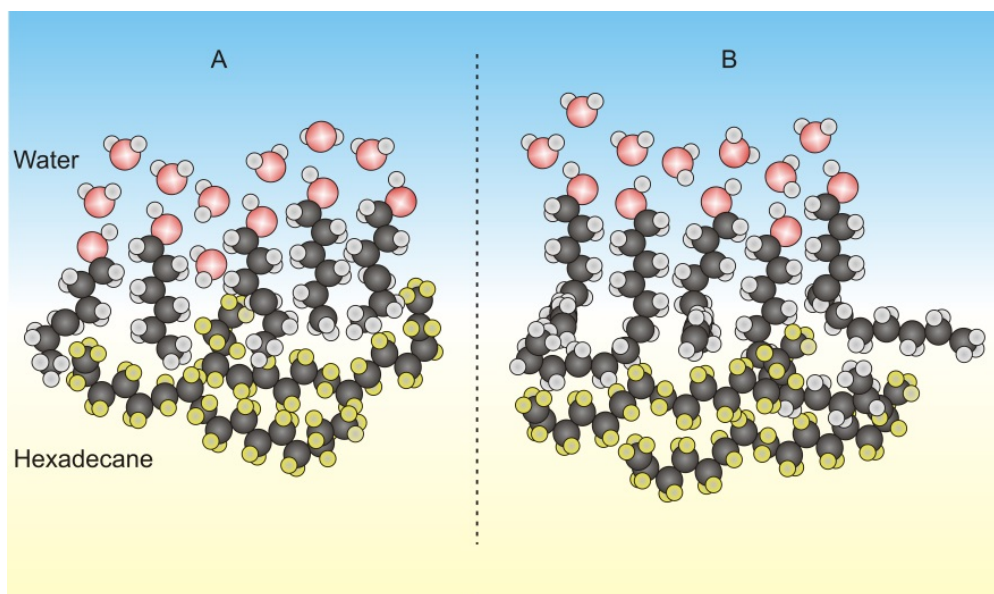


Figure 6.9 – Illustration of possible surface structures of 1-hexanol (A) and 1-dodecanol (B) at the hexadecane droplet/water interface.

Starting at the water side, the H-bonding network and the high chain density

result in a large degree of order between the C_nOH groups. Moving toward the oil phase the chance of forming a gauche defect increases.⁵⁷ For 1-dodecanol, we see that the distribution of orientational angles of the terminal CH_3 group with respect to the interfacial normal is broad and close to a random distribution. For 1-dodecanol, the oil is also minimally perturbed compared to the other shorter chain alkanols. This behavior can be explained by a structure that consists of alkyl chains of 1-dodecanol molecules that bend from a nearly perpendicular orientation (imposed by the water) into one that is more parallel (imposed by the oil), following the structure of the oil surface. The shorter alkyl chains will do the same thing on the water side but are not long enough to make a smooth transition to the more parallel oriented alkyl chain orientation of the oil phase. Aided by thermal fluctuations, they will perturb the oil phase more (as seen in Fig. 6.6). If the chains would not bend toward the interface but form structures of more perpendicularly oriented chains, we would not expect the result of Figs. 6.5 and 6.6. Namely, unbent alkanols would distort the oil molecules independent of chain length and would also have different d^+/r^+ ratios.²⁶⁵ Figure 6.9 shows an illustration of possible structures that agree with the above considerations. To arrive at this particular illustration, we have taken into consideration that the end methyl groups are most likely SF visible as they are thermally free to adopt any conformations (which is clear from the analysis in Fig. 6.4). For the methylene groups, we consider that only the CH_2 groups that are neither even in number nor oriented parallel to the interface are SF active.

6.3.6 A comparison to the alkanol/water and alkanol/air interfaces

The water/dodecanol/air interface^{51,53–56} is characterized by alkyl chains with very few gauche-trans defects (reporting a d^+/r^+ ratio for 1-dodecanol of < 0.1 for the solid phase and 0.3 for the liquid phase) and an almost perpendicular chain orientation with respect to the interface. Here, the layer consists of a relatively tightly packed structure of alkyl chains with projected areas of 21.5 \AA^2 per molecule in the solid phase (below $38.5 \text{ }^\circ\text{C}$) and 23.8 \AA^2 (Ref.⁵⁵, ellipsometry and SFG) or 25 \AA^2 (XRD, Ref.²⁵⁶) for the liquid phase. The difference with the oil/water interface is the absence of a hydrophobic condensed phase that participates in dispersive interactions. In absence of a liquid oil phase, the dispersive attraction between the alkyl chains results in a more tightly packed layer.

SFG measurements in reflection mode from the C_1OH - C_8OH /air interface showed that the alkanol alkyl chains have as well a preferential orientation toward the air^{52,57} but with a very broad orientational distribution, and a larger amount of gauche-

trans disorder that increases with the chain length. For the 1-hexanol/air interface, the reported d^+/r^+ ratio is approximately ~ 0.6 and for 1-octanol it is approximately 0.9. In this case, the H-bonding interaction is different (namely, between the alkanols only), which likely results in a different packing and thus different chain conformations.

The planar hexadecane/1-hexanol/water interface was studied with temperature-dependent surface tension measurements.²⁸² Fits with various models reported on a projected surface area of $28\text{--}70 \text{ \AA}^2$. Anomalies in the temperature dependence of the surface tension and the relative insensitivity of Gibbs free energies on chain length were attributed to hexanol induced structural rearrangement of the water at the interface.

Alkanols with longer chain lengths ($C_{20}\text{--}C_{30}$) were studied with X-ray diffraction at the hexane/water interface. A typical projected surface area of 23 \AA^2 was retrieved for these liquid-like layers. It was also found that disorder increases from the headgroup downward and that for every five alkanol chains there is one intercalating hexane molecule. In addition, there is also some water on the top of the surface layer.²⁸¹

Comparing our data to the above studies, we see that there is a qualitative agreement: The changes in the water structure corroborate the anomalies in the temperature-dependent surface tension measurements, the projected surface areas and free energy of adsorption are in the same range as the reported XRD and surface tension measurements, and the amount of alkyl chain disorder (as empirically reported on by the d^+/r^+ ratios) is in between that of liquid alkanols and “solid” alkanols at the air/water interface. These differences are probably caused by the presence/absence of oil and water that provide constraints on the possible geometries that can be adopted by the alkanols. Compared to hexadecane droplets dispersed in water and covered with charged surfactants of dodecyl trimethylammonium bromide (DTAB) and sodium dodecyl sulfate (SDS),¹⁰⁴ we find that there are clear differences in surface density (which is much higher in the case of the neutral alkanols) and surface oil and surface water structure. While all surfactants studied change the water structure, they do so differently. The same is true for the oil phase. Thus, by spectroscopically measuring the oil, the surfactant, and the water on these nanoscopic droplets we see that the specific chemical interactions are highly relevant to the interfacial properties rather than just the concept of geometrical packing.

6.4 Conclusions

We have obtained molecular level insight into the molecular structural aspects of the transition from a hydrophobic to an aqueous phase, using a dispersion of ~100 nm hexadecane droplets in water that also contains 1-pentanol, 1-hexanol, 1-octanol, or 1-dodecanol. We examined the alkyl chain conformation of the alkanols and the oil, the surface density of the alkanols and the structural changes imposed on the water using a combination of second harmonic and sum frequency scattering. The hexadecane/1-dodecanol/water interface has a chain conformation that represents that of a fluid layer with a wide distribution of tilt angles of the terminal CH₃ groups. Changing the chain length of the alkanol, the alkanol alkyl chains adopt a conformation that generates indistinguishable SF spectra for pentanol to dodecanol, whereby the alkanols with chain length longer than 6 C atoms all form films with comparable chain densities. In contrast, the alkyl chains of the oil phase are relatively more distorted with respect to the pure oil/water interface as the alkyl chain length of the alkanol decreases. The surface density was determined more accurately by means of an SFS isotherm of 1-hexanol, which generated a projected surface density of $29 \pm 5 \text{ \AA}^2$ and a free energy of adsorption of $\Delta G = -26.3 \pm 0.7 \text{ kJ/mol}$. With increasing 1-hexanol density the interfacial water structure loses its initial orientational alignment in a way that matches with the added number of interfacial 1-hexanol molecules. The found conformations differ significantly from that reported on the alkanol/water and alkanol/air interface, which can be explained by the balance between dispersive and H-bonding interactions.

7 Three Dimensional Nano “Langmuir Trough” for Lipid Studies

A three-dimensional-phospholipid monolayer with tunable molecular structure was created at the surface of oil nanodroplets from a mixture of phospholipids, oil, and water. This simple nanoemulsion preparation technique generates an in-situ prepared membrane model system with controllable molecular surface properties that resembles a lipid droplet. The molecular interfacial structure of such a nanoscopic system composed of hexadecane, 1,2-dipalmitoyl-*sn*-glycero-3-phosphocholine (DPPC), and water was determined using vibrational sum frequency scattering and second harmonic scattering techniques. The droplet surface structure of DPPC can be tuned from a tightly packed liquid condensed phase like monolayer to a more dilute one that resembles the liquid condensed/liquid expanded coexistence phase by varying the DPPC/oil/water ratio. The tunability of the chemical structure, the high surface-to-volume ratio, and the small sample volume make this system an ideal model membrane for biochemical research.

7.1 Introduction

Lipid membranes are one of the most fundamental structures in biological systems. They provide the essential barrier between the intra- and extra-cellular domains, form an essential environment for receptors, proteins, and peptides, and conduct charge.⁴³ Crucial membrane properties such as fluidity, heterogeneity, alkyl chain, and head-group structure, as well as the influence of water and electrolytes on lipid membranes can be inferred from molecular level studies using, for example, sum frequency generation,^{59,130,284–295} X-ray diffraction,^{296–300} neutron reflectivity,^{301–303} fluorescence microscopy,^{304,305} and pressure-area isotherms^{306,307} in combination with molecular dynamics simulations.^{308–315} Phospholipid Langmuir monolayers at the air/water or substrate/water interface have been widely used as a model system in these studies, and it has been proven to be an invaluable tool for the understanding of molecular level interactions that underlie the properties of the monolayer. However, the absence of a liquid hydrophobic phase that is always present in a bilayer membrane might influence the applicability of the results to real membranes. In addition, several important membrane constituents (e.g., unsaturated phospholipids, cholesterol) oxidize in air.⁵⁹ Furthermore, a typical monolayer experiment in a Langmuir trough requires a sizable volume of water (typically > 18 mL) and being a single monolayer in nature only produces a tiny surface-to-volume ratio. This means that fundamental issues with impurities and heterogeneities can arise easily and that for membrane-protein interactions relatively large quantities of rare compounds are needed.^{259,260,285} A system that mimics the structure of a lipid droplet, that is, a solution of nanoscopic liquid hydrophobic droplets that are covered by phospholipids in water,⁶⁰ would dramatically reduce these issues, because the interfacial layer can be prepared in situ by sonication in a small volume (< 1 mL), which would still have a large surface-to-volume ratio (6000 cm² for 2 vol % droplets with 100 nm radius in 1 mL).

In this chapter, we demonstrate the creation and characterization of three-dimensional (3D) DPPC monolayers at the hexadecane nanodroplet/water interface with a tunable molecular structure. We used DPPC in combination with hexadecane and water to facilitate a comparison to already characterized monolayer systems (DPPC Langmuir monolayers). Hexadecane is chosen as it has been successfully applied in the formation of black lipid membranes³¹⁶ and forms nanoemulsions that are stable for many months.¹⁴³ By mixing oil (hexadecane), water, and lipid in different ratios we create nanoemulsions.⁴⁴ The droplets have interfacial monolayers whose surface structure can be varied from a tightly packed layer that closely resembles the liquid condensed (LC) phase to a more dilute layer that resembles the liquid

condensed/liquid expanded (LC/LE) coexistence phase. Molecular level insight into the interfacial structure was achieved by using SFS and SHS. We utilized SFS to probe not only the surface composition of the oil and the lipid phase independently (by means of selective deuteration^{266,317,318}) but also to demonstrate tunable lipid packing densities, reminiscent of lipid monolayers made in a Langmuir trough. The alkyl chain conformations were determined empirically using the amplitude ratio (referred to as the d^+/r^+ ratio) of the symmetric methylene (d^+) and the symmetric methyl (r^+) stretch vibrational modes.^{119,265,266} A value of $d^+/r^+ \ll 1$ is associated with a stretched all-trans alkyl chain conformation, whereas a value of $d^+/r^+ > 1$ indicates that gauche defects dominate the measured vibrational spectrum. Furthermore, we determined the orientation of the lipid headgroups in the LC phase from the vibrational fingerprints of the phosphate group in the SFS spectrum. SHS,^{99,100} which reports on the difference in orientational directionality of the water molecules in the interfacial region compared to the orientational directionality in the bulk solution,¹⁰³ was used as a probe for the interfacial water around the nanoscopic droplets.¹⁰⁰

7.2 Creation of 3D lipid monolayers on oil nanodroplets

7.2.1 Materials

Hexadecane ($C_{16}H_{34}$, 99.8%, Sigma-Aldrich), d_{34} -hexadecane ($C_{16}D_{34}$, 98% d, Cambridge Isotope), 1,2-dipalmitoyl-*sn*-glycero-3-phosphocholine (DPPC, 99%, Avanti) and 1,2-dipalmitoyl- d_{62} -*sn*-glycero-3-phosphocholine-1,1,2,2- d_4 -N,N,N-trimethyl- d_9 (d_{75} -DPPC, 99%, Avanti) were used as received. All aqueous solutions were made with ultra-pure water (H_2O , Milli-Q UF plus, Millipore, Inc., electrical resistance of 18.2 megohm-cm; D_2O , 99.8%, Armar, > 2 megohm-cm). Glassware was cleaned with a 3:1 mixture of concentrated sulfuric acid (95-98%, Sigma Aldrich) and hydrogen peroxide solution (30%, Reactolab SA), after which it was thoroughly rinsed with ultrapure water (H_2O , Milli-Q UF plus, Millipore, Inc., electrical resistance of 18.2 megohm-cm).

7.2.2 3D monolayers on oil nanodroplets

3D monolayers on oil nanodroplets in water were prepared with 2 vol. % of hexadecane or d_{34} -hexadecane in D_2O (for SFS characterizations) or H_2O (for SHS characterizations). The solutions were mixed at a temperature of 45 °C (above the transition temperature of 41 °C for DPPC) with different amounts of DPPC powder using a hand-

held homogenizer (TH, OMNI International) for 4 minutes and an ultrasonic bath (35 kHz, 400 W, Bandelin) for the same duration. 3D lipid monolayers were created at the surface of the resultant oil nanodroplets. The size distribution and ζ -potential of the nanodroplets were measured with DLS and electrokinetic mobility measurements (ZS Nanosizer, Malvern). The nanodroplets had a mean hydrodynamic radius in the range of 75-260 nm with a PDI of less than 0.3. The hydrodynamic radii were calculated from the intensity autocorrelation function, using the optical properties of the liquids (hexadecane, d_{34} -hexadecane, H_2O and D_2O). The droplet dispersion was directly characterized with SFS measurements and was diluted to 0.1 vol. % of hexadecane with pure water for SHS characterizations. The data shown in Fig. 7.1A are taken from dispersions that have average hydrodynamic radii of 260, 230, 110, 75, and 90 nm for the systems containing 0.05, 0.1, 1, 5, and 10 mM of DPPC, respectively. Although the prepared nanoemulsions are stable for at least several months, all samples were freshly prepared before each measurement. The samples were stored and measured in sealed cuvettes. All characterization measurements were performed at 24 °C. The whole procedure from sample preparation to actual measurement took place in a time frame of no more than a few days.

7.3 Tunability of 3D lipid monolayers

DPPC monolayers at the air/water interface have a tunable surface packing density that can be varied from an LE phase that consists of disordered alkyl chains to an LC phase that consists of nearly perpendicularly oriented all-trans alkyl chains. This tunability is achieved by increasing the lateral surface pressure that results in an increase in the surface density of DPPC.^{284,285,288,291,319} A similar effect can be achieved in the nanodroplet system by simply varying the amount of DPPC in the solution.

Figure 7.1A shows SFS spectra of the C-H stretch modes for five different DPPC monolayers on d_{34} -hexadecane nanodroplets in D_2O that correspond to different amounts of DPPC that were added to the solution. The SSP spectra contain the following peaks:^{284,290,320,321} The symmetric (s)- CH_2 stretch mode ($\sim 2852\text{ cm}^{-1}$, d^+), the s- CH_3 stretch mode ($\sim 2876\text{ cm}^{-1}$, r^+), the antisymmetric (as) CH_3 stretch mode ($\sim 2965\text{ cm}^{-1}$, r^-), the s- CH_2 -Fermi resonance ($\sim 2919\text{ cm}^{-1}$, d_{FR}^+), the s- CH_3 -Fermi resonance ($\sim 2935\text{ cm}^{-1}$, r_{FR}^+), and the as- CH_2 stretch mode ($\sim 2905\text{ cm}^{-1}$, d^-). Table 7.1 shows values of the spectral parameters obtained from fittings following the procedure described in Sec. 5.3.3. Figure 7.1A shows that with increasing DPPC concentration the SFS amplitude of the d^+ mode decreases (and vanishes at 1 mM), while the amplitude

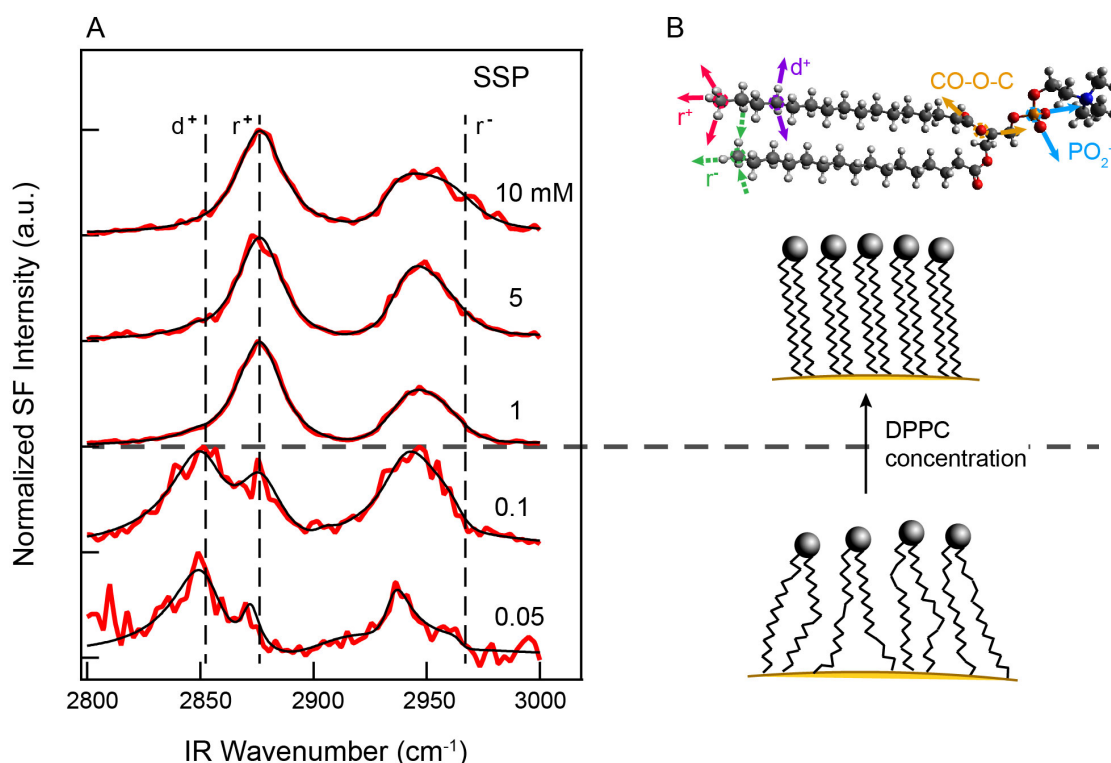


Figure 7.1 – The surface structure of DPPC at the hexadecane nanodroplet/water interface. (A) SFS spectra of DPPC monolayers on 2 vol. % d_{34} -hexadecane nanodroplets in D_2O taken for different DPPC bulk concentrations in the C-H stretch region. The SFS spectra were recorded in the SSP polarization combination. The spectral fits (black lines) were obtained using the procedure described in Sec. 5.3.3. (B) Molecular model of DPPC with arrows indicating the atomic motions that correspond to the probed vibrational modes, and an illustration of the conformational changes that occur when the concentration is changed.

of the r^+ mode increases. Correspondingly the d^+/r^+ ratio decreases from 2.0 ± 0.2 (for 0.05 mM) to ~ 0 (for > 1 mM). Thus, with more DPPC present in the system, it appears that the DPPC monolayer alkyl chains become more ordered with less gauche defects (as illustrated in Fig. 7.1B). Comparing this data to SFG spectra taken from DPPC at the air/water interface for different surface pressures,^{284,285} we see that the spectra in Fig. 7.1A are nearly identical. The 3D monolayers prepared at high concentration (> 1 mM, Fig. 7.1A) display no detectable gauche defects and are similar to the spectra of the LC phase.²⁸⁵ The lower concentration spectra (0.05 mM, 0.1 mM, Fig. 7.1A) are similar to the ones obtained for a mixture of the LC and LE phase, that is, a coexistence region in a planar two-dimensional Langmuir film.^{284,285,291} The surface structure of the 3D DPPC monolayer is thus tuned by varying the DPPC/oil/water ratio.

mode	C-H stretch modes						
	ω_i (cm ⁻¹)	γ_i (cm ⁻¹)	0.05 mM	0.1 mM	1 mM	5 mM	10 mM
			A_i	A_i	A_i	A_i	A_i
d ⁺	2852	12	0.84	0.71	0	0	0
d _{FR} ⁺	2905	8	0.20	0.08	0	0	0
d ⁻	2919	14	0.77	0.21	0	0.10	0.10
r ⁺	2876	11	0.41	0.59	1.00	1.08	1.41
r _{FR} ⁺	2937	14	0.47	0.71	0.66	0.82	0.45
r ⁻	2965	14	-0.13	-0.19	-0.35	-0.38	-0.42
A _{NR}			0	0	0.07	0.15	0.17
φ_{NR}			0	0	41°	48°	68°
d ⁺ /r ⁺			2.0	1.2	0	0	0

Table 7.1 – Fitted frequency, amplitude, and linewidth for the DPPC spectra in the C-H stretch region of the hexadecane nanodroplet/DPPC/water interface of Fig. 7.1.

7.4 Surface density and chain orientation of DPPC

As the spectra of Fig. 7.1A bear great resemblance to those observed for DPPC at the air/water interface, we can estimate the DPPC surface density on the oil droplets by comparing the d⁺/r⁺ amplitude ratios of the SFS spectra in Fig. 7.1A with those obtained for DPPC at the air/water interface²⁸⁵, for which a simultaneous lipid density measurement was performed. In doing so, we assumed here that the d⁺/r⁺ amplitude ratio is independent of chemical environment, which seems reasonable because the C-H stretch modes are localized vibrational modes. Figure 7.2A shows the d⁺/r⁺ amplitude ratio and projected area per molecule of a planar air/DPPC/water interface, where the black data points were adapted from Ref.²⁸⁵. The d⁺/r⁺ amplitude ratios of the 3D DPPC monolayers, obtained from the spectral fits to Fig. 7.1A (Table 7.1), are indicated by blue squares. The red curve represents a power law fit to the d⁺/r⁺ amplitude ratios as a function of projected surface area per DPPC molecule of the planar air/DPPC/water interface. By fitting the d⁺/r⁺ value of the 3D DPPC monolayer (Fig. 7.1A) onto this fit curve, we can obtain, as indicated by the corresponding value on the X-axis, a projected molecular surface area that a DPPC molecule occupies in the monolayer. For the DPPC monolayers that were prepared with a DPPC concentration > 1 mM, a projected molecular surface area of ~48 Å² was obtained. For the lower concentrations, bigger projected areas of 71 Å² (0.1 mM) and 78 Å² (0.05 mM) were

obtained.

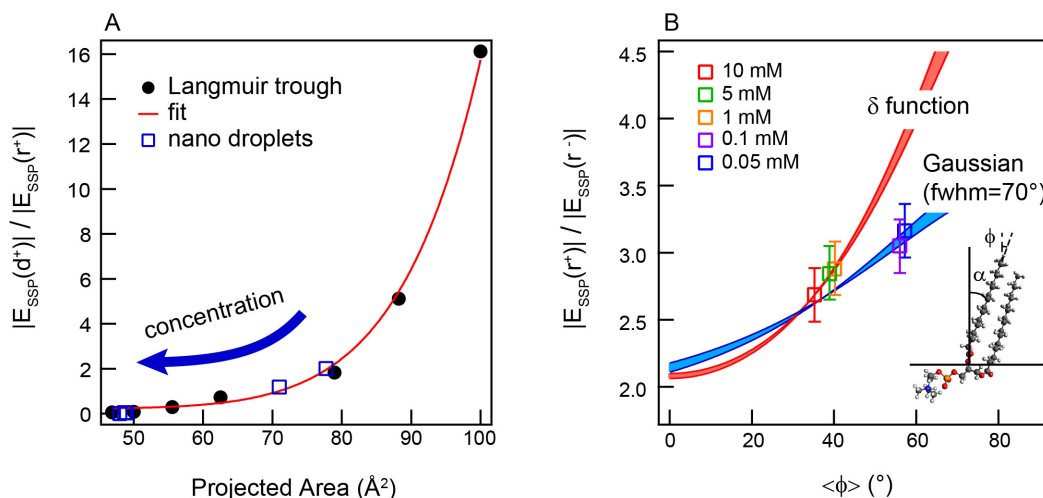


Figure 7.2 – Surface density and average tilt angle of the DPPC chains. (A) Comparison of the d^+/r^+ ratio and projected area per molecule between an air/DPPC/water planar interface (black data points were adapted from Ref.²⁸⁵) and a DPPC monolayer at an oil nanodroplet/water interface (blue squares, from fits to the spectra in Fig. 7.1A). The red line represents a power law fit to the data from the air/DPPC/water planar interface. The arrow indicates the direction of increasing DPPC concentration in the nanodroplet dispersion. (B) Regions of calculated amplitude ratios of the r^+ and r^- methyl stretch modes of the tail CH_3 groups of the 3D DPPC monolayers at the oil nanodroplet/water interface as a function of the average tilt angle $\langle\phi\rangle$ of the tail CH_3 groups with respect to the surface normal. Both a δ -function distribution (to represent an ordered DPPC monolayer, red area) and a Gaussian function (assuming an angular FWHM of 70° , to represent a disordered DPPC monolayer, blue area) were used. For the hyperpolarizability ratio β_{aac}/β_{ccc} , a value of 3.4 was used.²⁴⁶ Droplet radii that correspond to the average of the measured distribution (by DLS) were used in the computation. The open squares represent the d^+/r^+ values from fits of the SFS spectra in Fig. 7.1A.

The corresponding average tilt angles $\langle\alpha\rangle$ of the DPPC alkyl chains can be determined based on the order of the chains and the orientation of the tail CH_3 group.²⁸⁴ The average tilt angle $\langle\phi\rangle$ of the tail CH_3 group with respect to the droplet surface normal can be retrieved, following the same procedure described in Sec. 6.3.1, from the SSP amplitude ratio of the r^- and r^+ modes.^{110,137} Figure 7.2B shows a computation of the r^+/r^- amplitude ratio as a function of $\langle\phi\rangle$. Two different scenarios are considered in this figure. A δ -function distribution of tilt angles (red area) was employed to model a uniformly tilted monolayer, along with a Gaussian distribution with an FWHM of 70° (blue area) to model a more disordered monolayer. The open squares represent the data points obtained from the fits of the SFS spectra in Fig. 7.1A. The data points for the more ordered alkyl chains lie on top of the curves calculated for the δ -function distribution, which indicates that the alkyl chains are not only all-trans, but also oriented in a narrow range of tilt angles comparable to the structure of an LC monolayer. From the values of $|E(r^+)/|E(r^-)| = 2.9 \pm 0.2$ (1 mM), 2.8 ± 0.2

(5 mM), 2.7 ± 0.2 (10 mM), and the relation between the CH_3 and chain tilt angle²⁸⁴ of $\langle\alpha\rangle = |41.5^\circ - \langle\phi\rangle|$, we then found for $\langle\alpha\rangle$ values of $1.6 \pm 4^\circ$, $2.1 \pm 4^\circ$, and $6.2 \pm 4^\circ$, respectively. Because the values do not change much, it appears that an ordered layer is already formed for 1 mM, which is compressed only a little bit further with added DPPC. Indeed, it can be calculated that for an average radius of 110 nm and a droplet volume percentage of 1%, 0.94 mM of DPPC is needed to cover the entire droplet surface area (assuming a projected molecular area of 48 \AA^2). This indicates that, in contrast to single tail charged surfactants,^{104,143} zwitterionic phospholipids can form densely packed monolayers, much like those at an air/water interface. The found tilt angles are in qualitative agreement with the values found for the LC phase at the air/water interface²⁸⁴ for which the tilt angle is typically found to be $\sim 25^\circ$. Qualitative agreement also exists with X-ray scattering measurements from a mixed monolayer of DPPC and hexadecane at the air/water interface.³⁰⁰ Our system has DPPC tails adjacent to a condensed phase that limits the degree of freedom in the direction normal to the surface, especially at higher (> 1 mM) DPPC concentrations. On the other hand, for lower DPPC concentrations, we have seen that monolayers with more gauche defects in the alkyl chains are formed. For these monolayers, the data points lie on top of the curves calculated for the broad Gaussian distribution, which agrees with the chains being in a more disordered LC/LE coexistence phase.^{284,285,291} The chain tilt angles of 0.05 mM and 0.1 mM DPPC monolayers were found to be $16 \pm 4^\circ$, and $14 \pm 4^\circ$ from the $|E(r^+)|/|E(r^-)|$ ratios of 3.2 ± 0.2 and 3.1 ± 0.2 , respectively. This is again in qualitative agreement with previous experimental observations at the air/water interface²⁸⁴ and follows the trend that a monolayer adjacent to a condensed phase appears to be more restricted in its motion.

7.5 The molecular structures of the interfacial oil and water

7.5.1 Oil structure

To understand if the surrounding liquids are affected in their structure by DPPC, we measured the conformational changes in the interfacial oil chains and the change in interfacial alignment of the water molecules. The interfacial oil structure was determined by recording SFS spectra of the oil molecules in the C-H stretch region using selectively deuterated d_{75} -DPPC in combination with hydrogenated hexadecane molecules. Figure 7.3 shows the SFS spectra (in the SSP polarization combination)

of interfacial hexadecane molecules with d_{75} -DPPC at three different concentrations corresponding to the monolayers that resemble the LC and LC/LE coexistence phases and the pure oil/water interface (using 1, 0.1, and 0 mM DPPC, respectively). Comparing the SFS spectra of the three different interfaces in Fig. 7.3, the spectral shape of hexadecane is shown to change. As the DPPC concentration in the solution (and at the interface) increases, more SFS signal of the hexadecane d^+ mode was obtained and the d^+/r^+ ratio value increases from 1.0 ± 0.2 (0 mM) to 1.8 ± 0.2 (0.1 mM) and 2.2 ± 0.2 (1 mM). Thus, while the DPPC alkyl chains increase in order, the hexadecane alkyl chains

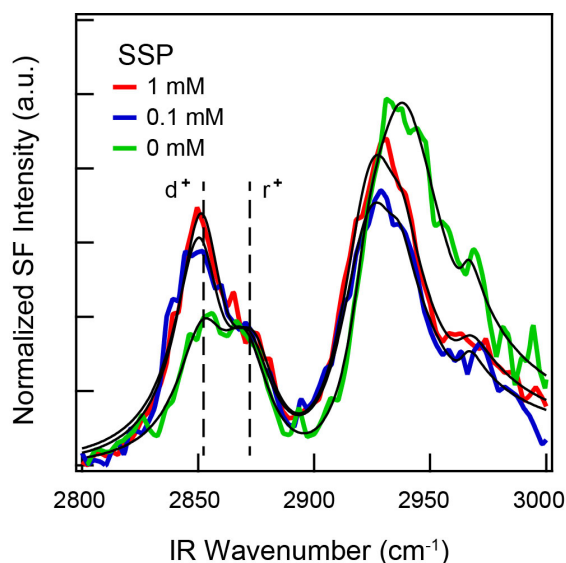


Figure 7.3 – The molecular structure of interfacial oil covered with a DPPC monolayer. SFS spectra in the C-H stretch region of hexadecane nanodroplets prepared with d_{75} -DPPC at different concentrations corresponding to surface densities of $\sim 48 \text{ \AA}^2/\text{molecule}$, $\sim 70 \text{ \AA}^2/\text{molecule}$, and $\infty \text{ \AA}^2/\text{molecule}$ (no DPPC added). The spectra are normalized by the maxima of the r^+ peak for a clear comparison of the d^+/r^+ ratios.

display more gauche defects. This can be understood as follows: Alkane chains at the surface of pure oil nanodroplets in pure water are predominantly oriented along the interfacial plane to reduce the amount of hydrophobic contacts.^{270,272,279} The DPPC chains are nonpolar and thus lift this restriction allowing the hexadecane chains to experience more degrees of freedom, which is manifested in more spectral gauche defects. From the above spectra, it cannot, however, be concluded that the hexadecane chains orient themselves in a parallel manner to the DPPC alkyl chains as suggested by studies conducted on the planar water/mixed hexadecane-DPPC monolayers.^{300,322} If this would be the case, we would expect to observe an increase in the r^+ and a decrease in the d^+ mode, which is opposite from what was observed here. It thus appears that there is some interaction, but this interaction is most likely restricted to the end of the

DPPC alkyl chains as was observed earlier for alkanol monolayers¹¹⁰ and calculated for the interaction between CCl_4 and DPPC at the air/water interface.³⁰⁸

7.5.2 Water structure

The alignment of interfacial water around the DPPC monolayer was measured with SHS, which reports on the difference in orientational directionality of the water molecules in the interfacial region compared to that in the bulk solution.^{103,207,267,268} As elegantly shown by Eisenthal and co-workers²⁰⁷, this can be understood by noting

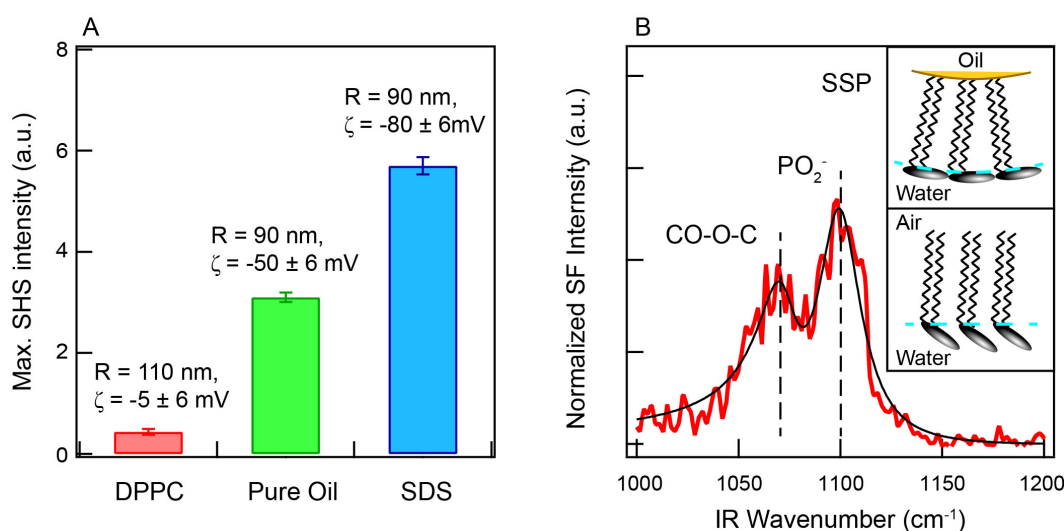


Figure 7.4 – Hydration of DPPC monolayers. (A) Comparison of the maximum SHS intensity of nanodroplets with a dense DPPC monolayer (1 mM, $R = 110$ nm, $\zeta = -5 \pm 6$ mV), an SDS monolayer (1 mM, $800 \text{ \AA}^2/\text{molecule}$, $R = 90$ nm, $\zeta = -80 \pm 6$ mV) to that with a neat oil droplet/water interface ($R = 90$ nm, $\zeta = -50 \pm 6$ mV).¹⁰⁴ (B) SFS spectrum of DPPC (1 mM) in the P-O stretch region. The spectral fits (black lines) were obtained using the procedure described in Sec. 5.3.3. The inset illustrates the different headgroup orientation of the DPPC monolayer on the surface of hexadecane nanodroplets (top), compared with that at the planar air/water interface (bottom).

that, for a nonresonant SHS process¹⁴⁵ as probed here, the SH intensity depends quadratically on the number density of each molecule that is both dipolar and present in the non-centrosymmetric interfacial region. Because water has the largest hyperpolarizability (which also contributes quadratically) and because it greatly outnumbers the other species, the SHS signal reports primarily on the water orientation. Figure 7.4A shows the SHS intensity of a DPPC monolayer in the LC phase on hexadecane nanodroplets in water, the pure oil nanodroplet/water interface from hexadecane nanodroplets in water, and a negatively charged sodium dodecyl sulfate (SDS) monolayer with a projected surface area of $\sim 8 \text{ nm}^2/\text{dodecyl sulfate anion}$ on hexadecane

nanodroplets in water.¹⁰⁴ The data was recorded at the scattering angle of maximum intensity using the PPP polarization combination. The graph represents the SHS intensity change as induced by the nanodroplets (i.e., the SHS intensity from the main bulk phase is subtracted from the raw data) relative to the HRS signal of pure water. ζ -potential values are also shown for a direct surface charge comparison.

For the pure oil/water interface, there is some preferential orientation of water molecules that consists of a small excess of water molecules with their H atoms pointing toward the oil phase.^{264,283} Upon adding dodecyl sulfate anions, this interfacial alignment increases, as there is cooperativity between the H-bonding interaction with the sulfate headgroups and the charge-dipole interaction.^{104,105} In contrast, an ordered densely packed DPPC monolayer induces a drastic reduction in the SHS signal of the water molecules. Thus, by adding DPPC the preferential average alignment of water along the radial direction is almost completely lost. This suggests that the water molecules are preferentially oriented parallel to the interfacial plane. If this is the case, we expect that the DPPC headgroup should be oriented with the P and N atoms nearly in plane to facilitate this type of water alignment. The interfacial orientation of the headgroup for the LC like system can be inferred from Fig. 7.4B, which shows the SFS spectrum in the P-O stretch region for the solution with 1 mM DPPC. Table 7.2 shows values of the spectral parameters obtained from fitting to Eq. 5.24. Here, two

mode	P-O stretch modes		
	ω_i (cm ⁻¹)	γ_i (cm ⁻¹)	A_i
s-CO-O-C	1073	12	0.54
s-PO ₂ ⁻	1100	13	1.06
A_{NR}			0.14
φ_{NR}			174°

Table 7.2 – Fitted frequency, amplitude, and linewidth for the DPPC spectrum in the P-O stretch region of the hexadecane nanodroplet/DPPC/water interface with 1 mM DPPC in the solution.

resonances are observed at ~ 1070 cm⁻¹ for s-CO-O-C stretch mode (orange arrows in Fig. 7.1B) and at ~ 1100 cm⁻¹ for the s-PO₂⁻ stretch mode (blue arrows in Fig. 7.1B) of DPPC in a hydrated monolayer. These assignments are in agreement with previous SFG studies.^{289,321,323} For both modes to be visible in the SFS spectra, their dipole orientation has to have a component that lies along the surface normal. It can be seen that both modes give rise to a strong SFS signal, which indicates that the P-N

headgroup axis has a significant component that lies along the surface plane (putting the probed modes aligned along the surface normal). For a planar DPPC monolayer at the air/water interface, a very similar spectrum is observed²⁸⁹ and MD simulations showed that the P-N axis is oriented at an angle of $\sim 90^\circ$ away from the surface normal.³⁰⁷ Given the spectral shape and similarities to the air/water SFG data, it is likely that the headgroup of DPPC is tilted away from the normal of the nanodroplet surface and is on average oriented parallel to the interface. Thus, the orientation of the DPPC headgroup in the 3D monolayer with a small degree of curvature matches with what is expected based on the loss of water alignment along the droplets surface normal. Comparing this water response to the water SFG signal in reflection mode from the air/DPPC/water interface we note that the obtained SHS signal appears to be relatively smaller than the SFG signal. This would suggest that the orientational distribution of the headgroup is narrower and more parallel to the interface in the 3D monolayer on the droplet. This could be due to a surface curvature effect: The lipid headgroups have slightly more surface area ($4.3 \pm 0.7\%$) that could lead to a more tilted headgroup structure by reducing the geometric restrictions between the zwitterionic head groups that exist in a planar geometry (a schematic illustration can be seen in Fig. 7.4B).

7.6 Conclusions

Summarizing, we have created 3D phospholipid monolayers with a tunable molecular structure on oil nanodroplets by mixing oil, water, and DPPC in different ratios. The choice of components was inspired by biomimetic film formation (such as black lipid membranes and Langmuir monolayers); however, monolayers of any kind of lipids can potentially be formed with this new method. Molecular level insight into the interfacial structure of this system was obtained with SFS and SHS. At high concentrations, the DPPC molecules form a monolayer on the surface with alkyl chains that are oriented along the surface normal. The SFS spectra display no detectable gauche defects. The headgroup spectrum agrees with a headgroup orientation that is on average parallel to the interface. Upon decreasing the amount of DPPC in the solution, the monolayer spectra show more gauche defects and the chain orientational distribution becomes broad with a larger average tilt angle (i.e., away from the interfacial normal). Comparison of the SF spectra to those obtained from an air/DPPC/water interface for which the molecular density has been determined allows us to also estimate the average projected surface area per DPPC molecule. The spectra and analysis indicate

that the high-density layers have a structure reminiscent of the LC phase, while the lower density films have a structure that is similar to the LC/LE coexistence region. The surface oil chains do influence the alkyl chains of the lipids, but not to the degree that complete mixing with parallel alignment is observed. Water alignment that is initially present at the bare oil droplet/water interface is almost completely reduced to zero by a condensed DPPC monolayer. The proposed 3D monolayers can be prepared in situ in the liquid phase, which reduces any issues with chemical instability that occurs, for example, for cholesterol and 1,2-dioleoyl-*sn*-glycero-3-phosphocholine (DOPC).⁵⁹ Moreover, sample volumes are kept very small (< 1 mL), while retaining a high surface-to-volume ratio, which favors the use of biochemical compounds that are difficult to obtain in a large quantity (such as most proteins). In addition, the controllability of the monolayer structure and the similarity to naturally occurring lipid droplets make it an ideal model system for biochemical and soft functional materials research on membrane interactions with molecular sensitivity. The system also allows itself to be used in microfluidic chambers, bringing the possibility of biochemical screening in lipid layers with molecular sensitivity closer to reality.

8 Summary and Outlook

8.1 Summary

The main focuses of this thesis were ion-water interactions in electrolyte solutions (Part I) and molecular interactions at aqueous nanoscale interfaces (Part II).

In Part I (Ch. 2 - 4) of this thesis, we treated two open questions about electrolyte solutions that are crucial for understanding ion-water interactions: (1) What is the spatial range of the interaction of ions with liquid water? (2) What is the connection between the molecular structure and the macroscopic properties that are influenced by electrolytes, such as surface tension, viscosity, and the hydration free energy? Are these long-range or only short-range? To obtain molecular-level insights into these questions, we employed fs-ESHS to probe ion-induced structural and electronic changes in the bulk water. The theoretical background and experimental details of fs-ESHS were provided in Ch. 2.

In Ch. 3, we presented a systematic fs-ESHS study of dilute electrolyte solutions (up to 100 mM) for 21 different ion pairs. We found that ions induce long-range non-ion-specific perturbations in the H-bond network of water. These perturbations start to appear at ionic strengths $< 10\mu\text{M}$ and lead to an increase in orientational order in the H-bond network of water. The collective orientational order extends as far as 70 hydration shells. We also observed significant differences in the fs-ESHS intensities between electrolyte solutions of light and heavy water. Ions impose a smaller effect on the orientational order of heavy water than on that of light water due to nuclear quantum effects. This ion-induced orientational order in the water network can be linked to changes in the surface tension of electrolyte solutions. The electrolyte concentration where the ion-induced orientational order saturates matches the critical concentration ($\sim 1\text{ mM}$) of the 80-year mysterious minimum in the surface tension

of electrolyte solutions (the Jones-Ray effect). The decrease in the surface tension at micromolar concentrations may be explained by a qualitative change in the surface propensity of ions due to collective interactions between nanoscopic "ordered domains" of water around ions and the interface.

In Ch. 4, we studied the same interactions in concentrated electrolyte solutions focusing on cations. We used fs-ESHS to probe changes in the charge distribution around ions as well as structural orientational order of water molecules in the extended hydration shells for a series of chloride salt solutions at concentrations from 0.5 M to 4 M. We observed ion specificity in both the local electronic anisotropy and the nanoscopic orientational ordering of water. Both observables are influenced more by cations with larger valencies and smaller sizes and follow a direct Hofmeister trend. The ion-induced structural changes in the H-bond network of water are strongly correlated with the viscosity B-coefficient and the hydration free energy of ions. Such a connection between the nanoscopic and macroscopic changes provides a possibility to construct a better molecular model for specific ion effects in aqueous solutions.

In Part II (Ch. 5 - 7) of this thesis, we focused on molecular interactions at aqueous nanoscale interfaces. We used SFS to selectively probe the structure of interfacial molecules and SHS to probe the interfacial water ordering. Details of the measurements were provided in Ch. 5.

In Ch. 6, we studied the nanoscopic hydrophobe/water interface and related interactions by probing the molecular structure of the interface formed with amphiphilic alkanols. We obtained insights into the molecular structural aspects of the transition from a hydrophobic phase to an aqueous phase by using a dispersion of ~100 nm radius hexadecane droplets in water that contains 1-pentanol, 1-hexanol, 1-octanol, or 1-dodecanol. The hexadecane/1-dodecanol/water interface has a chain conformation that represents that of a fluid layer with a wide distribution of the tilt angle of the terminal CH₃ groups. Alkyl chains of alkanols from pentanol to dodecanol adopt a conformation that generates indistinguishable SFS spectra. Alkanols with chain lengths longer than 6 C atoms all form films with comparable densities. In contrast, the alkyl chains of the oil phase are relatively more distorted with respect to the pure oil/water interface as the alkyl chain length of alkanols decreases. The surface density of alkanol molecules was determined by means of an SFS isotherm of 1-hexanol, which generated a projected surface density of $29 \pm 5 \text{ \AA}^2$ and a free energy of adsorption of $\Delta G = -26.3 \pm 0.7 \text{ kJ/mol}$. With increasing the 1-hexanol surface density, the interfacial water structure loses its initial orientational alignment in a way that matches with the added number of interfacial 1-hexanol molecules. These found conformations differ significantly from that reported at the planar alkanol/water and

alkanol/air interface, which can be explained by the balance between dispersive and H-bonding interactions.

In Ch. 7, we presented a new model membrane at aqueous nanoscale interfaces: 3D phospholipid monolayers with a tunable molecular structure on oil nanodroplets created by mixing oil, water, and DPPC in different ratios. The choice of components was inspired by biomimetic film formation (such as black lipid membranes and Langmuir monolayers); however, monolayers of any kind of lipids can potentially be formed with this new method. We used SFS and SHS to characterize the interfacial molecular structure of this nanoscopic model membrane. This new in-situ prepared membrane model system possesses controllable surface properties and mimics lipid droplets in cells. The interfacial structure of DPPC can be tuned from a tightly packed LC phase like monolayer to a more dilute one that resembles the LC/LE coexistence phase by varying the DPPC/oil/water ratio. The tunability of the chemical structure, the high surface-to-volume ratio, and the small sample volume make this system ideal for studies of molecular interactions of lipids in membranes.

8.2 Outlook

In the first part of this thesis, we have experimentally demonstrated that electrolytes induce long-range orientational order and free energy changes in the H-bond network of water. We observed a link between the ion-induced water ordering and the anomalies in the surface tension of electrolyte solutions at concentrations ~ 1 mM. This link indicates a bulk origin of the surface tension that is traditionally considered as a pure surface phenomenon. These findings refresh our understandings of the spatial range of ion-water interactions and provide a new perspective to explaining surface phenomena based on changes in the bulk. Considerations of ion-water interactions at a long length scale larger than one nanometer are thus needed to have a complete understanding of various processes in aqueous solutions as ions are omnipresent. Besides, despite the small differences in the molecular properties, we also observed significant differences between light and heavy water in both ion-induced ordering in the bulk water network and changes in the surface tension. This finding well proves the significance of nuclear quantum effects on the H-bonding and so the water network and provides new materials for both experimental and theoretical studies of nuclear quantum effects. Meanwhile, the new experimental findings in this thesis also call for developments in theoretical modeling of long-range ion-water interactions in dilute electrolyte solutions. Current mean-field models have severe

limitations in quantitative prediction of the experiment results due to the assumption that water behaves as a dipolar gas. H-bonding between water molecules can hardly be described by mean-field models, neither can nuclear quantum effects be. At the same time, MD simulations are typically limited to simulating either “infinite dilutions” or concentrated solutions ($> 1\text{ M}$). Only a few MD simulations showed some long-range responses of water to ions but still cannot completely predict the experiment observations reported in this thesis. Better ways are required to incorporate ingredients on a more detailed level.

For concentrated electrolyte solutions ($> 100\text{ mM}$), we also observed cation-specific changes in both the charge distribution and molecular structure in extended hydration shells of ions. The microscopic structural changes in the bulk water network can be correlated with macroscopic properties of aqueous solutions and follow a direct Hofmeister trend for the studied cation series. This finding once again reveals the underlying connection between macroscopic phenomena and the bulk water structure. It suggests a bulk-origin, water-mediated specific cation effects in aqueous solutions, which differs from specific anion effects that are commonly thought as directly surface-related. Further studies of specific cation effects especially in the aspects of how the water network evolves are of great interest to clarify the mechanism of specific cation effects in biological processes. One example is to use fs-ESHS to study the influence of cations on the solvation of proteins in aqueous solutions by probing structural changes in the water network in the presence of different ions and proteins. Also, the influence of anions on the bulk water network in concentrated solution and its connection to the commonly considered "surface-related" specific anion effects are an interesting topic for subsequent studies with fs-ESHS. Meanwhile, MD simulations of these concentrated electrolyte solutions are desired but challenging as it is necessary to find proper polarizable models for different ions. How to interpret the measured incoherent and coherent fs-ESHS responses in a comprehensive way and disentangle different structural and electronic contributions from the fs-ESHS signal is also a topic for future studies.

In the second part of this thesis, we presented a new membrane model system (3D phospholipid monolayer at aqueous nanoscale interfaces). This in-situ prepared model membrane possesses tunability in its molecular structure similar with that of the Langmuir monolayer while having additional advantages of the large surface-to-volume ratio, small sample volume requirements, and good chemical stability. For the proof-of-concept, we created a 3D DPPC model membrane in this thesis and characterized its molecular structure using SFS and SHS. The work of this thesis demonstrates that SFS and SHS can be used to obtain molecular-level insights into the

interfacial structures of molecules and the hydration of the membrane, respectively. Applying these two techniques to the new membrane model system provides us with a new viewing angle of biological processes occurring in membranes with molecular-level details. As subsequent studies, further characterizations of this model membrane composed of different types of lipids would give us a complete understanding and so better control of the properties of this membrane model system. For instance, an interesting topic is the roles of the lipid hydrophilic headgroup and hydrophobic tails in the formation of lipid membranes. More importantly, this membrane model system provides a new platform for extensive studies of interactions between lipid membranes and ions, biomolecules, and water in an environment close to the reality. The adsorption/aggregation behavior of biomolecules to the lipid membrane, the ion binding to specific sites in the membrane, and the change in the molecular structure of the membrane induced by changes in temperature are exemplary topics that are of great interest to be studied with this new membrane model system.

List of Publications

The present thesis is based on the following publications / manuscripts:

Chapter 3: Y. Chen, H. I. Okur, N. Gomopoulos, C. Macias-Romero, P. S. Cremer, P. B. Petersen, G. Tocci, D. M. Wilkins, C. Liang, M. Ceriotti, S. Roke. Electrolytes induce long-range orientational order and free energy changes in the H-bond network of bulk water. *Sci. Adv.*, 2:e1501891, 2016.

Chapter 4: Y. Chen, H. I. Okur, C. Liang, S. Roke. Orientational ordering of water in extended hydration shells of cations is ion-specific and correlates directly with viscosity and hydration free energy. *submitted*, 2017.

Chapter 6: Y. Chen, K. C. Jena, S. Roke. From hydrophobic to hydrophilic: The structure and density of the hexadecane droplet/alkanol/water interface. *J. Phys. Chem. C*, 119:17725-17734, 2015.

Chapter 7: Y. Chen, K. C. Jena, C. Lütgebaucks, H. I. Okur, S. Roke. Three dimensional nano "Langmuir trough" for lipid studies. *Nano Lett.*, 15:5558-5563, 2015.

Other publications not described within this thesis:

- H. I. Okur, Y. Chen, N. Smolentsev, E. Zdrali, and S. Roke. Interfacial Structure and Hydration of 3D-Lipid Monolayers in Aqueous Solution. *J. Phys. Chem. B*, in press, 2017.
- R. Scheu, Y. Chen, H. B. de Aguiar, B. M. Rankin, D. Ben-Amotz, S. Roke. Specific ion effects in amphiphile hydration and interface stabilization. *J. Am. Chem. Soc.*, 136:2040-2047, 2014.
- R. Scheu, B. M. Rankin, Y. Chen, K. C. Jena, D. Ben-Amotz, S. Roke. Charge asymmetry at aqueous hydrophobic interfaces and hydration shells. *Angew. Chem. Int. Ed.*, 53:9560-9563, 2014.

List of Publications

- N. Smolentsev, Y. Chen, K. C. Jena, M. A. Brown, S. Roke. Sum frequency and second harmonic generation from the surface of a liquid microjet. *J. Chem. Phys.*, 141:18C524, 2014.
- R. Scheu, Y. Chen, M. Subinya, S. Roke. Stern layer formation induced by hydrophobic interactions: A molecular level study. *J. Am. Chem. Soc.*, 135:19330-19335, 2013.
- A. G. F. de Beer, Y. Chen, R. Scheu, J. C. Conboy, S. Roke. Analysis of complex spectra using Fourier filtering. *J. Phys. Chem. C*, 117:26582-26587, 2013.

Bibliography

- [1] Oxford University Press. water. Oxford Dictionaries. <http://www.oxforddictionaries.com/definition/english/water>.
- [2] A. Szent-Gyorgyi. Welcoming Address. In W. Drost-Hansen and James S. Clegg, editors, *Cell-Associated Water*, pages 1–2. Academic Press, 1979.
- [3] M. Chaplin. Water Structure and Science. http://www1.lsbu.ac.uk/water/water_molecule.html.
- [4] P. Ball. Water as an active constituent in cell biology. *Chem. Rev.*, 108:74–108, 2008.
- [5] D. J Tobias and J. C. Hemminger. Getting specific about specific ion effects. *Science*, 319:1197–1198, 2008.
- [6] W. Kunz. Specific ion effects in liquids, in biological systems, and at interfaces. *Pure Appl. Chem.*, 78:1611–1617, 2006.
- [7] Y. Zhang and P. S. Cremer. Chemistry of Hofmeister anions and osmolytes. *Annu. Rev. Phys. Chem.*, 61:63–83, 2010.
- [8] P. Jungwirth and P. S. Cremer. Beyond Hofmeister. *Nat. Chem.*, 6:261–263, 2014.
- [9] P. B. Petersen and R. J. Saykally. On the nature of ions at the liquid water surface. *Annu. Rev. Phys. Chem.*, 57:333–364, 2006.
- [10] H. Jenkins and Y. Marcus. Viscosity B-coefficients of ions in solution. *Chem. Rev.*, 95:2695–2724, 1995.
- [11] Y. Marcus. *Ion properties*. Marcel Dekker, 1997.

- [12] P. Hünenberger and M. Reif. *Single-ion solvation: Experimental and theoretical approaches to elusive thermodynamic quantities*. Royal Society of Chemistry, 2011.
- [13] H. Ohtaki and T. Radnai. Structure and dynamics of hydrated ions. *Chem. Rev.*, 93:1157–1204, 1993.
- [14] Y. Marcus. Effect of ions on the structure of water: Structure making and breaking. *Chem. Rev.*, 109:1346–1370, 2009.
- [15] P. Jungwirth and D. J. Tobias. Specific ion effects at the air/water interface. *Chem. Rev.*, 106:1259–1281, 2006.
- [16] T. T. Duignan, M. D. Baer, and C. J. Mundy. Ions interacting in solution: Moving from intrinsic to collective properties. *Curr. Opin. Colloid Interface Sci.*, 23:58–65, 2016.
- [17] W. Kunz. *Specific ion effects*. World Scientific Publishing Company, 2010.
- [18] V. S. J. Craig. Bubble coalescence and specific-ion effects. *Curr. Opin. Colloid Interface Sci.*, 9:178–184, 2004.
- [19] Y. Zhang and P. S. Cremer. Interactions between macromolecules and ions: The Hofmeister series. *Curr. Opin. Chem. Biol.*, 10:658–663, 2006.
- [20] W. Kunz. Specific ion effects in colloidal and biological systems. *Curr. Opin. Colloid Interface Sci.*, 15:34–39, 2010.
- [21] P. Lo Nostro and B. W. Ninham. Hofmeister phenomena: an update on ion specificity in biology. *Chem. Rev.*, 112:2286–2322, 2012.
- [22] G. Jones and W. A. Ray. The surface tension of solutions. *J. Am. Chem. Soc.*, 57:957–958, 1935.
- [23] G. Jones and W. A. Ray. The surface tension of solutions of electrolytes as a function of the concentration I A differential method for measuring relative surface tension. *J. Am. Chem. Soc.*, 59:187–198, 1937.
- [24] G. Jones and W. A. Ray. The surface tension of solutions of electrolytes as a function of the concentration ii. *J. Am. Chem. Soc.*, 63:288–294, 1941.

-
- [25] G. Jones and W. A. Ray. The Surface Tension of Solutions of Electrolytes as a Function of the Concentration. III. Sodium Chloride. *J. Am. Chem. Soc.*, 63:3262–3263, 1941.
- [26] G. Jones and W. A. Ray. The surface tension of solutions of electrolytes as a function of the concentration. iv. magnesium sulfate. *J. Am. Chem. Soc.*, 64:2744–2745, 1942.
- [27] A. W. Adamson and A. P. Gast. *Physical chemistry of surfaces*. Wiley-Interscience, Sydney, 1997.
- [28] M. Dole. A theory of surface tension of aqueous solutions. *J. Am. Chem. Soc.*, 60:904–911, 1938.
- [29] P. B. Petersen and R. J. Saykally. Adsorption of ions to the surface of dilute electrolyte solutions: the Jones-Ray effect revisited. *J. Am. Chem. Soc.*, 127:15446–15452, 2005.
- [30] V. Venkateshwaran, S. Vembanur, and S. Garde. Water-mediated ion-ion interactions are enhanced at the water vapor-liquid interface. *Proc. Natl. Acad. Sci. U.S.A.*, 111:8729–8734, 2014.
- [31] L. Onsager and N. N. T. Samaras. The surface tension of debye-hückel electrolytes. *J. Chem. Phys.*, 2:528, 1934.
- [32] P. Jungwirth and B. Winter. Ions at aqueous interfaces: from water surface to hydrated proteins. *Annu. Rev. Phys. Chem.*, 59:343–66, 2008.
- [33] N. L. Jarvis and M. A. Scheiman. Surface potentials of aqueous electrolyte solutions. *J. Phys. Chem.*, 72:74–78, 1968.
- [34] I. Langmuir. Repulsive forces between charged surfaces in water, and the cause of the jones-ray effect. *Science*, 88:430–432, 1938.
- [35] I. Langmuir. The role of attractive and repulsive forces in the formation of tactoids, thixotropic gels, protein crystals and coacervates. *J. Chem. Phys.*, 6:873–896, 1938.
- [36] M. Dole and J. A. Swartout. A twin-ring surface tensiometer. i. the apparent surface tension of potassium chloride solutions. *J. Am. Chem. Soc.*, 62:3039–3045, 1940.

- [37] L. A. Wood and L. B. Robinson. A test of Langmuir's interpretation of the Jones-Ray effect. *J. Chem. Phys.*, 14(4):258–262, 1946.
- [38] F. A. Long and G. C. Nutting. The relative surface tension of potassium chloride solutions by a differential bubble pressure method1. *J. Am. Chem. Soc.*, 64:2476–2482, 1942.
- [39] A. S. Coolidge. Imaginary contact angles and the jones-ray effect. *J. Am. Chem. Soc.*, 71:2153–2167, 1949.
- [40] M. Manciu and E. Ruckenstein. Ions near the air/water interface: I. compatibility of zeta potential and surface tension experiments. *Colloids Surf., A*, 400:27–35, 2012.
- [41] J. Saïen and M. Mishi. Equilibrium interfacial tension and the influence of extreme dilutions of univalent salts: An expression of the “Jones–Ray effect”. *J. Chem. Thermodyn.*, 54:254–260, 2012.
- [42] K. T. Nguyen, A. V. Nguyen, and G. M. Evans. Interactions between halide anions and interfacial water molecules in relation to the jones-ray effect. *Phys. Chem. Chem. Phys.*, 16:24661–24665, 2014.
- [43] J. M. Berg, J. L. Tymoczko, and L. Stryer. *Biochemistry*. W. H. Freeman, 2012.
- [44] T. G. Mason, J. N. Wilking, K. Meleson, C. B. Chang, and S. M. Graves. Nanoemulsions: Formation, structure, and physical properties. *J. Phys. Condens. Matter*, 18:R635–R666, 2006.
- [45] M. M. Fryd and T. G. Mason. Advanced nanoemulsions. *Annu. Rev. Phys. Chem.*, 63:493–518, 2012.
- [46] A. Gupta, H. B. Eral, T. A. Hatton, and P. S. Doyle. Nanoemulsions: Formation, properties and applications. *Soft Matter*, 12:2826–2841, 2016.
- [47] H. B. de Aguiar, J. Samson, and S. Roke. Probing nanoscopic droplet interfaces in aqueous solution with vibrational sum-frequency scattering: A study of the effects of path length, droplet density and pulse energy. *Chem. Phys. Lett.*, 512:76–80, 2011.
- [48] A. Pockels. Surface Tension. *Nature*, 43:437, 1891.
- [49] I. Langmuir. The constitution and fundamental properties of solids and liquids. II. liquids. *J. Am. Chem. Soc.*, 39:1848–1906, 1917.

-
- [50] W. D. Harkins, E. C. H. Davies, and G. L. Clark. The orientation of molecules in the surfaces of liquids, the energy relations at surfaces, solubility, adsorption, emulsification, molecular association, and the effect of acids and bases on interfacial tension. *J. Am. Chem. Soc.*, 39:354–364, 1917.
- [51] G. A. Sefler, Q. Du, P. B. Miranda, and Y. R. Shen. Surface crystallization of liquid n-alkanes and alcohol monolayers studied by surface vibrational spectroscopy. *Chem. Phys. Lett.*, 235:347–354, 1995.
- [52] R. Lu, W. Gan, B. Wu, Z. Zhang, Y. Guo, and H. Wang. C-H stretching vibrations of methyl, methylene and methine groups at the vapor/alcohol (n = 1-8) interfaces. *J. Phys. Chem. B*, 109:14118–14129, 2005.
- [53] G. R. Bell, C. D. Bain, and R. N. Ward. Sum-frequency vibrational spectroscopy of soluble surfactants at the air/water interface. *J. Chem. Soc. Faraday Transactions*, 92:515, 1996.
- [54] R. Braun, B. D. Casson, and C. D. Bain. A sum-frequency study of the two-dimensional phase transition in a monolayer of undecanol on water. *Chem. Phys. Lett.*, 245:326–334, 1995.
- [55] B. D. Casson, R. Braun, and C. D. Bain. Phase transitions in monolayers of medium-chain alcohols on water studied by sum-frequency spectroscopy and ellipsometry. *Farad. Discuss.*, 104:209, 1996.
- [56] E. Tyrode, C. M. Johnson, A. Kumpulainen, M. W. Rutland, and P. M. Claesson. Hydration state of nonionic surfactant monolayers at the liquid/vapor interface: Structure determination by vibrational sum frequency spectroscopy. *J. Am. Chem. Soc.*, 127:16848–16859, 2005.
- [57] C. D. Stanners, Q. Du, R. P. Chin, P. Cremer, G. A. Somorjai, and Y. R. Shen. Polar ordering at the liquid-vapor interface of n-alcohols (C1-C8). *Chem. Phys. Lett.*, 232:407–413, 1995.
- [58] Kibron Inc. MicroTroughXS: Specifications. <http://www.kibron.com/e-shop/langmuir-troughs/mtxs>.
- [59] J. F. D. Liljeblad, V. Bulone, E. Tyrode, M. W. Rutland, and C. M. Johnson. Phospholipid monolayers probed by vibrational sum frequency spectroscopy: Instability of unsaturated phospholipids. *Biophys. J.*, 98:L50–L52, 2010.

- [60] K. Tauchi-Sato, S. Ozeki, T. Houjou, R. Taguchi, and T. Fujimoto. The surface of lipid droplets is a phospholipid monolayer with a unique fatty acid composition. *J. Biol. Chem.*, 277:44507–44512, 2002.
- [61] P. A. Franken, A. E. Hill, C. W. Peters, and G. Weinreich. Generation of optical harmonics. *Phys. Rev. Lett.*, 7:118–119, 1961.
- [62] Y. R. Shen. *The principles of nonlinear optics*. Wiley classics library. Wiley-Interscience, 2003.
- [63] A. G. Lambert, P. B. Davies, and D. J. Neivandt. Implementing the theory of sum frequency generation vibrational spectroscopy: A tutorial review. *Appl. Spectr. Rev.*, 40:103–145, 2005.
- [64] R. J. Ellingson and C. L. Tang. High-repetition-rate femtosecond pulse generation in the blue. *Opt. Lett.*, 17:343–345, 1992.
- [65] R. J. Ellingson and C. L. Tang. High-power, high-repetition-rate femtosecond pulses tunable in the visible. *Opt. Lett.*, 18:438–440, 1993.
- [66] M. Ghotbi and A. Ebrahim-Zadeh. M Esteban-Martin. Tunable, high-repetition-rate, femtosecond pulse generation in the ultraviolet. *Opt. Lett.*, 33:345–347, 2008.
- [67] M. Flörsheimer, R. Paschotta, U. Kubitscheck, C. Brillert, D. Hofmann, L. Heuer, G. Schreiber, C. Verbeek, W. Sohler, and H. Fuchs. Second-harmonic imaging of ferroelectric domains in LiNbO₃ with micron resolution in lateral and axial directions. *Appl. Phys. B*, 67:593–599, 1998.
- [68] R. D. Wampler, D. J. Kissick, C. J. Dehen, E. J. Gualtieri, J. L. Grey, H. Wang, D. H. Thompson, J. Cheng, and G. J. Simpson. Selective detection of protein crystals by second harmonic microscopy. *J. Am. Chem. Soc.*, 130:14076–14077, 2008.
- [69] P. J. Campagnola, M. Wei, A. Lewis, and L. M. Loew. High-resolution nonlinear optical imaging of live cells by second harmonic generation. *Biophys. J.*, 77:3341–3349, 1999.
- [70] P. J. Campagnola and L. M. Loew. Second-harmonic imaging microscopy for visualizing biomolecular arrays in cells, tissues and organisms. *Nature Biotechnol.*, 21:1356–1360, 2003.

-
- [71] N. Bloembergen and P. S. Pershan. Light waves at the boundary of nonlinear media. *Phys. Rev.*, 128:606–622, 1962.
- [72] N. Bloembergen, R. K. Chang, S. S. Jha, and C. H. Lee. Optical second-harmonic generation in reflection from media with inversion symmetry. *Phys. Rev.*, 174:813–822, 1968.
- [73] C. C. Wang. Second-harmonic generation of light at the boundary of an isotropic medium. *Phys. Rev.*, 178:1457–1460, 1969.
- [74] P. Guyot-Sionnest, W. Chen, and Y. R. Shen. General considerations on optical second-harmonic generation from surfaces and interfaces. *Phys. Rev. B*, 33:8254–8263, 1986.
- [75] T. F. Heinz. Second-order nonlinear optical effects at surfaces and interfaces. In *Nonlinear surface electromagnetic phenomena*, chapter 5, pages 353–416. Elsevier, New York, 1991.
- [76] F. Brown and M. Matsuoka. Effect of adsorbed surface layers on second-harmonic light from silver. *Phys. Rev.*, 185:985–987, 1969.
- [77] G. L. Richmond, J. M. Robinson, and V. L. Shannon. Second harmonic generation studies of interfacial structure and dynamics. *Prog. Surf. Sci.*, 28:1–70, 1988.
- [78] Y. R. Shen. Surface properties probed by second-harmonic and sum-frequency generation. *Nature*, 337:519–525, 1989.
- [79] C. T. Williams and D. A. Beattie. Probing buried interfaces with non-linear optical spectroscopy. *Surf. Sci.*, 500:545–576, 2002.
- [80] K. B. Eisenthal. Liquid Interfaces Probed by Second-Harmonic and Sum-Frequency Spectroscopy. *Chem. Rev.*, 96:1343–1360, 1996.
- [81] R. W. Terhune, P. D. Maker, and C. M. Savage. Measurements of nonlinear light scattering. *Phys. Rev. Lett.*, 14:681–684, 1965.
- [82] S. Roke and G. Gonella. Nonlinear light scattering and spectroscopy of particles and droplets in liquids. *Annu. Rev. Phys. Chem.*, 63:353–378, 2012.
- [83] S. J. Cyvin, J. E. Rauch, and J. C. Decius. Theory of hyper-Raman effects (nonlinear inelastic light scattering): Selection rules and depolarization ratios for the second-order polarizability. *J. Chem. Phys.*, 43:4083, 1965.

- [84] R. Bersohn, Y. Pao, and H. L. Frisch. Double-quantum light scattering by molecules. *J. Chem. Phys.*, 45:3184, 1966.
- [85] M. Kauranen and A. Persoons. Theory of polarization measurements of second-order nonlinear light scattering. *J. Chem. Phys.*, 104:3445, 1996.
- [86] K. Clays and A. Persoons. Hyper-Rayleigh scattering in solution. *Phys. Rev. Lett.*, 66:2980–2983, 1991.
- [87] D. B. Hollis. Review of hyper-Rayleigh and second-harmonic scattering in minerals and other inorganic solids. *Am. Mineral.*, 73:701–706, 1988.
- [88] D. P. Shelton and J. E. Rice. Measurements and calculations of the hyperpolarizabilities of atoms and small molecules in the gas phase. *Chem. Rev.*, 94:3–29, 1994.
- [89] X. Hua and J. I. Gersten. Theory of second-harmonic generation by small metal spheres. *Phys. Rev. B*, 33:3756–3764, 1986.
- [90] J. I. Dadap, J. Shan, K. B. Eisenthal, and T. F. Heinz. Second-harmonic Rayleigh scattering from a sphere of centrosymmetric material. *Phys. Rev. Lett.*, 83:4045–4048, 1999.
- [91] J. I. Dadap, J. Shan, and T. F. Heinz. Theory of optical second-harmonic generation from a sphere of centrosymmetric material: Small-particle limit. *J. Opt. Soc. Am. B*, 21:1328, 2004.
- [92] N. Yang, W. E. Angerer, and A. G. Yodh. Angle-resolved second-harmonic light scattering from colloidal particles. *Phys. Rev. Lett.*, 87:103902, 2001.
- [93] Y. Pavlyukh and W. Hübner. Nonlinear Mie scattering from spherical particles. *Phys. Rev. B*, 70:245434, 2004.
- [94] A. G. F. de Beer and S. Roke. Nonlinear Mie theory for second-harmonic and sum-frequency scattering. *Phys. Rev. B*, 79:155420, 2009.
- [95] A. G. F. de Beer, S. Roke, and J. I. Dadap. Theory of optical second-harmonic and sum-frequency scattering from arbitrarily shaped particles. *J. Opt. Soc. Am. B*, 28:1374–1384, 2011.
- [96] S. Viarbitskaya, V. Kapshai, P. van der Meulen, and T. Hansson. Size dependence of second-harmonic generation at the surface of microspheres. *Phys. Rev. A*, 81:053850, 2010.

-
- [97] S. Wunderlich, B. Schürer, C. Sauerbeck, W. Peukert, and U. Peschel. Molecular Mie model for second harmonic generation and sum frequency generation. *Phys. Rev. B*, 84:1–9, 2011.
- [98] G. Gonella and H. Dai. Second harmonic light scattering from the surface of colloidal objects: Theory and applications. *Langmuir*, 30:2588–2599, 2014.
- [99] H. Wang, E. C. Y. Yan, E. Borguet, and K. B. Eisenthal. Second harmonic generation from the surface of centrosymmetric particles in bulk solution. *Chem. Phys. Lett.*, 259:15–20, 1996.
- [100] K. B. Eisenthal. Second harmonic spectroscopy of aqueous nano- and microparticle interfaces. *Chem. Rev.*, 106:1462–1477, 2006.
- [101] P. Ray. Size and shape dependent second order nonlinear optical properties of nanomaterials and their application in biological and chemical sensing. *Chem. Rev.*, 110:5332–5365, 2010.
- [102] E. C. Y. Yan, Y. Liu, and K. B. Eisenthal. New method for determination of surface potential of microscopic particles by second harmonic generation. *J. Phys. Chem. B*, 102:6331–6336, 1998.
- [103] R. Scheu, Y. Chen, M. Subinya, and S. Roke. Stern layer formation induced by hydrophobic interactions: A molecular level study. *J. Am. Chem. Soc.*, 135:19330–19335, 2013.
- [104] R. Scheu, Y. Chen, H. B. de Aguiar, B. M. Rankin, D. Ben-Amotz, and S. Roke. Specific ion effects in amphiphile hydration and interface stabilization. *J. Am. Chem. Soc.*, 136:2040–2047, 2014.
- [105] R. Scheu, B. M. Rankin, Y. Chen, K. C. Jena, and D. Ben-Amotz. Charge asymmetry at aqueous hydrophobic interfaces and hydration shells. *Angew. Chem. Int. Ed.*, 53:9560–9563, 2014.
- [106] B. Schürer, S. Wunderlich, C. Sauerbeck, U. Peschel, and W. Peukert. Probing colloidal interfaces by angle-resolved second harmonic light scattering. *Phys. Rev. B*, 82:241404, 2010.
- [107] B. Schurer, M. Hoffmann, S. Wunderlich, L. Harnau, U. Peschel, M. Ballauff, and W. Peukert. Second harmonic light scattering from spherical polyelectrolyte brushes. *J. Phys. Chem. C*, 115:18302–18309, 2011.

- [108] C. Sauerbeck, B. Braunschweig, and W. Peukert. Surface charging and interfacial water structure of amphoteric colloidal particles. *J. Phys. Chem. C*, 118:10033–10042, 2014.
- [109] Y. Chen, K. C. Jena, C. Lütgebaucks, H. I. Okur, and S. Roke. Three dimensional nano “Langmuir trough” for lipid studies. *Nano Lett.*, 15:5558–5563, 2015.
- [110] Y. Chen, K. C. Jena, and S. Roke. From hydrophobic to hydrophilic: The structure and density of the hexadecane droplet/alkanol/water interface. *J. Phys. Chem. C*, 119:17725–17734, 2015.
- [111] N. Smolentsev, C. Lütgebaucks, H. I. Okur, A. G. F. de Beer, and S. Roke. Intermolecular headgroup interaction and hydration as driving forces for lipid transmembrane asymmetry. *J. Am. Chem. Soc.*, 138:4053–4060, 2016.
- [112] G. Gonella, C. Lütgebaucks, A. G. F. de Beer, and S. Roke. Second harmonic and sum-frequency generation from aqueous interfaces is modulated by interference. *J. Phys. Chem. C*, 120:9165–9173, 2016.
- [113] C. Lütgebaucks, G. Gonella, and S. Roke. Optical label-free and model-free probe of the surface potential of nanoscale and microscopic objects in aqueous solution. *Phys. Rev. B*, 94:195410, 2016.
- [114] B. Dick, A. Gierulski, G. Marowsky, and G. A. Reider. Determination of the nonlinear optical susceptibility $\chi^{(2)}$ of surface layers by sum and difference frequency generation in reflection and transmission. *Appl. Phys. B*, 38:107–116, 1985.
- [115] C. Hirose, N. Akamatsu, and K. Domen. Formulas for the analysis of surface sum frequency generation spectrum by CH stretching modes of methyl and methylene groups. *J. Chem. Phys.*, 96:997–1004, 1992.
- [116] C. Hirose, N. Akamatsu, and K. Domen. Formulas for the analysis of the surface SFG spectrum and transformation coefficients of cartesian SFG tensor components. *Appl. Spectrosc.*, 46:1051–1072, 1992.
- [117] X. D. Zhu, H. Suhr, and Y. R. Shen. Surface vibrational spectroscopy by infrared-visible sum frequency generation. *Phys. Rev. B*, 35:3047–3050, 1987.
- [118] A. L. Harris, C. E. D. Chidsey, N. J. Levinos, and D. N. Loiacono. Monolayer vibrational spectroscopy by infrared-visible sum generation at metal and semiconductor surfaces. *Chem. Phys. Lett.*, 141:350 – 356, 1987.

-
- [119] P. Guyot-Sionnest, J. H. Hunt, and Y. R. Shen. Sum-frequency vibrational spectroscopy of a Langmuir film: Study of molecular orientation of a two-dimensional system. *Phys. Rev. Lett.*, 59:1597–1600, 1987.
- [120] A. L. Harris, L. Rothberg, L. H. Dubois, N. J. Levinos, and L. Dhar. Molecular vibrational energy relaxation at a metal surface: Methyl thiolate on Ag(111). *Phys. Rev. Lett.*, 64:2086–2089, 1990.
- [121] C. D. Bain, P. B. Davies, T. H. Ong, R. N. Ward, and M. A. Brown. Quantitative analysis of monolayer composition by sum-frequency vibrational spectroscopy. *Langmuir*, 7:1563–1566, 1991.
- [122] J. C. Owrutsky, J. P. Culver, M. Li, Y. R. Kim, M. J. Sarisky, M. S. Yeganeh, A. G. Yodh, and R. M. Hochstrasser. Femtosecond coherent transient infrared spectroscopy of CO on Cu(111). *J. Chem. Phys.*, 97:4421–4427, 1992.
- [123] T. H. Ong, P. B. Davies, and C. D. Bain. Sum-frequency spectroscopy of monolayers of alkoxy-terminated alkanethiols in contact with liquids. *Langmuir*, 9:1836–1845, 1993.
- [124] N. Watanabe, H. Yamamoto, A. Wada, K. Domen, C. Hirose, T. Ohtake, and N. Mino. Vibrational sum-frequency generation (VSFG) spectra of n-alkyltrichlorosilanes chemisorbed on quartz plate. *Spectrochim. Acta Mol. Biomol. Spectrosc.*, 50:1529–1537, 1994.
- [125] Q. Du, R. Superfine, E. Freysz, and Y. R. Shen. Vibrational spectroscopy of water at the vapor/water interface. *Phys. Rev. Lett.*, 70:2313–2316, 1993.
- [126] G. L. Richmond. Structure and bonding of molecules at aqueous surfaces. *Annu. Rev. Phys. Chem.*, 52:357–389, 2001.
- [127] Y. Shen and V. Ostroverkhov. Sum-frequency vibrational spectroscopy on water interfaces: Polar orientation of water molecules at interfaces. *Chem. Rev.*, 106:1140–1154, 2006.
- [128] A. M. Jubb, W. Hua, and H. C. Allen. Environmental chemistry at vapor/water interfaces: Insights from vibrational sum frequency generation spectroscopy. *Annu. Rev. Phys. Chem.*, 63:107–130, 2012.
- [129] S. Nihonyanagi, J. A. Mondal, S. Yamaguchi, and T. Tahara. Structure and dynamics of interfacial water studied by heterodyne-detected vibrational sum-frequency generation. *Annu. Rev. Phys. Chem.*, 64:579–603, 2013.

- [130] C. M. Johnson and S. Baldelli. Vibrational sum frequency spectroscopy studies of the influence of solutes and phospholipids at vapor/water interfaces relevant to biological and environmental systems. *Chem. Rev.*, 114:8416–8446, 2014.
- [131] C. S. Tian and Y. R. Shen. Recent progress on sum-frequency spectroscopy. *Surf. Sci. Rep.*, 69:105–131, 2014.
- [132] M. A. Donovan, Y. Y. Yimer, J. Pfaendtner, E. H. G. Backus, M. Bonn, and T. Weidner. Ultrafast reorientational dynamics of leucine at the air–water interface. *J. Am. Chem. Soc.*, 138:5226–5229, 2016.
- [133] E. C. Y. Yan, L. Fu, Z. Wang, and W. Liu. Biological macromolecules at interfaces probed by chiral vibrational sum frequency generation spectroscopy. *Chem. Rev.*, 114:8471–8498, 2014.
- [134] P. A. Covert and D. K. Hore. Geochemical insight from nonlinear optical studies of mineral–water interfaces. *Annu. Rev. Phys. Chem.*, 67:233–257, 2016.
- [135] S. Roke, W. G. Roeterdink, J. E. G. J. Wijnhoven, A. V. Petukhov, A. W. Kleyn, and M. Bonn. Vibrational sum frequency scattering from a submicron suspension. *Phys. Rev. Lett.*, 91:258302, 2003.
- [136] S. Roke, M. Bonn, and A. V. Petukhov. Nonlinear optical scattering: The concept of effective susceptibility. *Phys. Rev. B*, 70:1–10, 2004.
- [137] A. G. F. de Beer and S. Roke. Obtaining molecular orientation from second harmonic and sum frequency scattering experiments in water: Angular distribution and polarization dependence. *J. Chem. Phys.*, 132:234702, 2010.
- [138] S. Roke. Nonlinear optical spectroscopy of soft matter interfaces. *ChemPhysChem*, 10:1380–1388, 2009.
- [139] S. Roke, O. Berg, J. Buitenhuis, A. van Blaaderen, and M. Bonn. Surface molecular view of colloidal gelation. *Proc. Natl. Acad. Sci. U.S.A.*, 103:13310–13314, 2006.
- [140] C. M. Johnson, A. B. Sugiharto, and S. Roke. Surface and bulk structure of poly-(lactic acid) films studied by vibrational sum frequency generation spectroscopy. *Chem. Phys. Lett.*, 449:191–195, 2007.
- [141] A. G. F. de Beer, H. B. de Aguiar, J. F. W. Nijssen, and S. Roke. Detection of buried microstructures by nonlinear light scattering spectroscopy. *Phys. Rev. Lett.*, 102:095502, 2009.

-
- [142] M. L. Strader, H. B. de Aguiar, A. G. F. de Beer, and S. Roke. Label-free spectroscopic detection of vesicles in water using vibrational sum frequency scattering. *Soft Matter*, 7:4959, 2011.
- [143] H. B. de Aguiar, A. G. F. de Beer, M. L. Strader, and S. Roke. The interfacial tension of nanoscopic oil droplets in water is hardly affected by SDS surfactant. *J. Am. Chem. Soc.*, 132:2122–2123, 2010.
- [144] J. D. Jackson. *Classical electrodynamics*. Wiley, 1998.
- [145] R. W. Boyd. *Nonlinear Optics*. Academic Press, 3 edition, 2008.
- [146] D. M. Bishop, B. Kirtman, H. A. Kurtz, and J. E. Rice. Calculation of vibrational dynamic hyperpolarizabilities for H₂O, CO₂, and NH₃. *J. Chem. Phys.*, 98:8024, 1993.
- [147] A. V. Gubskaya and P. G. Kusalik. The total molecular dipole moment for liquid water. *J. Chem. Phys.*, 117:5290, 2002.
- [148] C. J. Fecko, J. D. Eaves, J. J. Loparo, A. Tokmakoff, and P. L. Geissler. Ultra-fast hydrogen-bond dynamics in the infrared spectroscopy of water. *Science*, 301:1698–1702, 2003.
- [149] J. B. Asbury, T. Steinell, K. Kwak, S. A. Corcelli, C. P. Lawrence, J. L. Skinner, and M. D. Fayer. Dynamics of water probed with vibrational echo correlation spectroscopy. *J. Chem. Phys.*, 121:12431–12446, 2004.
- [150] K. Clays and A. Persoons. Hyper-Rayleigh scattering in solution. *Rev. Sci. Instrum.*, 63:3285–3289, 1992.
- [151] T. Verbiest, M. Kauranen, A. Persoons, M. Ikonen, J. Kurkela, and H. Lemmetyinen. Nonlinear optical activity and biomolecular chirality. *J. Am. Chem. Soc.*, 116(20):9203–9205, 1994.
- [152] D. P. Shelton. Accurate hyper-Rayleigh scattering polarization measurements. *Rev. Sci. Instrum.*, 82(11):113103, 2011.
- [153] D. P. Shelton. Electric field of Ions in solution probed by hyper-Rayleigh scattering. *J. Chem. Phys.*, 130:114501, 2009.
- [154] N. Gomopoulos, C. Lütgebaucks, Q. Sun, C. Macias-Romero, and S. Roke. Label-free second harmonic and hyper Rayleigh scattering with high efficiency. *Opt. express*, 21:815–821, 2013.

- [155] B. E. A. Saleh and M. C. Teich. *Fundamentals of Photonics*. Wiley Series in Pure and Applied Optics. Wiley, 2007.
- [156] J. Ohkubo, T. Kato, H. Kono, and Y. Fujimura. Molecular alignment in a liquid induced by a nonresonant laser field: Molecular dynamics simulation. *J. Chem. Phys.*, 120:9123–9132, 2004.
- [157] I. Howell and G. W. Neilson. Li^+ hydration in concentrated aqueous solution. *J. Phys.: Condens. Matter*, 8:4455–4463, 1996.
- [158] R. Mancinelli, A. Botti, F. Bruni, M. A. Ricci, and A. K. Soper. Perturbation of water structure due to monovalent ions in solution. *Phys. Chem. Chem. Phys.*, 9:2959–2967, 2007.
- [159] A. K. Soper and K. Weckström. Ion solvation and water structure in potassium halide aqueous solutions. *Biophys. Chem.*, 124:180–191, 2006.
- [160] S. Bouazizi, S. Nasr, N. Jaïdane, and M. Bellissent-Funel. Local order in aqueous NaCl solutions and pure water: X-ray scattering and molecular dynamics simulations study. *J. Phys. Chem. B*, 110:23515–23523, 2006.
- [161] S. Bouazizi and S. Nasr. Local order in aqueous lithium chloride solutions as studied by X-ray scattering and molecular dynamics simulations. *J. Mol. Struct.*, 837:206–213, 2007.
- [162] I. Waluyo, D. Nordlund, U. Bergmann, D. Schlesinger, L. G. M. Pettersson, and A. Nilsson. A different view of structure-making and structure-breaking in alkali halide aqueous solutions through X-ray absorption spectroscopy. *J. Chem. Phys.*, 140:244506, 2014.
- [163] A. Nilsson, D. Nordlund, I. Waluyo, N. Huang, H. Ogasawara, S. Kaya, U. Bergmann, L.-Å Näslund, H. Öström, Ph. Wernet, K. J. Andersson, T. Schiros, and L. G. M. Pettersson. X-ray absorption spectroscopy and X-ray Raman scattering of water and ice; an experimental view. *J. Electron. Spectrosc. Relat. Phenom.*, 177:99–129, 2010.
- [164] J. D. Smith, R. J. Saykally, and P. L. Geissler. The effects of dissolved halide anions on hydrogen bonding in liquid water. *J. Am. Chem. Soc.*, 129:13847–13856, 2007.
- [165] R. Buchner, G. T. Hefter, and P. M. May. Dielectric relaxation of aqueous NaCl solutions. *J. Phys. Chem. A*, 103:1–9, 1999.

-
- [166] Y. Marcus and G. Hefter. Ion pairing. *Chem. Rev.*, 106:4585–621, 2006.
- [167] K. Yoshida, K. Ibuki, and M. Ueno. Estimated ionic B-coefficients from NMR measurements in aqueous electrolyte solutions. *J. Sol. Chem.*, 25:435–453, 1996.
- [168] K. J. Tielrooij, N. Garcia-Araez, M. Bonn, and H. J. Bakker. Cooperativity in ion hydration. *Science*, 328:1006–1009, 2010.
- [169] A. W. Omta, M. F. Kropman, S. Woutersen, and H. J. Bakker. Negligible effect of ions on the hydrogen-bond structure in liquid water. *Science*, 301:347–349, 2003.
- [170] M. L. Cowan, B. D. Bruner, N. Huse, J. R. Dwyer, B. Chugh, E. T. J. Nibbering, T. Elsaesser, and R. J. D. Miller. Ultrafast memory loss and energy redistribution in the hydrogen bond network of liquid H₂O. *Nature*, 434:199–202, 2005.
- [171] I. A. Heisler and S. R. Meech. Low-frequency modes of aqueous alkali halide solutions: Glimpsing the hydrogen bonding vibration. *Science*, 327:857–861, 2010.
- [172] S. Funkner, G. Niehues, D. A. Schmidt, M. Heyden, G. Schwaab, K. M. Callahan, D. J. Tobias, and M. Havenith. Watching the low-frequency motions in aqueous salt solutions: The terahertz vibrational signatures of hydrated ions. *J. Am. Chem. Soc.*, 134:1030–1035, 2012.
- [173] J. T. O. O’Brien and E. R. Williams. Effects of ions on hydrogen-bonding water networks in large aqueous nanodrops. *J. Am. Chem. Soc.*, 134:10228–10236, 2012.
- [174] J. S. Prell, J. T. O’Brien, and E. R. Williams. Structural and electric field effects of ions in aqueous nanodrops. *J. Am. Chem. Soc.*, 133:4810–4818, 2011.
- [175] M. Ceriotti, G. A. Tribello, and M. Parrinello. Demonstrating the transferability and the descriptive power of sketch-map. *J. Chem. Theory Comput.*, 9:1521–1532, 2013.
- [176] G. Stirnemann, E. Wernersson, P. Jungwirth, and D. Laage. Mechanisms of acceleration and retardation of water dynamics by ions. *J. Am. Chem. Soc.*, 135:11824–11831, 2013.
- [177] E. Lindahl, B. Hess, and D. van der Spoel. GROMACS 3.0: A package for molecular simulation and trajectory analysis. *J. Mol. Model.*, 7:306–317, 2001.

- [178] J. L. F. Abascal and C. Vega. A general purpose model for the condensed phases of water: TIP4P/2005. *J. Chem. Phys.*, 123:234505, 2005.
- [179] X. Zhu, P. E. M. Lopes, and A. D. MacKerell. Recent developments and applications of the CHARMM force fields. *WIREs Comput. Mol. Sci.*, 2:167–185, 2012.
- [180] S. Miyamoto and P. A. Kollman. Settle: An analytical version of the SHAKE and RATTLE algorithm for rigid water models. *J. Comput. Chem.*, 13:952–962, 1992.
- [181] T. Darden, D. York, and L. Pedersen. Particle mesh Ewald: An N·log(N) method for Ewald sums in large systems. *J. Chem. Phys.*, 98:10089, 1993.
- [182] H. J. C. Berendsen, J. P. M. Postma, W. F. van Gunsteren, A. DiNola, and J. R. Haak. Molecular dynamics with coupling to an external bath. *J. Chem. Phys.*, 81:3684, 1984.
- [183] G. Bussi, D. Donadio, and M. Parrinello. Canonical sampling through velocity rescaling. *J. Chem. Phys.*, 126:014101, 2007.
- [184] K. W. Bewig and W. A. Zisman. The wetting of gold and platinum by water. *J. Phys. Chem.*, 69:4238–4242, 1965.
- [185] P. N. Butcher and D. Cotter. *The elements of nonlinear optics*. Cambridge University Press, 1991.
- [186] D. P. Shelton. Hyper-Rayleigh scattering from correlated molecules. *J. Chem. Phys.*, 138:154502, 2013.
- [187] A. G. F. de Beer and S. Roke. Sum frequency generation scattering from the interface of an isotropic particle: Geometrical and chiral effects. *Phys. Rev. B*, 75:245438, 2007.
- [188] A. G. F. de Beer, R. K. Campen, and S. Roke. Separating surface structure and surface charge with second-harmonic and sum-frequency scattering. *Phys. Rev. B*, 82:235431, 2010.
- [189] E. Hendrickx, K. Clays, and A. Persoons. Hyper-Rayleigh scattering in isotropic solution. *Acc. Chem. Res.*, 31:675–683, 1998.
- [190] D. P. Shelton. Long-range orientation correlation in water. *J. Chem. Phys.*, 141:224506, 2014.

-
- [191] A. V. Gubskaya and P. G. Kusalik. The multipole polarizabilities and hyperpolarizabilities of the water molecule in liquid state: An ab initio study. *Mol. Phys.*, 99:1107–1120, 2001.
- [192] D. P. Shelton. Long-range orientation correlation in liquids. *J. Chem. Phys.*, 136:044503, 2012.
- [193] S. Habershon, T. E. Markland, and D. E. Manolopoulos. Competing quantum effects in the dynamics of a flexible water model. *J. Chem. Phys.*, 131:024501, 2009.
- [194] X. Z. Li, B. Walker, and A. Michaelides. Quantum nature of the hydrogen bond. *Proc. Natl. Acad. Sci. U.S.A.*, 108:6369–6373, 2011.
- [195] J. Drzymala and J. Lyklema. Surface tension of aqueous electrolyte solutions. thermodynamics. *J. Phys. Chem. A*, 116:6465–6472, 2012.
- [196] P. B. Petersen, J. C. Johnson, K. P. Knutsen, and R. J. Saykally. Direct experimental validation of the Jones–Ray effect. *Chem. Phys. Lett.*, 397:46–50, 2004.
- [197] J. Liu, R. S. Andino, C. M. Miller, X. Chen, D. M. Wilkins, M. Ceriotti, and D. E. Manolopoulos. A surface-specific isotope effect in mixtures of light and heavy water. *J. Phys. Chem. C*, 117:2944–2951, 2013.
- [198] Y. Nagata, R. E. Pool, E. H. G. Backus, and M. Bonn. Nuclear quantum effects affect bond orientation of water at the water-vapor interface. *Phys. Rev. Lett.*, 109:226101, 2012.
- [199] S. Kedenburg, M. Vieweg, T. Gissibl, and H. Giessen. Linear refractive index and absorption measurements of nonlinear optical liquids in the visible and near-infrared spectral region. *Opt. Mater. Express*, 2:1588, 2012.
- [200] S. A. Clough, Y. Beers, G. P. Klein, and L. S. Rothman. Dipole moment of water from Stark measurements of H₂O, HDO, and D₂O. *J. Chem. Phys.*, 59:2254, 1973.
- [201] J. Barthel, K. Bachhuber, R. Buchner, and H. Hetzenauer. Dielectric spectra of some common solvents in the microwave region. Water and lower alcohols. *Chem. Phys. Lett.*, 165:369–373, 1990.
- [202] K. R. Srinivasan and R. L. Kay. Pressure dependence of the dielectric constant of H₂O and D₂O. *J. Chem. Phys.*, 60:3645, 1974.

- [203] T. Kobayashi, K. Sasagane, F. Aiga, and K. Yamaguchi. Calculation of frequency-dependent first hyperpolarizabilities using the second-order Møller–Plesset perturbation theory. *J. Chem. Phys.*, 110:11720, 1999.
- [204] O. Christiansen, J. Gauss, and J. F. Stanton. Frequency-dependent polarizabilities and first hyperpolarizabilities of CO and H₂O from coupled cluster calculations. *Chem. Phys. Lett.*, 305:147–155, 1999.
- [205] Y. Luo, H. Ågren, O. Vahtras, P. Jørgensen, V. Spirko, and H. Hettema. Frequency-dependent polarizabilities and first hyperpolarizabilities of H₂O. *J. Chem. Phys.*, 98:7159, 1993.
- [206] D. P. Shelton. Gas phase hyper-Rayleigh scattering measurements. *J. Chem. Phys.*, 137:044312, 2012.
- [207] S. Ong, X. Zhao, and K. B. Eisenthal. Polarization of water molecules at a charged interface: Second harmonic studies of the silica/water interface. *Chem. Phys. Lett.*, 191:327–335, 1992.
- [208] J. L. Barrat and J. P. Hansen. *Basic concepts for simple and complex liquids*. Cambridge University Press, 2003.
- [209] B. J. Berne and R. Pecora. *Dynamic light scattering*. Wiley-Interscience, 1976.
- [210] N. H. March and P. Tosi. *Atomic dynamics in liquids*. Dover, 1991.
- [211] K. D. Collins. Ions from the Hofmeister series and osmolytes: Effects on proteins in solution and in the crystallization process. *Methods*, 34:300–311, 2004.
- [212] W. Kunz, P. Lo Nostro, and B. W. Ninham. The present state of affairs with Hofmeister effects. *Curr. Opin. Colloid Interface Sci.*, 9:1–18, 2004.
- [213] H. J. Bakker. Structural dynamics of aqueous salt solutions. *Chem. Rev.*, 108:1456–1473, 2008.
- [214] S. Ansell, A. C. Barnes, P. E. Mason, G. W. Neilson, and S. Ramos. X-ray and neutron scattering studies of the hydration structure of alkali ions in concentrated aqueous solutions. *Biophys. Chem.*, 124:171–179, 2006.
- [215] I. Waluyo, C. Huang, D. Nordlund, U. Bergmann, T. M. Weiss, L. G. M. Pettersson, and A. Nilsson. The structure of water in the hydration shell of cations from X-ray Raman and small angle X-ray scattering measurements. *J. Chem. Phys.*, 134:064513, 2011.

-
- [216] Q. Sun. Raman spectroscopic study of the effects of dissolved NaCl on water structure. *Vib. Spectrosc.*, 62:110–114, 2012.
- [217] R. Buchner and G. Hefter. Interactions and dynamics in electrolyte solutions by dielectric spectroscopy. *Phys. Chem. Chem. Phys.*, 11:8984–8999, 2009.
- [218] N. Ottosson, G. Öhrwall, and O. Björneholm. Ultrafast charge delocalization dynamics in aqueous electrolytes: New insights from Auger electron spectroscopy. *Chem. Phys. Lett.*, 543:1–11, 2012.
- [219] N. Ottosson, M. Odelius, D. Spångberg, W. Pokapanich, M. Svanqvist, G. Öhrwall, B. Winter, and O. Björneholm. Cations strongly reduce electron-hopping rates in aqueous solutions. *J. Am. Chem. Soc.*, 133:13489–13495, 2011.
- [220] A. S. Thomas and A. H. Elcock. Molecular dynamics simulations of hydrophobic associations in aqueous salt solutions indicate a connection between water hydrogen bonding and the Hofmeister effect. *J. Am. Chem. Soc.*, 129:14887–14898, 2007.
- [221] M. Carrillo-Tripp, H. Saint-Martin, and I. Ortega-Blake. A comparative study of the hydration of Na^+ and K^+ with refined polarizable model potentials. *J. Chem. Phys.*, 118:7062–7073, 2003.
- [222] Y. Chen, H. I. Okur, N. Gomopoulos, C. Macias-Romero, P. S. Cremer, P. B. Petersen, G. Tocci, D. M. Wilkins, C. Liang, M. Ceriotti, and S. Roke. Electrolytes induce long-range orientational order and free energy changes in the H-bond network of bulk water. *Sci. Adv.*, 2:e1501891, 2016.
- [223] Y. Zhou, J. H. Morais-Cabral, A. Kaufman, and R. MacKinnon. Chemistry of ion coordination and hydration revealed by a K^+ channel-Fab complex at 2.0 Å resolution. *Nature*, 414:43–48, 2001.
- [224] S. Varma and S. B. Rempe. Tuning ion coordination architectures to enable selective partitioning. *Biophys. J.*, 93:1093–1099, 2007.
- [225] K. D. Collins. Ion hydration: Implications for cellular function, polyelectrolytes, and protein crystallization. *Biophys. Chem.*, 119:271–281, 2006.
- [226] J. W. Ponder. TINKER: Software tools for molecular design, version 7.0. <http://dasher.wustl.edu/tinker/>.

- [227] M. L. Laury, L. Wang, V. S. Pande, T. Head-Gordon, and J. W. Ponder. Revised parameters for the AMOEBA polarizable atomic multipole water model. *J. Phys. Chem. B*, 119:9423–9437, 2015.
- [228] A. Grossfield, P. Ren, and J. W. Ponder. Ion solvation thermodynamics from simulation with a polarizable force field. *J. Am. Chem. Soc.*, 125:15671–15682, 2003.
- [229] G. J. Martyna, M. E. Tuckerman, D. J. Tobias, and M. L. Klein. Explicit reversible integrators for extended systems dynamics. *Mol. Phys.*, 87:1117–1157, 1996.
- [230] G. H. Golub and C. F. Van Loan. *Matrix computations*. Johns Hopkins University Press, 3 edition, 1996.
- [231] N.R. Draper and H. Smith. *Applied regression analysis*. Wiley, 1998.
- [232] V. Kello, B. O. Roos, and A. J. Sadlej. Electric properties of the chloride-ion. *Theor. Chim. Acta.*, 74:185–194, 1988.
- [233] P. Atkins and J. de Paula. *Atkins' physical chemistry*. Oxford University Press, 2010.
- [234] J. N. Israelachvili. *Intermolecular and surface forces*. Academic Press, 3 edition, 2010.
- [235] D. Feller, E. D. Glendening, D. E. Woon, and M. W. Feyereisen. An extended basis set ab initio study of alkali metal cation–water clusters. *J. Chem. Phys.*, 103:3526, 1995.
- [236] M. D. Baer and C. J. Mundy. An ab initio approach to understanding the specific ion effect. *Farad. Discuss.*, 160:89–101, 2013.
- [237] M. Dal Peraro, S. Raugei, P. Carloni, and M. L. Klein. Solute-solvent charge transfer in aqueous solution. *ChemPhysChem*, 6:1715–1718, 2005.
- [238] M. Soniat and S. W. Rick. The effects of charge transfer on the aqueous solvation of ions. *J. Chem. Phys.*, 137:044511, 2012.
- [239] T. Tokushima, Y. Harada, O. Takahashi, Y. Senba, H. Ohashi, L. G M Pettersson, A. Nilsson, and S. Shin. High resolution X-ray emission spectroscopy of liquid water: The observation of two structural motifs. *Chem. Phys. Lett.*, 460:387–400, 2008.

-
- [240] J. Traube. The attraction pressure. *J. Phys. Chem.*, 14:452–470, 1910.
- [241] T. Corridoni, R. Mancinelli, M. A. Ricci, and F. Bruni. Viscosity of aqueous solutions and local microscopic structure. *J. Phys. Chem. B*, 115:14008–14013, 2011.
- [242] G. Jones and M. Dole. The viscosity of aqueous solutions of strong electrolytes with special reference to barium chloride. *J. Am. Chem. Soc.*, 51:2950–2964, 1929.
- [243] W. M. Cox and J. H. Wolfenden. The viscosity of strong electrolytes measured by a differential method. *Proc. R. Soc. London, A*, 145:475–488, 1934.
- [244] K. D. Collins. Charge density-dependent strength of hydration and biological structure. *Biophys. J.*, 72:65–76, 1997.
- [245] C. F. Bohren, E. E. Clothiaux, and D. R. Huffman. *Absorption and Scattering of Light by Small Particles*. Wiley-VCH, 2007.
- [246] H. Wang, W. Gan, R. Lu, Y. Rao, and B. Wu. Quantitative spectral and orientational analysis in surface sum frequency generation vibrational spectroscopy (SFG-VS). *Int. Rev. Phys. Chem.*, 24:191–256, 2005.
- [247] A. J. Moad and G. J. Simpson. A unified treatment of selection rules and symmetry relations for sum-frequency and second harmonic spectroscopies. *J. Phys. Chem. B*, 108:3548–3562, 2004.
- [248] R. J. Hunter. *Foundations of colloid science*. Oxford University Press, Oxford ; New York, 2nd edition, 2001.
- [249] R.J. Hunter. *Zeta Potential in Colloid Science: Principles and Applications*. Academic Press, 1981.
- [250] R. W. O’Brien, B. R. Midmore, A. Lamb, and R. J. Hunter. Electroacoustic studies of moderately concentrated colloidal suspensions. *Faraday Discuss. Chem. Soc.*, 90:301–312, 1990.
- [251] R. Borsali and R. Pecora. *Soft-Matter Characterization*. Soft-Matter Characterization. Springer Netherlands, 2008.
- [252] K. Levenberg. A method for the solution of certain non-linear problems in least squares. *Q. Appl. Math.*, 2:164–168, 1944.

- [253] D. W. Marquardt. An algorithm for least-squares estimation of nonlinear parameters. *J. Soc. Ind. Appl. Math.*, 11:431–441, 1963.
- [254] M. H. Abraham, G. S. Whiting, R. Fuchs, and E. J. Chambers. Thermodynamics of solute transfer from water to hexadecane. *J. Chem. Soc. Perkin Trans. 2*, pages 291–300, 1990.
- [255] J. Als-Nielsen and D. McMorrow. *Elements of Modern X-Ray Physics*. Wiley & Sons, 2001.
- [256] B. Berge, O. Konovalov, J. Lajzerowicz, A. Renault, J. P. Rieu, M. Vallade, J. Als-Nielsen, G. Grübel, and J. F. Legrand. Melting of short 1-alcohol monolayers on water: Thermodynamics and X-ray scattering studies. *Phys. Rev. Lett.*, 73:1652–1655, 1994.
- [257] C. D. Bain. Sum-frequency vibrational spectroscopy of the solid-liquid interface. *J. Chem. Soc., Faraday Trans.*, 91:1281, 1995.
- [258] M. M. Knock, G. R. Bell, E. K. Hill, H. J. Turner, and C. D. Bain. Sum-frequency spectroscopy of surfactant monolayers at the oil-water interface. *J. Phys. Chem. B*, 107:10801–10814, 2003.
- [259] C. Delcerro and G. J. Jameson. The behavior of pentane, hexane, and heptane on water. *J. Colloid Interf. Sci.*, 78:362–375, 1980.
- [260] A. Goebel and K. Lunkenheimer. Interfacial tension of the water/n-alkane interface. *Langmuir*, 13:369–372, 1997.
- [261] D. E. Gragson, B. M. McCarty, and G. L. Richmond. Ordering of interfacial water molecules at the charged air/water interface observed by vibrational sum frequency generation. *J. Am. Chem. Soc.*, 119:6144–6152, 1997.
- [262] L. F. Scatena, M. G. Brown, and G. L. Richmond. Water at hydrophobic surfaces: weak hydrogen bonding and strong orientation effects. *Science*, 292:908–912, 2001.
- [263] M. G. Brown, D. S. Walker, E. A. Raymond, and G. L. Richmond. Vibrational sum-frequency spectroscopy of alkane/water interfaces: Experiment and theoretical simulation. *J. Phys. Chem. B*, 107:237–244, 2003.
- [264] S. Strazdaite, J. Versluis, E. H. G. Backus, and H. J. Bakker. Enhanced ordering of water at hydrophobic surfaces. *J. Chem. Phys.*, 140:054711, 2014.

-
- [265] O. Esenturk and R. A. Walker. Surface vibrational structure at alkane liquid/vapor interfaces. *J. Chem. Phys.*, 125:174701, 2006.
- [266] E. Tyrode and J. Hedberg. A comparative study of the CD and CH stretching spectral regions of typical surfactants systems using VSFS: Orientation analysis of the terminal CH₃ and CD₃ groups. *J. Phys. Chem. C*, 116:1080–1091, 2012.
- [267] P. B. Petersen and R. J. Saykally. Probing the interfacial structure of aqueous electrolytes with femtosecond second harmonic generation spectroscopy. *J. Phys. Chem. B*, 110:14060–14073, 2006.
- [268] K. C. Jena, P. A. Covert, and D. K. Hore. The effect of salt on the water structure at a charged solid surface: differentiating second- and third-order nonlinear contributions. *J. Phys. Chem. Lett.*, 2:1056–1061, 2011.
- [269] H. B. de Aguiar, R. Scheu, K. C. Jena, A. G. F. de Beer, and S. Roke. Comparison of scattering and reflection SFG: A question of phase-matching. *Phys. Chem. Chem. Phys.*, 14:6826–6832, 2012.
- [270] H. B. de Aguiar, M. L. Strader, A. G. F. de Beer, and S. Roke. Surface structure of sodium dodecyl sulfate surfactant and oil at the oil-in-water droplet liquid/liquid interface: A manifestation of a nonequilibrium surface state. *J. Phys. Chem. B*, 115:2970–2978, 2011.
- [271] R. N. Ward, D. C. Duffy, P. B. Davies, and C. D. Bain. Sum-frequency spectroscopy of surfactants adsorbed at a flat hydrophobic surface. *J. Phys. Chem.*, 98:8536–8542, 1994.
- [272] R. Vácha and S. Roke. Sodium dodecyl sulfate at water–hydrophobic interfaces: A simulation study. *J. Phys. Chem. B*, 116:11936–11942, 2012.
- [273] J. Samson, R. Scheu, N. Smolentsev, S. W. Rick, and S. Roke. Sum frequency spectroscopy of the hydrophobic nanodroplet/water interface: Absence of hydroxyl ion and dangling OH bond signatures. *Chem. Phys. Lett.*, 615:124–131, 2014.
- [274] K. M. Wilkinson, L. Qunfang, and C. D. Bain. Freezing transitions in mixed surfactant/alkane monolayers at the air–solution interface. *Soft Matter*, 2:66, 2006.
- [275] D. N. Nikogosyan. *Properties of optical and laser-related materials: A handbook*. John-Wiley sons, New York, 1997.

- [276] J. E. Bertie, M. K. Ahmed, and H. H. Eysel. Infrared intensities of Liquids. 5. Optical and dielectric-constants, integrated-intensities, and dipole-moment derivatives of H₂O and D₂O at 22 °C. *J. Phys. Chem.*, 93:2210–2218, 1989.
- [277] G. J. Simpson and K. L. Rowlen. An SHG magic angle: Dependence of second harmonic generation orientation measurements on the width of the orientation distribution. *J. Am. Chem. Soc.*, 121:2635–2636, 1999.
- [278] J. G. Davis, K. P. Gierszal, P. Wang, and D. Ben-Amotz. Water structural transformation at molecular hydrophobic interfaces. *Nature*, 491:582–585, 2012.
- [279] J. L. Rivera, C. McCabe, and P. T. Cummings. Molecular simulations of liquid-liquid interfacial properties: water-n-alkane and water-methanol-n-alkane systems. *Phys. Rev. E*, 67:011603, 2003.
- [280] H. Wang, E. C. Y. Yan, Y. Liu, and K. B. Eisenthal. Energetics and population of molecules at microscopic liquid and solid surfaces. *J. Phys. Chem. B*, 102:4446–4450, 1998.
- [281] M. L. Schlossman and A. M. Tikhonov. Molecular ordering and phase behavior of surfactants at water-oil interfaces as probed by X-ray surface scattering. *Annu. Rev. Phys. Chem.*, 59:153–177, 2008.
- [282] G. Caminati, D. Senatra, and G. Gabrielli. 1-hexanol and 1-tetradecanol adsorption at the water-oil interface. *Langmuir*, 7:1969–1974, 1991.
- [283] R. Vácha, S. W. Rick, P. Jungwirth, A. G. F. de Beer, H. B. de Aguiar, J. Samson, and S. Roke. The orientation and charge of water at the hydrophobic oil droplet-water interface. *J. Am. Chem. Soc.*, 133:10204–10210, 2011.
- [284] S. Roke, J. Schins, M. Müller, and M. Bonn. Vibrational spectroscopic investigation of the phase diagram of a biomimetic lipid monolayer. *Phys. Rev. Lett.*, 90:128101, 2003.
- [285] E. H. G. Backus, D. Bonn, S. Cantin, S. Roke, and M. Bonn. Laser-heating-induced displacement of surfactants on the water surface. *J. Phys. Chem. B*, 116:2703–2712, 2012.
- [286] M. Bonn, S. Roke, O. Berg, A. Stamouli, and M. Müller. A Molecular View of Cholesterol-Induced Condensation in a Lipid Monolayer. *J. Phys. Chem. B*, 108:19083–19085, 2004.

-
- [287] M. Sovago, E. Vartiainen, and M. Bonn. Observation of buried water molecules in phospholipid membranes by surface sum-frequency generation spectroscopy. *J. Chem. Phys.*, 131:161107, 2009.
- [288] G. Ma and H. C. Allen. DPPC Langmuir monolayer at the air-water interface: Probing the tail and head groups by vibrational sum frequency generation spectroscopy. *Langmuir*, 22:5341–5349, 2006.
- [289] X. Chen, W. Hua, Z. Huang, and H. C. Allen. Interfacial water structure associated with phospholipid membranes studied by phase-sensitive vibrational sum frequency generation spectroscopy. *J. Am. Chem. Soc.*, 132:11336–11342, 2010.
- [290] R. Walker, J. C. Conboy, and G. Richmond. Molecular structure and ordering of phospholipids at a liquid-liquid interface. *Langmuir*, 13:3070–3073, 1997.
- [291] R. A. Walker, J. A. Gruetzmacher, and G. L. Richmond. Phosphatidylcholine monolayer structure at a liquid-liquid interface. *J. Am. Chem. Soc.*, 120:6991–7003, 1998.
- [292] M. R. Watry, T. L. Tarbuck, and G. L. Richmond. Vibrational sum-frequency studies of a series of phospholipid monolayers and the associated water structure at the vapor/water interface. *J. Phys. Chem. B*, 107:512–518, 2003.
- [293] W. Liu, Z. Wang, L. Fu, R. M. Leblanc, and E. C. Y. Yan. Lipid compositions modulate fluidity and stability of bilayers: Characterization by surface pressure and sum frequency generation spectroscopy. *Langmuir*, 29:15022–15031, 2013.
- [294] J. A. Mondal, S. Nihonyanagi, S. Yamaguchi, and T. Tahara. Three distinct water structures at a zwitterionic lipid/water interface revealed by heterodyne-detected vibrational sum frequency generation. *J. Am. Chem. Soc.*, 134:7842–7850, 2012.
- [295] J. Kim, G. Kim, and P. S. Cremer. Investigations of water structure at the solid/liquid interface in the presence of supported lipid bilayers by vibrational sum frequency spectroscopy. *Langmuir*, 17:7255–7260, 2001.
- [296] V. Kaganer, H. Möhwald, and P. Dutta. Structure and phase transitions in Langmuir monolayers. *Rev. Mod. Phys.*, 71:779–819, 1999.

- [297] J. Als-Nielsen, D. Jacquemain, K. Kjaer, F. Leveiller, M. Lahav, and L. Leiserowitz. Principles and applications of grazing incidence X-ray and neutron scattering from ordered molecular monolayers at the air-water interface. *Phys. Rep.*, 246:251–313, 1994.
- [298] K. Kjaer, J. Als-Nielsen, C. A. Helm, L. A. Laxhuber, and H. Möhwald. Ordering in lipid monolayers studied by synchrotron x-ray diffraction and fluorescence microscopy. *Phys. Rev. Lett.*, 58:2224–2227, 1987.
- [299] C. M. Knobler and R. C. Desai. Phase transitions in monolayers. *Annu. Rev. Phys. Chem.*, 43:207–236, 1992.
- [300] G. Brezesinski, M. Thoma, B. Struth, and H. Mohwald. Structural changes of monolayers at the air/water interface contacted with n-alkanes. *J. Phys. Chem.*, 100:3126–3130, 1996.
- [301] M. Schalke and M. Lösche. Structural models of lipid surface monolayers from X-ray and neutron reflectivity measurements. *Adv. Colloid Interface Sci.*, 88:243–274, 2000.
- [302] R. K. Thomas. Neutron reflection from liquid interfaces. *Annu. Rev. Phys. Chem.*, 55:391–426, 2004.
- [303] S. Krueger. Neutron reflection from interfaces with biological and biomimetic materials. *Current Opinion in Colloid and Interface Science*, 6:111–117, 2001.
- [304] H. M. McConnell. Structures and transitions in lipid monolayers at the air-water interface. *Annu. Rev. Phys. Chem.*, 42:171–195, 1991.
- [305] C. F. Monson, X. Cong, A. D. Robison, H. P. Pace, C. Liu, M. F. Poyton, and P. S. Cremer. Phosphatidylserine reversibly binds Cu^{2+} with extremely high affinity. *J. Am. Chem. Soc.*, 134:7773–7779, 2012.
- [306] M. C. Phillips and D. Chapman. Monolayer characteristics of saturated 1,2-diacyl phosphatidylcholines (lecithins) and phosphatidylethanolamines at the air-water interface. *Biochim. Biophys. Acta*, 163:301–313, 1968.
- [307] S. L. Duncan and R. G. Larson. Comparing experimental and simulated pressure-area isotherms for DPPC. *Biophys. J.*, 94:2965–2986, 2008.

-
- [308] H. Dominguez, A. M. Smondyrev, and M. L. Berkowitz. Computer simulations of phosphatidylcholine monolayers at air/water and CCl₄/water interfaces. *J. Phys. Chem. B*, 103:9582–9588, 1999.
- [309] R. Vácha, P. Jurkiewicz, M. Petrov, M. L. Berkowitz, R. A. Böckmann, J. Barucha-Kraszewska, M. Hof, and P. Jungwirth. Mechanism of interaction of monovalent ions with phosphatidylcholine lipid membranes. *J. Phys. Chem. B*, 114:9504–9509, 2010.
- [310] W. F. D. Bennett and D. P. Tieleman. Computer simulations of lipid membrane domains. *Biochim. Biophys. Acta*, 1828:1765–1776, 2013.
- [311] W. Shinoda, R. Devane, and M. L. Klein. Zwitterionic lipid assemblies: Molecular dynamics studies of monolayers, bilayers, and vesicles using a new coarse grain force field. *J Phys. Chem. B*, 114:6836–6849, 2010.
- [312] D. J. Tobias, K. Tu, and M. L. Klein. Atomic-scale molecular dynamics simulations of lipid membranes. *Curr. Opin. Colloid Interface Sci.*, 2:15–26, 1997.
- [313] D. Rose, J. Rendell, D. Lee, K. Nag, and V. Booth. Molecular dynamics simulations of lung surfactant lipid monolayers. *Biol. Chem.*, 138:67–77, 2008.
- [314] Y. N. Kaznessis, S. Kim, and R. G. Larson. Simulations of zwitterionic and anionic phospholipid monolayers. *Biophys. J.*, 82:1731–1742, 2002.
- [315] J. Faraudo and A. Travesset. Phosphatidic acid domains in membranes: effect of divalent counterions. *Biophys. J.*, 92:2806–2818, 2007.
- [316] T. Gutsmann, T. Heimburg, U. Keyser, K. R. Mahendran, and M. Winterhalter. Protein reconstitution into freestanding planar lipid membranes for electrophysiological characterization. *Nat. Protoc.*, 10:188–198, 2014.
- [317] H. H. Klump, B. P. Gaber, W. L. Peticolas, and P. Yager. Thermodynamic properties of mixtures of deuterated and undeuterated dipalmitoyl phosphatidylcholines (Differential scanning calorimetry/lipid bilayers/membranes). *Thermochimica Acta*, 48:361–366, 1981.
- [318] N. Tokutake, B. Jing, H. Cao, and S. L. Regen. Quantifying the effects of deuterium substitution on phospholipid mixing in bilayer membranes. a nearest-neighbor recognition investigation. *J. Am. Chem. Soc.*, 125:15764–15766, 2003.

- [319] S. Z. Can, C. F. Chang, and R. A. Walker. Spontaneous formation of DPPC monolayers at aqueous/vapor interfaces and the impact of charged surfactants. *Biochim. Biophys. Acta*, 1778:2368–2377, 2008.
- [320] J. Liu and J. C. Conboy. Structure of a gel phase lipid bilayer prepared by the Langmuir-Blodgett/Langmuir-Schaefer method characterized by sum-frequency vibrational spectroscopy. *Langmuir*, 21:9091–9097, 2005.
- [321] X. Chen and H. C. Allen. Interactions of dimethylsulfoxide with a dipalmitoylphosphatidylcholine monolayer studied by vibrational sum frequency generation. *J. Phys. Chem. A*, 113:12655–12662, 2009.
- [322] M. Thoma and H. Möhwald. Phospholipid monolayers at hydrocarbon/water interfaces. 162:340–349, 1994.
- [323] J. F. D. Liljeblad, V. Bulone, M. W. Rutland, and C. M. Johnson. Supported phospholipid monolayers. The molecular structure investigated by vibrational sum frequency spectroscopy. *J. Phys. Chem. C*, 115:10617–10629, 2011.

Curriculum Vitae

Yixing Chen (陈怡星)

Av. d'Echallens 56, 1004 Lausanne, Switzerland

Email: chenyx1987@gmail.com

Born on 16.09.1987 in Hunan, China

Chinese

Education

École Polytechnique Fédérale de Lausanne (EPFL), Switzerland

2017 **Ph.D.** in Photonics. Thesis director: Prof. Sylvie Roke.

Thesis: *Molecular insights in aqueous systems: From electrolyte solutions to aqueous nanoscale interfaces*

Friedrich-Schiller-Universität Jena (FSU Jena), Germany

2011 **M.Sc.** in Photonics. Thesis director: Prof. Stefan Skupin;

Co-director: Dr. Andreas Heinrich.

Thesis: *Scattering light of nano-particles*

Nankai University & Tianjin University, China

2009 **B.Sc. & B.Eng.** (dual degrees) in Opto-electronics.

Professional Experience

École Polytechnique Fédérale de Lausanne (EPFL), Switzerland.

2012 – 2017 Assistant-Doctorant on physical chemistry, nanoscale interface sciences, colloids and emulsions: Theoretical modeling and nonlinear spectroscopy.

Carl Zeiss AG, Germany.

2011 Research intern (master thesis) on interfacial nanoparticle characterization: Theoretical modeling and light scattering experiments.

Institute of Condensed Matter Theory and Solid State Optics, FSU Jena, Germany.

2010 – 2011 Research intern on theoretical modeling of THz generation from ionizing laser pulses in gases.

Institute for Optics and Quantum Electronics, FSU Jena, Germany.

2010 – 2011 Research intern on defects detection of laser active medium: Theoretical modeling and optical detection.

Teaching Experience

École Polytechnique Fédérale de Lausanne (EPFL), Switzerland.

2013 – 2015 Teaching assistant in Photonics and Microengineering.

Physics and Astronomy Department, FSU Jena, Germany.

2009 – 2010 Tutor in Physics.

Soft Skills

Language	English (fluent), Chinese(native)
Computer	Matlab, Mathematica, Igor Pro, Labview, Adobe Illustrator, MS-Office, Latex

Awards

2017	Chinese Government Award for Outstanding Self-financed Students Abroad, China.
2009 – 2011	ASP Scholarship, Federal Government of Germany, Germany.
2008	People's Scholarship, Tianjin University, China.
2006 – 2007	University Scholarship, Nankai University, China.
2005	Second Prize, Chinese Physics Olympiad (high school), China.

Extracurricular Activities

Basketball:	Lausanne Université Club Basketball, Switzerland. 2016 – 2017 Chinese Student & Scholars Association Lausanne, Switzerland. 2016 - 2017
Tennis, Skiing	

Lausanne, March 2017

